UNIVERSITY OF SOUTHAMPTON

ANNEALING STUDIES OF DETECTOR MATERIALS FOR UNCOOLED THERMAL IMAGING

Paul Peter Donohue

Doctor of Philosophy

FACULTY OF ENGINEERING AND APPLIED SCIENCE

DEPARTMENT OF ELECTRONICS AND COMPUTER SCIENCE

May 2001

UNIVERSITY OF SOUTHAMPTON

ABSTRACT

FACULTY OF ENGINEERING AND APPLIED SCIENCE
DEPARTMENT OF ELECTRONICS AND COMPUTER SCIENCE

Doctor of Philosophy

ANNEALING STUDIES OF DETECTOR MATERIALS FOR UNCOOLED THERMAL IMAGING

by Paul Peter Donohue

Uncooled thermal imaging is a key technology for military applications. The sensors used are thermal detectors which respond to changes in temperature resulting from absorption of infrared radiation, generally in the 8-14μm waveband. In the UK these have been principally based on the pyroelectric effect in ferroelectric materials which have been incorporated into hybrid detectors where the detector elements are machined from bulk ceramic, either lead zirconate titanate (PZT) or lead scandium tantalate (PST), and then flip-chip bonded to a readout IC (ROIC). Since this is equipment and labour intensive, detectors are expensive to produce and, in addition, the detector structures used limit the achievable noise equivalent temperature difference (NETD) to ~100mK in the scene.

To reduce cost and improve performance over the hybrid approach, the next generation of uncooled detectors will be based on an integrated technology, where the detector is fabricated in the form of a microbridge by the surface micromachining of the thin film materials, including the ferroelectric, required to form the structure. Fabrication can be done in two ways, either a fully integrated approach where layers are built up directly on the ROIC, or via a composite route where the detectors are fabricated on an intermediate wafer that is then flip chip bonded to the ROIC.

The work reported determines the thermal budget of the ROIC and the optimum processes for the deposition and annealing of ferroelectric PST thin films for use in integrated IR detector arrays. Investigation into the ROIC used in the UK programme has found that the thermal budgets were 550°C for 4 hours for sputtering and 600°C for 30s for rapid thermal processing (RTP). Research into thin film PST using a low-temperature deposition/high temperature anneal has been carried out. Deposition at 300°C by single and dual RF magnetron sputtering gave a poorly crystallised pyrochlore/amorphous structure. RTP annealing was successfully employed to convert this to the required perovskite phase, although not within the ROIC thermal budget, and found to offer distinct advantages over oven annealing. At temperature-time products achievable using the composite approach, PST with relaxor ferroelectric properties was found to give materials merit figures for IR detection of up to $5.8\pm0.9\times10^{-5}Pa^{-1/2}$, well in excess of those reported from other thin film ferroelectric materials. In conjunction with a high efficiency detector structure this will enable fabrication of detectors of sub 100mK NETD.

In addition to the work on PST, excimer laser annealing of low-temperature deposited PZT has been investigated for use in a fully integrated detector fabrication process. Modelling has shown that the PZT could be heated preferentially to induce perovskite formation whilst the ROIC could be kept within its thermal budget, but that the short laser pulse resulted in extreme surface heating of and poor heat distribution in the PZT. Using a bespoke temporal pulse-extender the laser pulse was lengthened from 25ns to 375ns, lowering surface temperatures and improving heat distribution in the PZT. Pulse-extended excimer laser annealing of 0.5μm thick PZT was found to be capable of transforming over half the film. The transformable depth was limited by a problem associated with the melting of the lead oxide component of the as deposited PZT, and was less than that required for the detector structures under consideration in the UK programme.

Contents

List of Figures

List of Tables

Acknowledgements

The success of the UK uncooled thermal imaging has been in no small measure due to Rex Watton, who's dedication and huge personal effort have seen the programme through some difficult times. Without Rex's support and patronage the work presented in this thesis would not have been possible and he is thanked accordingly. I would also like to reserve special thanks for Mike Todd and Paul Manning, encouragement and support from both of whom were indispensable. DERA is thanked for providing the financial support that has enabled me to pursue the external PhD that has resulted in this thesis.

I would like to thank my colleagues at DERA for their invaluable technical support, in particular Mike Todd, Rex Watton, Mike Slater, Mark Harper, Graham Monnington, Carl Anthony, Jason Jones, David Wallis, Chris Reeves and John Russell. Also the contribution of the staff of the Nanotechnology group at Cranfield University, particularly Zhaorong Huang and Roger Whatmore, are very much appreciated. Anil Patel of BAE Systems and John Fox, David Wilcock and Nick Stogdale of Phoenix VLSI are thanked for technical assistance and valuable discussions. Phil Rumsby of Exitech Ltd. is thanked for his illuminating discussions and assistance with the excimer laser annealing work.

Special thanks are also due to Harvey Rutt who has supervised me through this work. Your support, guidance and enthusiasm have kept me going through thick and thin. The contribution of your stories and tales of adventure cannot be underestimated.

I would like to thank my family for their love and support, as always Sian and Niamh and also my parents for making all this possible. Finally I would like to thank Hugh Seton, Mike Todd, Jason Jones, Peter Fairley and William Lea for your friendship, support and encouragement.

Author’s Declaration

I declare that the material presented in this thesis is my own work. Where results have been either wholly or partly gained from collaboration with colleagues this has been indicated in the relevant chapters and duly acknowledged. The work is original and has not been previously submitted for the award of a degree.

Definitions and Abbreviations

Frequently used definitions and abbreviations in this thesis are listed below:

A	Area
α	Optical absorption coefficient
BST	Barium Strontium Titanate
C	Capacitance
D	Electric displacement (Chapter 2)
D	Thermal Diffusivity (Chapters 7 & 8)
δ	Diffuseness parameter
DRAM	Dynamic Random Access Memory
E	Electric field
ε_0	Permittivity of free space
EDS	Energy Dispersive Spectroscopy
ε_r	Relative permittivity
ε_r^{max}	Maximum relative permittivity
ν	Frequency
FeRAM	Ferroelectric Random Access Memory
F_D	Material merit figure
FIB	Focussed Ion Beam
I	Current
I_{per}	Perovskite rocking curve integrated intensity
I_{pyr}	Pyrochlore rocking curve integrated intensity
IR	Infrared
JCPDS	Journal of the Centre for Powder Diffraction Studies
k	Optical extinction coefficient
κ	Reciprocal permittivity (Chapter 2)
κ	Thermal conductivity (except Chapter 2)
MTF	Modulation Transfer Function
n	Refractive index

NEP	Noise Equivalent Power
NETD	Noise Equivalent Temperature Difference
p	Pyroelectric coefficient
PMN	Lead Magnesium Niobate
P_s	Spontaneous polarisation
PST	Lead Scandium Tantalate
PZT	Lead Zirconate Titanate
R	X-Ray range
ρ	Density
R	Reflectivity
Ra	Average surface roughness
RAB	Radiation Absorbed in the Bridge
ROIC	Readout Integrated Circuit
Rq	RMS surface roughness
RTP	Rapid Thermal Processing
SAED	Small Area Electron Diffraction
SEM	Scanning Electron Microscope
T	Temperature
t	Time
tanδ	Tangent of phase angle of lossy dielectric
T_a	Ambient temperature
T_c	Curie temperature
TEM	Transmission Electron Microscope
T_{max}	Temperature of the dielectric maximum
$T_{interface}$	Maximum temperature at ferroelectric/platinum interface
$T_{silicon}$	Maximum temperature at top surface of silicon
$T_{surface}$	Maximum temperature at top surface of ferroelectric
V	Voltage
ϖ	Angular frequency
XAC	eXtended Area Collector
XRD	X-Ray diffraction

YBCO	Yttrium Barium Cuprate
ZAF	Atomic number, absorption and fluorescence correction factor

Chapter 1:

Introduction

1.1 Background

Thermal imaging has long been recognised as an important technology for military applications, effectively turning night into day on the battlefield and affording a full 24 hour engagement capability. Applications of this technology include night vision requirements for vehicles, aircraft, ships and troops as well as use in terminally guided sub-munitions and missiles. As thermal imaging technology has become more established, through military patronage, an increasing number of commercial applications have arisen. As in the military arena these systems enjoy a wide range of uses including fire fighting, medical thermography, night vision for automotive uses, non-destructive evaluation, heat management and monitoring for safety and security purposes.

In the UK and elsewhere current in-service military thermal imagers are based on photon detectors, based on narrow gap semiconductors such as CMT, which are normally operated in the 70-80K temperature range via the use of cryogenic refrigerators such as Joule-Thomson effect coolers or closed cycle cooling engines [1]. These systems are in general composed of either a linear or small two-dimensional array of detectors which in conjunction with precision scanning optics produces the visible representation of the IR scene [1, 2], although large staring arrays are available. Perceived disadvantages of the current in-service systems are high power consumption, high weight, high initial purchase cost, high in-service costs and a high logistical burden in battlefield operations, the latter being especially true for gas cooled systems.

The work presented in this thesis was performed on a UK MOD programme to research and develop uncooled thermal imagers for military use. Benefits of uncooled technology include low power consumption, low mechanical complexity due to the use of staring array technology dispensing with scanning requirements, low initial purchase cost, low in-service costs and low logistical burden. The majority of the cost and logistical benefits arise from the lack of cryogenic cooling and precision optical scanning requirements. In the UK the primary uncooled detector technology is based on the ferroelectric materials lead zirconate

titanate (PZT) and lead scandium tantalate (PST) [3], both of which exhibit a pyroelectric effect. Detectors fabricated using these materials are thermal detectors i.e. they respond to changes in temperature resulting from absorption of IR radiation, and are operated in the 8-14μm IR waveband. Although inherently not as sensitive as photon detectors, the use of staring array technology in conjunction with 8-14μm operation results in sufficient performance to rival, and ultimately replace, low- to mid range cooled systems.

Current generation ferroelectric based uncooled detectors are based on hybrid array technology [4]. This involves the fabrication of the detector structure from ferroelectric bulk ceramic material which is then connected to a readout IC (ROIC) via a flip chip bonding process[4]. Using the more sensitive material PST, with an applied electrical bias field, 256×128 and 384×288 element staring array detectors have been fabricated with noise equivalent temperature differences (NETD's) of ~100mK[5]. Disadvantages of this technology include relatively high production costs due to the labour and equipment intensive processing required and limited sensitivity due to the thermal performance of the hybrid detector structure. To overcome these disadvantages, research is in progress to replace the hybrid array technology with detectors fabricated using an integrated process in which the thin film detector materials are formed into a microbridge structure using surface micromachining techniques. Although the thin film ferroelectric material will have inferior properties to the ceramic, principally due to lower processing temperatures, this is more than made up for by the higher efficiency detector structure compared to that used in the hybrid approach.

The work reported in this thesis covers research into several aspects of integrated array technology, with particular emphasis on the material PST, which promises sub 100mK performance in large array formats. For a fully integrated process the detector layers are built up directly on top of the ROIC. This means that processing of the ferroelectric material must be within the thermal budget of the ROIC, which uses standard CMOS circuitry. Part of the thesis reports an investigation into the thermal budget limitations of the ROIC, information on which is scarce in the literature. Also reported are the results of annealing studies on PST and PZT thin films, deposited below the temperature at which the required perovskite phase is formed. The initial aim of this study was to investigate whether these materials could be converted to perovskite within the ROIC thermal budget

and give good materials merit figure for IR detection (F_D). Annealing of low temperature deposited PZT into the required perovskite phase was accomplished using a novel pulse-extended excimer laser heating technique. Part way through this work the advent of a composite wafer technology, where the microbridge structures are fabricated on an interconnect wafer which is then flip-chip bonded to the ROIC wafer, allowed a relaxation of the temperature restrictions on ferroelectric processing. As a consequence of this it was possible to investigate the effect on materials and electrical properties of PST by annealing at temperatures well in excess of the ROIC survival limits.

1.2 Structure of the Thesis

Some of the work reported in this thesis builds upon the knowledge and experience resulting from research programmes involved with hybrid uncooled IR detectors. In particular the work on thin film PST draws upon both previous bulk ceramic work [3, 6], performed by staff at BAE Systems Caswell, and thin film PST work [7] carried out by colleagues of the author at DERA Malvern.

The layout of the thesis is as follows: Chapter 2 details background information and some of the theoretical considerations relating to the work presented in the experimental chapters. Topics such as materials structures, ferroelectricity, thermal imaging and uncooled thermal detector structures are covered. In Chapter 3 the experimental techniques common to the work reported in the thesis are discussed. This chapter includes a detailed investigation into compositional analysis using the energy dispersive spectroscopy technique. Also covered are other materials analysis techniques as well as the methods of electrically characterising ferroelectric materials intended for use in uncooled IR detectors. Chapter 4 describes the investigation into the temperature limitations of the detector ROIC, in terms of both rapid thermal processing (RTP) and high temperature sputtering. Chapter 5 reports results of the deposition of thin film PST by single RF magnetron sputtering at 300°C, followed by both RTP and furnace annealing to convert the film to perovskite. Chapter 6 describes a similar study carried out on PST deposited at both 450°C and 300°C using dual RF magnetron sputtering. In particular, for the 300°C deposited PST a novel method of machine operation was used which greatly enhanced compositional control. Chapter 7 details the design of an experiment to perform excimer laser annealing of the ferroelectric layer along with thermal

modelling of the temperature distributions obtained during laser irradiation. This technique was aimed at a fully integrated process with the ferroelectric layer being preferentially heated by the laser, with the underlying ROIC temperature not being significantly increased. Modelling showed that this was possible but highlighted the problem of severe surface heating and poor temperature distribution in both PST and PZT thin films. To resolve this a novel pulse extension technique was used, which was shown by modelling to ease the temperature distribution problems. In Chapter 8 the pulse-extended excimer laser annealing of PZT thin films is reported, with conversion to perovskite being obtained. Finally Chapter 9 concludes the work, summarising the main results and suggesting areas of future work.

Chapter 2:

Background and Theory.

2.1 Introduction

The purpose of this chapter is to describe some of the concepts and terminology used throughout this thesis. A bottom up approach has been taken which starts with descriptions of basic crystal structures and progresses through the topics of ferroelectricity, dielectric properties, the pyroelectric effect, pyroelectric detector physics, thermal imaging and finally a description of uncooled thermal detector structures. The theory of the work on laser annealing of thin film ferroelectric materials has been kept separate and is presented in Chapter 7.

2.2 Crystal Structures

2.2.1 Perovskite Structure

Perovskites are a very important group of ferroelectrics, so called because their structure is that of the mineral perovskite, calcium titanate ($CaTiO_3$), which is actually orthorhombic. The idealised perovskite structure is centrosymmetric with the general formula ABO_3, where A is a monovalent or divalent metal and B is a tetravalent or pentavalent metal. Figure 2.1(a) shows the basic structure drawn with the A-site cation in the body centre position, in 12 coordination with surrounding oxygen ions. The B-site cations inhabit the cube corner positions, in 6 coordination with surrounding oxygen, while the oxygen atoms themselves are to be found between B-sites at the cube corners. An alternative view is shown in Figure 2.1(b) where the basic structure has been drawn with the B-site on the body centre. The A-site cations now inhabit the cube corners and the oxygen atoms are at the face centres and form an octahedron around the B-site.

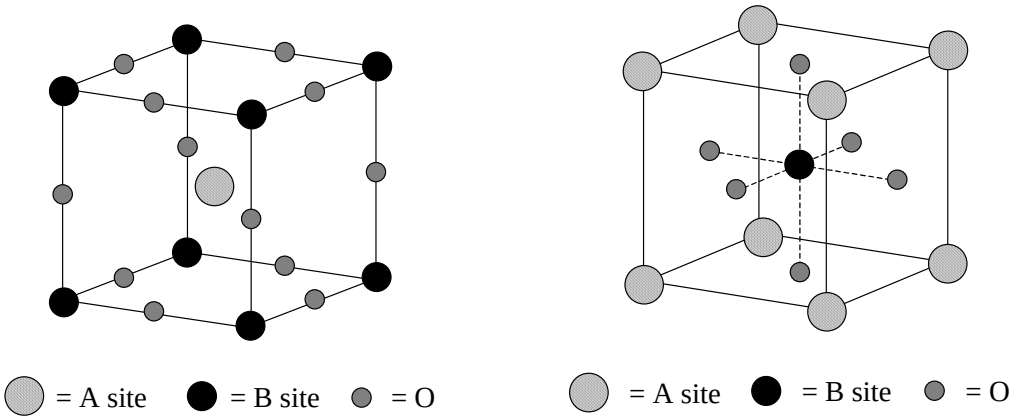

(a) (b)

Figure 2.1: Perovskite unit cell
(a) A-site cation at body centre (b) B-site cation at body centre.

The allowable cation combinations in the structure are governed by charge neutrality and structural constraints. Charge neutrality for the structure

$$A_x^{m+}B_y^{n+}O_3^{2-} \tag{2.1}$$

is given by

$$mx + ny - 6 = 0 \tag{2.2}$$

A simple example of this principle is the material lead titanate. Lead resides on the A-site as Pb^{2+} while titanium resides on the B-site as Ti^{4+}, giving overall charge neutrality. As well as charge neutrality constraints, for the structure to be stable there are also size constraints for the constituent cations. This size constraint is described by a tolerance factor t, due to Goldschmidt [8], of the perovskite structure to cation size which is given by

$$t = \frac{r_A + r_O}{\sqrt{2}\left(r_B + r_O\right)} \tag{2.3}$$

where r_A is the A-site cation radius (in 12 coordination), r_B is the B-site cation radius (in 6 coordination) and r_O is the oxygen ion radius. The tolerance factor has an approximate range of $0.95 \rightarrow 1.04$ for cubic symmetry and a somewhat larger range for distorted perosvkite structures. In reality most perovskite materials only take on the idealised structure above the Curie temperature. Below this temperature distortions in the structure result in non-aligned positive and negative charge centres giving rise to such properties as ferroelectricity, which is utilised by pyroelectric based uncooled IR detectors.

2.2.2 Pyrochlore Structure.

Pyrochlore is a competing phase in perovskite materials and may form either in preference to or along with the perovskite form. Oxide pyrochlores have the general formula $A_2B_2O_7$ (where A and B are metal ions) [9] and are isostructural to the mineral pyrochlore, $(NaCa)(NbTa)O_6F/(OH)$. A very extensive review of oxide pyrochlores is given by Subramanian et al [9]. Figure 2.2 shows the basic pyrochlore structure based on the fluorite structure [9, 10].

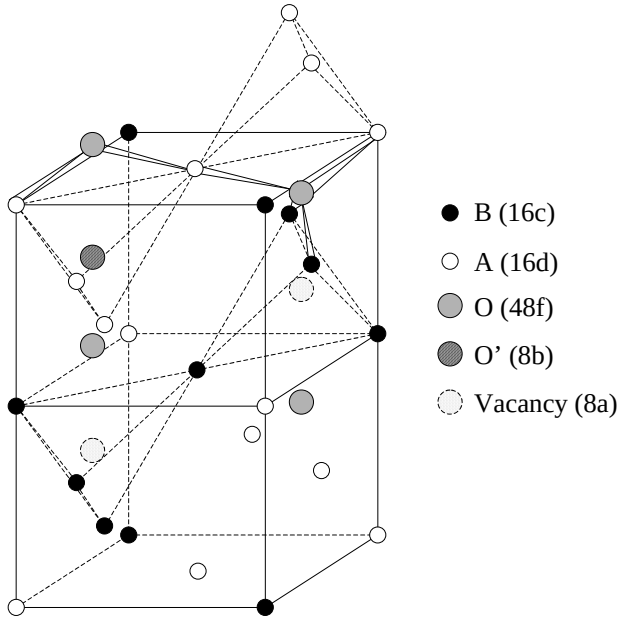

Figure 2.2: Pyrochlore unit cell based on a fluorite lattice[9, 10].

The pyrochlore structure is very tolerant to defects, in particular to deficiencies in either the large A cations or the oxygen ions[11, 9] and as such can have high ionic conductivity [9], an undesirable trait in a dielectric. A material with a true pyrochlore structure is characterised by the appearance in the X-Ray diffraction spectra of cell doubling (odd indexed) superlattice reflections which are absent if the material has a defect fluorite structure [12]. In their study of phase stability of $Pb(B'_xB''_{1-x})O_3$ complex perovskites Ling et al [11] found that a cubic pyrochlore formed as a competing or dominant phase to perovskite. The structure of this pyrochlore was found to be $Pb(B'_xB''_{1-x})^{4+}O_{3+y}$ where y can vary from 3 to 3.5 without affecting the stability. In terms of processing temperature pyrochlore was found to form a metastable state at low temperatures which could then be converted to perovskite using a high temperature anneal. Alternatively high temperature processing was found to favour the formation of perovskite directly.

Relatively few pyrochlore compounds are known to be ferroelectric, cadmium niobate ($Cd_2Nb_2O_7$) being one example [9], albeit at low temperatures (T_c~185K). In general pyrochlores are characterised by a low dielectric constant and high dielectric loss[11] and is undesirable in material used for ferroelectric-based uncooled IR detectors.

2.3 Lead Scandium Tantalate

Lead Scandium Tantalate (PST) is a complex perovskite of the form $A(B'B'')O_3$ with the formula $Pb(Sc_{1/2}Ta_{1/2})O_3$ and a ferroelectric-paraelectric phase transition at temperatures in the region 20-30°C [7, 13, 14]. The B-site contains Sc^{3+} and Ta^{5+} cations while the A-site is occupied by a Pb^{2+} cation, with charge neutrality being observed since the average B-site valency is four. PST has two forms in the perovskite state, generally referred to as ordered and disordered. In the disordered case the crystal has, above the Curie temperature, the basic perovskite form shown in Figure 2.1. The Sc^{3+} and Ta^{5+} cations are randomly distributed over the B-site positions. In the case of ordered PST the Sc^{3+} and Ta^{5+} cations are positioned on alternate B-sites, Figure 2.3 [15], forming a superlattice structure which has the effect of doubling the dimensions of the unit cell compared to the disordered case.

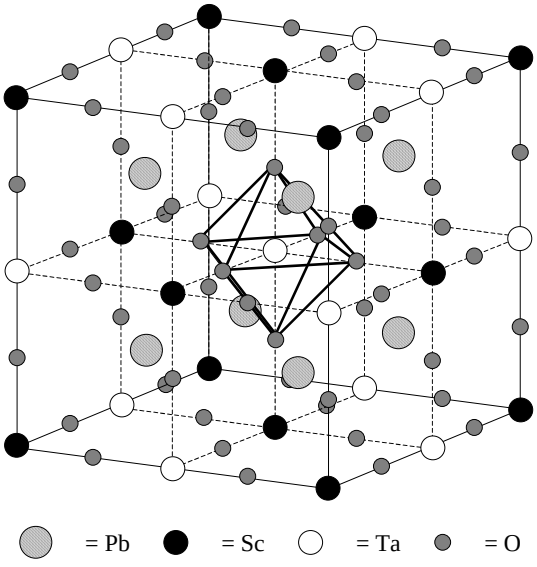

Figure 2.3: Ordered PST perovskite unit cell[15].

The tendency for PST to order is driven by the minimisation of the electrostatic and strain energies in the structure [16, 17] with strain energy involving the ionic radii and the electrostatic energy involving the ionic charge. A-site cation size has an effect on the

tendency to order [18]. An example of this are the disordered materials $Pb(Zn_{1/3}Nb_{2/3})O_3$ and $Ba(Zn_{1/3}Nb_{2/3})O_3$ while $Sr(Zn_{1/3}Nb_{2/3})O_3$, with its smaller A-site cation, is ordered. In some other complex perovskite structures such as Lead Magnesium Tungstate {$Pb(Mg_{1/2}W_{1/2})O_3$ or PMW} and Lead Holmium Niobate {$Pb(Ho_{1/2}Nb_{1/2})O_3$ or PHN} there is a strong tendency to order [16]. In PMW this is due to electrostatic considerations, i.e. the large charge difference between Mg^{2+} and W^{6+}. For PHN the tendency to order is due to strain considerations, i.e. to the large difference in the ionic radii of Ho^{3+} ($r_B = 0.89\sum$ [19]) and Nb^{5+} ($r_B = 0.64\sum$ [19]). In the case of PST the intermediate charge and size differences between Sc^{3+} ($r_B = 0.73\sum$[19]) and Ta^{5+} ($r_B = 0.64\sum$[19]) result in a less strong tendency to order. Galasso and Darby [20] found that for complex perovskites there is a critical minimum percentage difference in the B cation radii of between 7 and 17% for ordering to occur. For PST the percentage difference is only 12% while in the PHN example above it is 28% with the effect that PST exists on a boundary between always order and always disorder. It was for this reason PST was specifically chosen by Setter and Cross[13, 18] to investigate the effect of the degree of ordering on the ferroelectric properties.

The study by Setter and Cross [13, 18] found that ordering has a profound effect on the electrical properties of PST. They found that disordered PST exhibits a diffuse phase transition characteristic of a ferroelectric relaxor, while ordered PST exhibits a sharp first order ferroelectric phase transition. These types of transition are discussed in more detail in section 2.5 below. In disordered PST there is chemical inhomogeneity on the microscopic scale, as first suggested by Smolenski[21] to explain the dielectric properties of the material PMN. A simple but effective demonstration of how these micro-regions may come about was given by Cross [22], where a coin tossing experiment was used to determine the occupancy of the B-site locations for PST e.g. heads for scandium and tales for tantalum. The result of such an experiment is shown in Figure 2.4(a). Two regions are highlighted, one which is tantalum rich and another which is scandium rich. For comparison the ordered structure is shown in Figure 2.4(b).

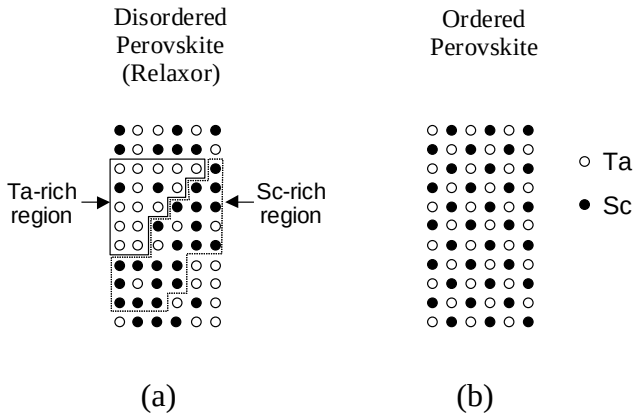

Figure 2.4: Disordered (a) and ordered (b) PST.

PST has a competing pyrochlore phase which forms at low temperatures and in material which is not stoichiometric with the perovskite phase [23]. This pyrochlore phase tends to degrade the ferroelectric properties of the material due to the formation of low dielectric constant inclusions which can form blocking layers and leakage paths. It will be shown in Chapters 5 and 6 of this thesis that this pyrochlore phase is metastable and can be converted to perovskite using high temperature annealing.

2.4 Lead Zirconate Titanate

Lead zirconate titanate (PZT) is an important material used in pyroelectric[24, 25], piezoelectric[26], electro-optic, DRAM[27] and ferroelectric memory[28, 27] applications. Bulk ceramic PZT is a solid solution of lead zirconate ($PbZrO_3$) and lead titanate ($PbTiO_3$), each having the a distorted form of the perovskite ABO_3 structure. At room temperature $PbTiO_3$ has a tetragonal distortion of the perovskite structure and is ferroelectric while $PbZrO_3$ has a rhombohedral distortion and is antiferroelectric. The solid solutions formed have a variety of structures and properties as indicated in the PZT system phase diagram[15] shown in Figure 2.5 below.

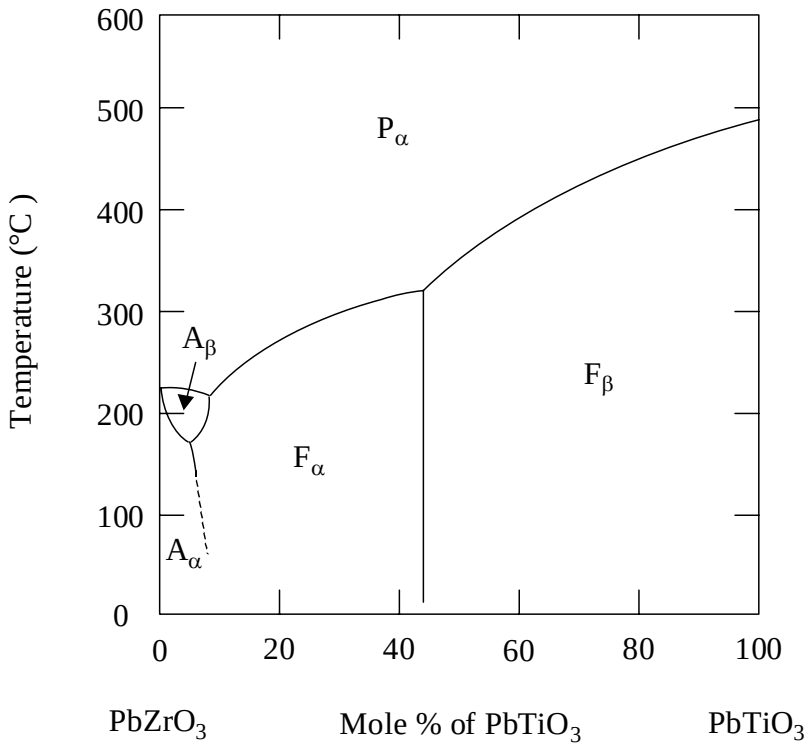

Figure 2.5: Phase diagram for the $PbTiO_3$-$PbZrO_3$ system[15].
P_α = paraelectric, cubic phase; A_α = antiferroelectric, orthorhomibic phase;
A_β = antiferroelectric; F_α = ferroelectric, rhombohedral phase;
F_β = ferroelectric, tetragonal phase.

PZT has a morphotropic phase boundary at a mole fraction ratio Zr/Ti ≈ 53/47 [29] at which the permittivity and piezoelectric coefficients achieve their maximum values [26]. Studies on the optimum mole fraction ratio of sol-gel spin deposited thin film PZT for pyroelectric applications [30, 24, 25] has been found to be in the range Zr/Ti = 25/75→30/70. In the section of this thesis dealing with laser annealing, PZT thin films of composition Zr/Ti = 30/70 have been studied. Perovskite thin films in this region of the phase diagram are ferroelectric with a tetragonal distortion of the classic perovskite structure.

PZT, like PST, has a competing pyrochlore phase[29, 12] which is not ferroelectric and so is undesirable. PZT pyrochlore is cubic with a nano-crystalline structure and forms as a metastable state at temperatures below the perovskite formation temperature [31, 32, 33]. Annealing the material at high temperatures can convert the pyrochlore material to the more stable perovskite structure [31, 32, 33].

2.5 Ferroelectricity

A ferroelectric crystal is one which exhibits an electric dipole moment even in the absence of an electric field, in addition a plot of the electric displacement against applied field shows a hysteresis loop. In the ferroelectric state the centres of positive and negative charge in a crystal do not coincide. Ferroelectricity usually disappears above a transition temperature referred to as the Curie temperature, T_c, above which the material is said to be paraelectric. A ferroelectric material is also pyroelectric if the spontaneous moment of polarisation, P_s, varies with temperature, dropping to zero either continuously or discontinuously at T_c.

There are two main types of ferroelectric phase transition, order-disorder and displacive. In the order-disorder type of transition atomic displacements in the paraelectric phase are about some double-well or multi-well configuration of sites and below the transition temperature they are about an ordered subset of these wells. In a displacive transition the atomic displacements in the paraelectric phase are oscillations about a non-polar site while below the transition temperature they are about a polar site. The class of order-disorder ferroelectrics includes crystals with hydrogen bonds in which the motion of the protons is related to the ferroelectric properties, for example potassium dihydrogen phosphate (KH_2PO_4). Displacive ferroelectrics include ionic crystal structures such as the perovskite structure. Figure 2.6 shows a schematic representation of a displacive phase transition from a centrosymmetric prototype. Above T_c the structure is centrosymmetric, i.e. the positive and negative ion charge centres coincide and there is no net dipole moment. Below T_c the positive ions are displaced relative to the negative ions with the result that the charge centres no longer coincide and a net dipole moment results. The main material reported in this thesis, PST, has a displacive transition.

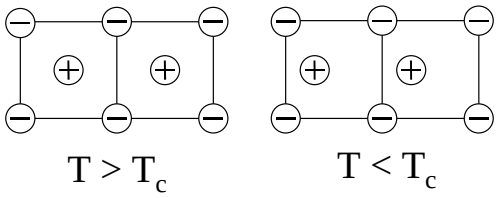

Figure 2.6: Schematic representation of a displacive paraelectric-ferroelectric phase transition.

A ferroelectric crystal is generally composed of small regions called domains within which the polarisation is in the same direction, but in adjacent domains the polarisation is in different directions. The net polarisation along a particular axis will depend on the ratio of oppositely aligned domains along that axis. If there are equal volumes of domains of opposite sense then the crystal will appear to be unpolarised whilst any imbalance will result in a net polarisation in the direction of the most populated domain orientation. The movement of domain walls and the nucleation and growth of new domains results in a change in the polarisation moment of the whole crystal. Changes in the dipole moment can be brought about by changing the temperature of the crystal or by applying an electric field. In the latter case polarisation changes are accomplished either by growth of existing domains antiparallel to the field, by domain-wall motion or by the nucleation and growth of antiparallel domains.

In polycrystalline materials, such as ceramics, each ceramic grain will have properties not unlike that of a single crystal. Because of presence of grain boundaries and the fact crystallographic axes of the grains are randomly orientated, the macroscopic properties of the ceramic will in general differ significantly from those of a single crystal. The situation is similar for polycrystalline thin films with the further complication of surface effects, such as space-charge fields arising from energy-band bending normal to the film surface[34], and the mechanical effects of the underlying substrate.

2.5.1 Second-Order Ferroelectric Phase Transitions

A ferroelectric with a second-order ferroelectric-paraelectric phase transition is characterised by a continuous reduction of the spontaneous polarisation, P_s, with increasing temperature, becoming zero at the transition temperature and above. An example of a material exhibiting this sort of transition is Barium Strontium Titanate ($BaSrTiO_3$ or BST for short). The form of P_s and ε_r curves versus temperature can be found using the Devonshire phenomenological theory of ferroelectrics [34]. A brief description of this theory follows, drawing heavily upon the treatment given by Lines and Glass [34].

In the Devonshire theory simplifying assumptions are made such that the electric displacement D (and hence P_s) and the applied field are directed along one of the crystallographic axes, all stresses are zero and the non-polar phase is centrosymmetric. This

theory expresses the elastic Gibbs free energy, G_1, of the system in a simple polynomial form [34]

$$G_1 = \left(\frac{\alpha}{2}\right)D^2 + \left(\frac{\gamma}{4}\right)D^4 + \left(\frac{\delta}{6}\right)D^6 \qquad (2.4)$$

where energy is measured from the non-polar phase and the polynomial is terminated at D^6 for mathematical simplicity. The coefficients α, β and γ are generally temperature dependent but are held constant in this example for simplicity. The parameter γ holds particular significance since its sign determines the order of the transition, positive for a second order transition and negative for a first order transition. Figure 2.7 shows a qualitative plot of G_1 versus D, the coefficient δ held positive. Two curves are shown, one with $\alpha>0$ and the other with $\alpha<0$. The minima of the curve represent the spontaneous polarisation P_s (D at zero applied field, i.e. $E=0=(\partial G_1/\partial D)_T$) as a function of temperature. With $\alpha<0$ there are two non-zero equilibrium values of P_s. With $\alpha>0$ $P_s = 0$ and P_s undergoes a continuous second-order transition as α passes through zero.

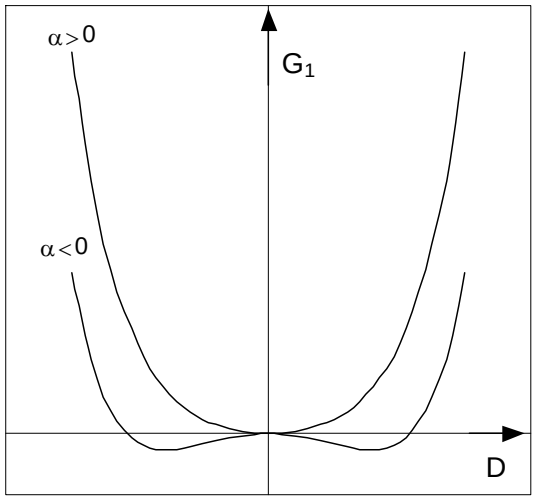

Figure 2.7: Qualitative plot of elastic Gibbs free energy versus displacement for a second order ferroelectric transition.

Differentiating G with respect to D at constant temperature yields the dielectric equation of state

$$E = \alpha D + \gamma D^3 + \delta D^5 \qquad (2.5)$$

The parameter α can now be seen to be the reciprocal of the zero field permittivity in the non-polar phase $\kappa^{X,T>Tc}$ which is assumed to have the following form near T_c

$$\kappa^{X,T>T_c} = \alpha = \beta\left(T - T_c\right) \tag{2.6}$$

where β is a positive constant. The spontaneous polarisation below and close to T_c is found by substituting $D=P_s$ at zero field into the dielectric equation of state, i.e.

$$P_s = \left(\frac{\beta\left(T_c - T\right)}{\gamma}\right)^{\frac{1}{2}} \tag{2.7}$$

Figure 2.8 shows a qualitative plot of P_s, using equation 2.7, for a second order phase transition. The isothermal reciprocal permittivity at zero field close to and below T_c is then

$$\kappa^{X,T} = \beta\left(T - T_c\right) + 3\gamma P_s^2 = 2\beta\left(T_c - T\right) \tag{2.8}$$

Figure 2.9 shows a qualitative plot of ε_r versus T plotted using equations 2.6 and 2.8. For an ideal second order material in the region of the transition the permittivity above T_c is twice that below T_c with a discontinuity at the transition temperature.

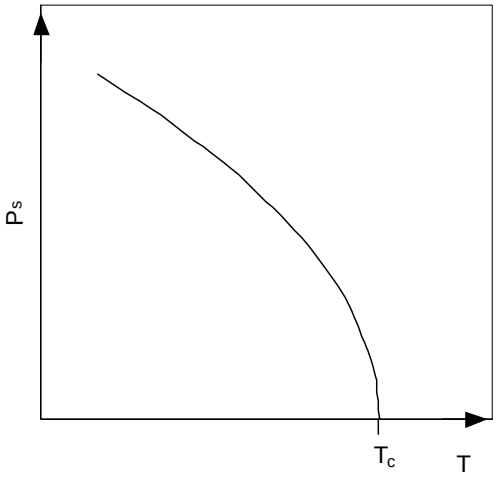

Figure 2.8: Qualitative plot of P_s versus (T/T_c) for an ideal second order phase transition.

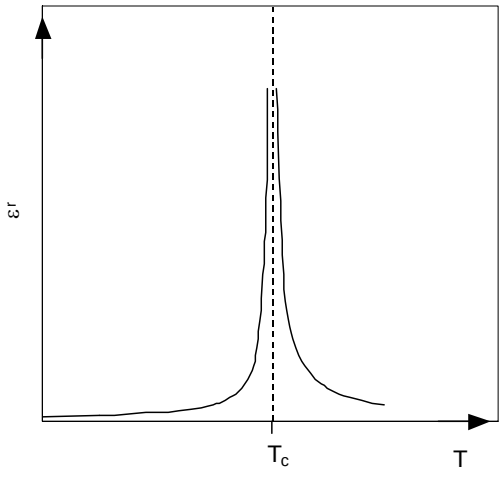

Figure 2.9: Qualitative plot of ε_r versus (T/T_c) for a an ideal second order phase transition.

2.5.2 First-Order Ferroelectric Phase Transitions

In contrast to a ferroelectric material with a second-order phase transition one with a first-order transition between the ferroelectric and paraelectric states is characterised by a continuous reduction of P_s as the transition temperature is approached with a discontinuous fall to zero at T_c itself. Examples of materials exhibiting this behaviour are Barium Titanate ($BaTiO_3$) and PST in its ordered form. To describe a first order transition the parameter γ in the Devonshire expression for the elastic Gibbs free energy is made negative and the parameter α, describing the reciprocal permittivity above the transition, is again written in the Curie-Weiss form

$$\alpha = \beta\left(T - T_0\right) \tag{2.9}$$

where T_0 is the Curie-Weiss temperature which is not equal to the transition temperature T_c. The elastic Gibbs function has the form

$$G_1 = \left(\frac{\beta}{2}\right)\left(T - T_0\right)D^2 - \left(\frac{\gamma'}{4}\right)D^4 + \left(\frac{\delta}{6}\right)D^6 \tag{2.10}$$

Figure 2.10 shows a qualitative plot of G_1 versus D. Unlike the second-order transition D can be seen to be multivalued when G_1=0 at the transition temperature.

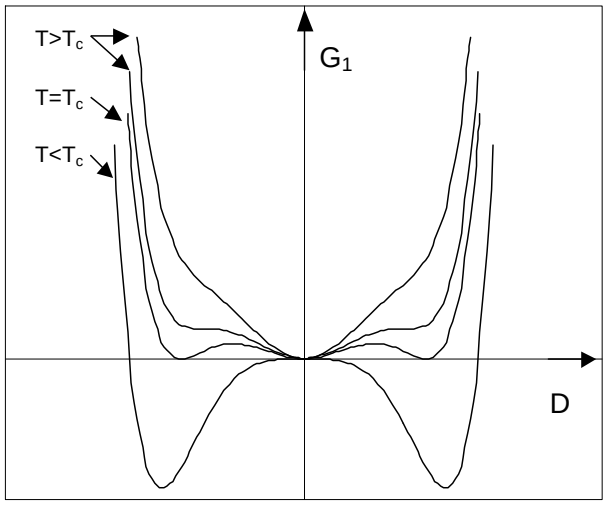

Figure 2.10: Qualitative sketch of elastic Gibbs free energy versus displacement for a second order ferroelectric transition.

As for the second-order case a zero-field first-order transition occurs when G_1 and $(\partial G_1/\partial D)_T$ are both zero i.e. when

$$\left(\frac{\beta}{2}\right)(T-T_0)-\left(\frac{\gamma'}{4}\right)P_s^2+\left(\frac{\delta}{6}\right)P_s^4=0 \tag{2.11}$$

and

$$\beta\left(T-T_0\right)-\gamma' P_s^2+\delta P_s^4=0 \tag{2.12}$$

which occurs when

$$T=T_c=T_0+\frac{3\left(\gamma'\right)^2}{16\beta\delta} \tag{2.13}$$

which substituted into equation (2.11) gives the spontaneous polarisation at the transition temperature as

$$P_s^2=\frac{3\gamma'}{4\delta} \tag{2.14}$$

Figure 2.11 shows a qualitative plot of the spontaneous polarisation around the transition temperature. The dielectric equation of state is given by

$$E=\beta\left(T-T_0\right)D-\gamma' D^3+\delta D^5 \tag{2.15}$$

solving this equation for D at zero field, i.e. the spontaneous polarisation, gives the reciprocal permittivity in the limits of the temperature approaching T_c from above and below as

$$\kappa^{X,T}=\frac{3\left(\gamma'\right)^2}{4\delta}+8\beta\left(T_c-T\right),\quad T\to T_c^- \tag{2.16}$$

and

$$\kappa^{X,T}=\frac{3\left(\gamma'\right)^2}{16\delta}+\beta\left(T-T_c\right),\quad T\to T_c^+ \tag{2.17}$$

Figure 2.12 shows a qualitative plot of ε_r versus T using equations 2.16 and 2.17, and illustrates that for an ideal first-order transition it is finite but discontinuous at the transition.

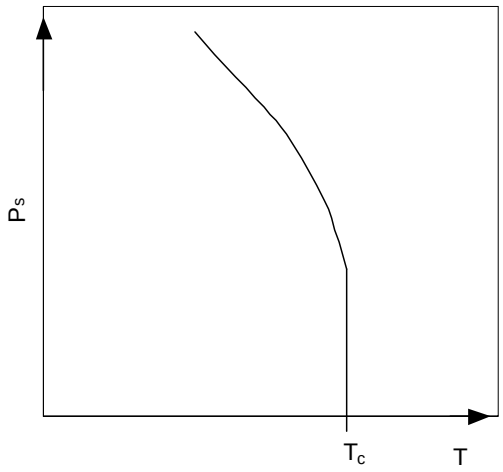

Figure 2.11: Qualitative plot of P_s versus T for an ideal first order phase transition.

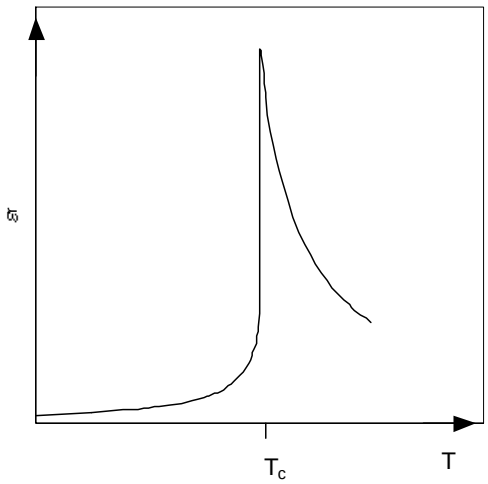

Figure 2.12: Qualitative plot of ε_r versus T for a an ideal second order phase transition.

2.5.3 Ferroelectric Relaxors and Diffuse Phase Transitions

So-called relaxor ferroelectrics are materials which have a diffuse phase transition which is neither first- or second-order in character i.e. there is a transition region (Curie region [21]) as opposed to a unique transition temperature. For a relaxor the spontaneous polarisation is not suddenly lost at T_c, as in first and second order ferroelectrics (discontinuity in d^2P_s/dT^2) but decays gradually to zero as illustrated in Figure 2.13. Also the permittivity reaches a maximum in the region around T_c, Figure 2.14, but it does not mark a phase change into the ferroelectric form. Instead the ferroelectric behaviour decays gradually to zero at a temperature above that at which the dielectric maximum occurs. A classic relaxor material is lead magnesium niobate ($PbMg_{1/3}Nb_{2/3}O_3$ or PMN for short) the properties of which, in ceramic form, were investigated extensively by Smolensky[21]. Smolensky put forward an explanation for this behaviour for PMN[21] in terms of a compositional fluctuation model. PMN is a complex perovskite with the $A(B'B'')O_3$ structure but there is no ordering of the Mg^{3+} and Nb^{5+} ions on the B-sites, as for disordered PST. This in turn leads to micro-regions on a nanometer scale[35] which have different Mg and Nb content, the extent of which is limited by charge neutrality considerations, and different Curie temperatures as a result. Over a wide temperature range there is then an intimate mixture of ferroelectric (polar) and paraelectric (non-polar) regions with the balance becoming more polar as the temperature is reduced. The polar nature of the material is then a superposition of the polar properties of these microregions, each having its own transition temperature[21, 36, 35] – hence

the resulting Curie range. Figures 2.13 and 2.14 show qualitative plots of the spontaneous polarisation and relative permittivity respectively[35, 36, 37]. The peak relative permittivity can be seen to reduce in magnitude and shift to higher temperatures as the frequency is increased and the spontaneous polarisation does not drop to zero at T_c in the manner of a standard ferroelectric. In Figure 2.13 the temperature indicated as T_f is the extrapolation of P_s to zero, neglecting the high temperature tail, as also corresponds to the temperature at which ε_r peaks as the frequency tends to 0Hz[35]. The region beyond this extending to the temperature at which P_s is zero is the Curie range and for PMN can extend over a range of 150°C[21, 36].

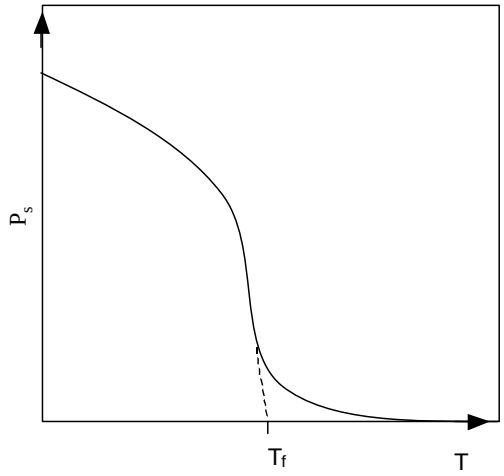

Figure 2.13: Qualitative plot of P_s versus T for a relaxor with a diffuse phase transition [35].

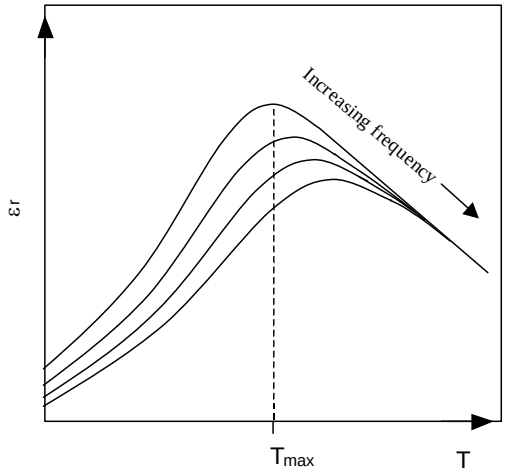

Figure 2.14: Qualitative plot of ε_r versus T for a relaxor with a diffuse phase transition [35, 37].

Smolensky found that in relaxor ferroelectrics ε_r just above the Curie temperature, T_c, was described not by the Curie-Weiss law, equation 2.9 in the previous section, but by a quadratic relation given by [21]

$$\frac{1}{\varepsilon_r(\upsilon,T)} = \frac{1}{\varepsilon_r^{\max}(\upsilon)}\left(1+\frac{\left[T-T_{\max}(\upsilon)\right]^2}{2\delta^2}\right) \qquad (2.18)$$

where ν is the frequency, T is the temperature, T_{max} is the transition temperature (temperature at which ε_r peaks) , ε_r^{max} is the dielectric constant at T_{max}, and δ is the diffuseness parameter.

An extension of the Smolensky model was made by Cross [22] who considered the stability of very small polar microregions using the Devonshire phenomenological theory discussed above. For a domain of macroscopic volume the potential barrier separating alternative domain states (e.g. the double potential well G_1 versus D curve for $T<T_c$ in Figure2.7, section 2.5.1) is >> kT and the domain is quite stable. Since ferroelectricity is a cooperative phenomenon , all energies scale with the volume so that as the domain size is reduced (to ~$100\sum^3$)[22] the potential barrier becomes comparable to kT and the polar regions become unstable. In this way microregions of varying size would become unstable at different temperatures resulting in a gradual loss of the polar nature of the material. This theory is termed the superparaelectric model in analogy to superparamagnetism.

A feature of relaxor materials is that both the permittivity and dielectric loss (tanδ) show strong dispersion with frequency with the maxima in both properties shifting to higher temperatures with increasing frequency. Cross in his review of relaxor ferroelectrics [22] grouped together the properties which distinguish a material as a relaxor with reference to PMN. These are:

(i) Strong dispersion of the permittivity and loss tangent with temperature and frequency, with the maximum in both properties shifting to higher temperature with increasing frequency. The peak in ε_r is also suppressed with increasing frequency and is broad in comparison to that of a standard ferroelectric.

(ii) True dielectric hysteresis at low temperatures which decays slowly to just non-linearity as the temperature is increased.

(iii) Optical and X-Ray evidence for the absence of a microscopic phase change below the Curie temperature.

The first two of these criteria, along with the Smolensky quadratic form for ε_r, will be used later in this thesis in order to classify the nature of the ferroelectric properties of PST thin films. A number of mechanisms have been postulated for the relaxation of the permittivity in relaxor ferroelectrics. Smolensky et al [21, 36] postulate that the relaxation phenomenon is due to the motion of domain walls in the compositional microregions. The domains are small and close to the phase transition there are stable and metastable domains, the latter created by thermal fluctuations. These metastable domains affect the domain wall motion of their stable counterparts resulting in dielectric relaxation. Viehland[35] et al suggest that the dispersion is due to variation in the relaxation times of microregions of different size, assuming a size distribution consistent with the superpararelectric model of Cross[22].

2.6 Pyroelectric Effect and Dielectric Bolometer Mode

The permittivity, $\varepsilon_0\varepsilon_r$, of a cubic dielectric material is given by the differential of the displacement, D, wrt the applied field, E, at constant temperature and strain, i.e.

$$\varepsilon_r\varepsilon_0 = \left(\frac{\partial D}{\partial E}\right)_{X,T} \tag{2.19}$$

For a non-linear dielectric such as a ferroelectric, where ε_r varies with applied field, the displacement is given by

$$D = P_s + \varepsilon_0 \int_0^E \varepsilon_r dE \tag{2.20}$$

where P_s is the spontaneous polarisation, i.e. the electric dipole moment per unit volume with no external field applied. Since D is effectively the surface charge density, the generalised pyroelectric coefficient, p, is a measure of the change in surface charge density when the temperature of the material changes and is given by

$$p = \left(\frac{\partial D}{\partial T}\right)_E = \frac{dP_s}{dT} + \varepsilon_0 \int_0^E \left(\frac{\partial \varepsilon_r}{\partial T}\right)_E dE \tag{2.21}$$

with the units $Cm^{-2}K^{-1}$. If no external field is applied then p reduces to the conventional pyroelectric coefficient (dP_s/dT). For ferroelectric materials with transition temperatures well above room temperature, such as PZT, then pyroelectric operation utilises the conventional pyroelectric coefficient. If however the material is close to its Curie

temperature then the second term in equation 2.21 becomes important. Above the transition temperature P_s is zero and so the contribution to the pyroelectric coefficient from the (dP_s/dT) term is correspondingly zero. If a bias field is then applied to the material then a pyroelectric coefficient is induced according to the second term in equation 2.21. Increasing the applied field has the effect of increasing the generalised pyroelectric coefficient but only up to a point. A ferroelectric is non-linear and the dielectric peak is depressed with increasing field, thereby reducing $(\partial\varepsilon_r/\partial T)$. This mode of operation, above the transition temperature and with an applied field is termed dielectric bolometer mode and is suited to ferroelectric materials with transition temperatures around room temperature such as BST and PST. The use of ferroelectric materials operated in dielectric bolometer mode in thermal radiation detectors was first reported by Hanel[38] and has since been shown to offer performance improvements of over a factor of two compared to "standard" ferroelectric devices [3, 6, 7, 39, 40].

2.7 Dielectric Loss

In a capacitor with an ideal dielectric the current I and voltage V are in quadrature and there is no loss of energy, i.e.

$$I = j\omega\varepsilon_r C_0 V \tag{2.22}$$

where ω is the angular frequency, C_0 is the vacuum capacitance and ε_r is the relative permittivity which is a real number. In reality dielectrics are not perfect and a component of the current is in phase with V, resulting in a phase angle of <90°, as shown in Figure 2.15.

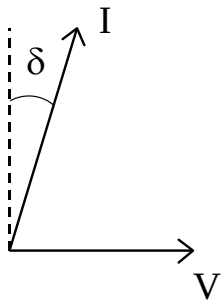

Figure 2.15: Phasor diagram for a lossy capacitor.

This effect is taken into account by making the relative permittivity a complex quantity, i.e.

$$\varepsilon_r = \varepsilon_r' - j\varepsilon_r'' \tag{2.23}$$

where the ε_r'' component represents the losses in the dielectric. The current-voltage relationship then becomes

$$I = j\omega\varepsilon_r' C_0 V + \omega\varepsilon_r'' C_0 V \tag{2.24}$$

The ratio of the magnitudes of the real and imaginary components of the current is

$$\frac{\omega\varepsilon_r'' C_0}{\omega\varepsilon_r' C_0} = \frac{\varepsilon_r''}{\varepsilon_r'} = \tan\delta \tag{2.25}$$

where tanδ is therefore a measure of the losses in the dielectric. In a ferroelectric the dielectric loss is due to spontaneous realignment of domain wall boundaries[38, 41, 42], the realignment of impurity dipoles[43] and a leakage current component due to defects and impurities[38, 41]. The application of an applied field effectively sweeps the domain walls out of the material resulting in a reduction in ε_r'', and hence tanδ - assuming that there is no increase in leakage.

2.8 Hysteresis

Ferroelectrics are a subset of the class of pyroelectric materials. The principle distinguishing feature between ferroelectrics and other pyroelectrics is that the polarisation can be reversed by the application of an applied electric field. Figure 2.16 [34, 44] shows a qualitative plot of the displacement versus applied field for an ideal ferroelectric. At low fields and very high fields a ferroelectric behaves like an ordinary dielectric but at the coercive field E_c (the applied field required to bring the polarisation to zero) polarisation reversal occurs giving a large dielectric non-linearity. Switching the polarisation is not a loss-less process and the area within the hysteresis loop is a measure of the energy required to reverse the polarisation twice. In a single domain the displacement has two possible values which correspond to opposite orientations of the spontaneous polarisation. For a multi-domain crystal the average displacement at zero applied field can lie anywhere between these two extremes. The saturation value of the displacement is equal to the spontaneous polarisation. In Figure 2.16 the zero field displacement is shown as P_r, the so called remnant polarisation, which is less than the spontaneous polarisation. This results either from reverse nucleation of domains occurring prior to reversal of the applied field or surface charges being unable to reach their equilibrium distributions during each half cycle

of the loop. As the temperature is increased towards the Curie temperature the spontaneous polarisation will fall and the area within the loop decreases.

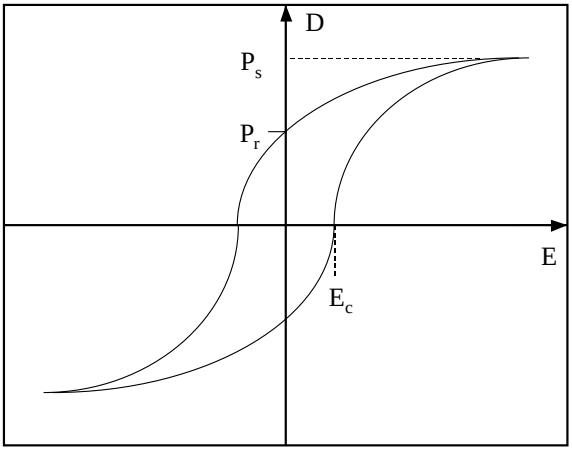

Figure 2.16: Ferroelectric hysteresis loop [34,44].

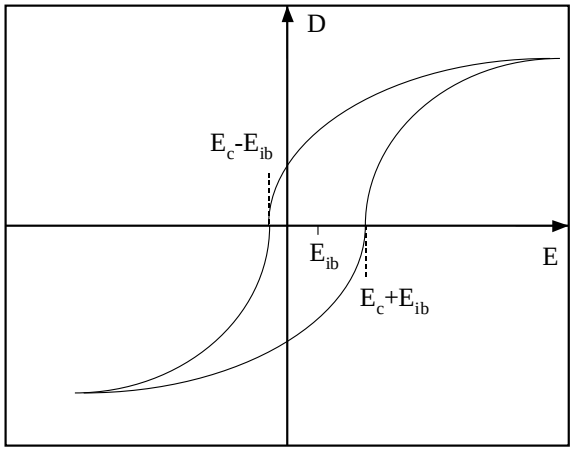

Figure 2.17: Biased ferroelectric hysteresis loop which may occur due to defects and impurities [34, 44].

Figure 2.17 shows a biased hysteresis loop which is symmetrical about a non-zero field E_{ib}, the so-called internal bias field of the material. This apparent internal bias field results from defects and inhomogeneities in the material [34, 45]. The resulting defect dipoles modify the local fields resulting in a change in the macroscopic polarisation and the coercive field required to bring both the spontaneous polarisation and polarisation due to the defects is E_c+E_{ib}. The PST thin films discussed in Chapter 6 exhibit displaced hysteresis loops and an apparent internal bias field.

2.9 Pyroelectric Detectors

2.9.1 Basic Principles

2.9.1.1 Signal

The signal generated from an idealised pyroelectric detector element can be derived using the schematic representation of Figure 2.18. The detector itself has an active area A, thickness d, and is connected to ambient through a thermal conductance G_T. The detector is illuminated by a radiation flux W_0 which in order to simplify the analysis is sinusoidally chopped and results in a pyroelectric current i_p. To read out the pyroelectric current the detector is connected to a simple source follower FET amplifier, with a bias resistor R_B. The following analysis applies equally well to detectors operated in either the conventional pyroelectric mode and dielectric bolometer modes by using the generalised pyroelectric coefficient defined in section 2.6 above.

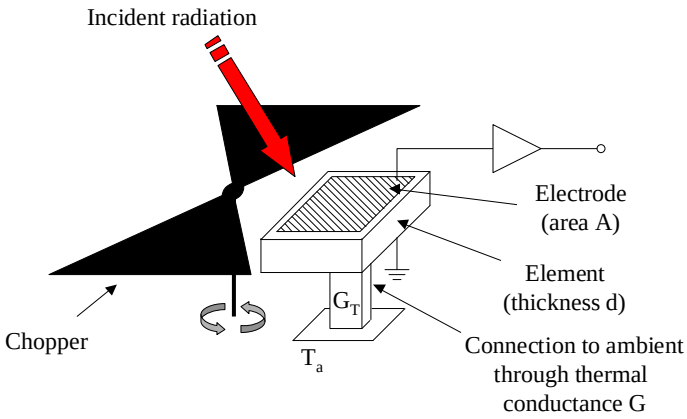

Figure 2.18: Schematic diagram of a simple pyroelectric detector. (*Original in colour*)

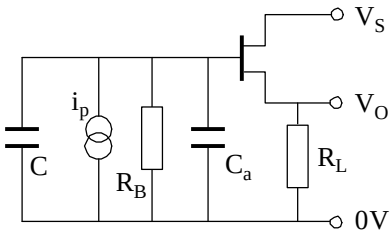

Figure 2.19: Equivalent circuit.

The radiation waveform incident on the detector surface is,

$$W(t) = W_0 e^{j\omega t} \tag{2.26}$$

Assuming that the detector can be treated as a single pole thermal filter then the equation describing the temperature is

$$\eta W(t) = \eta W_0 e^{j\omega t} = H\frac{dT}{dt} + G_T T \tag{2.27}$$

where T is the detector temperature (referenced to ambient), η is the absorption efficiency of the detector, H is the heat capacity. This equation has the solution

$$T = \frac{\eta W_0}{G_T + j\omega H} e^{j\omega t} \tag{2.28}$$

The pyroelectric charge generated by temperature rise T above ambient is

$$q = pAT \tag{2.29}$$

where A is the overlap area between the top and bottom electrodes and p is the pyroelectric coefficient. The pyroelectric current generated is

$$i_p = \frac{dq}{dt} = pA\frac{dT}{dt} = \frac{jpA\omega\eta W_0}{G_T + j\omega H} e^{j\omega t} \tag{2.30}$$

It is interesting to note that i_p = 0 when (dT/dt) = 0, hence the need for a chopper. The current responsivity R_i of the detector is defined as

$$R_i = \left| \frac{i_p}{W_0} \right| = \frac{pA\omega\eta}{G_T \left(1+\omega^2\tau_T^2\right)^{\frac{1}{2}}} \tag{2.31}$$

Where $\tau_T = (H/G_T)$ is the thermal time constant. The voltage output from the detector is given by

$$v = \frac{i_p}{G_E + j\omega C} = \frac{pA\omega\eta W_0}{\left(G_T + j\omega H\right)\left(G_E + j\omega C_E\right)} e^{j\omega t} \tag{2.32}$$

where $C_E = (C+C_a)$ i.e. the combination of the detector capacitance and amplifier capacitance, and $G_E = (1/R_B)$. The voltage responsivity is defined as

$$R_v = \left| \frac{v}{W_0} \right| = \frac{R_B pA\omega\eta}{G_T \left(1+\omega^2\tau_T^2\right)^{\frac{1}{2}} \left(1+\omega^2\tau_E^2\right)^{\frac{1}{2}}} \tag{2.33}$$

where $\tau_E = (C/G_E)$ is the electrical time constant. A plot of the voltage responsivity of a typical pyroelectric detector is shown in Figure 2.20, assuming that $\tau_E >> \tau_T$.

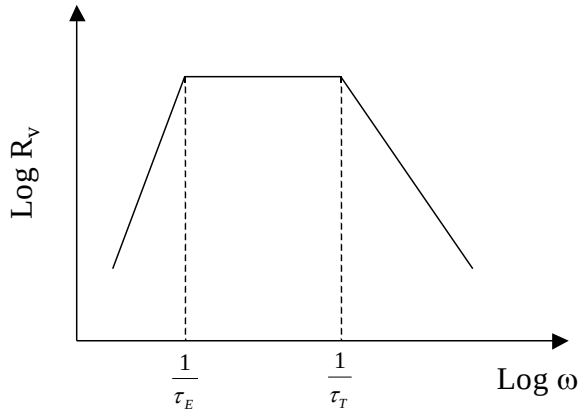

Figure 2.20: Pyroelectric detector voltage responsivity.

At high frequencies, i.e. $\omega >> \tau_T^{-1}$ and $\omega >> \tau_E^{-1}$, R_v simplifies to

$$R_v = \frac{R_B pA\omega\eta}{G_T\omega\tau_T\omega\tau_E} = \frac{pA\eta}{HC_E\omega} \tag{2.34}$$

If the stray capacitance is small compared to the detector capacitance, i.e. $C_E = C$, then

$$R_V = \frac{pA\eta}{HC_E\omega} = \frac{pA\eta}{(c'Ad)\left(\frac{A\varepsilon_0\varepsilon_r}{d}\right)\omega} = \frac{p\eta}{c'\varepsilon_0\varepsilon_r A\omega} \tag{2.35}$$

where c′ is the volume specific heat of the pyroelectric material.

2.9.1.2 Noise

The sensitivity of a pyroelectric detector is a function of both the responsivity and the noise generated in both the detector and the buffer amplifier. The noise terms discussed in this section are for a simple single element pyroelectric detector. When detectors are combined into arrays for imaging purposes the implications of the particular readout scheme must be taken into account[39, 46]. Figure 2.21 gives the equivalent noise circuit for the detector discussed in section 2.9.1.1 above.

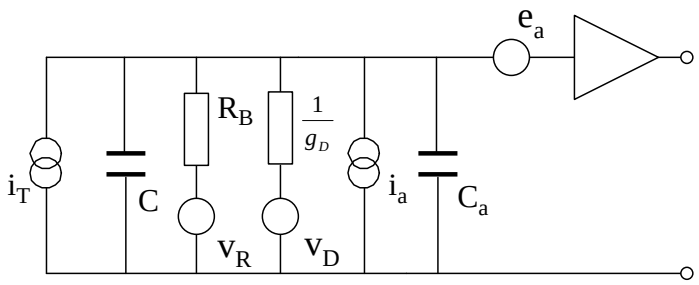

Figure 2.21: Noise equivalent circuit for simple pyroelectric detector.

The major noise sources in a detector are temperature fluctuation noise, Johnson noise in the bias resistor, amplifier noise and dielectric loss noise. The following discussion relates to noise in unit bandwidth. Temperature fluctuation noise arises due to power fluctuations through the thermal conductance linking the detector to ambient. These fluctuations occur even in thermal equilibrium and their rms value is given by [42, 47]

$$\Delta W_T = \left(4kT^2 G_T\right)^{\frac{1}{2}} \tag{2.36}$$

with the corresponding noise current given by

$$i_T = \frac{R_i\left(4kT^2 G_T\right)^{\frac{1}{2}}}{\eta} \tag{2.37}$$

where k is Boltzmanns constant and T is the absolute temperature. The resistor noise generated in the shunt resistor is given by the standard Johnson noise expression

$$v_R = \left(4kTR_B\right)^{\frac{1}{2}} \tag{2.38}$$

The noise due to the buffer amplifier is can be represented by two terms: an equivalent input voltage noise e_a, and an equivalent input current noise i_a.

If the detector capacitance has a dielectric loss tanδ then this corresponds to an equivalent AC conductance $g_D = \omega C \tan\delta$ [42]. The dielectric loss noise of this detector is the Johnson noise generated across this conductance [38, 42, 47]. The noise voltage in unit bandwidth is given by

$$v_D = \left(\frac{4kT}{\omega^2 C^2 g}\right)^{\frac{1}{2}} = \left(\frac{4kT\omega C\tan\delta}{\omega^2 C^2}\right)^{\frac{1}{2}} = \left(\frac{4kT\tan\delta}{\omega C}\right)^{\frac{1}{2}} \tag{2.39}$$

All of the noise sources, with the exception of the amplifier voltage noise e_a, are shunted by the detector capacitance (i.e. the detector acts as its own filter) and therefore fall with increasing frequency. For good low noise FET components however, the voltage noise dominates only at relatively high frequencies (>10^4Hz), well above the frequency of interest for thermal imaging (~50-100Hz).

The total equivalent input noise at the amplifier input is the rms summation of the above noise terms applied across the parallel combination of the detector impedance and the amplifier input impedance. The analysis by Porter[47] considered the relative magnitude of the noise sources for pyroelectric detectors of different areas and found that for a typical detector with a capacitance similar to the amplifier then the dielectric loss noise, v_D, tends to be the dominant noise source at operating frequencies above ~20Hz.

2.9.2 Performance Figures and Materials Figure of Merit

There are a number of performance figures used to quantify detector performance. One of the most useful of these is the noise equivalent power (NEP) which is the incident power

required to give an output signal equal in magnitude to the total rms noise voltage (ΔV_n) and is given by

$$NEP = \frac{\Delta V_n}{R_V} \tag{2.40}$$

The NEP of a detector is specified for unit bandwidth at a particular operating frequency and has the units $WHz^{-1/2}$. Another performance figure that is widely used is the specific detectivity, D^*, given by

$$D^* = \frac{A^{\frac{1}{2}}}{NEP} = \frac{R_V A^{\frac{1}{2}}}{\Delta V_n} \tag{2.41}$$

where A is the detector active area. Compared with NEP, D^* allows the direct comparison of detectors of different areas and also has the more aesthetically pleasing property that its value increases as detector performance increases. The D^* for a pyroelectric detector operated in the frequency range where it is dielectric loss-noise limited is, using equation 2.35 for the voltage responsivity,

$$D^* = \frac{p\eta A^{\frac{1}{2}}}{c'\varepsilon_0\varepsilon_r A\omega\left(\frac{4kT\tan\delta}{\omega C}\right)^{\frac{1}{2}}} = \frac{\eta}{\left(4kT\omega d\right)^{\frac{1}{2}}} \times \frac{p}{c'\left(\varepsilon_0\varepsilon_r \tan\delta\right)^{\frac{1}{2}}} \tag{2.42}$$

For such a detector D^* is optimised by maximising the quantity

$$\frac{p}{c'\sqrt{\varepsilon_0\varepsilon_r \tan\delta}} = F_D \tag{2.43}$$

where F_D is the materials merit figure for a dielectric loss noise limited pyroelectric detector, which is the common scenario with optimised readout electronics, and has the units $Pa^{-1/2}$.

The merit figure F_D has been used in this thesis to assess the performance of PST thin films reported in Chapters 5 and 6. Other merit figures are commonly used to assess the perfomance of pyroelectric materials. The merit figure F_V is derived from the materials parameters in the voltage response equation (2.35) and is given by

$$F_V = \frac{p}{c'\varepsilon_0\varepsilon_r} \tag{2.44}$$

F_V is useful for comparing different materials for their potential voltage responsivities. A further figure of merit is F_i is applicable when the readout amplifier capacitance is much greater than the element capacitance, in this case the voltage response is proportional to

$$F_i = \frac{p}{c'} \tag{2.45}$$

2.10 Thermal Imaging

2.10.1 Thermal Imager Types

A thermal imager samples an infrared radiation pattern in the scene and converts it, via an infrared detector and a display, into a visible image. The detectors used to accomplish task fall into two categories, photon detectors and thermal detectors.

Photon detectors rely on the excitation of carriers in a semiconductor due to absorption of infrared photons and are either photovoltaic or photoconductive. High performance photon detectors are normally operated at temperatures in the range 70-80K due to noise considerations with cooling generally provided by cryogenic refrigerators of either the cooling engine or Joule-Thomson type.

Thermal detectors rely on the absorption of radiation raising the temperature of the detector and changing one of the physical properties of the active material from which it is constructed. The categories of thermal detector types are bolometers, thermocouples and thermopiles, thermopneumatics and pyroelectrics. Bolometer based devices usually rely on a change of the electrical resistance of the responsive element with temperature, although the traditional dielectric bolometer relies on the temperature variation of ε_r in a linear dielectric. Resistance bolometers are made using semiconductor materials such as vanadium oxide (VO_x), amorphous silicon and also metals such as titanium. A change in electrical resistance of the element due to absorbed IR radiation is detected in an external circuit. Thermocouple and thermopile (arrays of thermocouples) based detectors rely on the thermovoltaic effect. In thermopneumatic detectors an IR radiation absorbing element is placed in a sealed, gas filled cell. Radiation absorption in the element heats the gas which increases the pressure in the cell. This increase in pressure results in a distortion of the

walls of the cell which can be detected optically via a mirror mounted on the cell wall. This type of detector is referred to as a Golay cell. Ferroelectric based pyroelectric effect detectors have already been described in section 2.9. If the ferroelectric has transition temperature well in excess of room temperature then the material is operated without an external bias in the conventional pyroelectric mode. Alternatively, if the ferroelectric has a transition temperature at or slightly below room temperature then application of a bias voltage induces pyroelectricity in the material via the dielectric bolometer mode discussed in section 2.6. Although detectors operated in this way are referred to as dielectric bolometers their operation is in fact as a pyroelectric rather than a traditional dielectric bolometer. The work presented in this thesis is concerned with aspects of materials processing for ferroelectric based uncooled detectors.

2.10.2 Blackbody Radiation

Every object whose temperature is not at absolute zero emits thermal radiation. At terrestrial temperatures this consists primarily of vibrational energy level transitions in molecules, and secondarily of reflection of radiation from other sources. Radiators of thermal energy are characterised by their radiation emission efficiencies as blackbodies, greybodies and selective radiators. The spectral emissivity, $\varepsilon(\lambda)$, describes the radiation efficiency at a particular wavelength. A blackbody is an idealised body whose surface emits and absorbs the maximum amount of available thermal energy at a given temperature i.e. $\varepsilon = 1$. A greybody has ε=constant<1 within a specified waveband while for a selective radiator the emissivity varies in the range $0 \leq \varepsilon \leq 1$, again over a specified waveband.

The fundamental principle of thermal radiation is the Planck blackbody radiation law, the basic premise of which is that thermal radiation is emitted in quanta by linear atomic oscillators in simple harmonic motion. The magnitude of these quanta is hc/λ where λ is the wavelength of the emitted thermal radiation. Planck's law gives the spectral flux density from a blackbody surface at temperature T as

$$W(\lambda,T) = \frac{2\pi hc^2}{\lambda^5}\left(\frac{1}{e^{\frac{hc}{kT\lambda}} - 1}\right) \tag{2.46}$$

Using this equation the spectral flux density has been plotted for various temperatures, Figure 2.22.

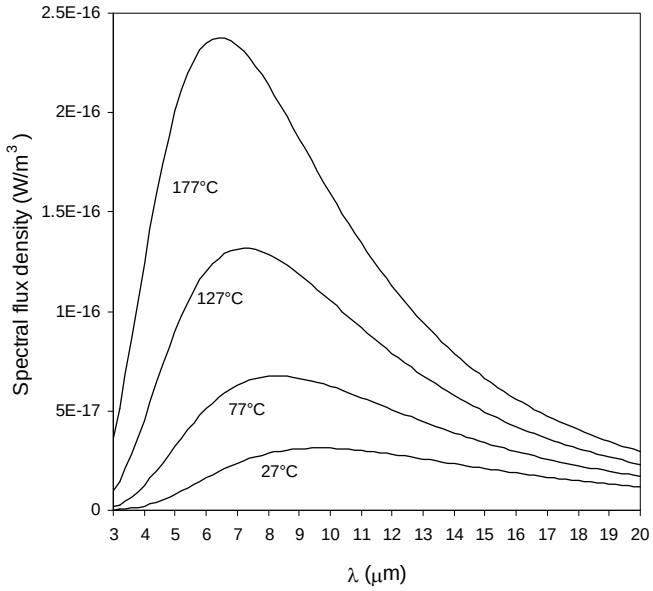

Figure 2.22: Spectral flux density for blackbodies at various temperatures.

λ_{max} (μm)	T (°C)
3	693
4	452
5	306
6	210
7	141
8	89
9	49
10	17
11	-10
12	-32
13	-50
14	-66

Table 2.1: Blackbody curve peak position versus temperature.

It can be seen from the figure that as the emitting body gets hotter the position of the peak in the spectrum shifts to lower wavelengths. The position of the peak at a particular temperature is given by Wien's displacement law

$$\lambda_{\max} T = \frac{hc}{4.965k} = 2.898 \times 10^{-3} mK \tag{2.47}$$

Using this the temperatures that give peaks at wavelengths between 3μm and 14μm can be calculated, see Table 2.1, and for objects around room temperature the blackbody curve can be seen to peak at ~10μm. The energy density on the focal plane of a staring array thermal imaging system can be calculated using the equation for the spectral flux density, equation 2.46 above, integrated over the appropriate wavelengths and solid angles. A detector at ambient temperature T_a will exchange radiation with a scene at temperature of T_s ($T_s > T_a$). The net amount of radiation arriving at the detector, assuming a near normal viewing angle and zero loss in the optical system, is given by

$$\frac{1}{4F^2}\left\{\int_{\lambda 1}^{\lambda 2} A(\lambda) W(\lambda, T_s)\, d\lambda - \int_{\lambda 1}^{\lambda 2} A(\lambda) W(\lambda, T_a)\, d\lambda\right\} \tag{2.48}$$

where A(λ) is the attenuation coefficient due to absorption and scattering in the transmitting atmosphere and F is the F-number of the optics. For a scene temperature of 301K and a detector ambient temperature of 300K, and neglecting absorption and scattering losses, i.e. A(λ) = 1 in the waveband of interest, then over a 8-14μm waveband with f/1 optics, integration gives the power density on the focal plane as 0.66W/m^2. The incident power at a single element of a detector with 56μm pitch would be 2.1nW. If the same integral is performed over a 3-5μm waveband then the power density on the focal plane is only 0.054W – an order of magnitude lower than for the 8-14μm waveband. These are the main wavebands used for infrared detection and are determined by atmospheric transmission, discussed in section 2.10.3 below. It can be seen that for uncooled IR detectors used to image objects around room temperature then the waveband of choice is 8-14μm. The fact that so little energy is available emphasises the need for a good thermal structure in an uncooled IR detector in order to maximise the temperature rise and hence, in a ferroelectric based device, the pyroelectric signal.

2.10.3 Atmospheric Transmission

Absorption by molecules is an important mechanism of tropospheric attenuation at infrared wavelengths. In particular the absorption bands of H_2O and CO_2 define the atmospheric window regions in the infrared. An example of atmospheric transmission, obtained using the LOWTRAN programme, is given from 3-15μm in Figure 2.23. The plot represents the transmission through 100m of atmosphere (horizontal) in a rural temperate mid-latitude region on a winters day with no cloud. The major absorbing species are indicated on the graph as water vapour and carbon dioxide which together define the main atmospheric transmission windows of 3-5μm and 8-14μm.

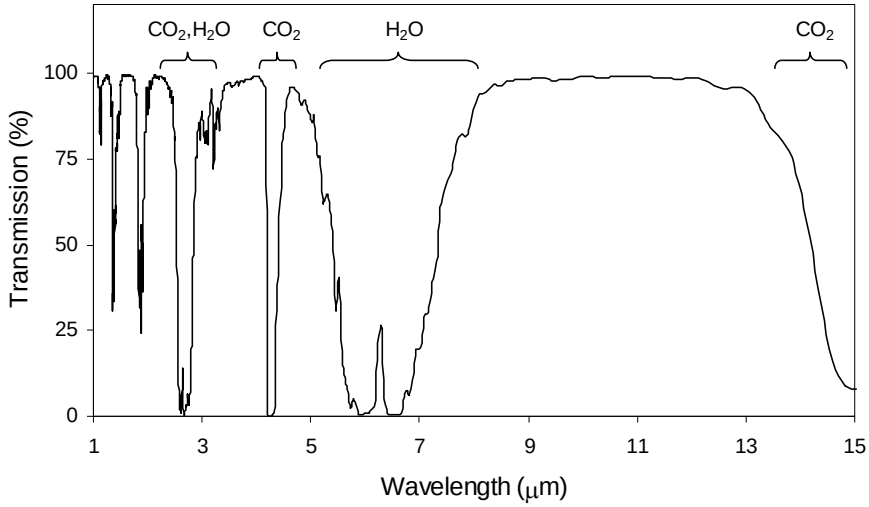

Figure 2.23: Atmospheric transmission in the infrared.

2.10.4 Ferroelectric Based Uncooled Detectors

2.10.4.1 Hybrid Detectors

Hybrid ferroelectric detectors are, as the name suggests, formed from a hybridisation of a detector structure with an ROIC[4]. A schematic diagram of a hybrid detector structure is shown in Figure 2.24 below. The ferroelectric layer is formed from hot pressed ceramic which is sawn into wafers and then thinned to a thickness of 15μm using lapping and polishing techniques. A top electrode/IR absorber structure is deposited onto the top surface and consists of a quarter wavelength thick polymer sandwiched between two metal layers. The metal in contact with the ferroelectric is highly reflective while the opposing metal is matched to the free space impedance of 377Ω/□ - the whole structure forming a resonant absorber [48, 49]. Deposited onto the rear surface of the ferroelectric is a pattern of individual element electrodes for solder bonding. For a high performance detector it is desirable to reticulate the ferroelectric into individual elements for two reasons. Firstly the ferroelectric materials used are piezoelectric as well as pyroelectric. This means that any flexure of the ceramic due to vibrations will result in voltage generation which will be indistinguishable from a pyroelectric signal. Secondly, without reticulation the heat absorbed is free to flow laterally to neighbouring elements thereby reducing the spatial resolution of the detector. Reticulation is carried out by a laser micromachining process[4] and results in groove widths of 10-20μm depending on detector pitch. A solder bump-bonding process is used to connect the detector structure to the ROIC with the solder bonds

being small, typically ~10μm in diameter, in order to improve the thermal isolation of the detector. A layer of polymer isolation on top of the ROIC, and a thin metal interconnect track further increase the thermal isolation of the detector structure.

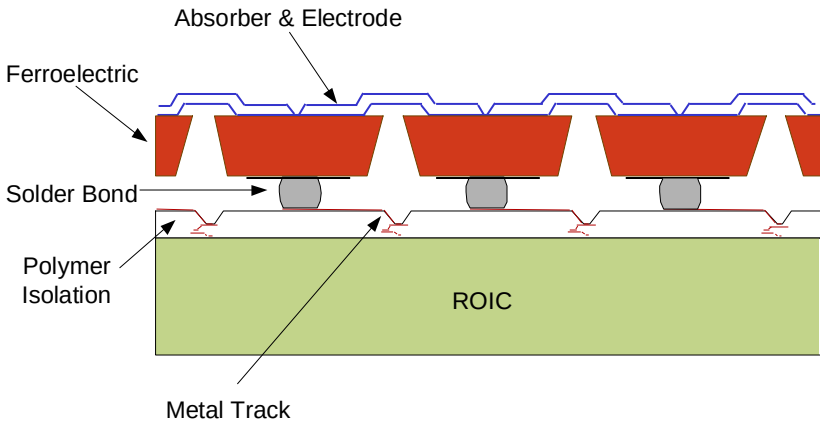

Figure 2.24: Hybrid detector structure.
(*Original in colour*)

The hybrid detector described is fabricated in the UK by BAE Systems Plc. in sizes of 100×100, 256×128 and 384×288 element staring array formats with individual elements on 100μm, 56μm and 40μm pitches respectively. The reason for the decrease in pitch size with increasing element count is to prevent the physical dimensions of the array from becoming too large from a ROIC fabrication/optics viewpoint. In terms of performance hybrid detectors are limited by the thermal properties of the structure. Even with a small solder bond and polymer isolation the thermal conductance to the ROIC is relatively high. This is partly made up for in the fact that the ferroelectric material can be processed at very high temperatures in order to optimise its properties. A further performance limitation is thermal cross-talk between neighbouring elements due to lateral diffusion of heat through the top electrode/absorber structure which limits the thermal resolution at high spatial frequencies.

2.10.4.2 Integrated Detectors

In addition to the performance limitations of hybrid detectors there are also process cost limitations. The ceramic processing, reticulation and soldering bonding are all equipment intensive and time consuming with the latter two steps being performed at the device scale. This ultimately results in cost implications for the final devices. A way around this problem

is to perform device processing on a whole wafer scale using thin film materials and surface micromachining techniques. Devices fabricated this way are referred to as integrated detectors since their fabrication involves deposition of detector layers directly onto the ROIC. In comparison with the hybrid detector approach the processing is less complex.

An example of an integrated ferroelectric IR detector is shown in Figure 2.25 below. Thermal isolation from the ROIC is afforded by a vacuum gap underneath the bridge and support legs which are long and thin. The vacuum gap is formed by etching away a sacrificial layer deposited prior to the main component films of the bridge structure. The bottom electrode is usually a thin film of a high temperature stable, oxidation resistant metal such as platinum [50, 51] which also acts as a lattice matched growth surface for the overlying ferroelectric thin film. A thin titanium top electrode has an impedance of 377Ω/□ which together with the ferroelectric and bottom electrode form a resonant structure for the absorption of IR radiation. For optimum absorption the cavity thickness should be λ/4. Since ferroelectric materials like PST and PZT have a refractive index of ~2.5 at 10μm this sets the ferroelectric layer thickness at ~1μm. This type of device is termed the *R*adiation *A*bsorbed in the *B*ridge or 'RAB' structure.

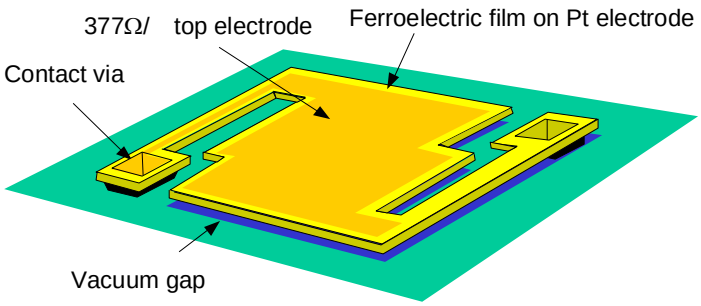

Figure 2.25: RAB detector element.
(*Original in colour*)

An alternative device structure, called an e*X*tended *A*rea *C*ollector (XAC), is shown in figure 2.26. In this structure the ferroelectric does not form the structural support component but is confined to a small region in the centre of the bridge. The support structure is made from a thin (~1000∑) thick oxide layer which has the advantage of reducing the thermal conductance of the device. The basic premise of the device is that heat energy absorbed in the extended area collector gives rise to an increased temperature rise in the ferroelectric active region as compared to the RAB structure since the overall thermal capacity is lower. Absorption in such a device is accomplished in two ways. The

ferroelectric active area has a relatively thick bottom electrode and a free space matched top electrode giving a resonant cavity in the same way as the RAB structure. Secondly the thin oxide bridge layer has a free space matched titanium overlayer. This combined with a metal reflector on the ROIC creates a resonant absorber when the bridge to ROIC distance is λ/4. For a vacuum gap this distance is 2.5μm for peak absorption at 10μm, however an oxide spacer layer is used to reduce the thickness of sacrificial material required. The ferroelectric thickness is generally <1μm and is set by an optimisation study involving radiation absorption and the thermal properties of the device as a whole.

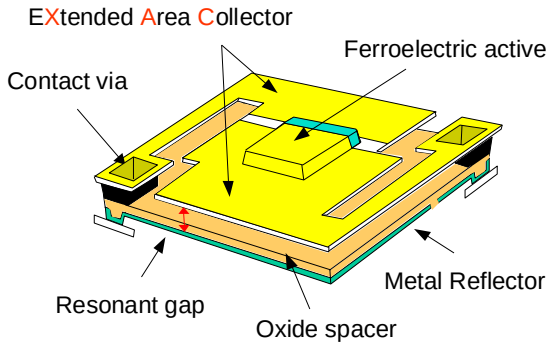

Figure 2.26: XAC detector element.
(*Original in colour*)

In comparison to the hybrid detector, the integrated designs, and especially the XAC, offer superior thermal performance since there is no significant thermal linkage between detector elements. As a result the high spatial frequency thermal MTF is close to that of the sampling function. A disadvantage of the integrated as compared to hybrid is that the ferroelectric must be in thin film form, which has two implications. Firstly the properties of thin film ferroelectrics (pyroelectric coefficient, dielectric loss, breakdown strength etc) are inferior to ceramics. Secondly the processing temperatures available are limited to those that leave the underlying ROIC undamaged.

2.10.5 Composite Detector Technology

A new detector design is being researched in the group in which the author works which separates the high temperature fabrication processes from the constraints of the readout circuitry, the latter being discussed in Chapter 4. This is known as the 'composite' array design since it combines elements of both the hybrid and integrated array technologies. The concept is shown schematically in Figure 2.27. Microbridge pixels are fabricated as per the

integrated technology except that instead of being formed directly on the ROIC, they are formed on to a high density interconnect silicon wafer. The detector die are then flip-chip bonded to the ROIC die as in the established hybrid array process – allowing electrical connection to each element through a solder bond and conducting channel. The key to the design is in fabricating the high density interconnect wafers using materials which can withstand high temperature processing.

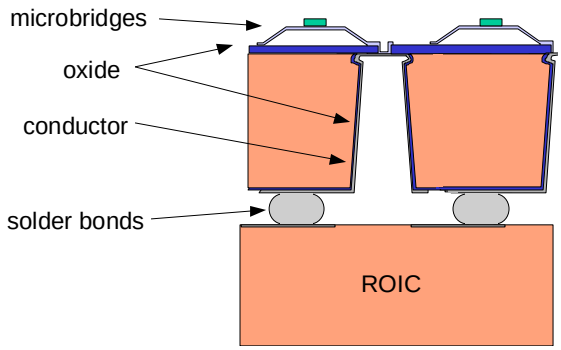

Figure 2.27: Schematic representation of composite array structure.
(*Original in colour*)

As well as removing the temperature constraints, the composite array design brings with it several other important benefits for detector array fabrication, the main one being independence from the ROIC manufacturer. Firstly the interconnect wafers can be of a different wafer size to the ROIC wafers. Although there are benefits in maximising the number of arrays per wafer, it is expensive to tool all the post-process steps to match the large diameter foundry wafers. With foundries continually moving to larger wafer sizes this will be an on-going problem – particularly for R&D. The composite array approach gives freedom to choose any ROIC manufacturer and read-out design, with the only post-process required being to add the flip-chip interconnect metal and bonds to the ROIC. The highest temperature the ROIC experiences will then be the flip-chip bonding temperature, ~240°C, which is already well-established as acceptable. The composite detector design does involve additional processing, including more 'single-die' processes – such as flip-chip bonding – which will add to the cost of manufacture of the detector array. This may be offset due to the yield advantages of selecting 'good' detector die to bond to known 'good' ROIC die.

To form the high density interconnect wafer requires through-wafer-vias to be etched in the silicon on a pitch equal to the detector pixel pitch. These must be lined with insulator and

lined, or filled, with conductive material. This forms the signal connection from the microbridge through the solder-bond to the readout. The common contact can be tracked over the interconnect wafer surface and brought down through vias at the edge of the array. An anisotropic silicon etch process is used to form the vias, which involves etch-passivation cycles in an ICP reactive-ion etcher, using an SF_6 plasma. Figure 2.28 shows an example of the etch profiles of 20μm diameter vias on a 56μm pitch (note this wafer has been cleaved and hence a full via profile is not revealed). Typical etch times of 5 hours per wafer are achieved. High temperature insulator and conductor materials are used to line the vias, giving a via resistance around 100Ω, and the completed wafers can withstand processing temperatures up to 1000°C.

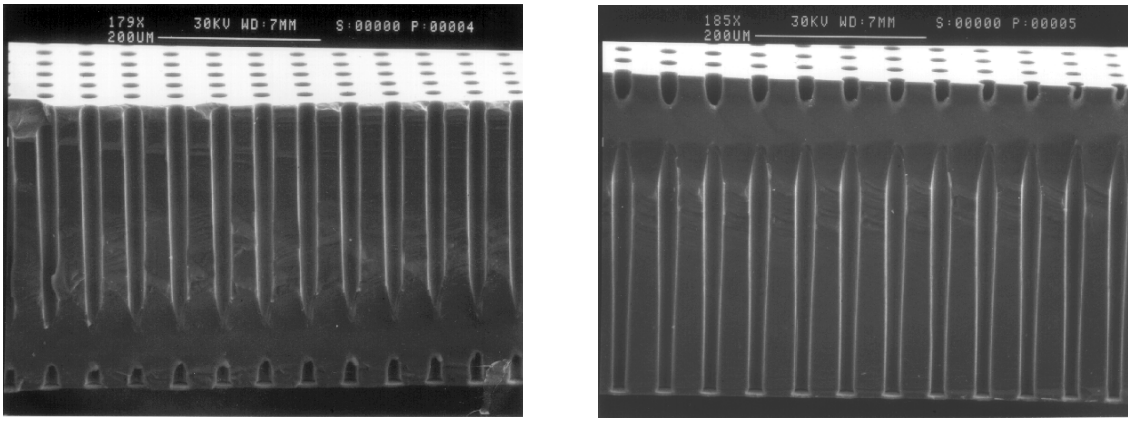

Figure 2.28: SEM cross-sections of plasma etched through-wafer vias.

Chapter 3:

Experimental Techniques.

3.1 Introduction

In this chapter the experimental techniques common to the work presented in this thesis are discussed. The techniques form a number of distinct groupings which are:

- Materials Deposition Techniques
- Annealing Techniques
- Materials Characterisation Techniques
- Electrical Characterisation

The first group, Materials Deposition Techniques, describes the procedures used for the deposition of the thin film materials studied and in particular PST and PZT thin films. The second group describes the annealing techniques, such as rapid thermal processing (RTP) and furnace annealing, which have been used to transform the structure of low-temperature deposited PST and PZT. Laser annealing is not discussed here but is considered in detail in Chapter 7. Materials characterisation techniques are used extensively both after deposition and after annealing in order to obtain yield information on the sample composition, crystallographic properties and microstructure. Finally, electrical characterisation was used to determine the dielectric and pyroelectric properties of PST thin films and thereby quantify their merit for use in uncooled IR detectors.

3.2 Deposition Techniques

3.2.1 Substrates

The substrates used for the deposition of PST were platinised silicon. These comprised a commercial (004) orientated 3" silicon wafer of thickness 0.4mm one face of which had been polished and then thermally oxidised to a depth of 0.8μm. This oxide buffer layer is necessary to prevent the formation of platinum-silicide at elevated temperatures. A 100∑ titanium adhesion layer is deposited onto the thermal oxide by RF sputtering in argon with the substrate held at 300°C. This layer is necessary since without it platinum, which does

not have a stable oxide, adheres poorly to SiO_2 and would tend to de-laminate. The platinum layer is then deposited by RF sputtering, again at 300°C, to a thickness of 1000∑.

The use of platinum as a bottom electrode is due to a number of factors. Firstly the oxygen content of the overlying ferroelectric layer and high processing temperatures, generally >500°C, restricts the useable materials to either conducting oxides, for example RuO_2, or oxidation resistant metals such as platinum [50]. Secondly platinum gives good lattice match to PST perovskite i.e. a = 3.9231∑ for platinum [52] and 4.068∑ for PST perovskite [53] (reduced unit cell).

3.2.2 PST Sputtering

The PST thin films discussed throughout this thesis have been deposited by RF magnetron sputtering. Sputtering of metals and oxide materials is a well established technique. In non-reactive sputtering a plasma discharge is initiated using either a dc or rf field in an inert gas, usually Argon, at low pressure. Material to be sputtered is held on a target plate and the substrate to be coated is placed on a substrate holder in close proximity to the target. A negative DC bias is developed across the target which attracts heavy gas ions from the plasma. On striking the target these ions eject target atoms which are then thermalised by multiple collisions in the plasma before arriving at the substrate. In magnetron sputtering magnets are placed beneath the target and serve to confine the electrons close to the target surface, resulting in a region of enhanced positive ion generation and target erosion known as a sputter or 'race' track, and also reducing electron bombardment of the substrate. In reactive sputtering the inert gas is replaced either wholly or in part by a reactive gas, e.g. oxygen or nitrogen. In this way compound films can be grown from single element metal targets. A complication in reactive sputtering is poisoning of the target elements by the reactive gas. An example is the sputtering of lead oxide from a pure lead metal target in an Ar/O_2 plasma. Oxygen from the plasma oxidises, or 'poisons', the lead target and vastly reduces its erosion rate. Lead oxide being an insulator also causes the target to charge which in a DC sputtering system can result in sparking. For this reason RF sputtering systems are used for easily oxidised metals such as lead, and insulating targets. RF sputtering is also used when depositing films from multi-component ceramic targets which are similar in composition to the desired film.

3.2.2.1 Single RF Magnetron Sputtering of PST.

The PST thin films discussed in Chapter 5 were deposited in conjunction with Mr. M.A. Todd of DERA using single RF magnetron sputtering in a Nordiko NM2000 sputtering system. The basic method is due to Watton and Todd [7, 39, 54] and is a variation of the technique proposed by Sayer [55, 56] for the deposition of PZT thin films using a multicomponent metal target and a single RF bias generator. Figure 3.1 shows a schematic representation of the target used for PST and consists of scandium sectors set into a 4" tantalum disc. Lead is obtained from small pellets placed in the sputter track which are replaced after every run. The sector angles are calculated to give the correct scandium and tantalum erosion rates for near stoichiometric PST, being 27.5° and 17.5° respectively, with the diameter of the lead pellets and their positioning on either the scandium or tantalum giving a measure of tunability of the composition of the deposited film. The substrate is clamped to a stainless steel plate which is heated from the rear by quartz lamps to a temperature of 300°C. This relatively low temperature eased the incorporation of lead into thin film and also improved run to run uniformity as well as growth machine reliability. To give uniform material the substrate holder was placed slightly off-axis above the target and rotated at 4rpm. The ambient atmosphere was argon/oxygen with an Ar/O_2 ratio of ~ 4.5% set by mass flow controllers and measured by a Hiden quadropole gas analyser. Typical deposition settings are given in Table 3.1 below.

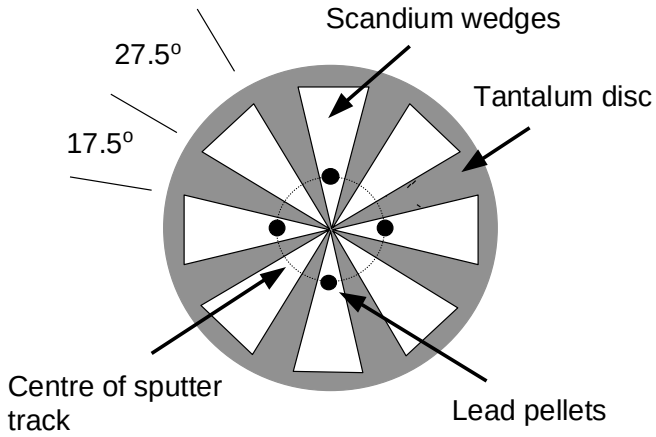

Figure 3.1: Single RF magnetron target.

Parameter	Value
Base pressure	$<1.5\times10^{-6}$mbar
Total sputter pressure	50mTorr
Argon flow	92sccm
Oxygen flow	4.5sccm
Ar/O_2 ratio (measured)	4.5%
RF bias power/voltage	68W/430V

Table 3.1: Typical deposition conditions

3.2.2.2 Dual RF Magnetron Sputtering of PST

A continuing problem with the single target sputtering system discussed in the previous section is that poisoning of the target by the oxygen results in a variable sputtering rates from the component metals. This can be compensated for by adjustment of the positioning and size of the lead pellets as well as varying the bias power, but it can be difficult to maintain the system within the window of acceptable PST composition. To eliminate this problem, as well as to coat larger area substrates, a two target system is used. Schematic illustrations of the system are shown in Figures 3.2 and 3.3. Two 8" targets, one lead and one combined scandium/tantalum are powered by separate RF bias generators. Figure 3.2 shows a schematic cross-section of the system. The substrate is clamped to a stainless steel holder with a bayonet fitting on the reverse. This is then attached to a substrate holder which has a heater bulb assembly capable of heating the substrate to ~550°C. Two motors on the substrate holder allow rotation and translation of the substrate.

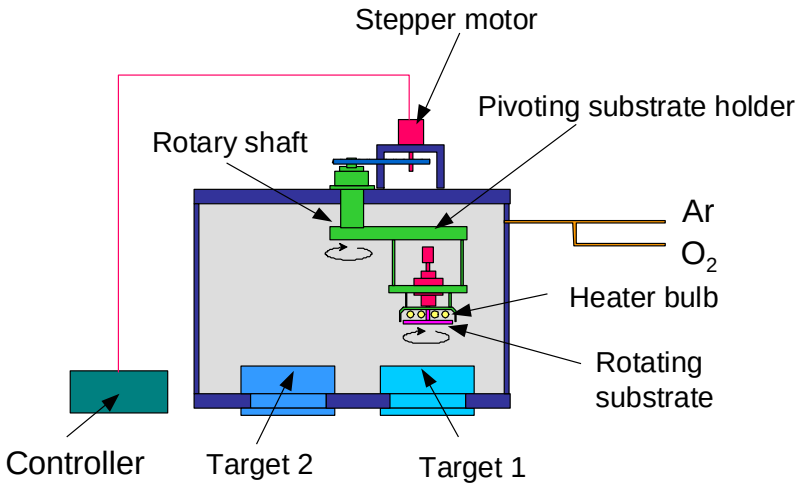

Figure 3.2: Schematic cross-section of dual RF magnetron deposition system. (*Original in colour*)

The relative bias powers used on the two targets gives control of the Pb:Sc+Ta ratio. The Sc:Ta ratio itself is controlled using a combination of RF power, scan speed, scan angle and also the relative areas of scandium and tantalum seen by the substrate. The PST film is deposited by programming in three substrate positions over each elemental area. During a run the substrate moves repeatedly between these positions giving fine layered film with typically ~200 layers per micron with each layer having the same average composition. This approach has resulted in excellent film compositional and thickness uniformity over 3" wafers.

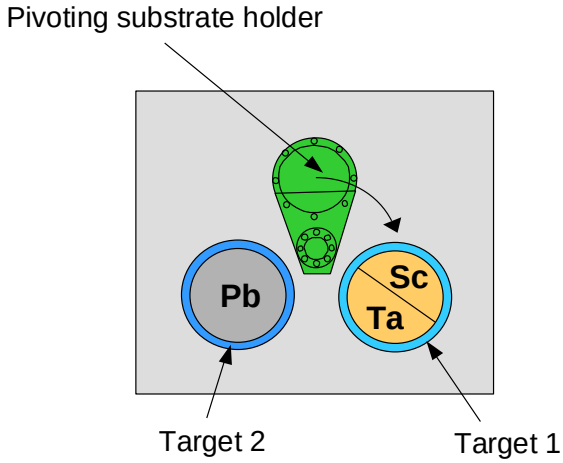

Figure 3.3: Schematic plan view of dual RF magnetron deposition system. (*Original in colour*)

Typical operating conditions for the sputtering of PST thin films are given in Table 3.2.

Parameter	**Value**
Base pressure	2×10^{-6}mbar
Total sputter pressure	6mTorr
Argon flow	9.6sccm
Oxygen flow	2.4sccm
Ar/O_2 ratio (measured)	12%
Sc/Ta target RF bias power/voltage	350W/137V
Pb target RF bias power/voltage	64W/42V
Substrate scan rate	0.56°/s
Substrate temperature	450°C

Table 3.2: Typical operating conditions for dual magnetron sputtering

One drawback of the mode of operation described is that that the erosion rates of the constituent metals varies over time in a highly non-linear fashion due to target oxidation, or

poisoning . This can be compensated for by adjustment of the RF bias powers on each target to avoid target oxidation. The particular conditions required to accomplish this tend not to result in the correct erosion rates of the three metals necessary to give PST thin films of required composition. To overcome this the sputtering system can be operated in an unstable regime where the oxidation state, and hence erosion rate, is constantly varying. Under such conditions the deposited thin films tend to pass through a 'window' of correct erosion rates during which thin films of the required composition are obtained.

An alternative deposition scheme to the one described has been devised by the author and colleagues which considerably eases compositional control. A detailed invention report can be found in appendix A1 of this thesis. The underlying principle of the alternative scheme is that the target conditions (bias/RF power) are set at levels whereby the erosion rate from each material is constant i.e. the rate surface oxidation is matched by the rate of oxide and non-oxidised material erosion. Computer control of the stepper motor used to adjust the substrate holder position, Figures 3.2 and 3.3, has enabled a timed sequence of movements and delays to be used. By varying the dwell time of the substrate over each of the three metals it is then possible to control the average composition of the resulting PST thin film in a relatively straightforward manner. Since the substrate moves successively between the lead, tantalum and scandium portions of the targets the deposited thin films consist of very thin alternate layers typically ~ 1.5-2nm in thickness. Some of the PST thin films discussed in Chapter 6 of this thesis have been deposited in this way. Typical deposition conditions are given in Table 3.3:

Parameter	Value
Base pressure	6.3×10^{-7}mbar
Total sputter pressure	8.8mTorr
Argon flow	15.5sccm
Oxygen flow	4.3sccm
Sc/Ta target RF bias power/voltage	531W/190V
Pb target RF bias power/voltage	99W/66V
Substrate temperature	300°C
Substrate to target distance	70mm
Substrate rotation rate	13rpm
Sc position dwell time	10s
Ta position dwell time	5s
Pb position dwell time	5s
Number of cycles	233
Total deposition time	103mins

Table 3.3: PST deposition conditions using "dwell time" method.

3.2.3 Sol-Gel Deposition of PZT

Sol-gel deposited PZT thin films used in the laser annealing studies of Chapter 8 were supplied by Dr. Anil Patel of BAE Systems. The sol-gel method used has been reported previously [57, 58]. The precursors were lead (II) acetate with titanium (IV) and zirconium (IV) butoxides. Sols with a Zr/Ti 30/70 molar ratio and 10% excess lead were prepared. Films were deposited by spin coating the solution onto electroded silicon wafers. The silicon (100) substrates have an amorphous surface oxide (400nm) grown thermally. Layers of titanium (5nm) and platinum (100nm) are RF sputtered onto the SiO_2 surface in a manner similar to the sputtered PST films with the exception that no substrate heating was employed. Thus a typical cross-section would be $Si/SiO_2/Ti/Pt/PZT$. Thin layers were deposited on the substrate by spinning at 3000rpm, followed by heating at 400˚C for 3 mins to drive off the solvent and initiate the crystallisation process. To avoid cracking, it has been necessary to repeat this process five times to give a film ~0.5μm thick. As deposited, and after baking at 400˚C the film is essentially amorphous, as shown by XRD.

3.3 Annealing Techniques

3.3.1 Rapid Thermal Processing

Rapid Thermal Processing (RTP) is a well established technique used widely in semiconductor device processing where there are thermal budget constraints. The system

used for the work presented in this thesis was an AG Associates Minipulse system. A schematic representation of the annealing chamber is shown in Figure 3.4 below. The transparent fused quartz sample chamber is enclosed within a water-cooled stainless steel housing which is gold coated to maintain high reflectivity well into the infrared. Surrounding this sample chamber are two banks of tungsten-halogen lamps, which are cooled by a flow of compressed air. A Sensarray single point process probe (a 4" silicon wafer with an embedded thermocouple) mounted on a quartz wafer holder, serves as both temperature sensor and, sample mounting platform. Radiant energy from the lamps, in the wavelength range 0.5-1.5μm with a small component around 5μm due to the warm quartz lamp tubes [59], heats both the process probe and the sample. Due to the configuration used, samples are heated radiatively at their top surface and conductively at their bottom surface. A process gas is continuously flowed through the sample chamber.

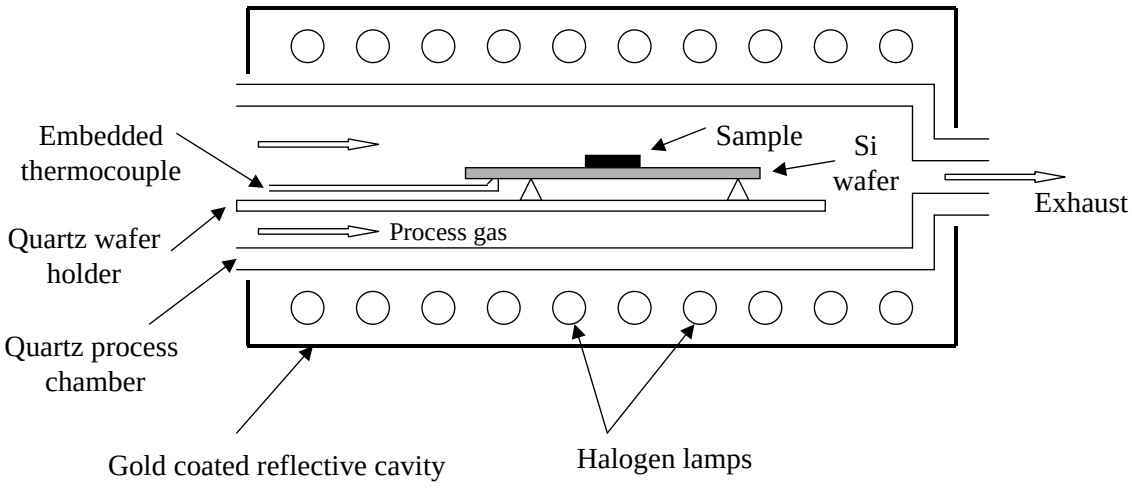

Figure 3.4: Schematic representation of the RTP chamber.

The RTP equipment was fully computer controlled with the output from the Sensarray process probe used as the input to a feedback loop which modulated the lamp intensity so as to control the sample temperature. A second computer was used to record the temperature of the process probe during each run. This was accomplished by connecting an auxiliary temperature output connection, on the rear of the RTP machine, to a digital multimeter that was itself connected to the computer using GPIB. The output of the multimeter was then sampled at regular intervals using a simple program written in Visual Basic. Graphical display of the RTP temperature profiles proved invaluable during the process of optimising the parameters of the temperature control algorithm.

3.3.2 Furnace Annealing

Furnace annealing studies on PST thin films were carried out using an SFL (Severn Furnaces Limited) Instron vacuum furnace, a schematic diagram of which is shown below in Figure 3.5. The system consists basically of a vacuum compatible quartz tube surrounded by a resistive heating element. Quartz baffle plates prevent excessive heating of the water cooled end caps during extended high temperature operation. A quartz sample tray, capable of holding several 4" wafers in a semi-upright position, is placed in the centre of the furnace tube during runs. For runs with smaller samples the specimens are placed on a horizontal sapphire wafer. Control of the ambient atmosphere is possible via a fomblinised rotary pump whereby the quartz tube can be evacuated and then backfilled to a desired pressure with a process gas, oxygen in the case of the work presented. The heat-up rate and cool-down rates are very slow in comparison with the RTP method at ~7.5°min^{-1} and ~1°Cmin^{-1} respectively.

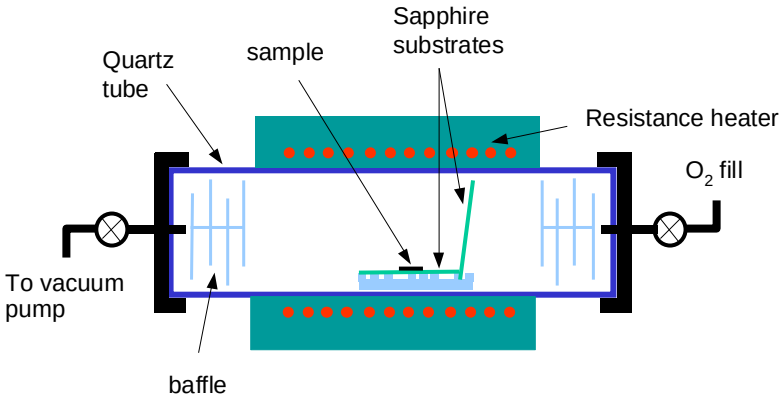

Figure 3.5: Schematic representation of vacuum furnace.
(*Original in colour*)

3.4 Materials Characterisation

3.4.1 SEM and X-Ray Microanalysis

Scanning electron microscope (SEM) analysis has been used throughout the work presented to examine the detailed surface morphology of both uncooled IR detector readout IC (ROIC) devices and also PST and PZT thin films, the latter both before and after annealing. Examination of ROIC devices, discussed in detail in Chapter 4, after thermal treatment was carried out. For high quality pictures a JOEL JSM6400F field emission SEM was used. For work involving PST and PZT thin films on platinised silicon, X-Ray microanalysis was used to determine the elemental composition of the films before and after annealing. A

Princeton Gamma Tech (PGT) IMIX Energy Dispersive Spectroscopy (EDS) system attached to a Cambridge S90B SEM was used for X-Ray microanalysis. This SEM has discrete acceleration voltage settings of 5-25KeV in 5KeV steps.

The technique of Energy Dispersive Spectroscopy (EDS) makes use of an X-Ray sensitive photodiode to record the X-Ray emission spectrum from a sample illuminated by the electron beam in a SEM. The PGT system uses a lithium-drifted silicon photodiode, with a beryllium window, operated at 77K to reduce noise and prevent movement of the lithium under the detector bias field. Figure 3.6 shows an X-Ray spectrum from bulk ceramic PST illuminated with a 15KeV electron beam. Characteristic X-Ray lines from lead, scandium and tantalum are observed.

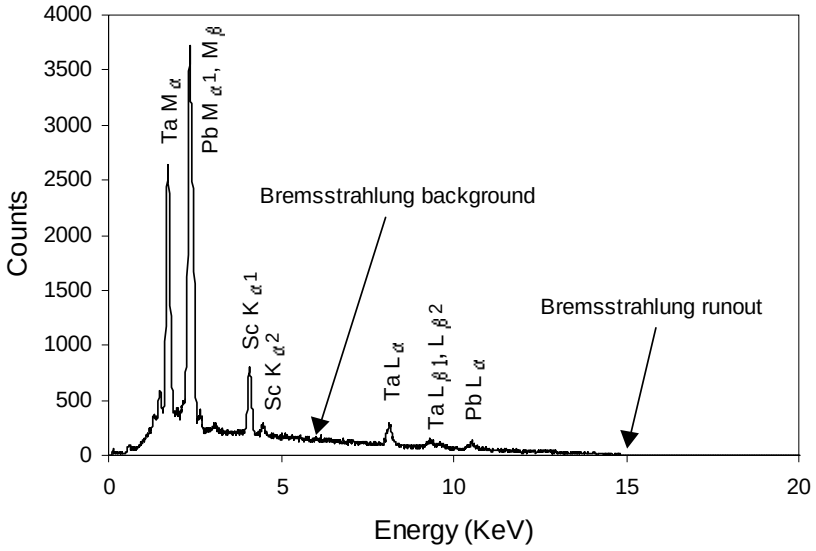

Figure 3.6: EDS spectrum from PST ceramic at 15KeV.

The composition of the thin PST and PZT films studied were obtained using the technique of quantitative X-Ray microanalysis[60, 61], or *quantitative analysis* for short. This well known technique uses a combination of computer based algorithms and reference spectra collected from materials standards to predict the sample composition responsible for generating the collected X-Ray spectrum. The basic premise of quantitative analysis is that if fluorescence and absorption contributions are small then the measured X-Ray intensity ratios (after bremsstrahlung background subtraction) are roughly equal to the mass or weight fractions of the emitting elements. In a real situation the contributions of

fluorescence and absorption of X-Rays generated in the sample are significant and corrections must be applied to the intensity contributions from different elements for accurate results to be obtained. The so-called '*ZAF*' correction method is used with the PGT system. As the name implies the ZAF method applies corrections to the collected spectra for the atomic number (Z) effect (atomic number affects the depth distribution of X-Ray generation), the absorption (A) effect (X-Rays generated within the sample suffer photoelectric absorption losses in transit to the surface) and the fluorescence (F) effect (X-Rays generated in one element in the sample can excite lines in another element).

For accurate reproducible results it is necessary to collect the reference spectra under well defined and reproducible conditions. Quantitative analysis assumes that all measurements for a given element, in both specimen and standards are performed with identical spectrometer response (i.e. the same efficiency, geometrical setup, calibration and resolution), at the same beam energy and under the same electron dosage. The latter condition requires that the SEM probe current be the same for the specimen to be analysed as when the reference spectra were collected. The SEM accelerating voltage should be set so as to give sufficient overvoltage (typically ⁄5KeV) to fully excite the X-Ray lines of interest. By ensuring the same analysis conditions for the specimen as were used for the standards then instrumental effects can be eliminated.

Standards used for quantitative analysis can either be pure single elements or alternatively a multielement standard of known composition can be used. If the latter is used then the analysed specimens must be close in composition to the multielement standard for accurate results to be obtained. Single element standards were used for the work presented and were made from polished pieces of scandium, tantalum, zirconium, titanium, platinum and copper (for detector calibration). A piece of freshly cut lead and a piece of unoxidised silicon wafer were also used. All of the standards were mounted on standard 12mm SEM stubs using conductive paint with care taken to ensure that the surface to be analysed was flat. In order to make sure that the standards and subsequently analysed samples received the same electron dosage a simple probe current measurement apparatus was set up. A Faraday cup was made by drilling a 1mm diameter, 10mm deep hole into a standard 12mm SEM stub. A standard 100μm optical aperture was then fixed over the hole using conducting paint. This modified stub was then placed onto the stub holder and in operation the beam (set to spot

mode) was directed down the centre of the aperture and the current flow due to absorbed charge was measured by connecting the ground return line for the sample stage to a calibrated Keithley 487 Picoammeter. Figure 3.7 below shows a plot of the measured probe currents as a function of SEM resolution and accelerating voltage. The setup used for standard spectra collection was a working distance of 10mm and probe currents of –0.836nA, -0.857nA and –0.853nA at 25KeV, 15KeV and 10KeV respectively. Since the system had a windowed detector it was not possible to analyse for light elements such as oxygen.

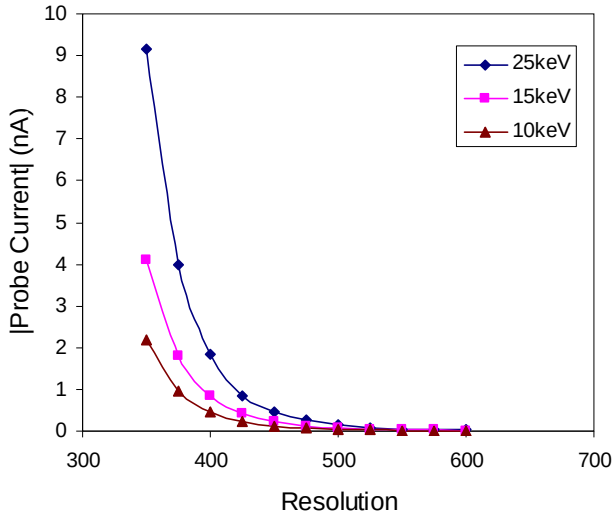

Figure 3.7: Measured probe current as a function of SEM resolution and accelerating voltage. (*Original in colour*)

The analysis method used with the PGT system was 'bulk sample' with oxygen included by 'stoichiometry'. In this scheme a PST specimen, for example, is modelled as a compound of the component oxides i.e. PbO, Sc_2O_3 and Ta_2O_5. For a thin film PST sample on platinised silicon, if the platinum and thermal oxide underlayers are included then the sample is modelled as a mixture of PbO, Sc_2O_3, Ta_2O_5, Pt and SiO_2. For the case of a thin film stack this is obviously inaccurate, since the absorption and fluorescence factors will be incorrect, and it has been found that the best results are obtained when materials such as PST and PZT can be analysed without including the other layers, in other words when the thin film can be made to appear as a bulk sample. Part of the reason for this is that problems can arise in quantitative analysis of the sample composition due to overlapping peaks in the X-Ray spectrum. In PST the problem arises due to overlap of the silicon $K_{\alpha 1}$

(1.74 KeV) and tantalum $M_{\alpha 1}$ (1.71 KeV) lines which would occur if the beam energy is sufficient for silicon X-Rays to be generated in the silicon dioxide layer (or even the silicon substrate itself) underlying the PST/Pt/Ti layer stack. In PZT there is an overlap between the zirconium $L_{\alpha}/L_{\beta 1}$ (2.04/2.12 KeV) and the platinum $M_{\alpha 1}/M_{\beta}$ (2.05/2.13 KeV) which causes problems when the beam energy is sufficient to cause X-Ray fluorescence in the underlying platinum. In these cases the system can have difficulty in separating out the contribution from overlapping elements.

In order to obtain accurate compositional measurements of the thin films, a detailed study of the electron penetration and X-Ray generation depth was carried out. To make PST and PZT thin films behave like bulk specimens it is necessary to ensure that X-Rays are generated only in the thin film and not in the underlying layers. For this purpose the X-Ray ranges (the maximum depth at which X-Rays are generated) were calculated using the Anderson-Hasler equation[60, 61],

$$\rho R = 0.064\left(E_0^{1.68} - E_c^{1.68}\right) \tag{3.1}$$

where ρ is the mean specimen density in g/cc, R is the X-Ray range in μm, E_0 is the SEM accelerating voltage in KeV and E_c is the critical excitation voltage for the elemental line considered. The X-Ray ranges for lead, scandium and tantalum in PST perovskite and pyrochlore at SEM acceleration voltages of 25KeV, 15KeV and 10KeV are given in Tables 3.4-3.6 below. PST densities used were the theoretical values from the JCPDS database, i.e. 9.09g/cc[53] for perovskite and 8.958g/cc[62] for pyrochlore. Since specimens were analysed with the electron beam incident at 45° the effective thickness of each layer is $\sqrt{2}\times$ the actual thickness.

Element	Line	E_c (KeV)	$R_{perovskite}$ (μm)	$R_{pyrochlore}$ (μm)
Sc	$K_{\alpha 1}$	4.09	1.50	1.52
Ta	L_{α}	8.15	1.33	1.35
Pb	L_{α}	10.55	1.20	1.22

Table 3.4: X-Ray ranges in PST perovskite and pyrochlore at 25KeV.

Element	Line	E_c (KeV)	$R_{perovskite}$ (μm)	$R_{pyrochlore}$ (μm)
Sc	$K_{\alpha 1}$	4.09	0.59	0.60
Ta	$M_{\alpha 1}$	1.71	0.65	0.66
Pb	$M_{\alpha 1}$	2.35	0.64	0.65

Table 3.5: X-Ray ranges in PST perovskite and pyrochlore at 15KeV.

Element	Line	E_c (KeV)	$R_{perovskite}$ (μm)	$R_{pyrochlore}$ (μm)
Sc	$K_{\alpha 1}$	4.09	0.26	0.27
Ta	$M_{\alpha 1}$	1.71	0.32	0.32
Pb	$M_{\alpha 1}$	2.35	0.31	0.31

Table 3.6: X-Ray ranges in PST perovskite and pyrochlore at 10KeV.

The X-Ray ranges in PST perovskite and pyrochlore are virtually identical and are ~1.36μm at 25KeV, ~0.64μm at 15KeV and ~0.3μm at 10KeV. The 25KeV ranges highlight the problem of penetration through to the underlying layers. As mentioned previously silicon X-Rays are a problem when analysing PST thin films on platinised silicon. Results of a further calculation of the X-Ray ranges in a PST/Pt(1000∑)/Ti(100∑) layer stack are given in Table 3.8, with the effective layer thicknesses and mean densities for various PST thicknesses given in Table 3.7.

PST thickness (μm)	PST effective Thickness (μm)	Layer stack effective Thickness (μm)	Mean density (g/cc)
0.6	0.85	1.04	10.77
0.8	1.13	1.28	10.40
1.0	1.41	1.56	10.17

Table 3.7: Effective thicknesses (45° incident angle) and mean densities for PST/Pt(1000∑)/Ti(100∑) layer stacks.

Element	Line	E_c (KeV)	$R_{0.6}$ (μm)	$R_{0.8}$ (μm)	$R_{1.0}$ (μm)
Sc	$K_{\alpha 1}$	4.09	1.26	1.31	1.34
Ta	L_{α}	8.15	1.12	1.16	1.19
Pb	L_{α}	10.55	1.01	1.05	1.07

Table 3.8: X-Ray ranges (25KeV) in 0.6μm ($R_{0.6}$), 0.8μm and 1μm PST perovskite/Pt/Ti.

It can be seen that at 25KeV, the X-Ray ranges are greater than the layer thicknesses for 0.6μm thick PST, and close to penetrating through to the underlying silicon dioxide for 0.8μm thick PST. A simple test of these calculations was made by analysing two PST samples deposited onto platinised silicon { PST(0.6μm)/Pt/Ti(100∑)/SiO_2(0.8μm)/Si }in the same sputtering run. One sample, piece A, had 1000∑ of underlying platinum while the other sample, piece B, had 5000∑. The thicker platinum on piece B acted as a barrier for both incident electrons and generated X-Rays. Figures 3.8 and 3.9 show the EDS spectra for pieces A and B respectively at 10KeV, 15KeV and 25KeV. The spectra at 10KeV and 15KeV are both identical and show no evidence of platinum – confirming that the generation depth for X-Rays is smaller than the effective sample thickness. There is however a marked difference in the 25KeV spectra for the two samples. Both spectra show evidence of platinum X-Ray generation while piece A, with the thinner platinum, shows apparent enhancement of the tantalum $M_{\alpha 1}$ peak due to silicon $K_{\alpha 1}$ X-Ray generation in the underlying SiO_2.

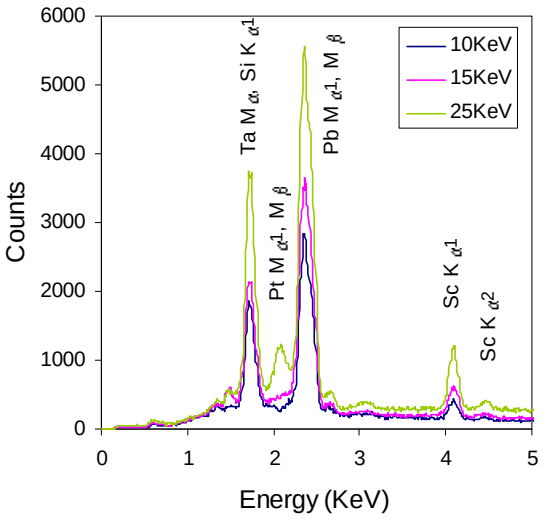

Figure 3.8: PST with 1000∑ of underlying Pt. (*Original in colour*)

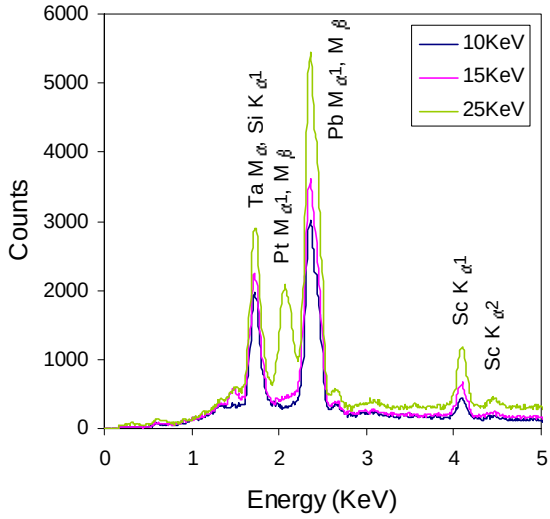

Figure 3.9: PST with 5000∑ of underlying Pt. (*Original in colour*)

For this reason analysis at 25KeV has not been used. Analysis at 15KeV has been found to give the best results (in terms of χ^2 and expected compositions) and gives a reasonable sampling depth in PST. Because of this compositional analysis on all PST samples of thickness ⁄0.5μm has been performed at 15KeV. As a check on the EDS system and analysis method a piece of stoichiometric PST ceramic (supplied by BAE Systems) was

used as a control sample. The composition was measured to be Sc:Ta:Pb = 1:1:2.01. The error on each element in the ratio Sc:Ta:Pb was found by repeated measurement of the control sample to be ±3%.

Similar calculations were performed for half micron thick PZT (sol-gel deposited) on platinised silicon. On the basis of the PST perovskite/pyrochlore results it was assumed that X-Ray ranges calculated for perovskite would be similar to those in pyrochlore. Again using the Anderson-Hasler equation the X-Ray ranges for 15KeV and 10KeV are shown in Table 3.9.

Element	Line	E_c (KeV)	R (15KeV) (μm)	R (10KeV) (μm)
Zr	L_α	2.04	0.7	0.35
Ti	K_α	4.51	0.64	0.28
Pb	M_α	2.35	0.71	0.34

Table 3.9: X-Ray ranges in PZT.

For a 0.5μm thick PZT film analysed at 45° (effective thickness 0.71μm), an accelerating voltage of 15KeV results in X-Ray ranges that penetrate through to the platinum, though only just, while at 10KeV X-Rays are generated in the PZT only. In practice, compositional measurement at 15KeV with platinum included in the quantitative analysis tends to give the expected results roughly half of the time. If platinum is left out then the zirconium content calculated is too high, indicating a definite platinum contribution. On some occasions the system mistakes the zirconium contribution entirely for platinum. Based on this, PZT specimens of thickness (PZT) □0.5μm have been analysed at 10KeV. The composition of as-deposited films expected from the starting sol has been used as a control.

3.4.2 X-Ray Diffraction Analysis

X-Ray Diffraction analysis, or *XRD* for short, has been used throughout the work presented to determine the crystallographic structure of the samples studied. XRD scans were performed in conjunction with the Materials Characterisation Department of DERA Malvern. Both a Siemens D5000 and a high resolution D5005 were used in standard Bragg-Brentano geometry[63] with Cu Kα radiation ($K_{\alpha1}$ λ=1.54051∑; $K_{\alpha2}$ λ=1.54433∑; relative intensity $K_{\alpha1}/ K_{\alpha2} \approx 2$) and the X-Ray tubes operated at 40mA and 40kV.

For phase identification use has been made of the crystallographic database of the Journal of the Centre for Powder Diffraction Studies (JCPDS). The database comprises XRD data taken from powder specimens and gives quantitative information on the diffracting planes i.e. Miller indices, d spacings, relative intensity and 2θ angles. The relative intensity of the signals from the diffracting planes are valid only for powder samples and therefore no use was made of this. The JCPDS files used are detailed in Table 3.10.

Material	Formula	JCPDS file
Silicon	Si	27-1402
Platinum	Pt	4-802
Lead Platinum intermetallic	$PbPt_x$	6-574
PST - perovskite	Pb_2ScTaO_6	43-134
PST - pyrochlore	$Pb_2Sc_{0.5}Ta_{1.5}O_{6.5}$	45-554
Lead Oxide - Litharge	PbO	5-561
Lead Oxide - Massicot	PbO	5-570
PZT – perovskite	Pb_2TiZrO_3	14-31
PZT – perovskite	$PbZr_{0.52}Ti_{0.48}O_3$	33-784

Table 3.10: JCPDS files.

A diffraction file for PZT pyrochlore is not available. Approximate peak positions for this phase have been gained from the literature [64]. The position of the silicon (004) peak was used as an internal standard for peak position, and hence lattice parameter, determinations.

3.4.3 Transmission Electron Microscopy

Transmission electron microscopy, or *TEM* for short, was used to determine the detailed microstructure of the thin films studied. All of the reported samples have been analysed using cross-sectional TEM where the material to be studied has been thinned to electron transparency using the techniques described in the sections below. Microscope facilities at both DERA Malvern and Cranfield University were utilised and the author is indebted to Dr. D. Wallis (DERA) and Dr. Z. Huang (Cranfield) for producing the TEM images used in this thesis. The DERA microscope is a JOEL 4000EX, whilst the Cranfield microscope is a Philips CM20.

Standard techniques such a light field imaging, dark field imaging and small area electron diffraction, or SAED. In bright field imaging all of the forward scattered electrons from the incident beam are allowed to proceed to the imaging screen. In dark field imaging the insertion of an appropriately placed aperture cuts off all but electrons scattered from crystal

planes of a particular orientation. SAED gives diffraction information from small areas of the sample, thereby allowing phase identification. For further information on these techniques the reader is referred to the excellent book by Williams and Carter [65].

3.4.3.1 Conventional Sample Preparation

Some of the samples analysed using TEM were prepared using conventional techniques by experienced staff both at DERA, in the Characterisation Department, and also by Dr. Z. Huang at Cranfield University. A brief description of this procedure is given below.

Firstly the starting material, for example a PST thin film on platinised silicon, is cleaved into 3mm wide bars. Two of these bars are then glued together, with PST facing PST, as shown in Figure 3.10. The bars are then sawn into 0.5mm wide strips.

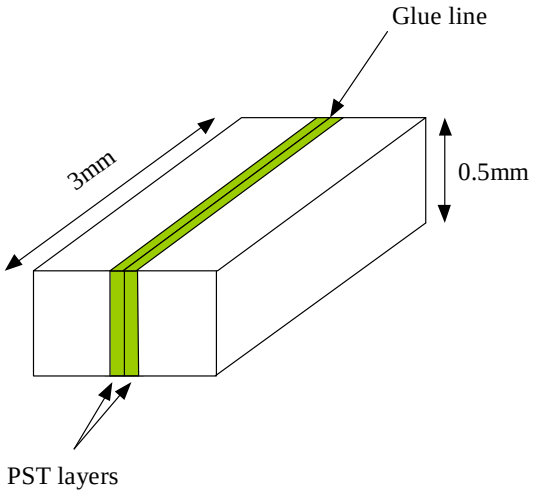

Figure 3.10: TEM sample sandwich.
(*Original in colour*)

The resulting strip is then waxed onto a glass stub with the PST/PST interface perpendicular to the stub surface. This stub is then placed in a jig and polished to reduce its thickness using progressively finer diamond pastes with the final polish using 0.25μm paste. Next the strip is removed from the stub and mounted, polished side down, onto a copper slot with the glue line parallel to the long axis of the slot – see Figure 3.11.

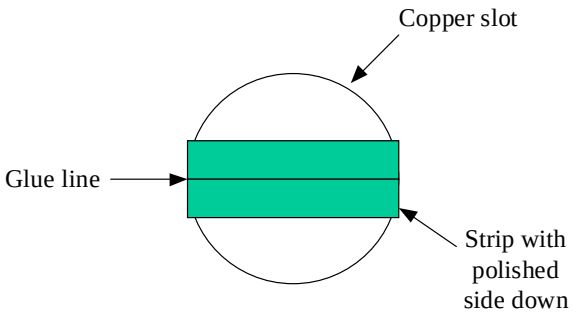

Figure 3.11: TEM sample on copper slot.
(*Original in colour*)

The copper slot is then waxed to a glass stub and the sample surface is polished using progressively finer diamond pastes until it is less than 10μm thick, with 0.25μm paste being used for the final polish. A good judge of the thickness of samples deposited onto platinised silicon is the colour of the transmitted light through the silicon. The thinned sample is then removed from the glass stub and placed in an ion beam miller where the PST and underlying layers are thinned to electron transparency using low angle, low energy ions.

3.4.3.2 Focussed Ion Beam Sample Preparation

An alternative to conventional TEM sample preparation is the use of Focused Ion Beam (FIB) techniques to form the ultrathin section, or lamella, for analysis by TEM. Some of the TEM results presented in this thesis have made use of this as a proprietary technique with the work performed at Micrion Ltd (Bristol). A Micrion 2500 single beam FIB system was used and comprised of a 50KeV gallium beam that could be used in either milling or imaging mode. Sample preparation by FIB has several advantages over conventional techniques. These include the fact that lamella can be formed from precisely located areas and also the success rate for usable lamella formation is high. Possible disadvantages are that the lamella can be relatively thick, the ion beam causes amorphisation in a near surface region the depth of which is dependent on the skill of the operator and also the samples are heavily implanted with gallium. For the purposes of lamella formation from PST and PZT thin films the first two may reduce the resolution of TEM images.

A brief description will be given on the preparation of a lamella with reference to Figure 3.12, which illustrates the process schematically. Step 1, in order to protect the region of material from which the lamella will be formed a protective tungsten plug is deposited onto the sample surface. This plug is deposited by cracking of tungsten hexacarbonile gas,

which is flowed over the sample surface, by the rastoring ion beam. Step 2, the ion beam is used to mill two pits, one either side of the of the tungsten plug. Step 3, milling continues to reduce the width of the ridge separating the two pits to 200-300nm, this ridge of material will eventually form the lamella. Step 4, the sample is tilted to allow a slot to be milled in the base of the ridge, thereby releasing it from the underlying material. For a PST film on platinised silicon this slot would be milled in the silicon substrate. Step 5, the sample is angled so that the one face of the lamella is parallel to the ion beam, this face is given a final polish to further thin the lamella and remove the most of the amorphised region. This process is repeated with the opposite face. The lamella is now <100nm – sufficiently thin for electron transparency. Step 6, two final cuts are made – indicated by red lines in Figure 3.12 – which release the lamella. Using an electrostatic probe the lamella is removed and placed on a holey carbon TEM grid.

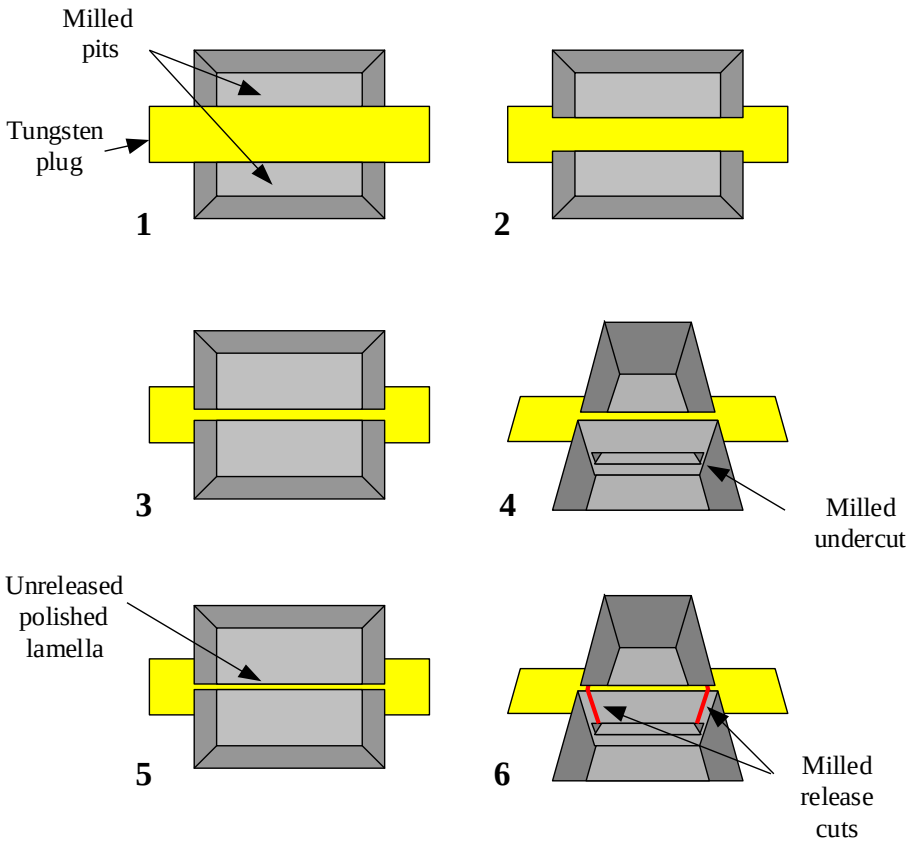

Figure 3.12: Schematic representation of TEM lamella preparation using FIB. (*Original in colour*)

Figure 3.13 below shows a FIB image of a PST lamella after release and prior to removal to a TEM grid. Remains of the tungsten plug can be seen clearly and surrounding the milled area is redeposited material. The lamella itself is so thin that it has begun to curl.

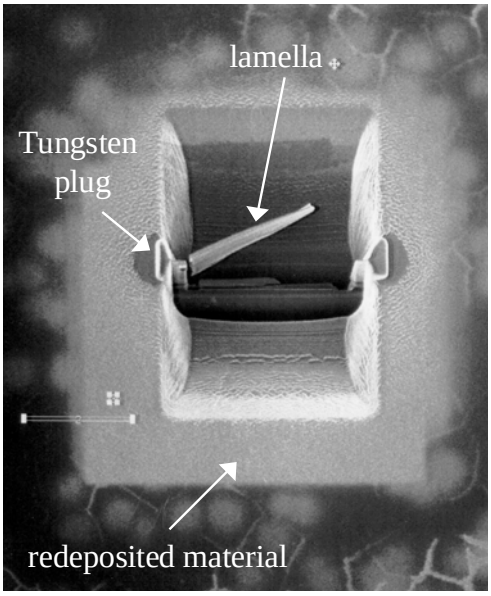

Figure 3.13: FIB image of TEM lamella prior to removal by electrostatic probe.

3.5 Electrical Characterisation

3.5.1 Electrodes

The bottom electrode on the PST films reported is the underlying platinum. To make electrical contact this is exposed either by physical abrasion or wet chemical etch. The top electrodes for the majority of samples are chromium-gold dots deposited through a shadow mask by sputtering, with the thin layer of chromium acting as an adhesion layer for the gold.

3.5.2 Dielectric Properties

The dielectric properties, namely ε_r and tanδ, were measured at 120Hz, 1500Hz and 10kHz using a Wayne-Kerr 6425 Component Analyser with an integral dc bias generator. The instrument was operated in parallel RC mode with an ac field amplitude of 50mV. Merit figure (F_D) values quoted in this thesis have been made using the 120Hz values of ε_r and tanδ. This was done for two reasons, firstly this is close to the operating frequency of a PST detector array of 100Hz but away from mains harmonic frequencies, and secondly within the minimum error (especially tanδ) parameter space of the component analyser for the film capacitance values investigated. For measurements of ε_r and tanδ as a function of temperature a simple apparatus based on an isothermal enclosure was used, Figure 3.14.

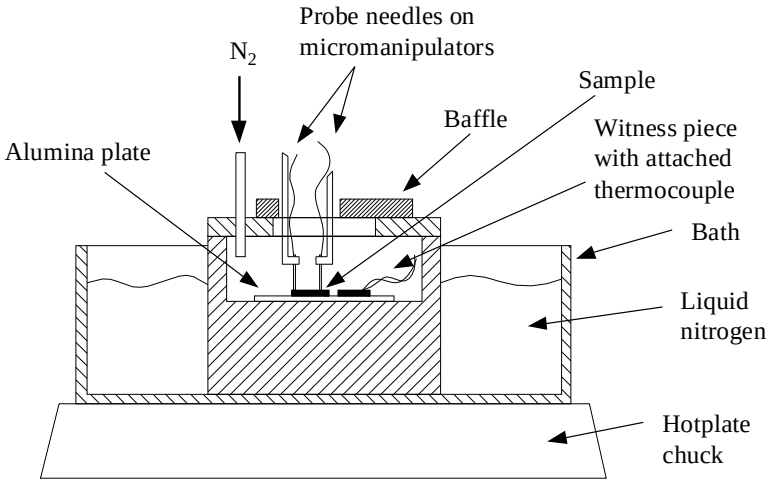

Figure 3.14: Dielectric test kit.

The sample was stuck to an alumina plate inside a cavity in a copper block. To ensure good thermal contact a high thermal conductivity paste was used. A witness piece with a K-type thermocouple attached to its surface using conductive paint was placed close to the sample and similarly stuck to the same alumina plate. The thermocouple was lead out to a calibrated Fluke 52 digital thermometer. Electrical contact was made to the sample through a hole in the chamber lid using probe needles attached to micromanipulators and to prevent condensation and icing at low temperatures, gaseous nitrogen was flowed into the chamber and foam baffles were used to prevent excessive ingress of air into the sample space. The copper enclosure sat inside an aluminium bath which itself sat on top of a hotplate chuck. To cool the sample liquid nitrogen was poured into the bath and to warm the sample the hotplate was turned on. In this way the sample temperature could be varied between ~ -150°C to 100°C. A simple computer program was used to read data from the Wayne-Kerr component analyser once the desired temperature was reached.

3.5.3 Pyroelectric Coefficient Measurements

The pyroelectric response of the PST thin film samples was measured by inducing a known temperature rise. The apparatus, due to Watton and Todd [7], is shown schematically in Figure 3.15.

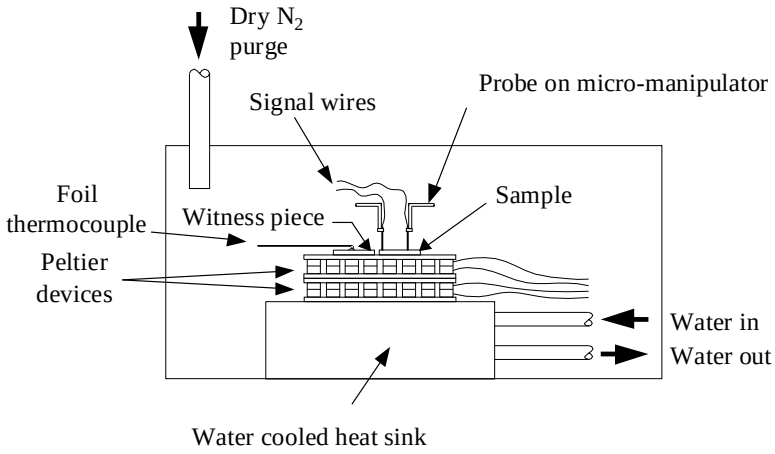

Figure 3.15: Pyroelectric coefficient measurement chamber.

The sample is adhered to the top of a stack of two Peltier devices with high thermal conductivity paste. Electrical contact to the top and bottom electrodes is made via probe needles attached to micro-manipulators. Calibrated temperature measurement is made using a witness piece comprising a PST film on platinised silicon with a K-type foil thermocouple attached to the surface using silver loaded paint. The output from a thermocouple amplifier is read out to a pc using a Fluke 8842A digital multimeter. The lower Peltier device is used to set the sample mean ambient temperature, in the range –20°C to 85°C, whilst the upper device is fed with a sinusoidal current sufficient to induce a ~0.1°C temperature variation in the sample. The frequency of the sinusoidal signal is low (0.1Hz) in order to ensure that thermal gradients do not develop within the sample under test. A DC bias can applied to the sample, using a programmable dc power supply, allowing the measurement of the generalised pyroelectric coefficient. The pyroelectric signal from the sample is fed into a calibrated electrometer amplifier, Figure 3.16, the output of which is read into a pc using a Fluke 8840A digital multimeter.

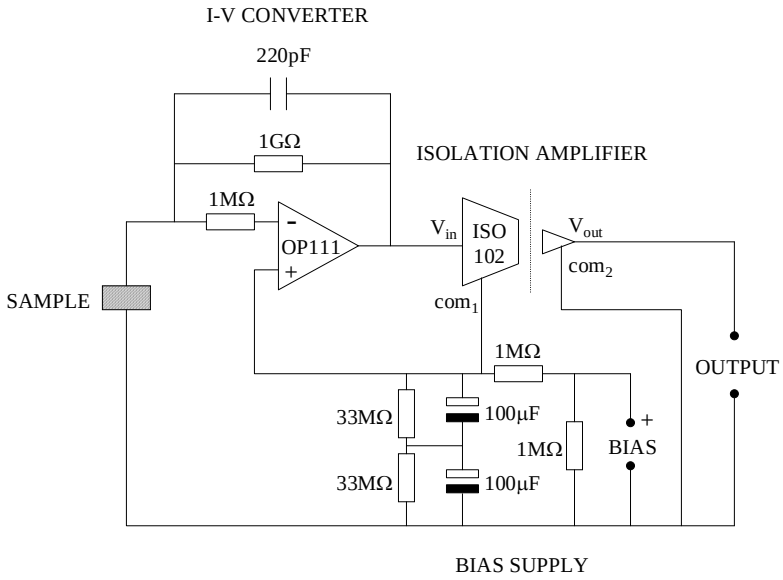

Figure 3.16: Amplifier circuit.

In the scheme used the temperature T of the sample is given by

$$T = T_a + \Delta T \sin \omega t \tag{3.2}$$

where T_a is the ambient temperature, ΔT is the amplitude of the induced sinusoidal temperature variation of angular frequency ω. The pyroelectric current *i* is given by

$$i = pA\frac{dT}{dt} = pA\omega\Delta T \cos \omega t \tag{3.3}$$

where *p* is the generalised pyroelectric coefficient and A is the electrode area. The output voltage *V* from the instrumentation amplifier is then given by

$$V = pA\omega R_f \Delta T \cos \omega t \tag{3.4}$$

where R_f is the magnitude of the feedback resistor (1GΩ) in the instrumentation amplifier, see Figure 3.16. The pyroelectric signal is seen to be 90° out of phase with the drive temperature. This provides a useful check of the source of the output signal since components due to sample resistance variations with temperature will be in phase with the drive temperature. When the pyroelectric signal has settled to a constant value, either after the application of a bias voltage or changing the mean sample temperature, its amplitude is sampled and the computer outputs the pyroelectric coefficient based on the ΔT and electrode area.

Other methods for measuring the pyroelectric signal in ferroelectric materials are used by other workers in the field. The two principle alternative methods are the constant scan method and the modulated radiation technique. The constant scan method, due to Byer and Roundy [66], utilises an oven or temperature controlled hot chuck to induce a known rate of heating in the sample under test. The constant rate of heating, typically ~1°C/min, then induces a pyroelectric current in the sample from which the pyroelectric coefficient can be calculated over the temperature range used. A potential problem with this method is that it does not differentiate the pyroelectric signal from other spurious signal sources due to effects such as leakage, resistance changes and thermal transients, although the use of positive and negative temperature ramps can be used to remove unwanted effects. The modulated radiation technique, due to Chynoweth [67], uses a chopped radiation source to induce a small temperature fluctuation in a sample with semi-transparent top electrodes. This method has the advantage over the method used in this thesis that the pyroelectric current can be measured at the operating frequency of a thermal imager, i.e. 25-100Hz. The disadvantage of this method is that the induced temperature rise in the sample is estimated, from indirect measurements, rather than measured directly. Also, at higher chopping rates it is possible to have a non-uniform temperature distribution in the sample which will give an incorrect pyroelectric coefficient measurement.

3.5.4 Resistivity Measurements

The resistivity of the PST thin films was measured using a calibrated Keithley 637 Source Measure unit used in conjunction with the sample mounting stage of the pyroelectric measurement apparatus discussed in section 3.5.3. The lower peltier device only was used to set a constant sample temperature with the Source Measure unit used in voltage source mode. "Zero" applied bias measurements were made with a source voltage of 0.1V with a settling time of five minutes between application of the bias and taking of readings. At higher applied bias voltages typically five readings would be taken at each bias with a five minute delay between readings.

3.5.5 Measurements of Hysteresis Loops

The hysteresis loops of some of the thin film samples discussed in this thesis were measured using a Radiant Technologies RT66A Ferroelectric Test System operated at 1kHz in virtual ground mode. Measurements were performed using the dielectric test kit described in

section 3.5.2 which allowed the sample temperature to be varied between ~ -100°C to +100°C. The author is indebted to Dr. Anil Patel of BAE Systems for the use of the RT66A equipment.

3.5.6 Errors in Electrical Measurements.

Electrical measurements made in the thesis are subject to experimental error which impacts on the accuracy of the quoted results. Quantities such as ε_r, tanδ and the pyroelectric coefficient are all subject to experimental errors which combine to give errors on the F_D values quoted.

For ε_r the experimental errors come from three sources which are the accuracy of the Wayne-Kerr component analyser (±0.05% for the capacitance values and frequency ranges considered), the error in the measurement of the PST thin film thickness (±250∑ using the Talysurf method giving ±2.5% error on a 1μm thick film) and the error in the measurement of the electrode diameter (±1.3% on a 1.5mm diameter electrode when measured using a travelling microscope). For the sample geometry considered the estimated combined absolute error in is ±5.2%. The relative error for measurements on the same electrode on the same sample is much lower at ±0.05%, reflecting the removal of the electrode area and PST thickness errors.

Error in the measurement of tanδ arises from the accuracy of the Wayne-Kerr component analyser which in the frequency range considered and for capacitances > 1.5nF (applicable for all PST film measurements presented in this thesis) is ±0.0005. This results in tanδ errors of ±3.3%, ±5% and ±10% for measured tanδ values of 1.5%, 1% and 0.5% respectively.

The pyroelectric coefficient measurement is subject to experimental errors from measurement of electrode area, PST film thickness and the amplitude of the drive temperature and the resulting signal voltage. For a 1μm thick PST film with a 1.5mm diameter electrode the estimated absolute error is ±5%, while the relative error between measurements on the same sample is ±2% - reflecting the fact that film thickness and electrode area errors are taken out.

All of the above errors combine when calculating the materials merit figure for each sample. In calculating F_D the PST heat capacity is taken as that for bulk ceramic at 2.7×10^6 J/m^{3}K, which is standard practice in work of this nature. Combining the above errors in ε_r, tanδ and p gives for a 1μm thick PST film with 1.5mm diameter electrodes an absolute error in F_D of ±11.8%, or a relative error for measurements on the same sample of ±6.2%. Quoted errors in the thesis are absolute unless indicated otherwise.

Chapter 4:

Thermal Processing Limitations of Uncooled IR Detector Readout Circuitry.

4.1 Introduction

The fabrication of an integrated IR detector requires that the post-processing necessary to form the detector elements does not detrimentally affect the underlying readout integrated circuit (ROIC). If the device processing schedule exceeds the allowed thermal budget for the ROIC then thermally-induced damage would occur, resulting in yield implications for the whole process. The effects of such would be manifold with the worst case being that post-processing induces sufficient damage in the ROIC to totally prevent operation. Other initially less serious effects may result in reduced device lifetime or impaired performance due to noisy operation and parameter shift. The latter would be a natural consequence of the shift of the parameters of devices within the ROIC itself, i.e. transistors, diodes and thus amplifiers, voltage references etc.

In the UK the current generation of IR detector ROIC uses the standard foundry VLSI metallisation, Al-Cu-Si. This alloy gives the benefit of low resistivity as well as corrosion resistance, electromigration resistance and good adhesion [68, 69]. The addition of silicon (≈1%) to the aluminium suppresses a failure mode due to spiking. This results from the preferential dissolution of silicon, by diffusion at temperatures of 450°C and above, into the aluminium of the interconnect metallisation [70, 71, 72] with the aluminium then filling the 'hole' in the silicon, which can result in the shorting of junctions. The addition of a TiN barrier layer [70, 72] between the Al and the underlying Si further protects against this type of failure. Addition of copper (typically 0.5%) to the Al-Si alloy considerably increases the electromigration resistance of the resulting metallisation. This effect is brought about by the added copper enhancing the activation energy of self-diffusion of aluminium [71].

Several thermal budget limitations arise due to the metallisation of the ROIC, with the absolute limit being the melting of aluminium at 660.5°C [73]. Another major concern about aluminium metallisation on silicon is the formation of surface projections, or hillocks [74], which can punch through insulating layers causing short-circuiting and junction failure.

Ericson et al [74] describe the formation of annealing hillocks in pure aluminium films as a result of heat treatment. D'Heurle [75] discusses the formation of these hillocks as a mechanism of stress relief. At elevated temperatures thermal expansion mismatch between the aluminium metallisation and the underlying silicon results in the former being in a state of highly compressive stress. A combination of grain boundary diffusion and creep processes relieves this stress through the formation of hillocks. It is also possible that Si precipitating out in the Al might provide the inhomogeneities required for hillock formation. Hanson et al [70] report concerns about diffusion of Si, and subsequent precipitation in the Al-Si-Cu, through the TiN barrier if the ROIC is held at temperatures above 450°C for extended periods. Indeed the TiN barrier itself is known to be prone to degradation at ~550°C and above [72, 76]. These problems introduce limitations to the thermal budget available for the growth of a ferroelectric layer directly onto the readout circuit.

The work reported in this chapter attempts to quantify the thermal budget limitations outlined above. To investigate the survivability of IR detector ROIC's to the processes required for the formation of the ferroelectric layer, a series of thermal trials was carried out. These were divided into a set of simulated sputtering runs and RTP runs, both of which are described in detail below. Electrical characterisation was used to determine the survival rate of the circuitry. Optical and SEM inspection located and identified any physical alteration of and damage to the metallisation.

4.2 Experiment

4.2.1 Test Samples

The ROIC's used for thermal trials were developed by DERA in conjunction with Phoenix VLSI and were from a design designated as Test Mask 5 (TM5), fabricated using the standard Al-Si-Cu metallisation discussed above. A 1μm thickness of silicon-oxynitride served as surface passivation layer. Die on TM5 consisted of 7×5 element readout circuits on either a 50μm (die 1) or 70μm (die 2) pitch. The output from each array was not multiplexed with each individual element having its own readout amplifier.

A total of five TM5 wafers were available for experimentation, each containing 338 die. Since this was an insufficient number of wafers to conduct the required experiments, each

was cut into eight pieces using a wafer dicing saw. Prior to sawing the wafers were spin coated with a protective layer of photoresist which was subsequently washed off. The choice of octant pieces was made due to the limitations on piece size imposed by electrical probe testing and also that each octant contained not less than ten of each die type, for statistical validity.

4.2.2 Simulated Sputtering

To test the survivability of ROIC's to the PST sputtering process a bespoke vacuum annealer was assembled, a schematic representation of which is shown in Figure 4.1. The author is indebted to Mr. G. Monnington of DERA for the conversion of his ion beam milling apparatus to the form required for this purpose. A rotary backed diffusion pump gave an operating pressure of 5mTorr, measured using a CVC pirani gauge. The ambient atmosphere was 5mTorr of Ar/10% O_2 which is representative of a PST sputtering system, although the gas was not in plasma form. Samples were held on a copper plate, nickel coated in order to prevent oxidation at elevated temperatures, which was heated from the underside to a maximum of 600°C using quartz-halogen lamps controlled by a Eurotherm 818 PID temperature controller and an R-type thermocouple clamped to the surface of the plate. Calibration of the temperature indicated by the PID controller was made using a second, K-type, thermocouple similarly clamped and read out to a calibrated Fluke 51 digital thermometer. Wafer pieces were held onto the sample holder using spring-loaded clips, thereby ensuring a good thermal contact.

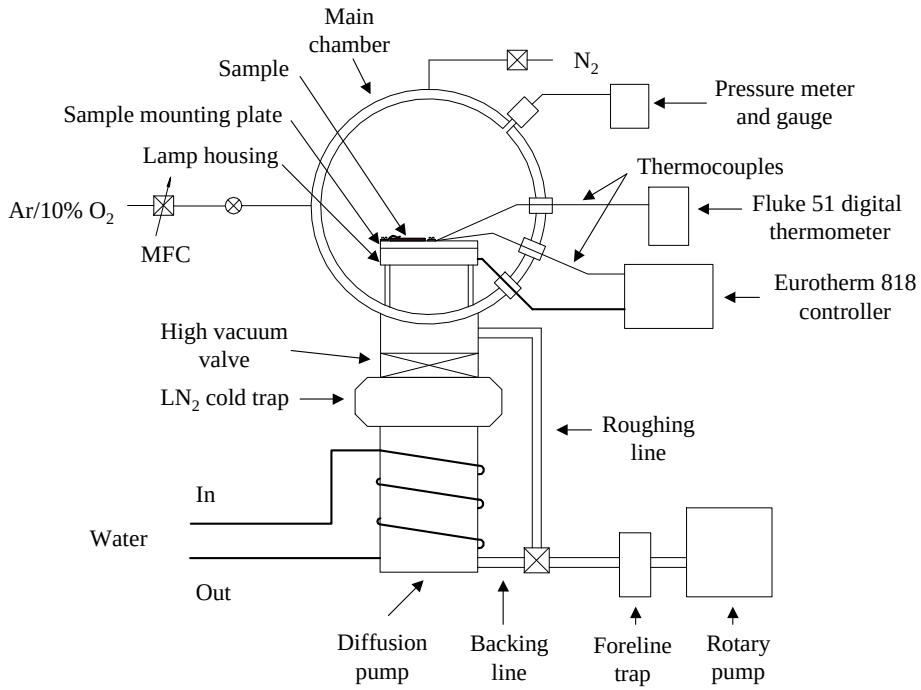

Figure 4.1: Schematic representation of the vacuum annealing equipment.

4.2.3 Rapid Thermal Processing in Argon

TM5 wafer pieces were RTP annealed using an AG Associates Minipulse system, described in detail in Chapter 3. A Sensarray single point process probe (a 3" silicon wafer with an embedded thermocouple) mounted on a quartz wafer holder, served as both temperature sensor and sample mounting platform. Argon was continuously flowed through the sample chamber. The RTP equipment was fully computer controlled with the output from the Sensarray process probe used as the input to a feedback loop which modulated the lamp intensity so as to control the sample temperature. A second computer was used to record the temperature of the process probe during each run by connecting an auxiliary temperature output connection to a digital multimeter that was itself connected to the computer using the GPIB. Using a simple programme written in Visual Basic the output of the multimeter was then sampled at regular intervals. Graphical display of the RTP temperature profiles proved invaluable during the process of optimising the parameters of the temperature control algorithm.

4.2.4 Electrical Testing

Die were probe tested by Phoenix VLSI using an IMS Logic Master XL-100 wafer prober (8") in conjunction with bespoke software routines, for which the author is indebted to Mr.

N. Stogdale and Mr. J.D. Wilcock. Probe testing was performed at three stages, these being:

(i) As received from the foundry and prior to sawing into octant pieces.

(ii) After sawing into octant pieces.

(iii) After thermal treatment.

The testing regime was a standard functionality test that all TM5 wafers received from the foundry undergo, comprising:

0. Probe continuity check.
1. Supply current (I_{DD}), power-up and power-down, 5V supply only.
2. DC bias generator voltages (V_{ref}), 5V supply only.
3. Channel amplifier toggle tests, true and inverse chequerboards (to test for short circuits and stuck outputs respectively) 4.75 and 5.25 V supplies.
4. Channel amplifier DC output voltage, 5V supply only.
5. Channel amplifier DC positive step gain, 5V supply only.

As a result of these tests each die was assigned a classification as follows:

Group ×: Not passing continuity.

Group 0: Passing continuity only.

Group 1: Passing continuity, supply current and DC bias generator tests only.

Group 2: Passing all tests, with 18 or fewer amplifiers failing checks 3, 4 and 5.

Group 3: Passing all tests completely, i.e. a fully working die.

It should be noted that these tests indicate circuit functionality only and do not give a true indication of device performance or potential for premature failure during operation.

4.2.5 Surface Roughness.

Changes in the roughness of the surface of the ROIC die can be indicative of potentially detrimental alteration of metallisation. Surface roughness can be altered by effects such as grain growth, pin holing, oxidation, and stress induced cracking and blistering in the metallisation. The surface roughness of the die was measured using a WYKO RST Plus optical surface profiler which uses white light interferometry to determine the relative

heights of surface features. A ×20 magnification objective was used, giving a lateral spatial resolution of 0.5μm and the vertical resolution was <1nm. One limitation of the equipment is that the surface must be reflective and free from transparent optically thin films and meant that only the bond pads of the ROIC die were suitable for measurement, since the rest of the circuitry had an overlying passivation layer of silicon oxy-nitride to a depth of approximately 1μm. Surface roughness statistics output by the WYKO software included the average surface roughness (Ra), the rms surface roughness (Rq) and the peak to valley value (Rt).

4.2.6 SEM and Optical Microscope Inspection.

Samples were inspected optically using an Olympus BH-2 microscope. Optical microscopy proved very useful in identifying areas of metallisation alteration, especially underneath the transparent passivation layer overlying everything except the bond pads. Higher resolution images were obtained using a JOEL JSM 6400F field emission SEM, which enabled good quality images to be obtained at the relatively modest acceleration voltage of 5keV, thereby minimising charging problems and potential ROIC damage.

4.3 Results

4.3.1 Simulated Sputtering

4.3.1.1 Temperature Profiles

The temperature of the sample plate was recorded at intervals throughout each simulated sputtering run, with a typical temperature profile shown in Figure 4.2 below. The ramp-up and ramp-down rates were modest, at 24°Cmin^{-1} and 17°Cmin^{-1} respectively, and typical of a PST sputtering system.

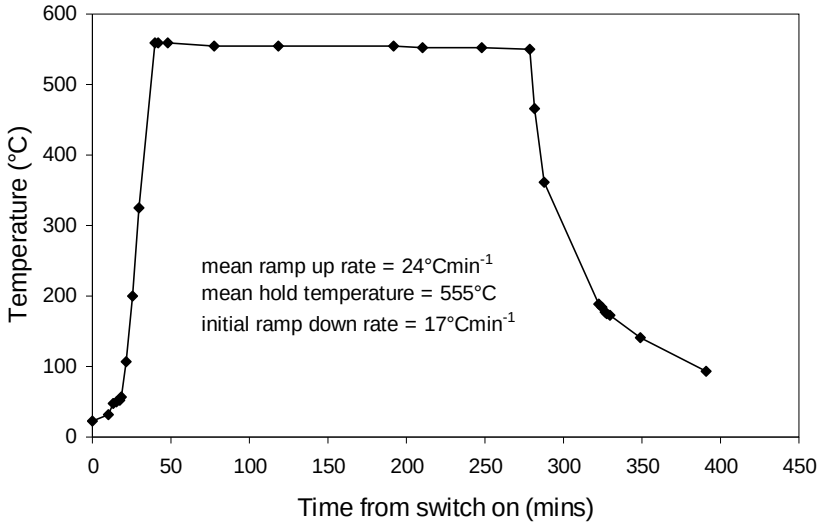

Figure 4.2: Temperature profile for a simulated sputtering run.

4.3.1.2 Thermal Regimes and Electrical Testing

The simulated sputtering regimes used for the TM5 pieces are detailed in Table 4.1. In all cases the hold time was four hours, with the hold temperature successively increased from 452°C to 575°C. A further run was carried out in air at atmospheric pressure to determine whether the ambient atmosphere had an appreciable effect on device survival.

Wafer	Piece	Hold Temperature (°C)	Hold Time (hours)	Ambient Atmosphere
0636097412D4	2	452	4	5mTorr Ar/10% O_2
0636097412D4	3	488	4	5mTorr Ar/10% O_2
0636097412D4	4	501	4	5mTorr Ar/10% O_2
0636097412D4	5	527	4	5mTorr Ar/10% O_2
0636097412D4	6	555	4	5mTorr Ar/10% O_2
0636097412D4	7	575	4	5mTorr Ar/10% O_2
3557300612C0	1	550	4	Air at s.t.p.

Table 4.1: Conditions used for simulated sputtering

Table 4.2 below shows the result of electrical testing (after sawing) both prior to and after thermal treatment with the yield figure being the ratio of the number of die passing the electrical tests before and after treatment. It can be seen from the table that the die survive simulated sputtering very well, even up to 575°C. The single die failure at 555°C is attributed to wafer edge damage, due to sawing, causing a probe needle contact problem. Die on the piece annealed in air at 550°C have obviously faired worse than their

counterparts annealed in 5mTorr Ar/10% O_2. The failure analysis summary shown in Table 4.3 shows that most die failed catastrophically, i.e. did not pass group × or group 0 tests. A plausible explanation for this is the silicon-oxynitride passivation becoming ineffective to preventing oxygen diffusion at elevated temperatures allowing some oxidation of the underlying metallisation.

Hold Temperature (°C)	Ambient Atmosphere	Passes prior to Thermal Treatment	Passes after Thermal Treatment	Yield (%)
452	5mTorr Ar/10% O_2	19	19	100
488	5mTorr Ar/10% O_2	27	27	100
501	5mTorr Ar/10% O_2	28	28	100
527	5mTorr Ar/10% O_2	24	24	100
555	5mTorr Ar/10% O_2	34	33	97
575	5mTorr Ar/10% O_2	34	34	100
550	Air at s.t.p.	26	5	19

Table 4.2: Before and after electrical testing results for simulated sputtering of TM5 octants.

Test classification				Main failure mechanism
×	0	1	2	
4	22	2	3	I_{DD} low, bandgap

Table 4.3: Failure analysis summary for air annealed sample.

4.3.1.3 Optical Inspection

Generally two areas were chosen for comparison between pieces, the metallisation around a bond pad and an area of metallisation on one of the op amp circuits. Figures 4.3 and 4.4 below show views of bond pad and op amp metallisation, respectively, on a die prior to thermal treatment. An inspection of all low-pressure annealed (5mTorr Ar/10% O_2) pieces revealed no obvious signs of damage, even at the highest temperature of 575°C.

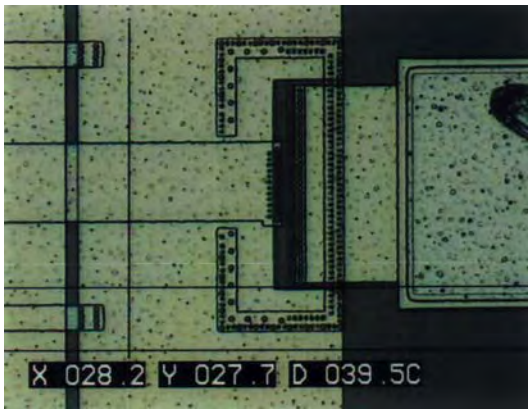

Figure 4.3: Bond pad metallisation on untreated die.
(*Original in colour*)

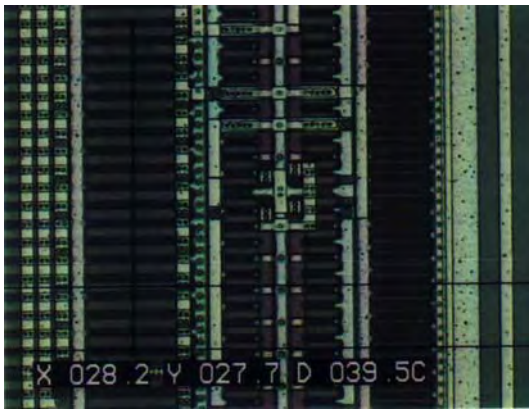

Figure 4.4: Op-amp metallisation on untreated die.
(*Original in colour*)

To assess the effect of ambient atmosphere on the ROIC an octant piece was annealed at 550°C in air. The electrical results from this sample, discussed above, gave a relatively low yield compared to the corresponding low-pressure annealed piece. Optical inspection showed visible signs of damage both on metallisation around the bond pads, Figure 4.5, and on the op-amp circuits, Figure 4.6.

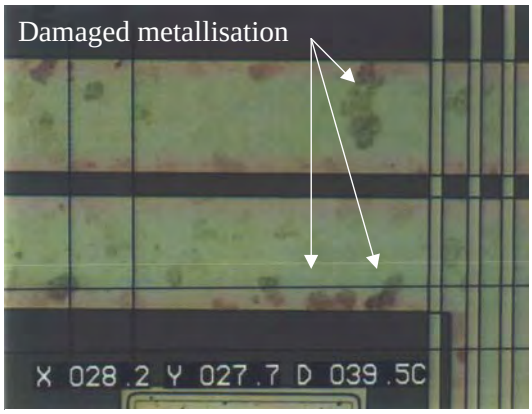

Figure 4.5: Damaged metallisation in the viscinity of a bond pad, die annealed in air.
(*Original in colour*)

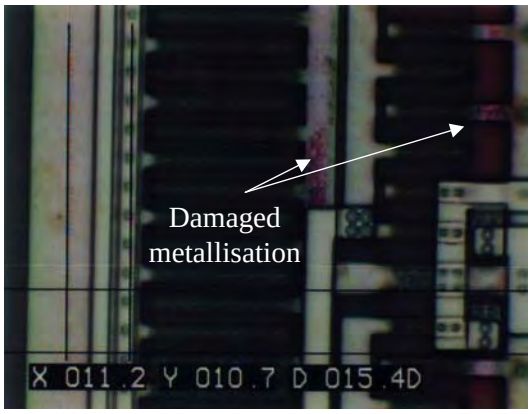

Figure 4.6: Damaged metallisation on an op-amp circuit, die annealed in air.
(*Original in colour*)

4.3.1.4 SEM Inspection.

An inspection was made of both as-received and heat treated samples using the SEM. For the simulated sputtering samples (5mTorr Ar/10% O_2) no apparent damage to the die was observed at temperatures up to 554°C with the images being indistinguishable from those

from the as-received wafer piece. At 575°C some pitting on the bond pads was observed, see Figure 4.7, but no other signs of damage were seen elsewhere on the die. The apparent rough surface on the bond pad was a foundry-processing artefact and was present on some as-received wafers. For the sample annealed in air at 550°C modification of the bond pads was observed, Figure 4.8. Both depressions in the metal surface and blistering was observed, along with some hillocking. Depression of the surface has been attributed to loss of aluminium by diffusion into the underlying silicon with the blistering thought to be due to an increase in compressive stress resulting in delamination and cracking. A cursory examination of the op-amp circuitry on the die was made but did not yield any useful information due to the charging problems caused by the silicon oxynitride passivation layer.

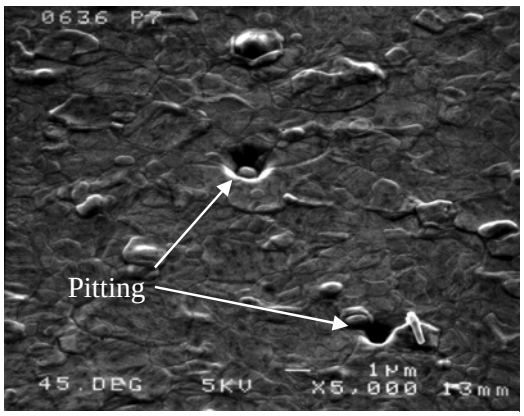

Figure 4.7: Pitting of bond pad after 575°C simulated sputter.

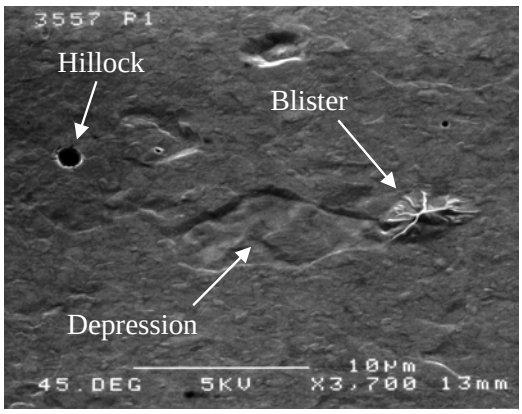

Figure 4.8: Bond pad after 4 hour air anneal at 550°C.

4.3.1.5 Surface Roughness.

The rms surface roughness' for an as received, air annealed, and all of the simulated sputtering samples are shown in Figure 4.9 below. For all samples an average was taken of the Rq values measured for four bond pads. Thermal damage effects observed using the SEM on the 575°C simulated sputtered and 550°C air annealed die were obviously insufficient to significantly change the measured Rq.

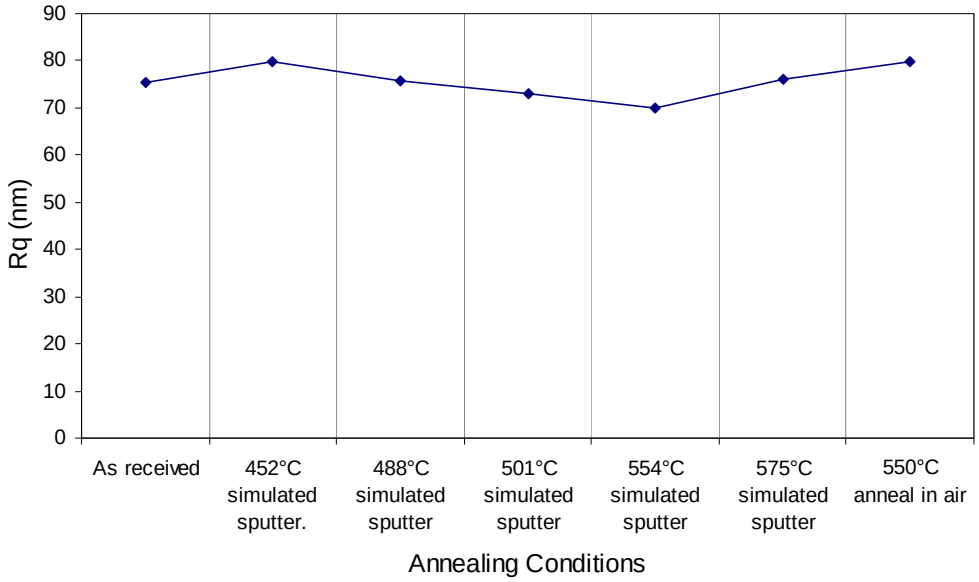

Figure 4.9: Rq for as received, air annealed and simulated sputtering samples.

4.3.2 Rapid Thermal Processing

4.3.2.1 Ambient Atmosphere

The ambient atmosphere chosen for RTP experiments was flowing argon. Ideally the RTP chamber would have been evacuated but the equipment used did not have this capability. Argon was chosen to give conditions representative of the anaerobic environment that the ROIC would experience during device processing, i.e. with sacrificial and barrier layers overlying it. It was also thought that the use of an inert atmosphere would allow yield changes due to purely thermal effects to be investigated, especially in light of the results from the air annealed sample discussed in section 4.3.2.1 above.

A short experiment was conducted to determine the best Ar flow conditions for prevention of oxidation of samples during the RTP runs. This entailed using a titanium coated silicon wafer, Ti(0.1μm)/SiO_2(0.8μm)/Si, cut into 1cm^2 pieces. The sheet resistivity, ρ_s, of the pieces was determined using a four point probe method. One piece was then RTP'd in flowing oxygen to check as to whether oxidation would occur by this method by measurement of ρ_s. A series of RTP runs was then performed using various argon flow rates and pre-run purge times, ρ_s being measured after each run. The minimum conditions to prevent oxidation (minimal change in ρ_s from the pre-annealed state) were determined to be an argon flow rate of 7l/min with a pre-run purge of 10 minute duration.

4.3.2.2 Temperature Calibration

A calibration of the temperature indicated by the RTP apparatus was performed in order to verify the set hold (or steady state) temperature and the also the ramp-up rate. To calibrate the hold temperature a $1cm^2$ piece of a PST coated platinised silicon wafer had a foil K-type rapid response thermocouple attached to it using high temperature cement. This thermocouple was connected to an RS Digital Thermometer and the wafer piece placed centrally on the Sensarray process probe (in common with all other samples reported in this thesis) inside the RTP chamber. At a programmed hold temperature of 600°C the indicated temperatures on the RTP apparatus and digital thermometer were in agreement to ±2.5°C. Combining this with the accuracy of the Sensarray process probe (0.1% of reading or 1°C) and the temperature variation due to the control algorithm of ±2.5°C gives a margin of error for the on the hold temperature of ±6°C which is insignificant compared to the 25°C temperature difference TM5 piece anneals.

Calibration of the programmed ramp-up rate was made by examination of a recorded temperature profile, Figure 4.10 below. The ramp rates during this run, Figure 4.11, were calculated by performing a simple numerical differentiation of the recorded temperature with respect to time. Taking only the ramp-up portion of the curve a line was fitted to the data, see Figure 4.12, with the calculated ramp rate of $47°Cs^{-1}$ comparing well with the programmed value of $50°Cs^{-1}$.

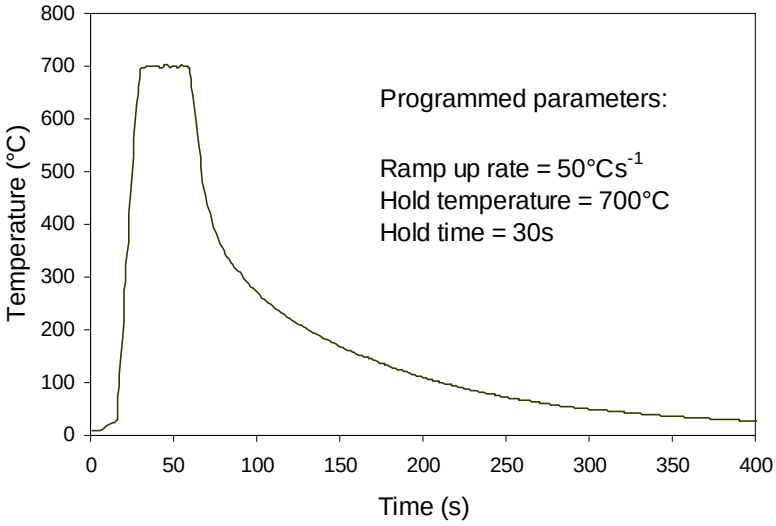

Figure 4.10: RTP Temperature Profile

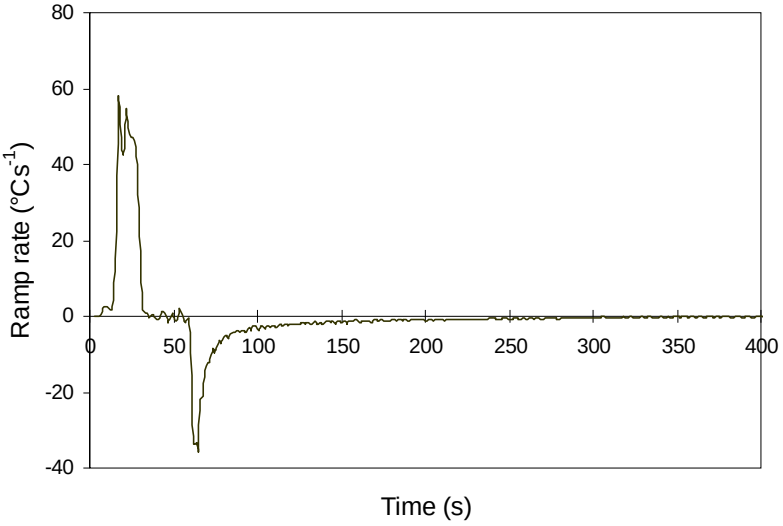

Figure 4.11: RTP ramp rates.

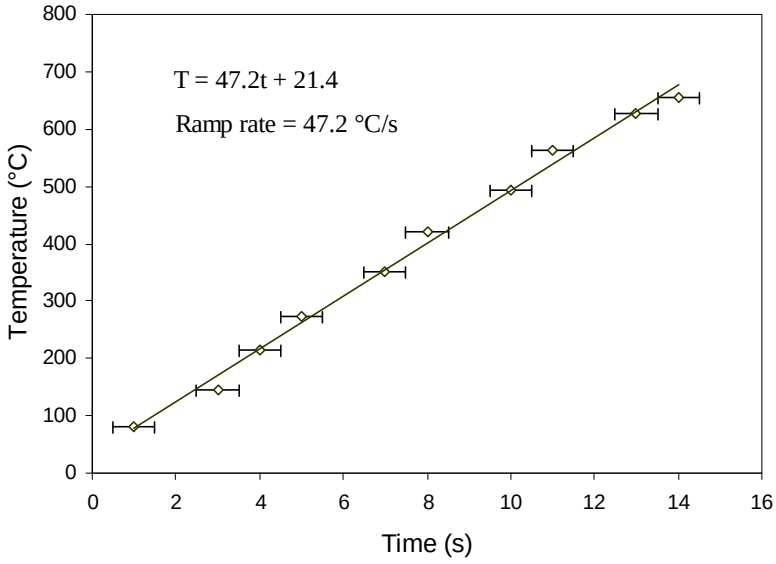

Figure 4.12: RTP ramp-up rate calibration. T is temperature in °C and t is time in seconds.

4.3.2.3 Thermal Regimes and Electrical Testing.

A set of RTP annealing regimes to test the survivability of the ROIC die is detailed in Table 4.4 below. The ramp up rate in each case was 50°Cs^{-1} with the hold times varied between 5 and 300s. Since the melting temperature of pure aluminium is 660.5°C [73], and slightly lower with the addition of a small amount of silicon [72], it was thought that die were not likely to survive long at hold temperatures of 650°C and 675°C. For these two temperatures the hold times were limited to 30s and 5s respectively. It has been assumed that any RTP

performed in a detector fabrication process would be to react the ferroelectric layer, which would have been deposited at low temperature. The experiments on simulated sputtering imply that sputter deposition of a ferroelectric layer at temperatures around 300°C would have no effect on the ROIC. Consequently the octant pieces used did not undergo a simulated sputter prior to RTP.

Hold Temperature (°C)	Hold Time (s)					
	5	10	30	60	120	300
600	3	3	3	3	3	3
625	3	3	3	3	3	3
650	3	3	3	6	6	6
675	3	6	6	6	6	6

Table 4.4: RTP regimes for TM5 octant pieces, 3denotes conditions used.

Yield figures for the electrical testing of the RTP'd die are given in Table 4.5 with a plot of yield against hold temperature and time shown in Figure 4.13. At 600°C there was no effect on the die for hold times up to 30s, except for a single failure at 10s hold time. Above 30s hold time there was a drastic decrease in pass rate with no die surviving beyond 60s. Increasing the hold temperature to 625°C resulted in a higher mortality rate. At 5s hold time the yield was 53%, dropping to 32% at 30s with no die surviving at 60s and beyond. Curiously the yield at 650°C for 5s, at 69%, was higher than for 625°C for 5s although no die survived at 10s and 30s. As expected no die survived at 675°C, with optical examination showing gross dispruption of the metallisation. The failure analysis summary of all wafer pieces, Table 4.6, shows that where failure occurs it is usually catastrophic i.e. die are classified as group × or group 0 with shorting being a major problem.

Wafer	Piece	Hold Temperature (°C)	Hold Time (s)	Passes prior to RTP	Passes after RTP	Yield (%)
3557300612C0	2	600	5	43	43	100
3557300612C0	3	600	10	40	39	98
3557300612C0	4	600	30	29	29	100
3557300612C0	5	600	60	33	8	24
3557300612C0	8	600	120	32	0	0
1706098712C5	1	600	300	38	0	0
1706098712C5	2	625	5	38	20	53
1706098712C5	3	625	10	43	17	40
1706098712C5	5	625	30	31	10	32
1706098712C5	4	625	60	35	0	0
1706098712C5	6	625	120	39	0	0
1706098712C5	7	625	300	32	0	0
1706098712C5	8	650	5	32	22	69
1046098112F0	1	650	10	36	0	0
1046098112F0	2	650	30	39	0	0
1046098112F0	3	675	5	35	0	0

Table 4.5: Before and after electrical testing results for RTP annealed TM5 octants.

Hold Temperature (°C)	Hold Time (s)	Test classification				Main failure mechanism
		×	0	1	2	
600	5	-	-	-	-	-
600	10	-	1	-	-	I_{DD} (high)
600	30	-	-	-	-	-
600	60	0	19	3	3	Vref
600	120	12	27	-	-	I/O shorts, bandgap, I_{DD}
600	300	39	-	-	-	I/O shorts
625	5	0	9	1	13	I_{DD} (high), Vref
625	10	0	19	0	8	I_{DD} (high) band gap
625	30	4	33	0	1	I_{DD} (high)
625	60	1	19	0	4	I_{DD} (high)
625	120	45	1	-	-	I/O shorts
625	300	19	16	-	-	I/O shorts, I_{DD} (high)
650	5	0	4	0	6	I_{DD} (high)
650	10	13	24	-	-	I/O shorts, I_{DD} (high)
650	30	20	26	-	-	I/O shorts, I_{DD} (high)
675	5	7	31	-	-	I/O shorts, I_{DD} (high)

Table 4.6: Electrical failure summary for RTP'd die.

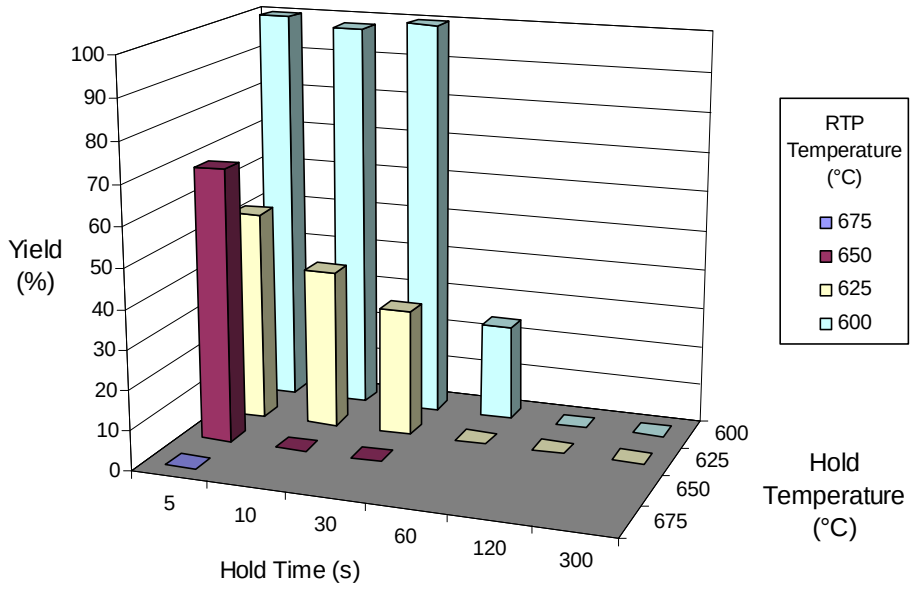

Figure 4.13: Yield of surviving die upon RTP.
(*Original in colour*)

4.3.2.4 Optical Inspection.

As for the samples subjected to simulated sputtering, section 4.3.1.3, the RTP'd pieces were visually inspected prior to electrical testing. A range of thermally induced damage effects were observed ranging from occasional hillocking in the metallisation to large scale discolouration, blistering and melting. Generally a low yield on electrical testing was concomitant with obvious signs of deterioration. Table 4.7 below gives a brief summary of some of the observed effects of RTP annealing on the metallisation.

Hold Temp. (°C)	Hold Time (s)					
	5	10	30	60	120	300
600	No effect	No effect	No effect	No effect	No effect	Bond pad blackening. Gold coloration of metal. Peeling
625	No effect	No effect	Blistering. Bond pad blackening.	Blistering. Bond pad blackening.	Blistering. Bond pad blackening. Gold coloration of metal.	Blistering. Bond pad blackening. Gold coloration of metal.
650	No effect	Blistering. Bond pad blackening.	Blistering. Bond pad blackening.	-	-	-
675	Blistering and melting	-	-	-	-	-

Table 4.7: Observations of metallisation after RTP.

Pictures representative of the effects referred to in Table 4.7 are shown in Figures 4.14 and 4.15 below.

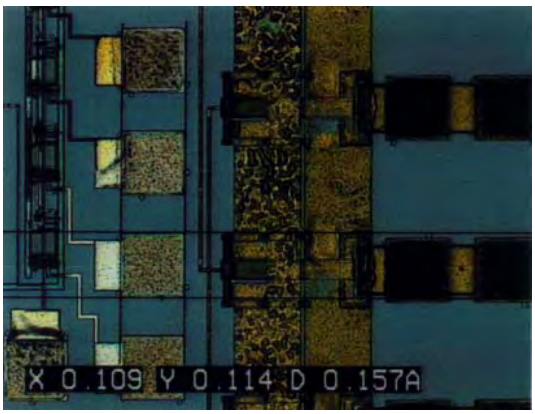

Figure 4.14: Gold discolouration of metallisation and blackening of bond pads (600°C, 300s). (*Original in colour*)

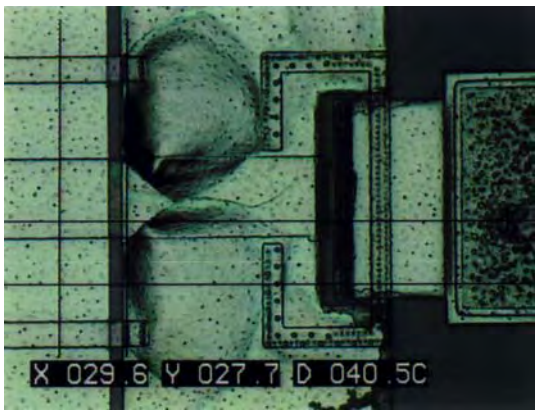

Figure 4.15: Blistering of metallisation (625°C, 30s). (*Original in colour*)

4.3.2.5 SEM Examination.

SEM inspection of the die after RTP revealed some interesting phenomena associated with annealing. Figure 4.16 below shows a bond pad after RTP at 600°C for 120s with pitting of the surface being clearly seen. Although this could only be observed clearly on the bond

pads due to the overlying passivation, it seems very likely that damage to the metallisation occurred elsewhere on the circuitry.

After 300s at 600°C the bond pads had suffered gross alteration, see Figure 4.17, and easily accounts for the dramatic increase in the measured surface roughness. Elsewhere on the die the metallisation had suffered very badly. Figure 4.18 shows evidence of blistering and cracking which is attributed to increasing compressive stress in the metallisation layers.

Figures 4.19 to 4.21 show some of the effects observed after RTP at 650°C for 30s. Damage to the bond pads was very evident, Figure 4.19, with roughening of the surface and blistering. Damage of metal tracks on the op-amp circuitry was also clearly observed with some having simply cracked, Figure 4.20, while on others strange 'cauliflower' type structures had developed, Figure 4.21. The latter are thought to be due to metallisation spewing out from cracks in the passivation due to the effects of heat and/or stress. Invariably these structures were observed where the metal track turned a corner and presumably reflect a weakness in the passivation layer at these points.

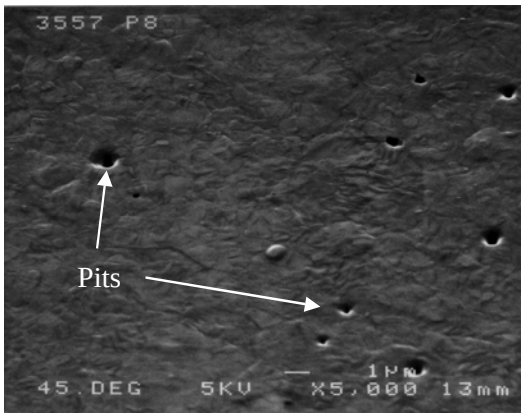

Figure 4.16: Pitting of bond pad metallisation after 120s RTP at 600°C.

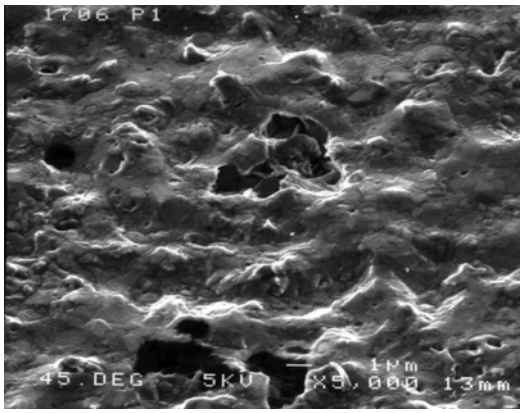

Figure 4.17: Damage to bond pad after 600°C RTP for 300s.

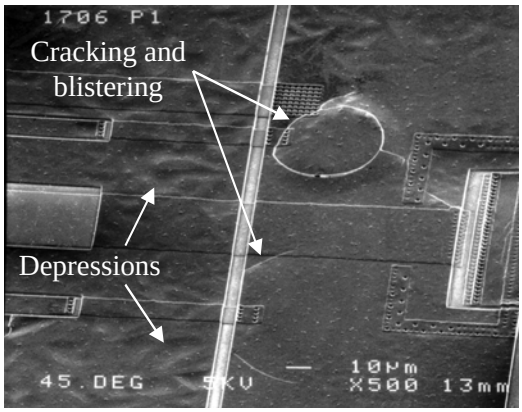

Figure 4.18: Damage to metallisation after 600°C RTP for 300s.

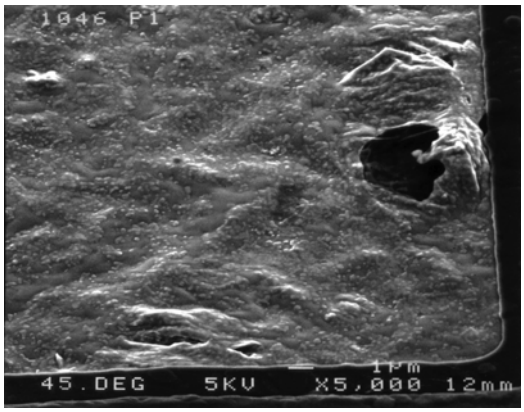

Figure 4.19: Damage to bond pad after 650°C RTP for 30s.

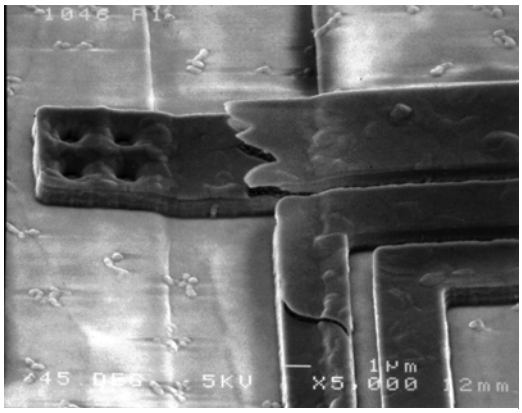

Figure 4.20: Damage to bond pad after 650°C RTP for 30s.

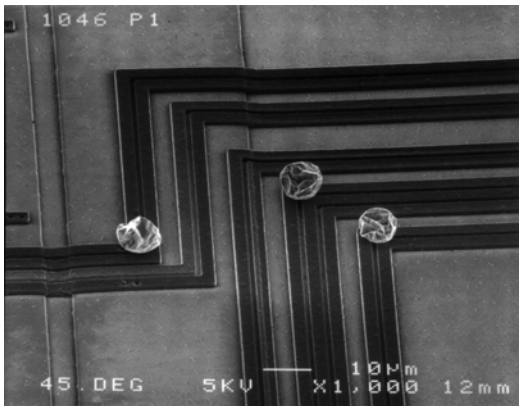

Figure 4.21: 'Cauliflower' structures in interconnect metallisation after 650°C RTP for 30s.

4.3.2.6 Surface Roughness of Bond Pads.

The rms surface roughness of the bond pads was measured for the samples that underwent RTP, Figure 4.22. Rq values for the all of 600°C RTP, except the 300s hold time, samples were around 47nm. This is lower than the level measured for the as-received and simulated sputtered, Figure 4.9, samples where Rq was around 76nm. As mentioned previously, some of the wafers supplied by the foundry suffered from a processing artefact whereby residual debris from one of the etch stages littered the surface of the die. These can be clearly observed in Figure 4.3, which shows a bond pad on an as received die, and explains the difference in Rq values.

RTP at 600°C for 300s was found to markedly increase the surface roughness of the bond pads, as did hold temperatures above 600°C for all hold times. This increase was found to

be commensurate with thermally induced damage to the metallisation observed using the SEM.

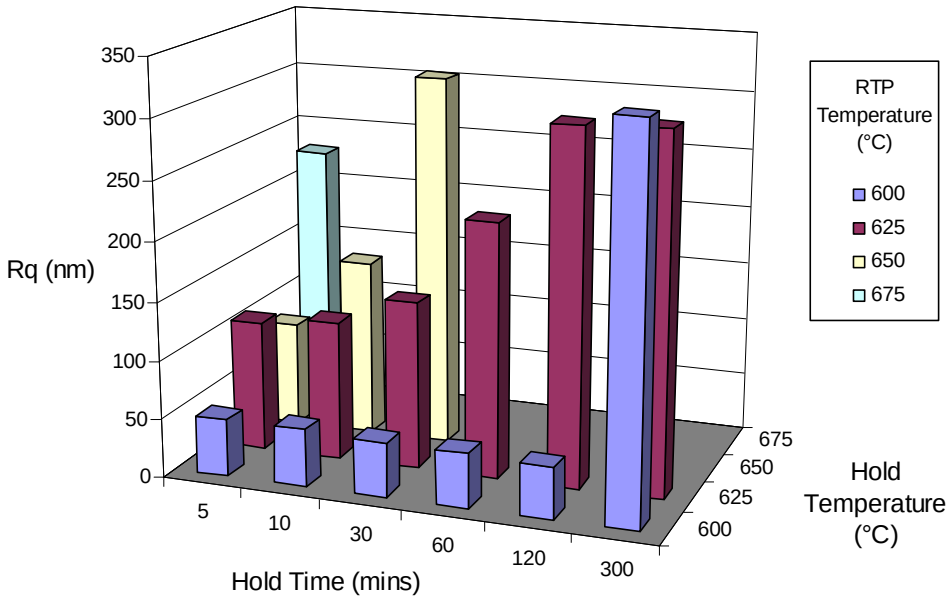

Figure 4.22: Bond pad surface roughness (Rq) after RTP.
(*Original in colour*)

4.4 Discussion.

Simulated sputtering of TM5 octant pieces gave interesting results with electrical tests showing that the die had survived well beyond the nominal 450°C processing limitation [74]. Indeed the only indication of metallisation alteration was small scale pitting of the bond pads observed on the sample annealed at 575°C. The wafer piece annealed in air at 550°C for 4 hours suffered catastrophic electrical failure. SEM and optical microscope observations revealed damage to the bond pad metallisation, possibly caused by oxidation effects, although surface roughness measurements revealed no significant change between any of the pieces. Damage to interconnect tracks suggests that the silicon oxynitride passivation layer has become permeable to oxygen at elevated temperatures. Oxidation of some of the metal interconnects would explain the main failure mechanism of low supply current.

This result is significant since it suggests that if the ROIC can be effectively shielded from oxygen then it will survive to higher temperatures. The question with the simulated sputtering is where the survivability boundary lies. Since pitting was observed on the bond

pads at 575°C then it is likely that metallisation elsewhere on the die would be affected in some way, potentially compromising the devices long term performance. Although the electrical testing gave a 100% yield, it must be remembered that the tests used look only for functionality of the die and do not address performance or lifetime issues. With this in mind it would seem sensible to limit the substrate temperature during a 4 hour sputtering run to 550°C.

RTP in argon between 600°C and 675°C met with mixed success in terms of device survivability. At a hold temperature of 600°C electrical testing showed the devices to have survived undamaged for up to 30s, except for a single failure at 10s hold time. Hold times longer than 30s resulted in a rapid drop off in survival rate with no functioning die beyond 60s. At the longest hold time of 300s the surface roughness of the bond pads increased dramatically and optical and SEM examination revealed gross disruption of the metallisation. Increasing the RTP hold temperature to 625°C hastened the onset of device failure, with no fully yielding wafer pieces at any of the hold times. After 5s and 10s the yield was 53% and 40% respectively with no visible ill effects although bond pad surface roughness had increased by over a factor of two compared with the corresponding 600°C runs. It was not until the hold time was increased to 30s that there was a visible deterioration of the metallisation, with effects such as blistering accompanying a low electrical yield. Although some die passed electrical tests even with severe blistering, their long-term performance must be called into question. Hold times longer than 30s resulted in total electrical failure of the die and, as with longer hold times at 600°C, severe visible damage. The principle cause of electrical failure on all samples was shorting, presumably primarily caused by hillocking and spiking of the aluminium.

The die given an RTP anneal at 650°C were not anticipated to survive for long hold times. This was borne out with 69% of die surviving for 5s and the yield dropping to zero for all longer hold times with shorting being the main failure mode. Interestingly the pass rate at 650°C for 5s was higher than for the same run at 625°C, although it is not obvious why this should be. SEM and optical inspection of failed die at hold times longer than 5s showed dramatic disruption of the metallisation, both on the bond pads and also on the interconnect tracks of the element amplifier circuits. This is not surprising considering that only 10°C separates this hold temperature form the melting temperature of pure aluminium, and with a ~1% silicon content the eutectic temperature will be slightly lower [72]. The anneal at 675°C

for 5s resulted in extensive damage to the metallisation and complete electrical failure of the die, as was suspected.

Taking the RTP results as a whole a tentative survival window can be worked out. If a yield threshold of 50% is set then this is 600°C for up to 30s, 625°C for 5s and 650°C for 5s. A lower yield threshold, say 40%, would extend the hold time at 625°C to 10s – beyond which visible damage to, and increasing surface roughness of, the metallisation becomes apparent. It must be remembered that other factors in the post processing will affect the total device yield, so that the lower the ROIC survival rate the more expensive the whole process becomes. Additionally, if a significant number of devices (say > 30%) are failing then it indicates that there is a major problem in the processing which may lead to premature failure in operation or relatively poor performance. With this in mind a sensible thermal budget limitation for the ROIC is 600°C for 30s.

The RTP results can be compared to the results of Hanson et al [70] who propose a direct on silicon focal plane array process for lead titanate microbridges. A similar RTP excersise was carried out to determine the limits of survivability of the ROIC, again using a standard functionality test for incoming die. The hold time-temperature graph obtained by Hanson et al is shown in Figure 4.23, where the temperature quoted beside each point represent the detector NETD that would result from measured properties of material processed under these conditions. It must be noted that these results carried with them little information about the nature of the process i.e. the RTP ramp rate, the processing atmosphere and what yield threshold constituted a fail. The question of the processing atmosphere is very important, as demonstrated by the results reported in this chapter.

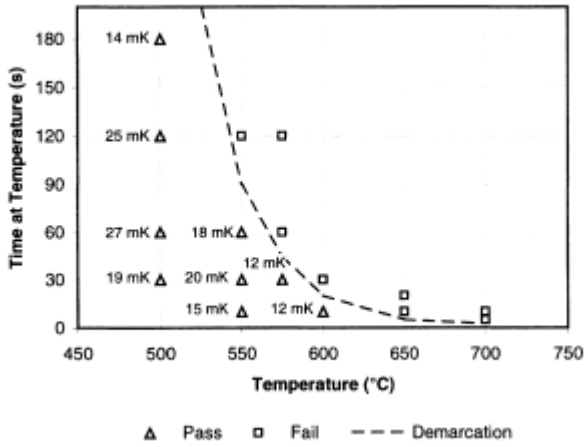

Figure 4.23: RTP pass-fail regimes determined by Hanson et al [70].

The pass-fail demarcation line in Figure 4.23 is in general agreement with the results obtained from RTP in argon although Hanson records no passes after 600°C for 10s. At the lower temperatures of 550°C and 575°C the survival times are 60s and 30s respectively. This is far shorter than the 4 hours of the simulated sputtering experiments. The cause of this apparent premature failure could either be oxidation of the ROIC metallisation, if processed in air or oxygen, or problems due to stresses induced by the rapid temperature changes during RTP.

Recently there have been moves by the semiconductor industry to replace aluminium based interconnect metallisation with copper. There are many reasons why a move to copper is attractive. The resistivity of copper, at 1.7μΩcm, is significantly lower than for that for aluminium, at 3.1μΩcm [77]. This introduces a number of tangible benefits [78]. Firstly, for fast applications the RC time constant of interconnects is reduced. The interconnect resistance is lowered, helping to reduce on chip power consumption. Secondly, copper has better electromigration resistance than aluminium, thereby enabling use in high current density applications. Lastly, fewer processing steps are required due to the use of Chemical Mechanical Polishing (CMP) and the fact that fewer metal layers are required, due to thinner tracks. Reduction of the required number of processing steps results in lower manufacturing costs. The introduction of copper with its higher melting temperature, 1085°C [73], might be seen as alleviating the thermal budget constraints of direct on silicon integrated IR detectors. However, the full benefits of the move to copper will only be realised by a corresponding move to replace SiO_2 interlevel dielectric by so-called low-k (low-ε_r) dielectric materials [77, 78, 79].

The introduction of low-k dielectrics, such as spin-on organic polymers and inorganic PTFE based compounds [79], will result in temperature limitations even more stringent than those determined in this chapter for TM5 ROIC's. The table presented in the article by Peters [79] shows that the likely low-k materials have cure temperatures <450°C, with only a few being stable at this temperature for short periods. It is likely that foundries will switch to copper/low-k processing for all applications [78], and not just high speed devices. Since the production volumes of IR detector ROIC's will be insufficiently large to be able to influence foundry practice, the future temperature limitation for post-processing will probably be in the region of 400°C or less, depending on the dielectric used. Unless a

bespoke fabrication facility is used this makes the use of the composite wafer technology, described in Chapter 2 of this thesis, not only attractive but ultimately essential, at least for ferroelectric based devices.

4.5 Summary.

A series of annealing studies has determined the thermal budget limitations of standard aluminium metallisation based thermal detector ROICs to sputtering and RTP annealing. Using a bespoke vacuum annealer the ROICs were found to survive with electrical yield unchanged form the pre-anneal value to a temperature of 575°C for a duration of 4 hours in an atmosphere of 5mTorr of Ar/10% O_2. Some small scale bond pad damage was observed and may mark the onset of alteration of the metallisation elsewhere on the die. With this in mind the time-temperature limitation for sputtering thin film PST onto substrates containing ROICs is 550°C for 4 hours. The partial pressure of ambient oxygen was found to be very important in determining the yield of surviving devices at elevated temperature with die annealed at 550°C for 4 hours in air (stp) suffering catastrophic electrical failure with visible damage to circuitry and metallisation. This is attributed to the silicon oxynitride passivation layer on the die becoming permeable to oxygen at this elevated temperature. RTP annealing trials in flowing argon (used to distinguish thermal failure from oxygen induced failure) revealed no significant number of device failures for hold times of up to 30s at 600°C with a sharp drop in yield at longer hold times, with shorting being the principle electrical failure mode. Higher temperature RTP anneals resulted in significant number of failed die and alteration of the metallisation, especially at 650°C and 675°C. From the point of view that a significant number of failed die may have implications on the long term functionality of surviving devices it would seem prudent to set the RTP thermal budget to 600°C for 30s. This of course assumes that any overlying ferroelectric would be deposited at temperatures at which the ROIC remains undamaged.

A review of recent semiconductor literature reveals a trend towards the introduction of copper based metallisation which at first sight would appear to offer the prospect of increasing the thermal budet limitations on the ROIC. Paradoxically, in order to realise the full benefits of copper metallisation the the use of low-k dielectrics with low cure temperatures, <450°C, looks set to reduce rather than extend the ROIC thermal budget –

assuming a general uptake of copper based metallisation. Unless a bespoke fabrication process is used a move away from a direct on silicon detector fabrication appoach to one based on the interconnect wafer technology then becomes desirable.

Chapter 5:

Single RF Magnetron Sputtering Deposition of Lead Scandium Tantalate at 300°C followed by Annealing.

5.1 Introduction.

The use of ferroelectric materials as the sensing medium in uncooled infrared detectors is well established. Devices made with these materials are thermal detectors, whereby a change in the temperature of the detector results in a change in the polarisation state of the ferroelectric - the pyroelectric effect [39], described in Chapter 2. The material lead scandium tantalate (Pb_2ScTaO_6, or PST for short) has been employed successfully in hybrid detectors in its hot pressed ceramic form [5] and currently forms the mainstay of the UK's high performance uncooled TI program. Since PST has a transition temperature between 20°C and 30°C, and the detectors are operated slightly above this temperature, then the normal mode of operation is termed the *dielectric bolometer* mode where an externally applied bias field results in an induced pyroelectric effect [6, 7, 39]. The IR detectors thus produced are around twice as sensitive as those based on lead zirconate titanate (PZT) which, having a Curie temperature at around 240°C, is operated in the conventional pyroelectric mode. Work reported in this chapter concerns thin film PST for integrated detector applications whereby the detector structure is itself formed by surface micromachining of a thin film layer stack. Using this method microbridge detectors can either be formed directly on top of the readout integrated circuitry (ROIC) or can be fabricated on a composite (see Chapter 2) wafer which can then be solder bump-bonded to the ROIC.

PST is an interesting material which has been the subject of much research in its bulk ceramic form [13, 80, 81], processed at temperatures in excess of 1200°C, but very little in the thin film form. As discussed in Chapter 2, the material in its perovskite phase is a mixed B-site cation form of the standard ABO_3 structure. In this form PST is ferroelectric and thus is the phase of interest from a thermal detector fabrication view point. The nature of this ferroelectricity is highly dependent on the arrangement of the scandium and tantalum cations on the B-sites, as shown by Setter and Cross [13, 80]. In the case of ordering of scandium and tantalum onto alternate B-site positions the material behaves as a first order ferroelectric with a unique transition temperature and a sharply peaked permittivity with

dielectric constants in the range 6000-20000 [37] depending on the preparation conditions. If the scandium and tantalum are randomly arranged on the B-sites then the material behaves as a relaxor ferroelectric [13, 22, 37, 80] where the dielectric maximum does not mark a ferroelectric/paraelectric phase change [22] and the transition temperature is not uniquely defined – there being a transition region rather than a transition temperature. In such materials there is what is termed a diffuse phase transition (DPT), described more fully in Chapter 2, where the transition is smeared out over a temperature interval the magnitude of which is dependent on the degree of long range chemical ordering [14]. An explanation for this behaviour was given by Smolenski [21] for the classic relaxor lead magnesium niobate (PMN) in terms of a compositional fluctuation model. For PST this model would suggest that the material consists of microregions, or Kanzig regions[21], on a 100-1000∑ scale with varying scandium and tantalum content. These regions have been observed by Kang et al [17] in HRTEM studies. Each of these Kanzig regions has a slightly different transition temperature the superposition of which gives the DPT.

Literature on PST in thin film form is scarce with what does exist being reported for a variety of substrate/electrode combinations, none of which are particularly suitable for device processing. Watton and Todd [7] reported the deposition of PST onto sapphire substrates via a two step sputtering process. Firstly a film of wolframite phase scandium tantalate $ScTaO_4$ was deposited which was then annealed. In a second step the annealed film was over coated with a reactively sputtered lead-oxide layer. The resulting layer stack was surrounded in lead-zirconate spacer powder and annealed at 900°C for up to 24 hours in air. At this temperature the lead oxide (melting temperature 886°C) formed a liquid flux which diffused into and reacted with the scandium tantalate to form PST. The resulting material was highly ordered and exhibited first order electrical characteristics with permittivities and induced pyroelectric coefficients in excess of 7500 and 6000$\mu C/m^2K$ respectively – parameters which compare very favorably with bulk. Similar results were obtained by Shorrocks et al [82, 83] using the two step method with sol-gel spin deposited layers. Sapphire has a good thermal expansion match with PST, however, for integrated detector applications the most realistic substrate material must be silicon, whether this be for the fully integrated or intermediate wafer processing routes. In addition, unlike the previous work on sapphire, the film must be grown on a conducting electrode. Lui and Payne [84] have reported on thin film PST on platinised silicon deposited by sol-gel spin casting which were dried at 300°C then fired at 650-700°C to produce the perovskite phase

with relaxor characteristics and permittivities in the range 3000-5000. Some ordering was observed by X-Ray diffraction after the samples were cooled at a rate of -1°C/hr from 700°C to 350°C. Bjormander et al [85] reported the growth of PST on yttrium barium cuprate (YBCO) buffer layer on $LaAlO_3$ substrates using laser ablation.

The aim of the work reported in this chapter was to investigate the nature of PST deposited at the relatively low temperature of 300°C onto platinised silicon by single RF magnetron sputtering [86], whether it can be converted into the required perovskite phase by post deposition annealing and what the suitability of this converted material is for use in an uncooled IR detector. Use of platinised silicon represents the idealised case where it is assumed that the underlying sacrificial layer will have no significant effect on the growth and properties of the PST. The deposition technique is very similar to that proposed by Sayer [55, 56, 87] using a sectored metal target, and has been described more fully in Chapter 3. Deposition at low temperatures has several important practical advantages which include ease of compositional control, due to lower volatility of the lead component, and improved growth machine reliability.

This deposition temperature is lower than the perovskite formation temperature in PST [86] and therefore necessitates a post-deposition annealing step to react the film into the required phase. The main technique used in the work reported in the chapter is rapid thermal processing (RTP) with one reported sample being annealed in a conventional furnace. RTP, already described in Chapters 3 and 4, has the advantage of controllability and suitability for incorporation into an integrated processing schedule. Due to high ramp rates the time spent at temperatures where the pyrochlore phase of PST forms, ~300°C-500°C, can be minimised. When the work described in this chapter was first begun the primary aim was to investigate the viability of producing perovskite PST with good F_D values within the ROIC thermal budget identified in Chapter 4, using the low-temperature deposition/short high temperature RTP route. Part way through the programme of work the intermediate wafer technology became available, allowing anneal temperature-times well in excess of the ROIC survival limits to be investigated. The use of RTP has been widely reported for other materials, however this is the first reported work for PST. Deposition of PZT via a sol-gel route [31, 32, 64, 88, 89, 90, 92] is well documented and involves deposition into a low temperature phase followed by a high temperature crystallisation step using RTP. A number of authors have reported a similar processing route for sol-gel barium titanate [78, 79, 93]. Other

deposition methods such as sputtering, for PZT [91] and lead niobate [94], and laser ablation, of PZT [33], have also been reported. The RTP regimes investigated typically involve temperatures in the range 600-800°C and hold times in the range 1 second to 5 minutes. The work reported in this chapter is similar in concept to that performed by Vasant Kumar et al [91] where PZT was sputter deposited at a substrate temperature of 200°C into a mixed oxide/pyrochlore phase which was converted to perovskite by a 650°C 10s RTP anneal.

5.2 Experiment

5.2.1 Deposition

A PST thin film of 0.6μm thickness was reactively rf sputtered at 300°C onto a platinised silicon substrate in a Nordiko NM2000 sputtering system using a single composite target (as described in Chapter 3), with the deposition conditions summarised in Table 5.1.

Deposition Parameter	Value:PST	Value:Pt	Value:Ti
Substrate temperature	300°C	300°C	300°C
Base pressure	1.5×10^{-6} mbar	5×10^{-7}mbar	5×10^{-7}mbar
Sputter pressure	50 mTorr	9 mTorr	9 mTorr
RF power	70W	300W	150W
Substrate bias	430V	1100V	100V
Argon flow	92 sccm	27sccm	27sccm
Oxygen flow	4.5 sccm	-	-
Ar/O_2 ratio (Hiden Quadropole)	4.5%	-	-

Table 5.1: Thin film deposition parameters.

PST film thickness was measured using a RTH Talysurf after deposition, and after annealing with cross-sectional SEM. The platinised silicon substrate was prepared using a 3" silicon substrate {(004) orientated}, thermally oxidised to a depth of 0.8μm - necessary to prevent reaction between the silicon and platinum. A titanium adhesion layer of ≈100∑ thickness was RF diode sputter deposited onto the oxidised surface with an overlayer of platinum of 1000∑ thickness deposited by RF magnetron sputtering. Table 5.1 summarises the deposition conditions for the titanium and platinum layers, which were deposited in a Nordiko NM2000 sputtering system without breaking vacuum. Deposited of the platinum was under zone 2 conditions of the Thornton model [95], giving a characteristically dense film of (111) fibre textured columnar grains. For annealing experiments the final wafer was diced into $1cm^2$ pieces.

5.2.2 Annealing

The annealing conditions for all samples investigated are shown in Table 5.2. RTP annealing was performed using an AG Associates Minipulse system, as described in Chapter 3, with the sample mounted on a Sensarray single point process probe wafer and the ramp rate set at 50°C/s with natural cooling. RTP was either performed in flowing O_2 ($2lmin^{-1}$) or flowing argon ($5lmin^{-1}$). A SFL Instron vacuum compatible tube furnace was used for conventional oven annealing, with the ramp rate set at the maximum obtainable value of ~7.5°C/min – very slow compared to the RTP method.

Sample	Identifier	Anneal method	Anneal temperature (°C)	Anneal time	Anneal atmosphere
PSTCH637 piece B6	Sample A	none	-	-	-
PSTCH637 piece A3	Sample B	RTP	650	30s	Flowing O_2
PSTCH637 piece A4	Sample C	RTP	750	30s	Flowing O_2
PSTCH637 piece B4	Sample D	RTP	850	30s	Flowing O_2
PSTCH637 piece B5	Sample E	RTP	700	300s	Flowing O_2
PSTCH637 piece B2	Sample F	RTP	700	300s	Flowing Ar
PSTCH637 piece B3	Sample G	Furnace	700	1hr	800mbar O_2

Table 5.2: Annealing conditions.

5.2.3 Electrodes and Instrumentation

The platinum underlying the PST served as a common bottom electrode. Circular top electrodes of 1.5mm diameter (checked with a travelling microscope) were formed by sputtering chrome/gold, in a Nordiko NM2000, through a shadow mask. Hysteresis loops were measured using a Radiant Technologies RT66A ferroelectric tester operated at 1kHz in virtual ground mode.

5.3 Results

5.3.1 Materials Characterisation

5.3.1.1 Compositional Analysis by Energy Dispersive Spectroscopy

Energy dispersive spectroscopy at 15KeV using single element standards was used to determine the elemental composition of the PST thin film. Each sample was analysed both before and after annealing with the composition quoted as a ratio to the scandium content, i.e. Sc:Ta:Pb. Experimental uncertainty on the Ta/Sc and Pb/Sc ratio's is ±3% (see Chapter 3). Table 5.3 below gives the results of this analysis.

Sample	Sc:Ta:Pb As deposited	Sc:Ta:Pb After annealing
B	1:0.99:2.28	1:1.01:2.25
C	1:1.02:2.33	1:1.07:2.33
D	1:1.05:2.36	1:1.00:2.10
E	1:0.98:2.30	1:1.03:2.25
F	1:1.01:2.33	1:1.03:2.28
G	1:0.99:2.35	1:1.01:2.27

Table 5.3: Sample composition before and after annealing.

As-deposited the mean composition was 1:1.01:2.33 giving a close to stoichiometric scandium to tantalum ratio and a 16% lead excess, the latter being known to aid the transformation to perovskite in PST and similar materials at low temperatures through an as yet unexplained process[4, 86, 96, 97, 98]. Only sample D, 850°C for 30s, showed a significant compositional alteration with the lead excess dropping from 18% to 5%, as might be expected since the anneal temperature is approaching the lead oxide melting temperature of 886°C.

5.3.1.2 Optical and Scanning Electron Microscope Analysis

An optical micrograph of sample A is shown in Figure 5.1, with the surface being featureless apart from occasional dark spots. The numbers indicated give the horizontal (X), vertical (Y) and diagonal (D) dimensions in microns of the square formed by the intersection of the four marker bars. Compositional analysis of these spots by EDS has shown them to be of the similar composition to the rest of the film and on this basis it is concluded that they are areas of enhanced growth, possibly due to a defect on the substrate

or alternatively due to dust which can occur when sputtering at relatively high pressure in oxygen containing plasmas. The corresponding electron micrograph is shown in Figure 5.2.

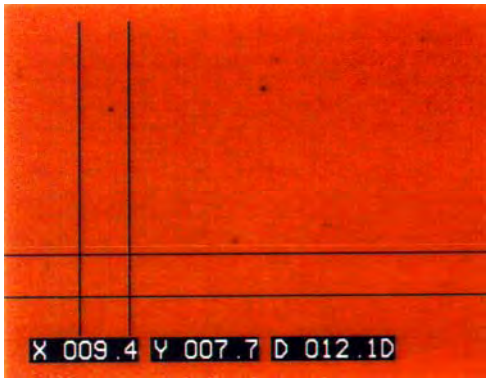

Figure 5.1: Optical picture of sample A (as-deposited).
(*Original in colour*)

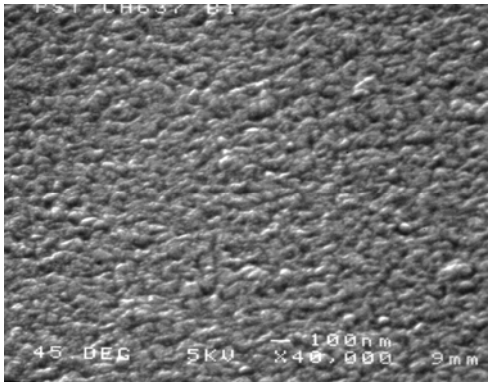

Figure 5.2: SEM picture of sample A (as-deposited).

Optical and SEM micrographs of sample B (650°C RTP) are shown in Figures 5.3 and 5.4 respectively. The optical picture shows a network of microcracks enclosing regions approximately 10μm in diameter, so called "crazy paving" regions, a feature regularly observed in PST grown on platinised silicon. Two distinct colours are present on the optical picture, which could possibly be caused by a difference of refractive index between completely and incompletely transformed (to perovskite) regions. The SEM picture shows that apart from the micro-cracks the surface is not significantly different from that of sample A.

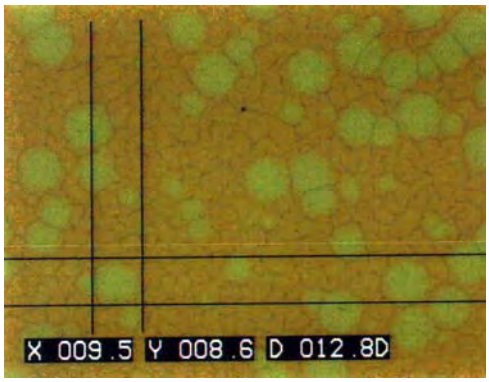

Figure 5.3: Optical picture of sample B (650°C RTP, 30s, O_2).
(*Original in colour*)

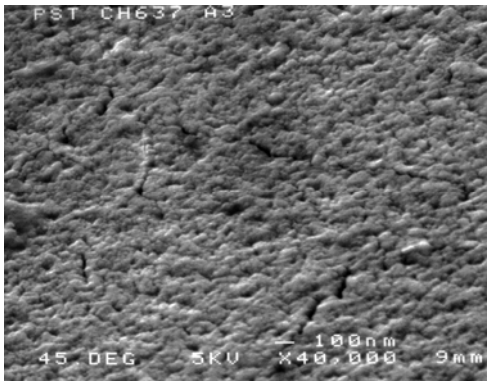

Figure 5.4: SEM picture of sample B (650°C RTP, 30s, O_2).

Figures 5.5 and 5.6 show optical and SEM pictures of sample C (750°C RTP). In the case of the optical picture the sample colour is uniform with crazy-paving of dimension ~4μm. The SEM picture is similar to that of sample B (650°C RTP), again with some micro-cracking visible.

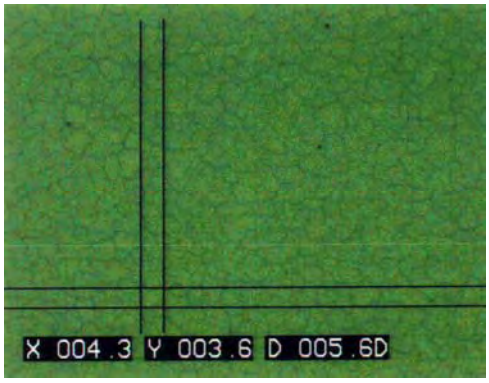

Figure 5.5: Optical picture of sample C (750°C RTP, 30s, O_2). (*Original in colour*)

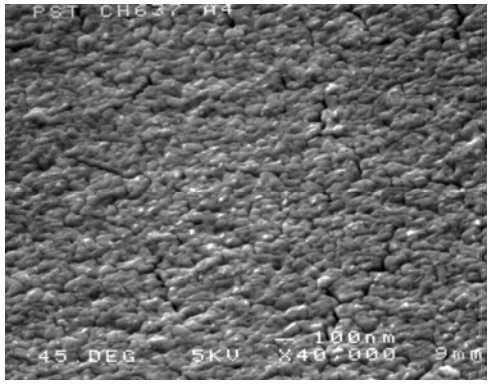

Figure 5.6: SEM picture of sample C (750°C RTP, 30s, O_2).

Optical and SEM pictures of sample D (850°C RTP) are shown in Figures 5.7 and 5.8, respectively. Optically there is little difference from sample C except that the crazy-paving is of slightly larger dimension at ~8-9μm. The SEM picture is markedly different from that of sample C and is not dissimilar to the surface morphology of RTP annealed PZT reported by Chen et al [90]. The surface is marked by small depressions, interpreted as regions where internal voids break the surface (verified by TEM analysis, discussed later), and smooth edged fissures, interpreted as grain boundaries. Apart from the voids and grain boundaries, the surface is smooth in comparison to the previously mentioned samples.

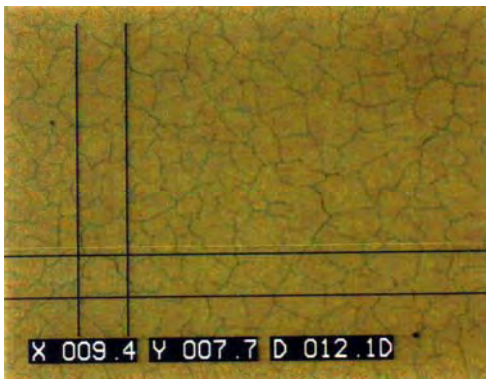

Figure 5.7: Optical picture of sample D (850°C RTP, 30s, O_2). (*Original in colour*)

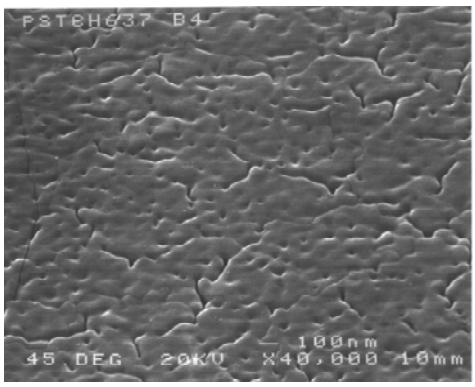

Figure 5.8: SEM picture of sample D (850°C RTP, 30s, O_2).

Figures 5.9 and 5.10 show optical and SEM pictures of sample E (700°C RTP, 5 mins, O_2). Optically the crazy paving observed in previous samples is present but is less distinct. The SEM picture of the surface is very similar to that of sample D, again with a pitted surface, although the grain boundary features appear to be on a finer pitch.

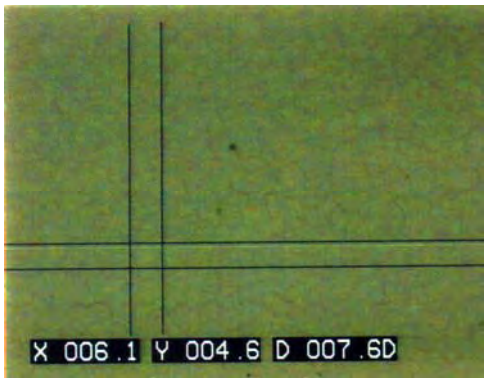

Figure 5.9: Optical picture of sample E (700°C RTP, 5 mins, O_2). (*Original in colour*)

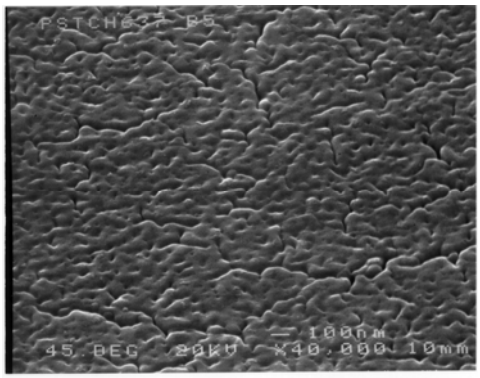

Figure 5.10: SEM picture of sample E (700°C RTP, 5mins, O_2).

Optical and SEM pictures of sample F (700°C RTP, 5 mins, Ar) are shown in Figures 5.11 and 5.12 respectively. Crazy paving can be seen optically and is on a larger pitch (~15μm) as compared to that of sample E (~6μm) which was similarly annealed, but in an oxygen atmosphere. Figure 5.13 is a plan view SEM showing a sizeable crack running across the surface.

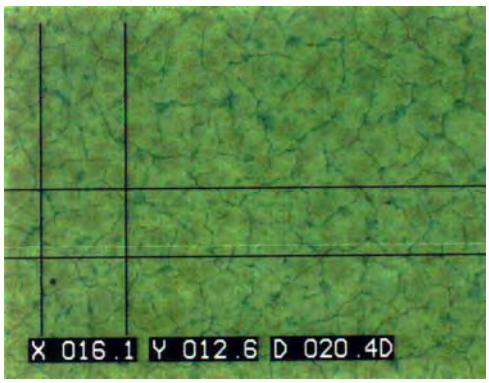

Figure 5.11: Optical picture of sample F (700°C RTP, 5 mins, Ar). (*Original in colour*)

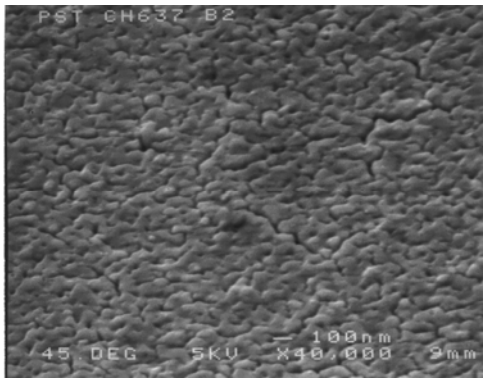

Figure 5.12: SEM picture of sample F (700°C RTP, 5 mins, Ar).

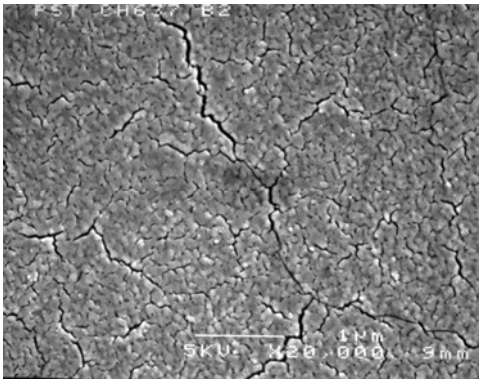

Figure 5.13: Plan view SEM picture of sample F showing cracking.

The final sample, sample G, was oven annealed in oxygen for comparison to oxygen RTP annealed samples. Optical pictures of the surface of this sample are shown at two different magnifications in Figures 5.14 and 5.15. The low magnification picture, Figure 5.14, shows two distinct types of surface morphology. One is of large scale crazy paving (~50μm feature size) clustered around large and distinct cracks whilst in between these is a second region of smaller scale crazy paving more akin to that observed on RTP annealed samples. Figure 5.15 shows a higher magnification image of the border between the two regions of different surface morphology. SEM pictures of the sample surface are shown in Figures 5.16 and 5.17. A large crack is clearly seen in Figure 5.16 along with smaller structures interpreted as grain boundaries. Figure 5.17 shows a higher magnification image revealing the same apparent voiding as observed in the RTP annealed samples.

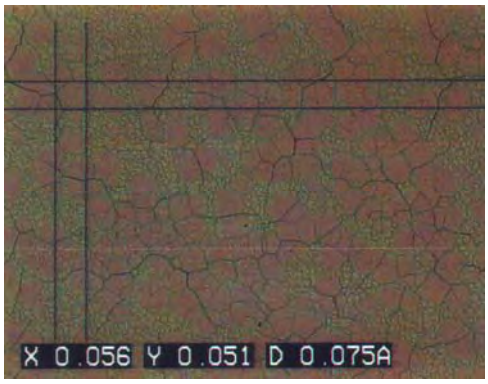

Figure 5.14: Optical picture of sample G (Oven, 700°C, 1hr). (*Original in colour*)

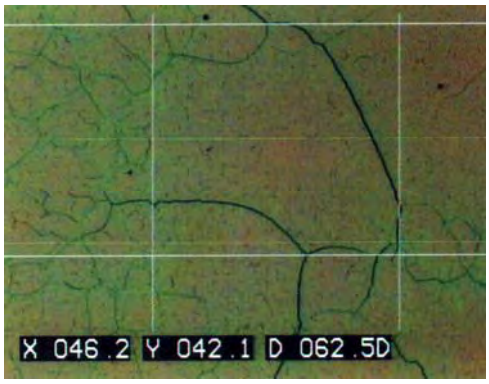

Figure 5.15: Optical picture of sample G showing large cracks. (*Original in colour*)

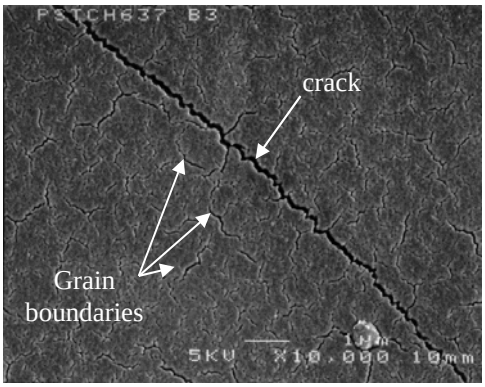

Figure 5.16: Plan view SEM picture of sample G showing large cracks as well as small cracks at grain boundaries.

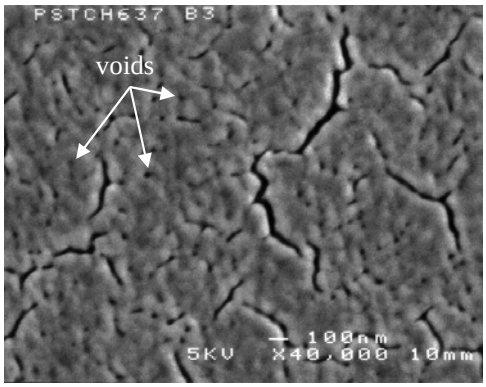

Figure 5.17: Plan view SEM picture of the surface of sample G showing voids.

5.3.1.3 X-Ray Diffraction Analysis

XRD θ-2θ scans in Bragg-Brentano geometry, as well as rocking curves, were measured on all samples both before and after annealing. θ-2θ data was normalised to the as-deposited sample using the platinum (111) reflection. Rocking curve data was normalised to the as-deposited sample using the platinum (111) rocking curve integrated intensity.

Figure 5.18, shows the θ-2θ scans for an as-deposited sample, sample A, and the RTP annealed (in O_2) samples B-E. Sample A gives platinum [52] and pyrochlore reflections [62] with a very low intensity perovskite (222) reflection [53]. The platinum is (111) textured, which is expected from an fcc material under the deposition conditions used. Diffraction from the platinum is so strong that a small K_β component is registered, resulting from a small amount of Cu-K_β radiation getting through the system. The pyrochlore gives two main reflections, the (220) and (222) although these are rather weak and broad, indicating a poorly crystallised pyrochlore/amorphous form. Absence of odd numbered reflections indicates that the pyrochlore is of the defect fluorite type rather than a true pyrochlore structure where superlattice reflections due to cell doubling would be observed [9, 12]. Sample B (650°C RTP, 30s) still registers a pyrochlore reflection after annealing, showing that the conditions used were insufficient to complete conversion. Sample C (750°C RTP, 30s) and D (850°C RTP, 30s) show no pyrochlore reflections, indicating complete removal of this phase by annealing. Sample E (700°C RTP, 5 mins) shows a very small reflection at the pyrochlore (222) position but no other pyrochlore reflections. It is possible that this has resulted from the formation of a lead-tantalate pyrochlore ($Pb_2Ta_2O_7$) formed by downwards

diffusion of lead and Tantalum from the PST along grain boundaries in the columnar grained platinum layer [99] at this high annealing temperature.

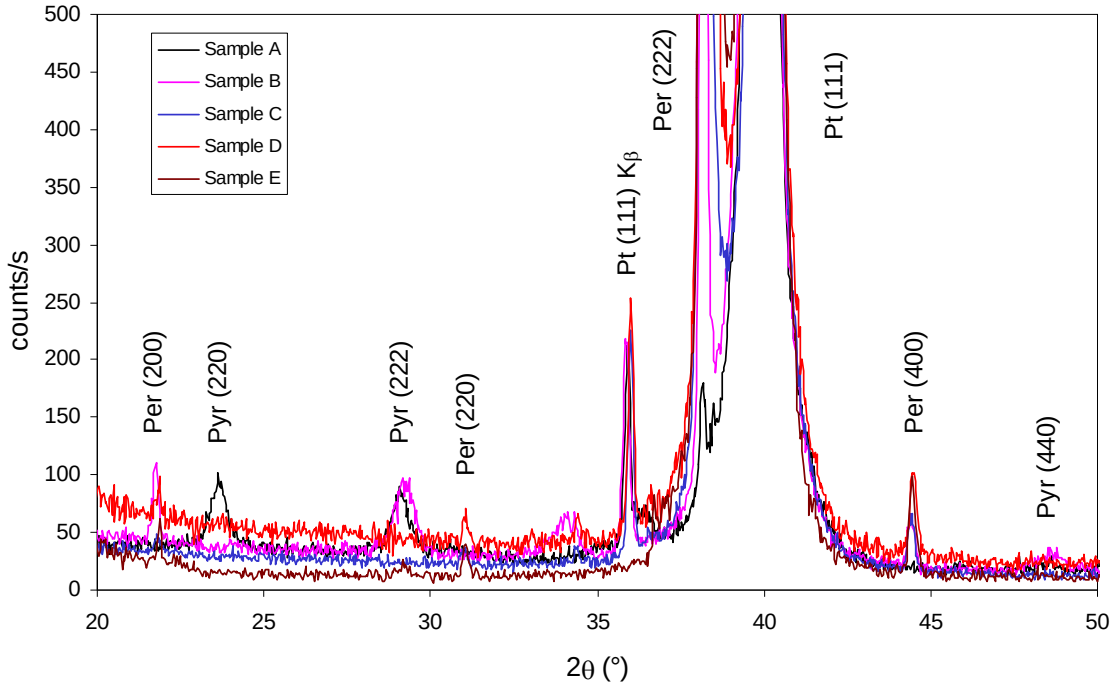

Figure 5.18: XRDθ-2θ scans for samples A-E. *Per*, *Pyr* and *Pt* indicate PST perovskite, PST pyrochlore and platinum reflections respectively.
(*Original in colour*)

A log intensity plot of the θ-2θ scans for the as-deposited material and samples A to E is given in Figure 5.19 and shows that the perovskite formed on annealing is largely (111) textured. Other low intensity perovskite reflections are also present, namely (200), (220) and (400). The (111) superlattice reflection at ~18.9°, due to cell doubling as a result of B-site cation ordering, was not observed and as a result of this the calculated unit cell dimension has been halved with respect to that listed in the JCPDS database [53], although the peak indices have been kept as those listed by the JCPDS to avoid confusion. Perovskite and platinum reflections in the scans can be seen to shift to higher angles upon annealing, an effect most likely due to a stress alteration in the tensile direction.

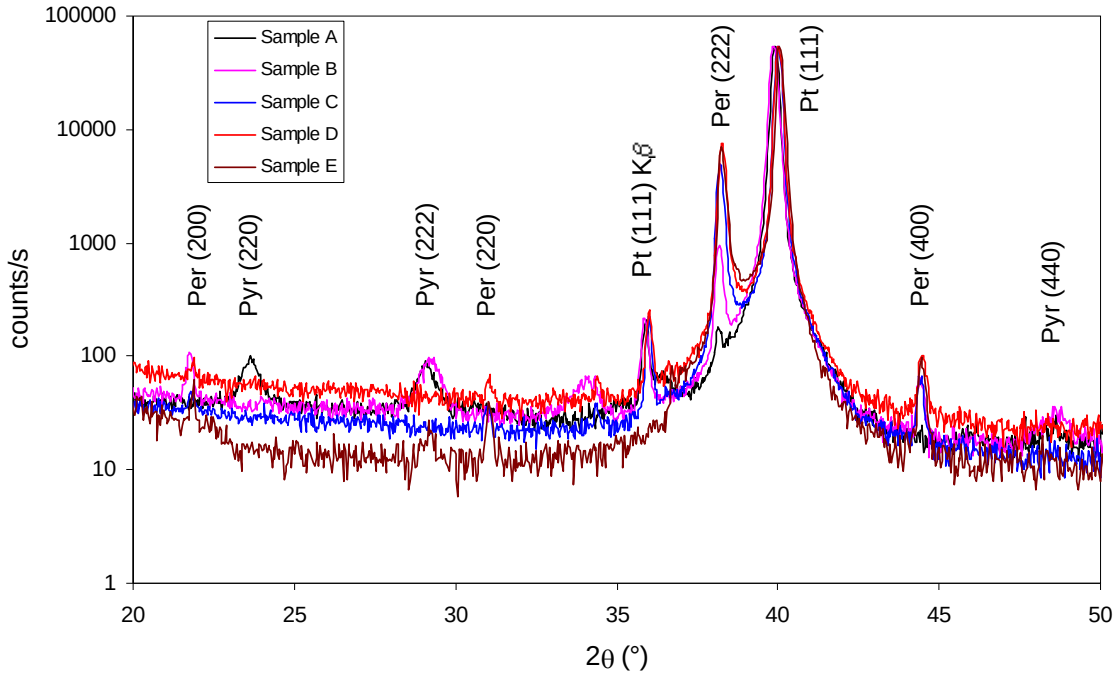

Figure 5.19: XRD θ-2θ scans for samples A-E. *Per*, *Pyr* and *Pt* indicate PST perovskite, PST pyrochlore and platinum reflections respectively.
(*Original in colour*)

Figure 5.20 shows the rocking curves of the platinum (111) and pyrochlore (222) reflections. The platinum is fibre textured with only a small spread about the preferred orientation (fwhm = 1.7°), while the pyrochlore (222) rocking curve is very broad indicating a non-textured phase.

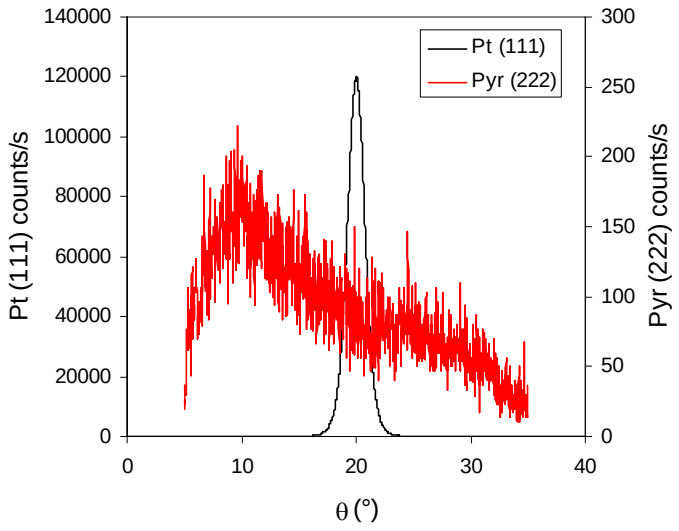

Figure 5.20: Pt (111) and pyrochlore PST (222) rocking curves for sample A (as-deposited).
(*Original in colour*)

The (222) texture of the perovskite strongly suggests that the growth of this phase is influenced by the underlying platinum. Rocking curves for the perovskite (222) reflections of samples B to E are shown in Figure 5.21 below and are sharp compared with the as-deposited pyrochlore. Table 5.4 summarises salient information from the rocking curves, giving the fwhm of the perovkite (222) and as-deposited platinum (111) rocking curves as well as the integrated intensity of the perovskite (222). For the 30s RTP anneals the perovskite (222) integrated intensity increases successively with increasing hold temperature, with the highest value being observed for the 850°C 30 second anneal. Interestingly the integrated intensity the longer anneal at 700°C for 5 minutes, sample E, was less than for the short RTP anneals at 750°C and 850°C. The integrated intensity is taken as a rough indication of perovskite 'content', or crystallinity, it would appear that higher temperature is having more influence on perovskite formation than longer time.

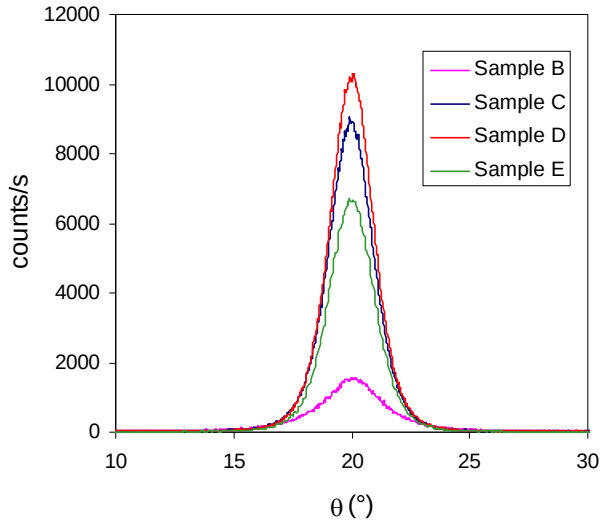

Figure 5.21: Perovskite (222) rocking curves after RTP annealing in O_2. (*Original in colour*)

Sample	Per (222) Integrated Intensity (counts/°s)	Per (222) Fwhm (°)	Pt (111) Fwhm (°)
B	6481	2.9	1.6
C	23166	2.2	1.7
D	25740	2.2	1.6
E	17166	2.2	1.7

Table 5.4: Rocking curve data for samples RTP annealed in O_2.

The θ-2θ scan for sample F (700°C RTP, 5 mins, Ar), Figure 5.22 below, also shows highly (222) textured perovskite with small reflections from other orientations. On the high angle shoulder of the perovskite (222) reflection is another reflection which has been labelled as the (111) reflection of the lead-platinum intermetallic Pt_xPb [100]. This phase has been observed by other workers in the field, most notably by Huang et al [101], who set x=3 after EDS analysis of TEM cross-sections of sol-gel prepared PZT, and Chen et al [102]. The initial stages of the sol-gel processes, prior to burn off of the residual carbon, was identified as creating the required anaerobic conditions for the formation of the intermetallic. RTP of

sample F in argon may well have provided an anaerobic environment, resulting in the reaction of some of the lead from the PST with the platinum from the underlying electrode.

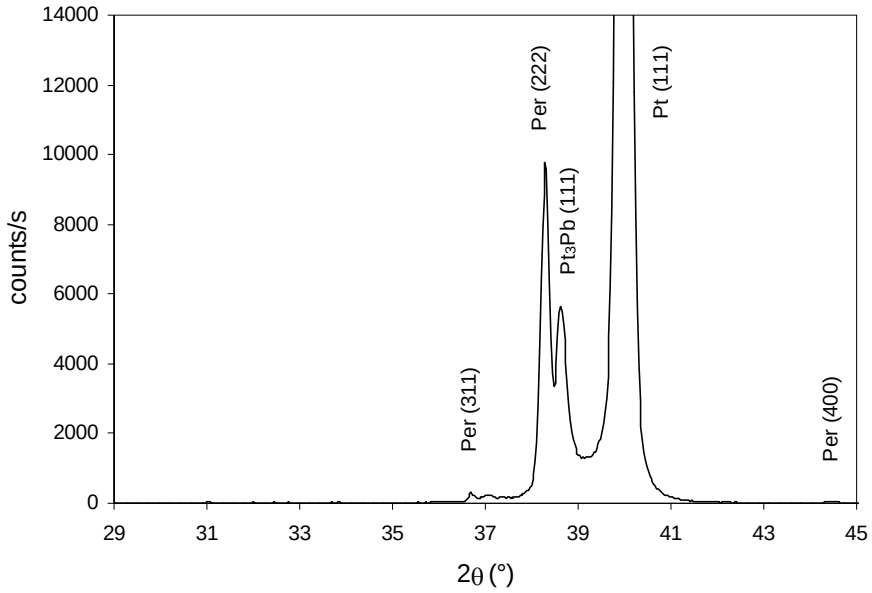

Figure 5.22: XRD θ/2θ scan of sample F (700°C RTP, 5 mins, Ar).

Figure 5.23 below shows the θ-2θ scan for sample G. Again the perovskite is highly (222) textured with no sign of ordering peaks and a small Pt_3Pb (111) reflection was observed.

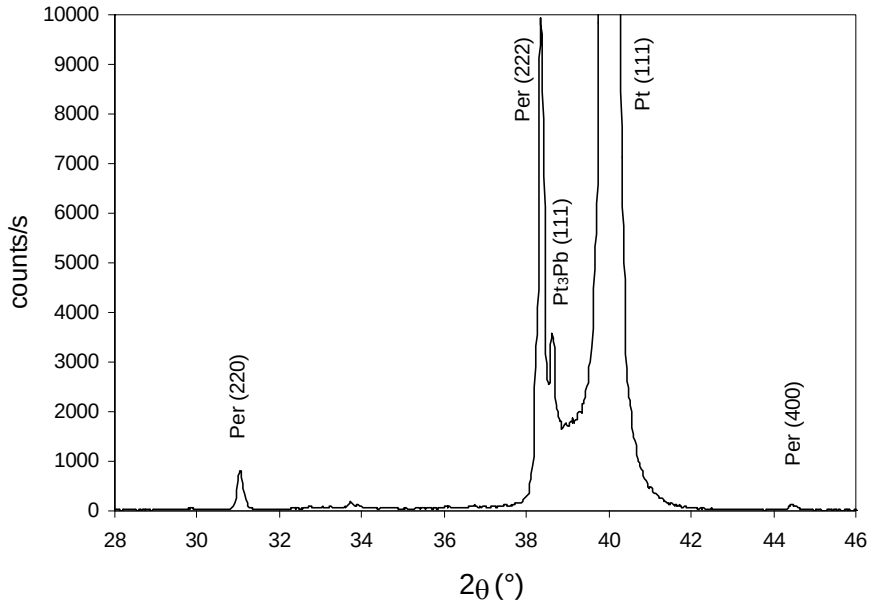

Figure 5.23: XRD θ-2θ scan of sample G (Oven 700°C, 1 hour, O_2).

Table 5.5 below gives the lattice parameters for the perovskite PST based on the reduced size unit cell associated with the disordered phase. The d-spacing of the (444) reflection ($2\theta \approx 81.7°$) was used in each case to avoid problems with the coincidence of the perovskite (222) and platinum (111) peaks. Since there was no evidence of ordering of the PST the lattice parameters in the table have been halved wrt those in the JCPDS database.

Identifier	Lattice Parameter (∑)
Sample B	4.082
Sample C	4.080
Sample D	4.075
Sample E	4.075
Sample F	4.080
Sample G	4.074

Table 5.5: Perovskite PST lattice parameters from (444) reflection.

Measured lattice parameters are slightly larger than that given for ceramic PST of 4.068∑ [53] but agrees well with the value of 4.075∑ for sol-gel PST grown on GGG substrates reported by Patel et al [83]. Differences between samples are not surprising since the lattice parameter can be affected by stress or chemical effects such as the substitution of Pb^{4+} onto the B-sites in the perovskite lattice, as demonstrated by Whatmore et al for similarly sputtered PST [96].

5.3.1.4 Transmission Electron Microscopy.

Cross sectional TEM analysis was performed on the samples in order to determine their microstructure, with the lamellae being formed using focussed ion beam techniques – as described in Chapter 3. All cross sections discussed are bright field unless otherwise stated. Figure 5.24 below shows a cross section of as-deposited material. As well as the PST, the underlying platinum electrode and titanium adhesion layer can be clearly seen, and also the tungsten capping layer left from the FIB processing. The PST is a dense film with faint vertical striations and no obvious crystalline structure. The light coloured layer at the PST/platinum interface is believed to be an artifact of the sample preparation process.

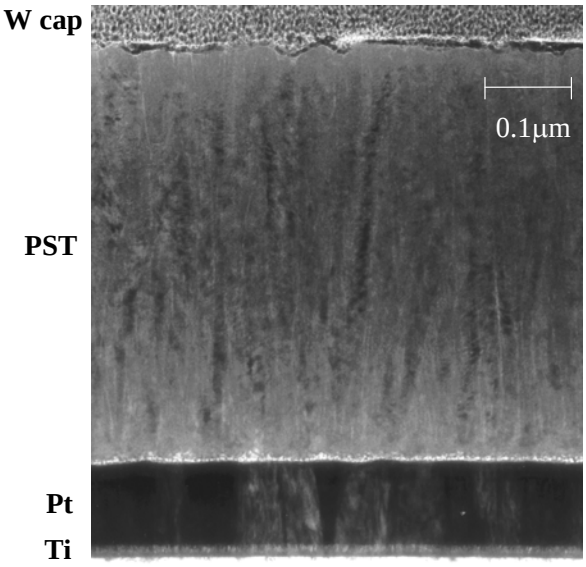

Figure 5.24: Cross-sectional TEM of sample A (as-deposited).

Figure 5.25 below shows the TEM cross-section of sample B (650°C RTP, 30s, O_2). The FIB processing has removed the top half of the PST, although the filamentous structure seen in the as-deposited material can still be observed. Voiding observed in higher temperature annealed samples is not seen.

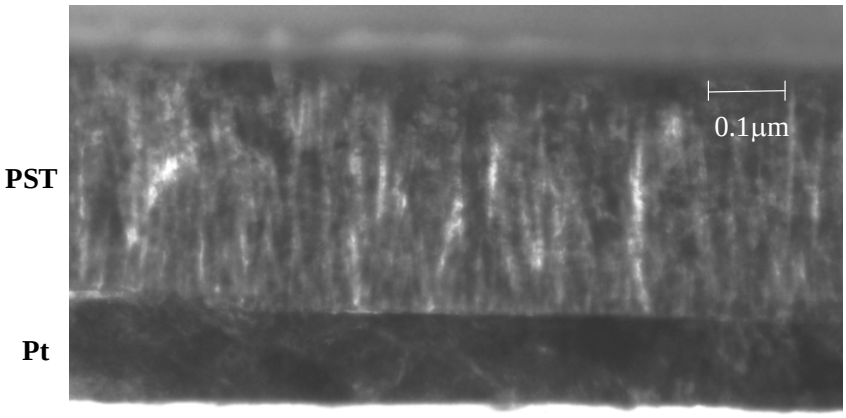

Figure 5.25: Cross-sectional TEM of sample B (650°C RTP, 30s, O_2).

A bright field TEM cross-section of sample C (750°C RTP, 30s) is shown in Figure 5.26 below. Unlike sample B (650°C RTP, 30s) the PST is characterised by the presence of voids which are not observed in PST deposited directly into the perovskite phase [86], see appendix A2 for TEM picture, but have been reported in low temperature deposited then annealed sol-gel derived PST thin films [83]. It is interesting to note that the bottom surface of the platinum has roughened and the titanium adhesion layer is no longer easily visible. This could be due to the diffusion of titanium upwards along the platinum grain boundaries,

as observed by Maeder et al[99] in their systematic study of bottom electrodes for ferroelectric thin films.

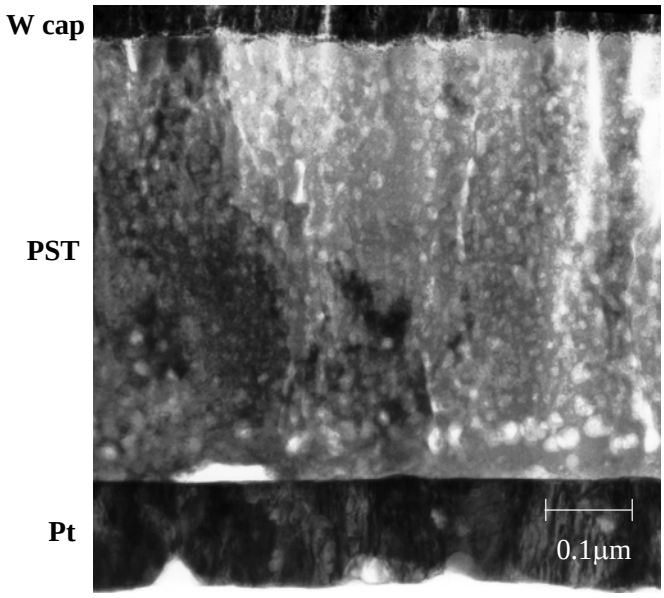

Figure 5.26: Cross-sectional TEM of sample C (750°C RTP, 30s, O_2).

The cross-sectional TEM pictures for sample D (850°C RTP, 30s, O_2) are shown in Figures 5.27 and 5.28 below. There has been gross voiding, due primarily to the volume change on conversion to perovskite – although it probably appears to be worse than it actually is due to the depth of field of the TEM. Inclusions in the silicon dioxide underlying the platinum can be clearly seen in Figure 5.28 and although these have not been positively identified they are likely to be caused by diffusion through the platinum of lead oxide from the PST, either along grain boundaries in the columnar grained platinum or through defects in the platinum such as pinholes. Oven annealing studies reported in Chapter 6 confirm that lead is the major metallic constituent of these inclusions in similarly annealed material.

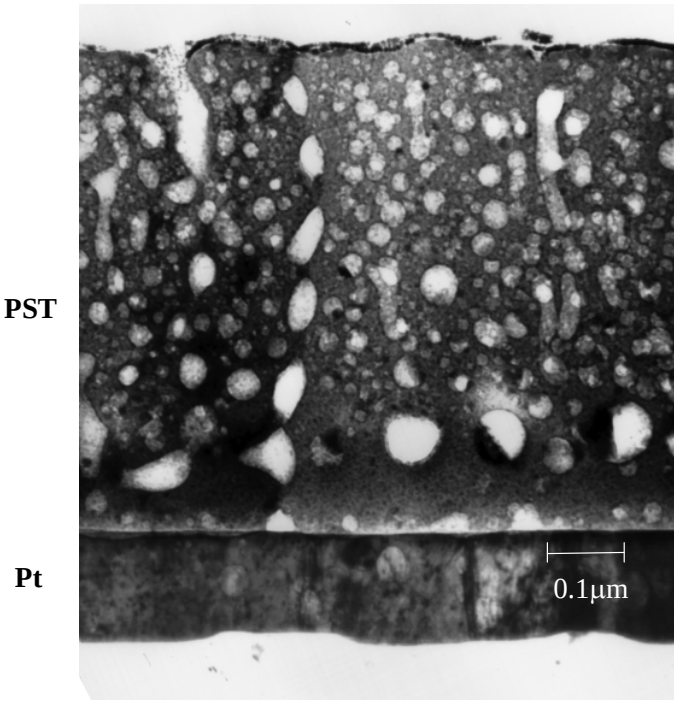

Figure 5.27: Cross-sectional TEM of sample D (850°C RTP, 30s, O_2).

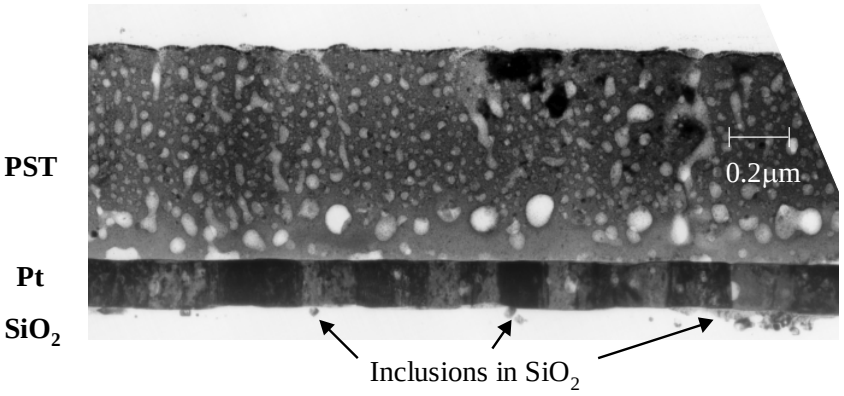

Figure 5.28: Cross-sectional TEM of sample D showing inclusions in SiO_2.

Figure 5.29 below shows the cross-sectional TEM of sample E (700°C RTP, 5 mins, O_2). It is similar to that for sample D (850°C RTP, 30s, O_2) and again there were inclusions in the SiO_2 underlying the platinum.

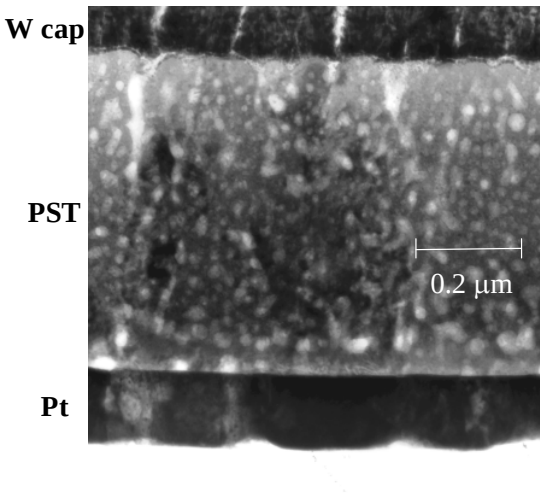

Figure 5.29: Cross-sectional TEM of sample E (700°C RTP, 5 mins, O_2).

5.3.2 Electrical Characterisation

Electrical characterisation of the PST samples consisted primarily of pyroelectric coefficient, dielectric properties and hysteresis loop measurements. The pyroelectric coefficient and dielectric properties (ε_r and $\tan\delta$) are required for the calculation of F_D, the materials merit figure for IR detection, discussed in Chapter 2. Hysteresis loop measurements were made to investigate an apparent internal bias field displayed by the PST thin films. In order that their relative contribution to F_D can be clearly seen, the pyroelectric coefficient and dielectric measurements for each of the samples are presented separately.

5.3.2.1 Sample B

Electrical measurements for sample B (650°C RTP, 30s, O_2) were characterised by low ε_r, typically < 200, and high $\tan\delta$, typically >10%. These are symptomatic of incomplete conversion of the PST to perovskite, as confirmed by the materials characterisation studies. PST in this form would be of no use in an IR detector and no further electrical measurements were carried out.

5.3.2.2 Sample C

Sample C (750°C RTP, 30s,O_2) showed no evidence of pyrochlore and electrical measurements were characteristic of perovskite PST. Figure 5.30 shows the dielectric properties as a function of temperature and measurement frequency with the broad peaks in ε_r and tanδ and their dispersion with frequency showing that the PST is behaving as a relaxor ferroelectric [13, 17, 22]. This is not surprising since XRD analysis revealed no evidence of the B-site cation ordering that would be required for first order ferroelectric behaviour, as reported by Watton and Todd [7] for thin film PST on sapphire. At 120Hz ε_r peaked at –10°C and tanδ at –80°C. The upturn in the 120Hz tanδ curve at higher temperatures is attributed to dc leakage effects caused by a marked reduction in resistivity above ~60°C.

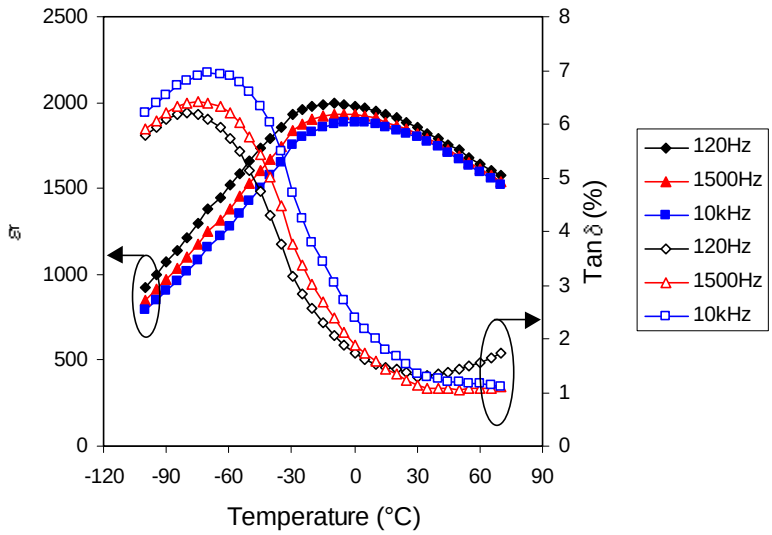

Figure 5.30: Zero applied field dielectric properties of sample C (750°C RTP, 30s) as a function of temperature and frequency.
(*Original in colour*)

The dielectric properties under applied are shown in Figure 5.31 below, with the application of the applied field in a positive sense resulting in a lowering of both ε_r and tanδ, due to the suppression of domain switching [7]. The apparent internal bias observed in the pyroelectric response was also in evidence with both ε_r and tanδ peaking between –0.8 and –1.7V/μm.

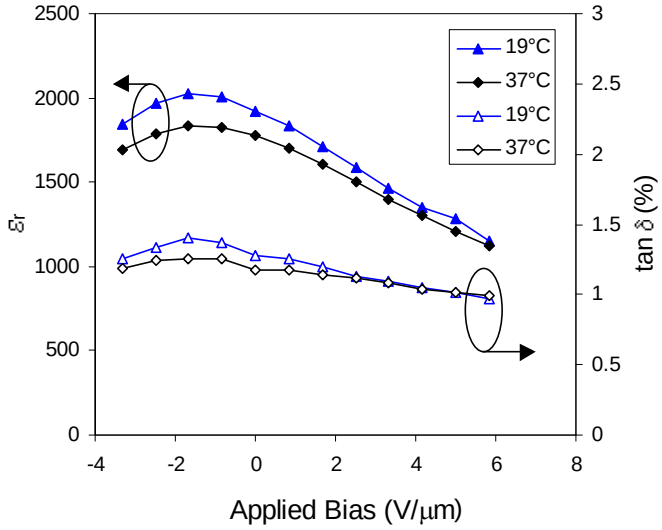

Figure 5.31: Dielectric properties of sample C (750°C RTP, 30s) at 120Hz as a function of applied bias and temperature. (*Original in colour*)

Pyroelectric coefficent measurements as a function of temperature and applied DC bias field are summarised in Figure 5.32 below. As can be seen from the figure there is a temperature variation, with the highest value of p being 741±37μC/m^{2}K at 37°C and 5.8V/μm. Interestingly, a significant pyroelectric response (236±12μC/m^{2}K) was observed at zero applied field, which would not be expected above the temperature of the dielectric maximum in a first or second order ferroelectric. In fact the reversal of the applied field (top electrode held negative) resulted in p being reduced to zero at –1.4V/μm (37°C), then reversing sign. Along with ε_r and tanδ peaking at negative applied fields this suggests a combination of two effects – namely an internal bias field of the the order of 1.4V/μm giving an induced pyroelectric component as well as the persistence of the spontaneous polarisation in this relaxor PST to temperatures in excess of the dielectric maximum.

The pyroelectric response is moderate compared with ordered thin film[7] and bulk PST [6] and is the result of the broad relaxor-type peak in ε_r. Since the induced pyroelectric coefficient is dependent on the temperature differential of ε_r, it will never be as high in relaxor material as it would for a film exhibiting sharply peaked first-order characteristics.

Figure 5.33 below shows the merit figure, F_D, (120Hz) calculated from the the measured values of p, ε_r and tanδ. Reasonable F_D values were obtained, 2.1±0.2×10^{-5}Pa$^{-1/2}$ at

5.8V/μm, even though the pyroelectric coefficient was moderate. The increase in F_D at higher applied bias fields was primarily due to suppression of ε_r and tanδ, which appear in the denominator in the F_D calculation.

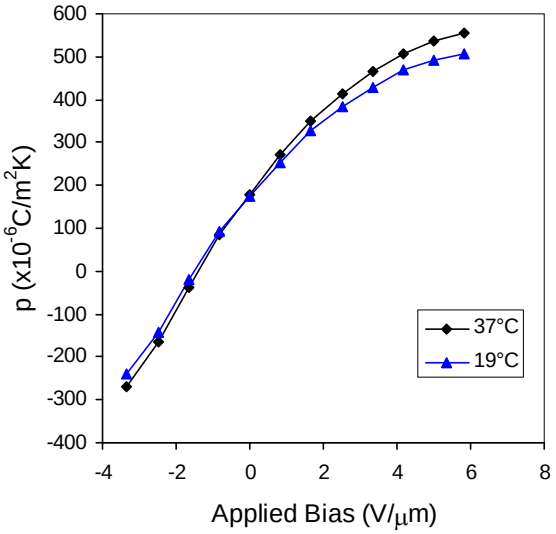

Figure 5.32: Pyroelectric coefficient of sample C (750°C RTP, 30s). (*Original in colour*)

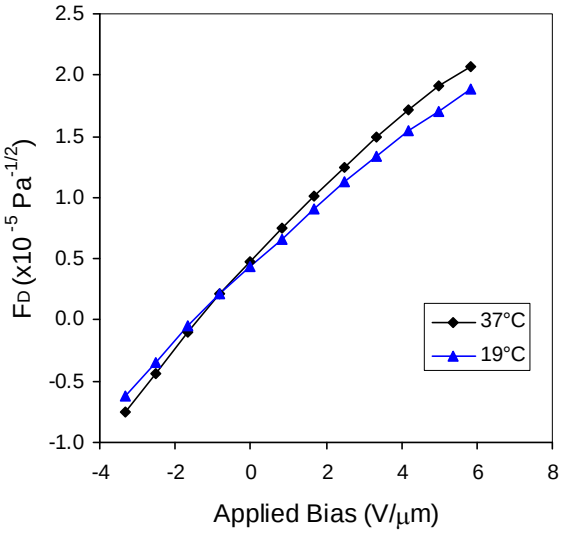

Figure 5.33: Materials merit figure of sample C (750°C RTP, 30s). (*Original in colour*)

5.3.2.3 Sample D

As for sample C (750°C RTP, 30s), sample D (850°C RTP, 30s, O_2) also exhibited only perovskite reflections in the XRD θ-2θ scans. The zero applied field dielectric properties of this sample are shown in Figure 5.34 below. No B-site cation ordering was observed, despite the high anneal temperature, and consequently the dielectric behaviour is of the ferroelectric relaxor type. The low frequency (120Hz) peak in ε_r occurred at ~21°C, in the region of the transition temperature for bulk PST of 20-30°C, and significantly higher than for the -10°C value of sample C (750°C RTP, 30s) – with the maximum also being higher.

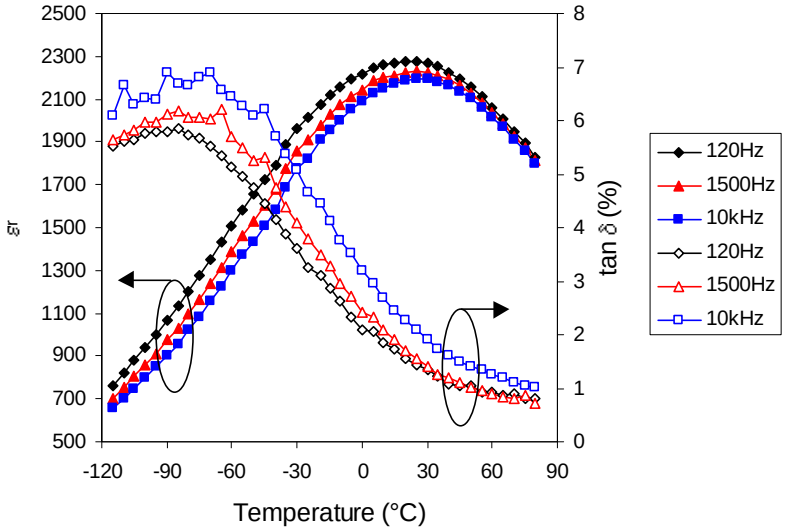

Figure 5.34: Zero applied field dielectric properties of sample D (850°C RTP, 30s) as a function of temperature and frequency.
(*Original in colour*)

The behaviour of ε_r and tanδ with temperature and applied field are shown in Figure 5.35 below. Both quantities are suppressed markedly with ε_r decreasing by over a factor of two at 8.3V/μm, compared with the zero field value. Application of the field brings the dielectric loss down to low values, for example 0.58±0.05% at 37°C and 8.3V/μm. Again ε_r and tanδ peaking at around –1.7V/μm suggests the presence of an internal bias field in the material.

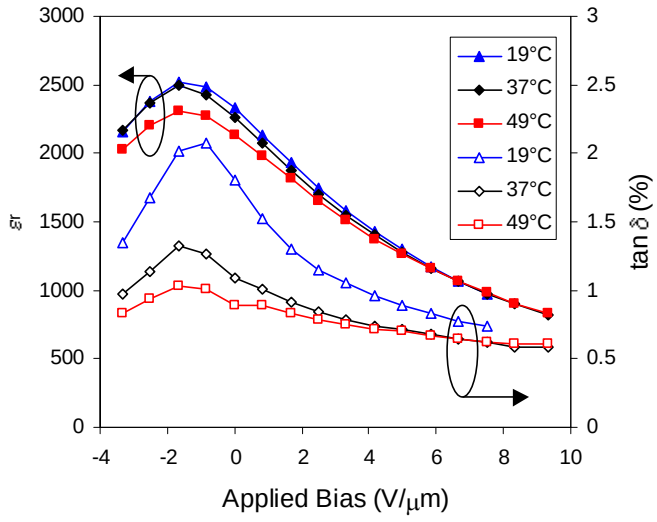

Figure 5.35: Dielectric properties of sample D (850°C RTP, 30s) at 120Hz as a function of applied bias and temperature.
(*Original in colour*)

Figure 5.36 below shows the measured pyroelectric response. Temperature dispersion is again evident with a marked difference in response between 19°C and 49°C. The pyroelectric response is higher than for sample C (750°C RTP, 30s) at the corresponding temperature and field. At 5.8V/μm and 37°C, p is 636±32μC/cm^{2}K as compared to 556±28μC/cm^{2}K for sample C. The material withstood a higher applied field of 8.3V/μm although the rate of increase of p is seen to decrease as the bias is increased. This is due to the flattening out of the ε_r versus temperature curve as the field is increased, with the result that there are successively smaller contributions to p, and is illustrated by the more extensive dielectric mesurements reported below for sample E (700°C RTP, 5 mins, O_2).

Figure 5.37 below shows F_D at 120Hz as a function of temperature and applied bias. The temperature dependence is pronounced with the highest values being 3.6±0.5×10^{-5}Pa$^{-1/2}$ and 3.8±0.5×10^{-5}Pa$^{-1/2}$ at 37°C and 49°C respectively. This plot shows very well that for a material behaving as a relaxor then good F_D values can be obtained if a sufficiently high electric field can be applied. Even though the contributions to the induced pyroelectric coefficient at higher fields are modest, this is compensated for by the suppression of ε_r and tanδ.

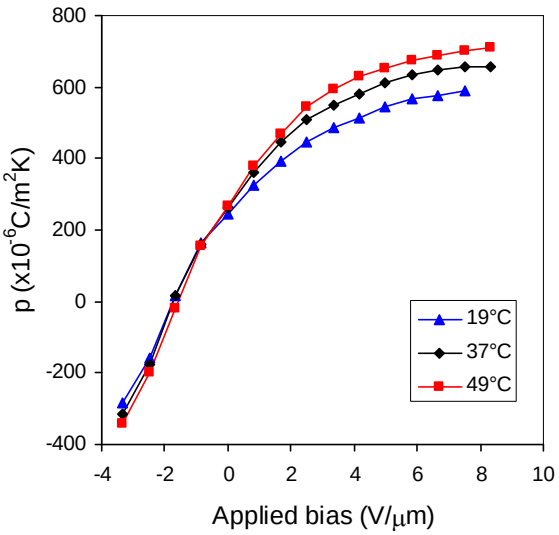

Figure 5.36: Pyroelectric coefficient of sample D (850°C RTP, 30s). (*Original in colour*)

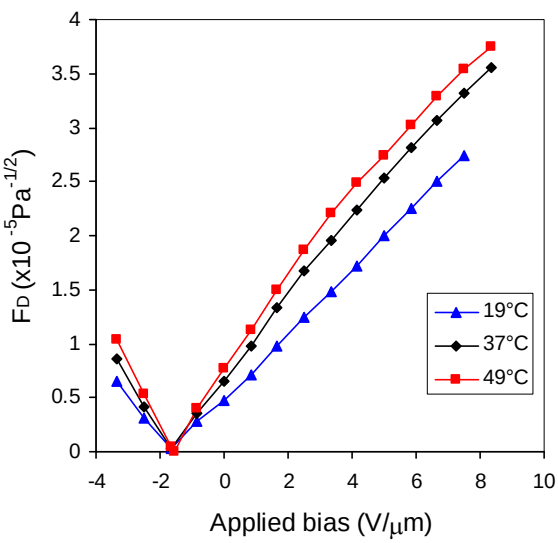

Figure 5.37: Materials merit figure (120Hz) of sample D (850°C RTP, 30s). (*Original in colour*)

5.3.2.4 Sample E

Sample E was annealed by RTP at an intermediate temperature, 700°C, for a longer time, 5 minutes, than samples C and D. The XRD θ-2θ scan showed only perovskite reflections. A slightly more extensive study of the dielectric properties of this sample was undertaken than for the other samples. Figure 5.38 below shows ε_r and tanδ as a function of temperature and measurement frequency. Again the curves are characteristic of a ferroelectric relaxor, as expected from the absence of B-site cation ordering in the material.

The effect of an applied bias field on the temperature dependence of ε_r and tanδ is shown in Figure 5.39. Both properties are suppressed by the field but ε_r especially becomes less sensitive to temperature ($\partial\varepsilon_r/\partial T$ is reduced). This illustrates well the point made for the induced pyroelectric response for sample C above, that for increasing applied bias the relative contributions to p are successively reduced. Application of a field in a negative sense (bottom electrode held positive) is seen to initially increase ε_r and tanδ before suppressing them, again suggesting the presence of an internal bias field. The shift of the peak in ε_r to lower temperatures with applied field, in either sense, is contrary to what is expected for a ferroelectric. This effect has also been observed by Bjormander et al [85] for pulse laser deposited PST thin films on an YBCO bottom electrode. At the time of writing no explanation can be offered for this behaviour.

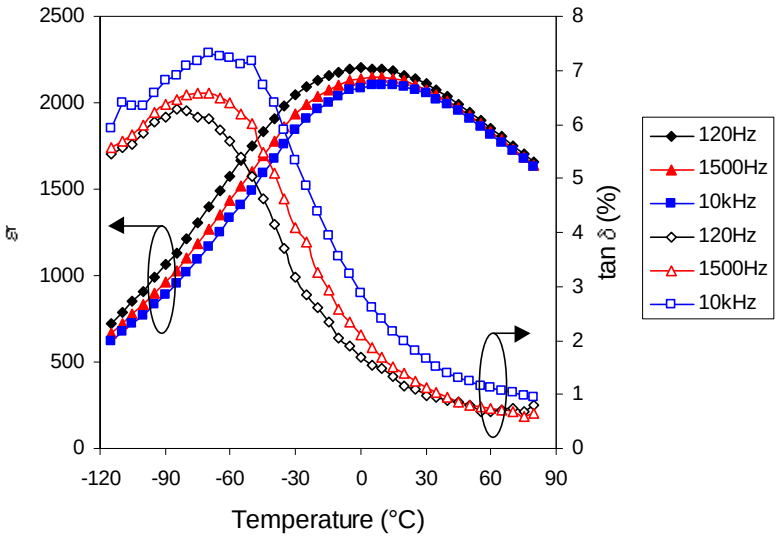

Figure 5.38: Zero applied field dielectric properties of sample E (700°C RTP, 5 mins) as a function of temperature and frequency.
(*Original in colour*)

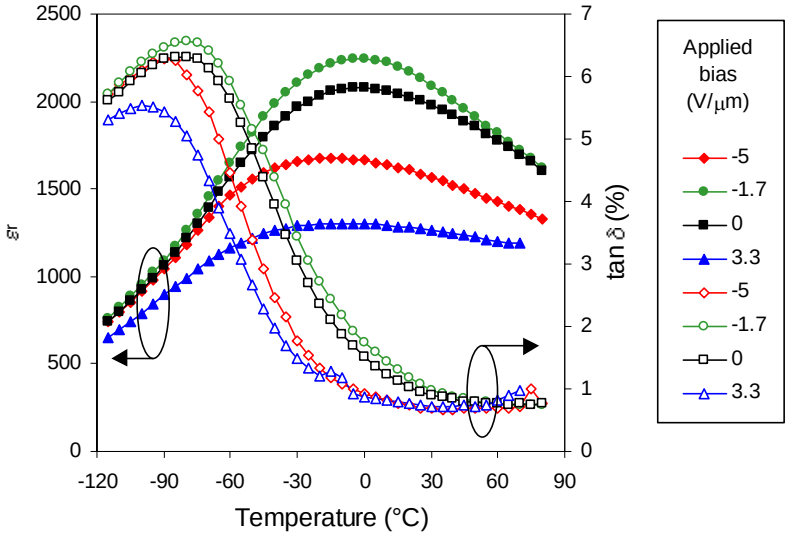

Figure 5.39: Dielectric properties of sample E (700°C RTP, 5 mins) at 120Hz as a function of temperature and applied bias.
(*Original in colour*)

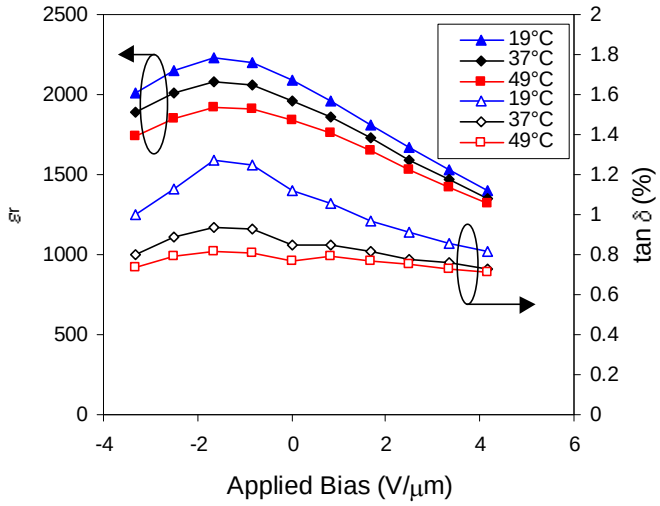

Figure 5.40: Dielectric properties of sample E (700°C RTP, 5 mins) as a function of applied bias and temperature.
(*Original in colour*)

Figure 5.41 shows the pyroelectric response of the PST film, with the results being similar to those reported for the other RTP conditions. The maximum field sustained before breakdown was 4.2V/μm, with the maximum pyroelectric coefficients at being 483±24μC/m^{2}K and 502±25μC/m^{2}K at 37°C and 47°C respectively.

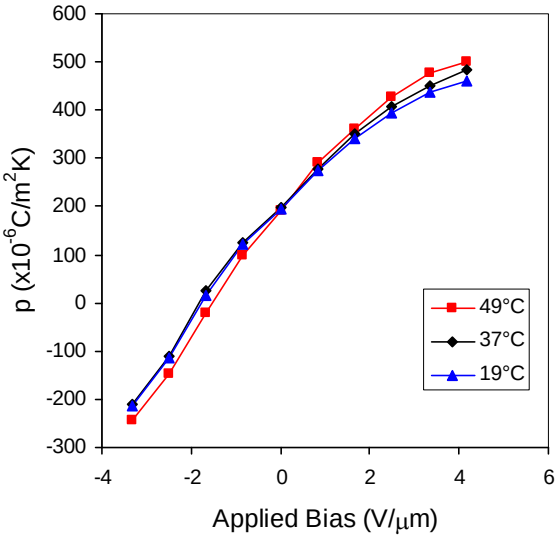

Figure 5.41: Pyroelectric coefficient of sample E (700°C RTP, 5 mins). (*Original in colour*)

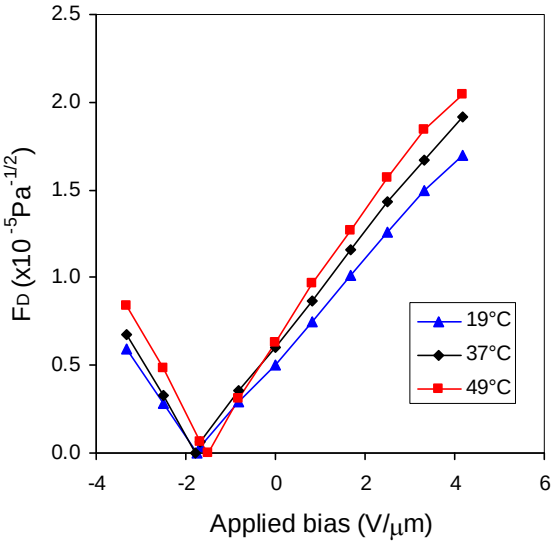

Figure 5.42: Materials merit figure of sample E (700°C RTP, 5 mins). (*Original in colour*)

The F_D values shown in Figure 5.42 are lower than for sample D (850°C RTP, 30s) but higher than those for sample C (750°C RTP, 30s) at the same applied field. Figure 5.43 illustrates the effect of resilience to applied field resulting in higher performance, with a maximum F_D value of $2.4\pm0.3\times10^{-5}Pa^{-1/2}$ recorded at 5.8V/μm.

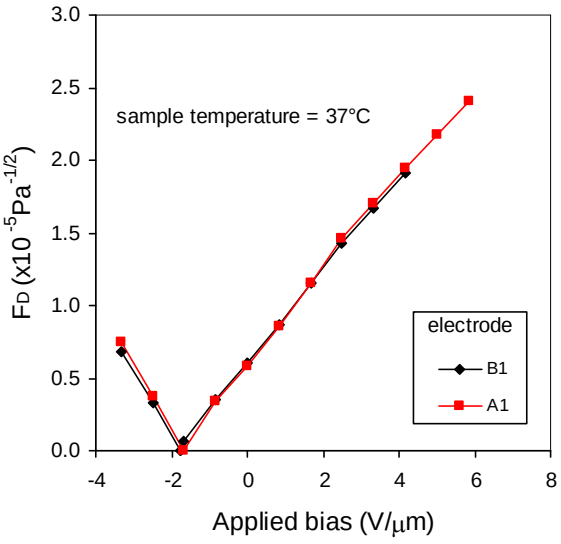

Figure 5.43: Materials merit figure of sample E showing effect of resilience to applied field. (*Original in colour*)

Hysteresis loops were measured to confirm the existance of an apparent internal bias field as suggested by the dielectric and pyroelectric coefficient measurements. Figures 5.44, 5.45 and 5.46 below show hysteresis loops measured at temperatures above and below the temperature of the dielectric maximum. Figure 5.44 shows a true hysteresis loop at –100°C and demonstrates the ferroelectric nature of the annealed PST. The saturation polarisation of ~20μC/cm^2 compares well with literature values for bulk ceramic PST of ~20μC/cm^2 [13] and also sol-gel thin film PST on platinised silicon [84], ~22μC/cm^2 at –80°C, and laser ablated PST on YBCO [85], ~20μC/cm^2 at –90°C. The loop can be seen to be displaced to the left on the voltage axis, confirming the presence of an internal bias field [45].

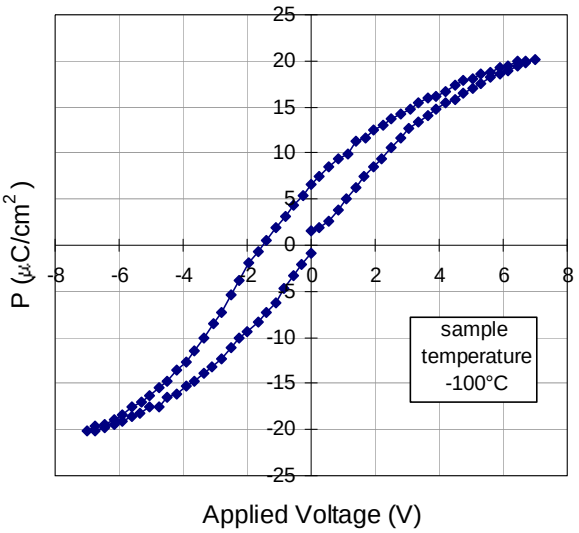

Figure 5.44: Hysteresis loop at –100°C showing ferroelectric behaviour and apparent internal bias.

The area within the hystersis loops decays slowly with increasing temperature and all loops show a shift on the voltage axis.

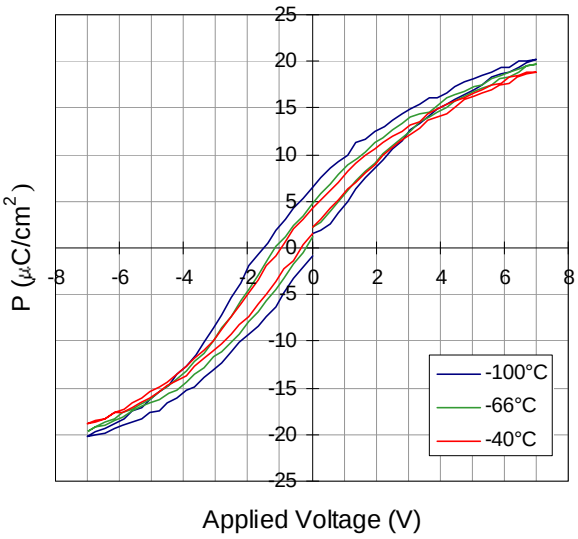

Figure 5.45: Hysteresis loops at –100°C, -66°C and –40°C. (*Original in colour*)

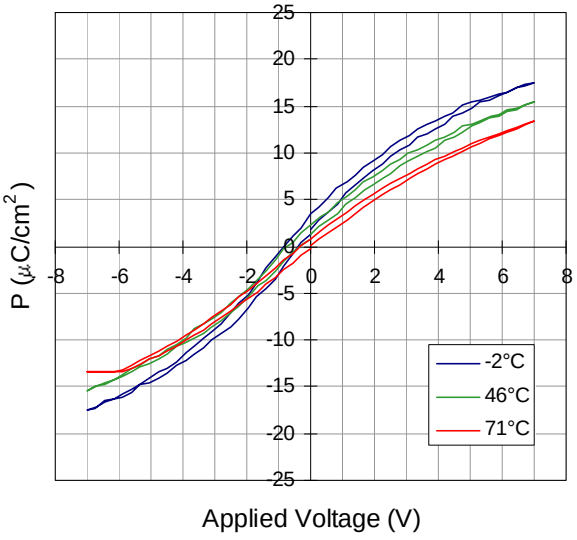

Figure 5.46: Hysteresis loops at –2°C, 46°C and 71°C. (*Original in colour*)

5.3.2.5 Resistivity Measurements.

Resistivity measurements were made on all samples over the range of applied bias fields using a Keithley 236 source measure unit. Resistivities $>10^{10}\Omega$m were recorded, well above the level at which other noise sources, apart from dielectric loss noise, become significant.

5.4 Discussion

It is well known that the structure of thin film ferroelectric mixed oxide materials is dependent on the deposition temperature, with a progression through the amorphous, pyrochlore and perovskite phases as the temperature is increased. Further to this some materials, such as PZT put down by techniques such as sol-gel spin deposition, are amorphous as-deposited and then crystallised into perovskite by a high temperature annealing step. In PZT this conversion occurs via a metastable pyrochlore phase. The work reported in the previous sections of this chapter is concerned with the investigation of the structural form of low temperature deposited PST and whether it can be converted to the required perovskite phase by a high temperature annealing step, as has been used for other materials. More specifically there was the ultimate requirement that this annealed material should have an electrical performance, in terms of the materials merit figure for IR detection

(F_D), at least as good as other competing materials, such as PZT, and PST deposited directly into the perovskite phase at 525°C. As mentioned in the introduction the major thrust of this work is to lower the deposition temperature of the PST so as to aid the control of the volatile lead component in the film, thereby making the deposition more straightforward and repeatable. When the work was first begun there was also the requirement to keep the low temperature deposition/high temperature annealing scheme within the limits of the thermal budget for the survival of the underlying ROIC, as would be present in an integrated detector. The temperature limitations of the ROIC were not well known but have been quantified by the work reported in Chapter 4, which concluded that after low temperature PST deposition (<<450°C) a post deposition RTP annealing step at a temperature of 600°C for up to 30 seconds was permissibile without damaging the ROIC. While the research was in progress the idea of the composite wafer fabrication technique, described in detail in Chapter 3, was put forward and has allowed a relaxation of the process temperature limitations by effectively decoupling the ROIC from the ferroelectric material processing. It is worth noting that an additional, but very tangible, benefit of operation at lower temperatures is improved reliability of the PST deposition equipment.

In order to investigate the low temperature deposition/high temperature annealing processing route, the starting material used was PST deposited at 300°C by single RF magnetron sputtering. This deposition technique, in its current form, is not regarded as production orientated due to problems with uniformly coating large area (≥4") substrates, although it was suitable for coating 3" substrates and allowed a proof of principle study to be undertaken. It is worth noting that platinised silicon was used throughout, with no consideration of the full device structure which would include both sacrificial and diffusion barrier layers. This is unrealistic but it decouples the PST materials problem from the sacrificial/barrier layer problem, which is whole area of research in its own right, and makes the assumption that it will be possible to make a device layer stack that 'looks' like platinised silicon to the PST.

When the work was begun it was not known what the form of the 300°C deposited PST would be – the phase diagram for PST is not available in the detail of a material such as PZT. A number of materials analysis techniques were used to resolve this, including XRD, SEM, EDS and TEM analyses as well as the simple technique of inspection using an optical

microscope. The as deposited material was roughly stoichiometric in scandium and tantalum with a slight lead excess (~15%) which has been found by other authors to both compensate for lead loss during high temperature processing and also promote perovskite formation[103]. Optical inspection revealed a featureless surface, apart from occasional dark spots - shown to be areas of enhanced PST growth. Inspection by SEM revealed a gently undulating surface morphology with no prominent features of evidence of grain structure. XRD was used to investigate the crystalline structure of the PST and revealed a poorly crystallised pyrochlore/amorphous material, with rocking curve analysis giving a broad fwhm of >10°. Detailed structural analysis showed that the PST had a filamentous structure, with each filament extending up from the PST/platinum interface to the PST surface. Each of these filaments was not a single grain of pyrochlore, but was in fact nanocrystalline pyrochlore. The structure of the starting material was encouraging in that the pyrochlore was only poorly crystallised, suggesting that complete conversion to perovskite should be possible.

In order to convert this as-deposited material to perovskite two principle techniques were used. The main technique was RTP which, as discussed in Chapters 3 and 4, has the advantage of rapid heat up and cool down rates of tens to hundred degrees per second. In practice this means that the temperature profiles that the PST experiences can be accurately controlled. A consequence of this is that the time spent at temperatures where a stable form of PST pyrochlore may form can be minimised. RTP was performed in both inert and oxidising atmospheres since it was not known whether the particular pyrochlore phase grown at 300°C is oxygen rich or oxygen deficient. The second annealing technique used was furnace annealing, which was undertaken for the purposes of comparison to RTP. Materials analysis of the annealed films was undertaken using the same techniques as were applied to the as deposited PST. Electrical analysis included measurement of the dielectric properties (ε_r and $\tan\delta$), the pyroelectric coefficient and most importantly F_D, the materials merit figure.

The samples RTP annealed in oxygen were structurally and crystallographically different depending on the anneal temperature/time. A 650°C RTP anneal for 30 seconds resulted in incomplete conversion of the as-deposited material to perovskite with a (222) texture. This effectively ruled out this processing scheme for the fully integrated detector fabrication

route. Structurally the PST had changed form with a bicoloured granular appearance optically, the two colours probably resulting from areas of predominantly perovskite or amorphous/pyrochlore having slightly different refractive indices. The granular appearance of the PST thin film, the so called crazy-paving pattern, is a characteristic that has been observed in PST deposited onto platinised silicon directly into the perovskite phase. This pattern was observed, to a lesser or greater extent, on all annealed samples. The surface morphology of the PST had changed little from that of the as-deposited material, apart from the appearance of some micro-cracks. XRD showed that the perovskite PST rocking curve fwhm (~2°) were very close to that of the underlying platinum (~1.6°), a common trait in all the RTP annealed samples, suggesting that the growth of the perovskite was strongly influenced by the platinum.

The higher temperature RTP anneals in oxygen showed virtually complete conversion of the starting material to perovskite with (222) texture as observed for the 650°C anneal. No superlattice peaks were registered in the XRD scans, an observation common to all of the annealed PST reported in this chapter, which indicates that no B-site cation ordering had occurred – even at the 850°C anneal temperature. Structurally these samples were very distinct from the as-deposited and 650°C annealed material with individual grains of the order of a few microns across. Such large grains are unusual in PST thin films on silicon substrates with the microstructure of PST deposited at 525°C (perovskite directly) being a dense array of columnar grains, ~0.1μm diameter – refer to appendix A2, extending up from the PST/platinum interface through to the PST surface giving a faceted so-called 'sharks tooth' surface morphology. It may also be noted that low temperature deposited PZT thin films have been observed to convert to perovskite with this dense columnar grained structure when RTP annealed in oxygen – refer to Chapter 8 section 8.3.4 for a cross-sectional TEM picture of such a sample. In the RTP annealed PST reported the large grains result from a low nucleation density of perovskite at the PST/platinum interface which may be caused by a greater lattice mismatch between the PST perovskite and the platinum (~5%) than there is between PZT perovskite and platinum (~3.5%). Another prominent feature of the surface morphology of the RTP annealed PST was pitting on the surface. This was caused by voids in the PST terminating at the surface, although voids were distributed throughout the thickness of the PST. This voiding is primarily due to the volume change upon conversion from the amorphous/pyrochlore phase to perovskite.

Using the pyrochlore and perovskite unit cell data from XRD measurements a simple calculation shows that the volume shrinkage on conversion is ~9%. In the reported PST the volume shrinkage has been taken up as voids, whereas in other materials such as PZT it is generally taken up as a thickness change in the film, as observed by Voigt et al [31], or at worst, clusters of voids around grain boundaries. A possible mechanism for void formation is the progression of a non-uniform growth front into the pyrochlore/amorphous matrix which closes off regions of unconverted material. These regions would then convert with the resulting volume change giving rise to a void, possibly lined with residual second phase material. It is worth noting that voiding appeared worst in the 850°C annealed material, which also registered a loss of lead from as-deposited – possibly contributing to the volume change. The voiding should not be a problem in device operation as long as it does not contribute to electrical breakdown. In fact one group has deliberately tried to produce porous films (using lead calcium titanate) for IR detector applications [104]. The increased porosity was seen to decrease ε_r thereby resulting in an increased merit figure.

As mentioned previously a sample was RTP annealed in argon to compare with samples annealed in oxygen. Other authors have tried annealing in argon with other materials, most notably the PZT results reported by Bursill and Brooks [89] where the transformation to perovskite was improved. The rationale behind this was that since the pyrochlore phase of PZT is more oxygenated than the perovskite phase then transformation is aided by relying on the oxygen content within the as-deposited film to grow the perovskite, rather than supplying excess oxygen from the annealing atmosphere which would favour pyrochlore formation. It was not clear what effect annealing in argon would have on PST since the oxidation state of the starting material was not known, nor was it clear from the literature since there is a general lack of information on PST pyrochlores. An RTP anneal at 700°C for 5 minutes resulted in a PST thin film that had been converted to perovskite with (222) texture and which structurally was very similar to the corresponding oxygen annealed sample. One key difference was the presence in the XRD scan of a peak corresponding to the (111) reflection of the lead-platinum intermetallic Pt_3Pb which indicated that a reaction had occurred between free lead in the PST and the platinum layer. The formation of such an intermetallic has been reported in PZT sol-gel deposition by Chen et al [102] and Huang et al [101] where reaction of the lead in the film with the underlying platinum occurs in the relatively anaerobic environment prior to complete removal of the sol-gel organic

component from the spin deposited film during firing. Such an anaerobic environment would be present during the RTP anneal in argon after the oxygen contained in the as-deposited PST has been used to form perovskite or been lost by outgassing.

Furnace annealing at 700°C, tried as an alternative to RTP, was successful in converting the as-deposited material to perovskite, again with (222) texture. Compared to the RTP method the furnace annealed sample had a poor surface morphology which was characterised by gross cracking of the PST, which was not observed on RTP annealed samples. A possible cause of this cracking is that during the slow heat up phase of the anneal the PST spends a long time (relative to the RTP method) at temperatures at which a well crystallised metastable pyrochlore is likely to form, ~400°C-500°C. If the whole of the PST film formed as this phase then conversion to perovskite at a higher temperature would result in a volume change possibly resulting in cracking. In the RTP anneal the samples pass through this region relatively quickly (ramp up rate ~50°C/s) with the result that the perovskite formation may be more direct, with no intermediate complete conversion to pyrochlore. It should be also noted that there is a significant thermal expansion mismatch between perovskite PST ($6.6\times10^{-6}K^{-1}$)[105] and the underlying silicon ($2.6\times10^{-6}K^{-1}$)[73], although if this were the sole reason for cracking then intuitively it might be expected that the RTP annealed samples would suffer more than the furnace annealed material – a scenario not backed up by the results.

Comprehensive electrical properties measurements were made on the annealed samples in order to ascertain the suitability of the PST for incorporation into uncooled IR detectors. Only the samples RTP annealed in oxygen yielded PST with good electrical properties. The sample RTP annealed in argon gave an electrically unstable film with low permittivity and high loss, possibly a result of either a disruption of the bottom electrode due to to the lead platinum intermetallic formation or due to oxygen non-stoichiometry leading to a poor quality perovskite film. The furnace annealed sample yielded no electrical information due to complete shorting between the top and bottom electrodes, which is unsurprising given the severe cracking in the PST. A summary of the measured electrical properties is given in Table 5.6 below and includes the maximum F_D values and corresponding pyroelectric coefficients, ε_r and tanδ and dielectric properties. Consultation of Appendix A7, containing results of modelled detector performance, will help the reader put the F_D values in context.

A general observation is that the electrical properties improved with either a higher temperature or a longer duration anneal.

Sample	RTP anneal	T_{max} (°C)	Applied Field (V/μm)	ε_r^{max}	tanδ (%)	p ($\mu C/m^2K$)	F_D ($\times 10^{-5} Pa^{-1/2}$)
C	750°C, 30s	37	5.8	1123 ±77	0.99 ±0.05	556±28	2.1±0.2
D	850°C, 30s	49	8.3	908 ±62	0.61 ±0.05	710±36	3.8±0.5
E	700°C, 5 mins	37	5.8	1149 ±78	0.64 ±0.05	525±26	2.4±0.3

Table 5.6: Maximum F_D values (120Hz) of samples RTP annealed in oxygen. ε_r^{max} is the maximum relative permittivity occuring at temperature T_{max}.

The samples RTP annealed in oxygen had dielectric properties indicative of a relaxor ferroelectric, which is unsurprising given the lack of B-site ordering which is required for first order ferroelectric properties in PST. The measured dielectric properties fulfilled the criteria for relaxors as laid down by Cross [22]. Firstly the films exhibit dispersion of the dielectric maximum with measurement frequency, in the manner of a relaxation dielectric where the dielectric maximum shifts to higher temperatures with increasing frequency. Secondly, hysteresis loops shows that the spontaneous polarisation is not suddenly lost at T_c (the temperature of the dielectric maximum), as would be the case with a first or second order ferroelectric, but decays gradually to just non-linearity. At temperatures well below the bulk ceramic PST Curie temperature, 20-30°C, the thin film PST has a true hysteresis loop, demonstrating its ferroelectric character. Further confirmation of the relaxor ferroelectric nature of the electrical properties was obtained by fitting the zero applied field ε_r curves, above the dielectric maximum, to the phenomenological quadratic form suggested by Smolenski [21] for the well known relaxor material PMN. The diffuseness parameter δ [21, 106] from this model which indicates the sharpness of the peak in ε_r (versus temperature), discussed in Chapter 2, has been calculated for the RTP annealed films at zero applied field above the temperature of the dielectric maximum, Table 5.7. Plots of $\varepsilon_r^{max}/\varepsilon_r$ versus $(T-T_{max})^2$, where ε_r^{max} and T_{max} are the dielectric maximum and the temperature of the dielectric maximum respectively, are shown in appendix A3. The δ values are high and compare with the values for bulk ceramic PST of 11, and thin film PST on sapphire of 34.

This reflects the fact that the zero field permittivity for these films is far less sharp than for PST ceramic or PST thin films grown on sapphire. A graph comparing the zero field permittivity of samples C (750°C RTP, 30s), D (850°C RTP, 30s) and E (700° RTP, 5 mins) to typical hot pressed ceramic PST and thin film PST on sapphire is shown in appendix A3. The difference in peak permittivity and sharpness is very marked, with ε_r^{max} of the best sample (D) of 2279±156 comparing with ~9000 for PST bulk ceramic and ~5500 for thin film PST on sapphire. Reasons for these differences could be manifold as the peak permittivity is affected by a number of factors. Setter and Cross found that the degree of B-site ordering in PST markedly affects the relative permittivity with well ordered films exhibiting high ε_r values and disordered PST giving relatively low ε_r values [13]. With the lack of B site ordering in the reported PST thin films it is unsurprising that the permittivity is low in comparison with ordered bulk ceramic. Other factors affecting ε_r include stresses induced on the film by the underlying substrate [82, 107] which were shown by Shorrocks et al [82] to reduce the magnitude, position and sharpness of the peak ε_r. Voiding of the film also results in a lowering of the permittivity [104]. Relatively low dielectric constant interfacial layers can also have marked effects in thin films [107].

Sample	ε_r^{max}	T_{max} (°C)	δ
C	1992±136	-10	107
D	2279±155	21	78
E	2200±150	3	98

Table 5.7: ε_r^{max}, T_{max} and δ values (120Hz) for RTP annealed PST.

A further interesting result of the electrical characterisation was the confirmation of the presence of an effective internal bias field [34, 45] which manifested itself as an offset on the hysteresis loops [34, 45] as well as maximum ε_r and tanδ values at non-zero applied field. The zero field pyroelectric coefficient was non-zero and could, with the application of a field in the negative sense (top electrode held negative), be brought to zero and have its sign reversed by a field of $\sim -1.5 \rightarrow -2$V/μm. This phenomenon of internal bias field is well known in other ferroelectric systems [108], an example being alanine doped Triglycine Sulphate (TGS) [34] where there is partial exchange of one of the glycine groups for alanine molecules. These alanine molecules are not free to rotate and have their dipoles pointing in the same direction, resulting in a macroscopic irreversible polarisation which polarises the

TGS in a preferred direction. The internal bias field obtained from hysteresis loops is directly proportional to the amount of alanine present. Arlt and Neumann [45] have investigated the origin of internal bias in ferroelectric ceramics with studies of niobium doped barium titanate showed that oxygen vacancies result in defect dipoles. Electric fields from these induces an energetic difference between the two poling directions, thus appearing as an internal bias field. In the PST thin films reported it is very possible that there are defects present due to a degree of non-stoichiometry.

From the reported electrical measurements it is clear that relaxor properties in PST have important implications for obtaining high F_D values. We recall from Chapter 2 that the induced pyroelectric coefficient depends on the integral over the applied field of the quantity $\partial\varepsilon_r/\partial T$. RTP annealed material reported in this chapter have diffuse dielectric properties which yield induced pyroelectric coefficients under bias of at most ~500-700$\mu C/m^2K$. These are moderate compared to bulk ceramic PST which, due to very sharply peaked dielectric properties – resulting from ordering and consequent near first order properties, yields induced pyroelectric coefficients of $6mC/m^2K$ at $5V/\mu m$ [6] and as a result F_D values of $\sim 16\times10^{-5}Pa^{-1/2}$ at applied fields of this order. In spite of this good F_D values were obtained due to the fact that ε_r and $\tan\delta$ are low to begin with and are further suppressed by the applied field, resulting in an improved merit figure even when the induced pyroelectric coefficient starts to saturate due to flattening of the dielectric response with increasing applied field. This is the route to high performance in such relaxor materials and thus high performance is directly related to the ability to sustain high bias fields.

High temperature RTP anneals resulted in disruption of the platinum/titanium interface with the silicon dioxide. Inclusions of lead rich material were also seen in the silicon dioxide layer. These effects are due to diffusion of the titanium adhesion layer upwards and lead oxide and possibly tantalum from the PST downwards along the grain boundaries of the columnar grained platinum bottom electrode layer. As mentioned previously this effect has been observed by Maeder et al [99] in a study of the stability of bottom electrode layers. The electrode structure used, 1000∑ of platinum with a 100∑ titanium adhesion layer, is a standard configuration widely used in the field of ferroelectric thin films due to its temperature stability and oxidation resistance. Since the temperatures investigated in this

chapter are relatively high it may be necessary to consider stabilising, or optimising, the bottom electrode structure for high temperature annealing. Although problems such as delamination of the various layers has not been observed, it is possible that difficulties could occur during a device fabrication process. A number of possible ways of achieving this stabilisation have been put forward by Maeder et al [99]. The most successful of these, in terms of prevention of adhesion layer diffusion and inclusions in the SiO_2 layer, was to replace the titanium adhesion layer with one of tantalum, which proved stable at elevated temperatures and an effective barrier to lead diffusion.

5.5 Summary.

The work reported in this chapter demonstrates that PST deposited onto platinised silicon at 300°C by single magnetron RF magnetron sputtering forms a poorly crystallised pyrochlore/amorphous structure. It has been shown for the first time that this as-deposited material can be converted to the required perovskite by high temperature annealing. RTP annealing in an oxygen ambient produced the most promising results but a 650°C anneal for 30s was insufficient to fully convert the starting material, effectively ruling out a fully integrated approach to detector fabrication – based on the thermal budget limitations reported in Chapter 4. The best electrical properties were obtained after an 850°C 30s anneal which gave an F_D value of $3.8\pm0.5\times10^{-5}Pa^{-1/2}$. RTP annealing in argon was seen to be less successful than oxygen with evidence for interaction of lead in the PST with the underlying platinum to form an intermetallic in the relatively anaerobic annealing environment. Although perovskite PST was formed the electrical properties were poor, making it unsuitable for detector fabrication purposes. Furnace annealing of PST in an oxygen ambient was also tried but resulted in films with poor morphological properties in comparison with RTP annealing, specifically gross cracking of the PST which resulted in shorting between top and bottom electrodes and would therefore also be unsuitable for device fabrication.

Detailed structural analysis showed that unlike PST deposited directly into the perovskite phase, the perovskite formed by this low temperature deposition/high temperature anneal route is not dense but is characterised by a high density of void-like structures. The grains that grow are large and reflect the low nucleation density of perovskite on the platinum

bottom electrode which may be due to a higher lattice mismatch between platinum and perovskite PST than in materials such as PZT. Investigation of the electrical performance of the oxygen RTP annealed PST revealed material with ferroelectric relaxor type electrical properties, which was expected since there was no observed B-site ordering – even at the highest anneal temperatures. The broad dielectric peaks resulted in only a moderate pyroelectric coefficients (;$\partial\varepsilon_r/\partial T$), compared with bulk ceramic (ordered) PST and high F_D values therefore relied on suppression of ε_r and tanδ with applied field. In this way high performance of the PST thin films reported is directly related to breakdown strength.

A potential problem encountered with the current platinum electrode structure is diffusion of lead, and possibly tantalum, from the PST into the underlying silicon dioxide. Although adhesion problems due to layer interface disruption have not been found it may be prudent to consider stabilising the bottom electrode structure for high temperature annealing to circumvent any possible problems that may occur during device fabrication. Without such stabilisation the reported results indicate approximately the likely thermal budget available when using the composite wafer approach i.e. a short RTP anneal of the order of a minute or two at 850°C which can be extended as the hold temperature is lowered. To this end it is interesting that the properties of the 700°C/5mins and 850°C/30s RTP samples are quite similar, at the same applied fields, indicating that a trade off could be made between temperature and time.

Overall, the measured F_D values are relatively modest compared with bulk ceramic PST (F_D ~ $16\times10^{-5}Pa^{-1/2}$) and thin PST deposited on Sapphire (F_D ~ $8\text{-}11\times10^{-5}Pa^{-1/2}$) but compare well with thin film PZT (F_D ~$2\times10^{-5}Pa^{-1/2}$ [109]) and 525°C (perovskite directly) deposited PST (F_D ~$2\times10^{-5}Pa^{-1/2}$). Since PST on Sapphire is currently of no use to an integrated detector fabrication programme, without a reliable and cost effective thin film transfer technique, the results reported do represent a proof of principle that on silicon substrates the low temperature deposition/high temperature anneal technique can provide a significant performance improvement over other silicon substrate based materials and techniques. Further benefits include improved control of lead incorporation into the as-deposited PST film and improved growth machine reliability at this relatively low deposition temperature. The most promising route is a high temperature RTP anneal in oxygen which at 850°C would require the composite wafer approach to detector fabrication. With merit figures in

excess of $3.5\times10^{-5}Pa^{-1/2}$ this gives the promise of high performance uncooled detectors if this PST is incorporated into a high efficiency thermal structure such as the XAC design.

Chapter 6:

Dual RF Magnetron Sputtering Deposition of Lead Scandium Tantalate at 300°C and 450°C followed by Annealing.

6.1 Introduction

This chapter reports annealing work performed on thin film PST deposited onto platinised silicon by dual RF magnetron sputtering. The deposition equipment, described more fully in Chapter 3, comprises two targets, which in combination with substrate translation and rotation allows wafers up to 4" diameter to be uniformly coated with PST. In comparison with the annealing trials performed using single magnetron sputtering, described in Chapter 5, this method is better suited to production of dielectric bolometer uncooled IR detectors. The main objective of this chapter is to investigate whether low temperature deposited PST using the dual magnetron technique can be converted into the required perovskite phase by post-deposition annealing, as demonstrated in Chapter 5 for single magnetron deposition at 300°C, with good electrical properties - principally a high materials merit figures for IR detection. Deposition using the dual magnetron technique produces layered films, in contrast to the single magnetron technique where there is more intimate mixing of the elemental components. It was not known at the start of this work whether films could be transformed into perovskite PST by post-deposition annealing. The reported results fall into two broad categories: Firstly the RTP annealing of 450°C deposited PST, which in effect is a repeat of some of the RTP work of Chapter 5 for PST deposited at this higher temperature. Secondly the annealing of PST deposited onto platinised silicon at 300°C using the novel 'dwell time' method of operating the dual magnetron deposition system – described more fully in section 6.2.2 below and Chapter 3. Use of this deposition technique meant that the starting material was potentially different from that reported in Chapter 5. Consequently there were additional questions to be answered which included the form of the as-deposited material and its behavior upon annealing, i.e. could it be transformed and if so what were its electrical properties? More specifically did the low temperature deposition/high temperature anneal route result in PST with a high figure of merit for IR detection? Annealing regimes investigated with this 300°C deposited material include a comparison of

oven-only annealing with combined RTP/oven annealing. As well as this, RTP-only annealing is also investigated with both low and high temperature results presented.

For both the 450°C and 300°C PST annealing studies the majority of the temperatures-time regimes used are in excess of those at which the ROIC would survive (refer to Chapter 4). A consequence of this is that the deposition/annealing schemes could only be incorporated into a composite wafer based process (refer to Chapter 2) which has relaxed temperature restrictions compared to a fully integrated process. As in Chapter 5 both the materials and electrical properties of the annealed PST are presented.

6.2 Experiment

6.2.1 Deposition of PST at 450°C

A PST thin film of thickness 0.8μm was reactively RF sputtered at 450°C onto a platinised silicon substrate using an Scientific Vacuum Systems (SVS) Ltd. dual magnetron sputtering system, described in detail in Chapter 3. PST deposition work was performed in conjunction with Mark Harper of DERA. The PST deposition system was operated in conventional mode (see Chapter 3) with the RF bias power and target bias voltage used to control the erosion rates from the lead and combined scandium/tantalum targets and hence the PST thin film composition. Fine control of the scandium/tantalum ratio was via the rotational position of this substrate holder with respect to the target, as described in Chapter 3. Deposition conditions used for the PST thin film are given in Table 6.1.

Parameter	**Value**
Base pressure	2×10^{-6}mbar
Total sputter pressure	6mTorr
Argon flow	9.6sccm
Oxygen flow	2.4sccm
Ar/O_2 ratio (measured)	12%
Sc/Ta target RF bias power/voltage	350W/137V
Pb target RF bias power/voltage	64W/42V
Substrate scan rate	0.56°/s
Substrate temperature	450°C

Table 6.1: Sputtering conditions for 450°C deposited PST.

The thickness of the deposited PST was measured after deposition using a RTH Talysurf, and after annealing using cross-sectional SEM. A 3” silicon wafer {(004) orientated}, the

surface of which was thermally oxidised to a depth of 0.8μm, was used as a substrate. A titanium adhesion layer of thickness ≈100∑ was RF diode sputter deposited onto the surface followed by the RF magnetron sputtering of a 1000∑ thick platinum layer. Typical deposition conditions for the titanium and platinum layers can be found in section 5.2.1 of Chapter 5 of this thesis. The platinum acted as both a bottom electrode and a growth template for the PST thin film deposited on top of it. After PST deposition the wafer was diced into 1cm^2 pieces for annealing trials and characterisation.

6.2.2 Deposition of PST at 300°C

PST thin films of thicknesses between 0.85μm and 1.2μm were reactively RF sputtered at 300°C onto a platinised silicon substrate using the same SVS sputtering system described in the previous section. The PST was deposited with the system operated using the novel dwell time method described in Chapter 3. In this operating mode the metal targets were operated at optimum RF power and bias voltage levels such as to maintain the erosion rates at constant levels by overcoming the problem of target oxidation. PST film composition was then controlled by varying the amount of time that the substrate dwelled over each target. Table 6.2 below gives the deposition conditions used for the 300°C deposited PST films described in this chapter.

Parameter	**PST285**	**PST307**	**PST315**	**PST316**
Base pressure	6.3×10^{-7}mbar	6.3×10^{-7}mbar	6.3×10^{-7}mbar	6.3×10^{-7}mbar
Total sputter pressure	8.8mTorr	8.6mTorr	8.6mTorr	8.6mTorr
Argon flow	15.5sccm	17.5sccm	16.4sccm	17.8mTorr
Oxygen flow	4.3sccm	5.2sccm	4.1sccm	4.5sccm
Sc/Ta target RF bias power	531W	509W	520W	524W
Sc/Ta target bias voltage	190V	170V	170V	170V
Pb target RF bias power	99W	128W	133W	136W
Pb target bias voltage	66V	66V	66V	66V
Substrate temperature	300°C	300°C	300°C	300°C
Substrate to target distance	70mm	70mm	70mm	70mm
Substrate rotation rate	13rpm	13rpm	13rpm	13rpm
Sc position dwell time	10s	2.85s	6s	6s
Ta position dwell time	5s	12s	20s	20s
Pb position dwell time	5s	3s	6s	6s
Number of cycles	233	250	200	200
Total deposition time	103mins	107mins	143mins	143mins

Table 6.2: Sputtering conditions for 300°C deposited PST.

6.2.3 Annealing

Annealing studies were performed on both the 450°C and 300°C deposited PST thin films with the annealing methods being RTP, oven annealing and combined oven annealing/RTP. Studies where oven annealing were carried out were performed in conjunction with M.A. Todd of DERA. An AG Associates Minipulse, as described in Chapter 3, was used for RTP with the samples mounted on the integral Sensarray single point process probe. The ramp-up rate was set to $50°Cs^{-1}$ with natural cooling and the ambient atmosphere was flowing O_2 (2l/min). Oven annealing was performed using a SFL Instron vacuum compatible tube furnace, described in more detail in Chapter 3. Ramp-up and ramp-down rates for this system were 7.5°C/min and 1°C/min, which is very slow compared to the RTP system. The ambient atmosphere was 100mTorr of O_2. For the 450°C deposited PST samples RTP-only annealing was studied with the conditions used given in Table 6.3.

Sample	Identifier	Anneal method	Anneal Temperature (°C)	Anneal Time (s)	Anneal atmosphere
PST184 Piece 2	Sample A	none	-	-	-
PST184 Piece 4	Sample B	RTP	650	30	Flowing O_2
PST184 Piece 7	Sample C	RTP	750	30	Flowing O_2
PST184 Piece 10	Sample D	RTP	850	30	Flowing O_2
PST184 Piece 15	Sample E	RTP	850	30	Flowing O_2

Table 6.3: Annealing conditions used for 450°C deposited PST.

The 300°C deposited samples were used for a number of purposes, detailed in Table 6.4. Sample F is included for the purposes of the examination of the microstructure of PST (using TEM analysis) deposited at 300°C by the 'dwell time' method. Samples G and M provided as-deposited X-Ray data to be compared against the PST285 and PST315-PST316 series of samples. A study of Oven-only annealing compared against RTP- and combined RTP/Oven annealing was made using samples H to L with both materials and electrical analysis performed. Use of combined oven/RTP annealing was in response to a problem with oven only annealing – as will become clear in the following presented results and

discussion. Using samples N and O the materials and electrical properties of PST given a high temperature RTP annealed were investigated.

Sample	Identifier	Anneal method	Anneal Temperature (°C)	Anneal Time	Anneal atmosphere
PST307	Sample F	none	–	–	–
PST285 Piece E2	Sample G	none	–	–	–
PST285 Piece C1	Sample H	Oven	700	1hr	100mTorr O_2
PST285 Piece C2	Sample I	Oven	750	1hr	100mTorr O_2
PST285 Piece B2	Sample J	Oven	800	1hr	100mTorr O_2
PST285 Piece F2	Sample K	RTP/Oven	700/800	600s/1hr	100mTorr O_2/ Flowing O_2
PST285 Piece B1	Sample L	RTP	700	600s	Flowing O_2
PST316 Piece E3	Sample M	none	–	–	–
PST315 Piece D4	Sample N	RTP	850	30s	Flowing O_2
PST316 Piece D3	Sample O	RTP	850	120s	Flowing O_2

Table 6.4: Annealing conditions used for 300°C deposited PST.

6.2.4 Electrodes

The platinum underlying the PST thin films served as a common bottom electrode. Circular chromium/gold top electrodes with diameters between 0.75mm and 1.5mm diameter (checked using a travelling microscope) were sputter deposited through a shadow mask using a Nordiko NM2000 system.

6.3 Results: 450°C Deposited PST

6.3.1 Materials Characterisation of 450°C Deposited PST

6.3.1.1 Compositional Analysis by Energy Dispersive Spectroscopy

The elemental composition of the PST thin films deposited at 450°C was determined using energy dispersive spectroscopy (EDS), using single element standards and an accelerating voltage of 15KeV, which is optimum for these samples – for further detail refer to Chapter

3. Table 6.5 gives the results of the analysis before and after annealing with the composition quoted as the ratio to scandium, i.e. Sc:Ta:Pb, with errors on the Ta/Sc and Pb/Sc ratios being ±3% (see Chapter 3).

Sample	Sc:Ta:Pb As-deposited	Sc:Ta:Pb After annealing
A	1:0.98:2.29	–
B	1:1.05:2.36	1:0.98:2.19
C	1:1.05:2.37	1:0.97:2.18
D	1:0.99:2.18	1:0.99:2.12
E	1:1.06:2.29	–

Table 6.5: EDS results before and after annealing.

All annealed samples have had their lead content reduced from the as-deposited values, but have not dropped below perovskite PST stoichiometry.

6.3.1.2 Optical and Scanning Electron Microscope Analysis

The surface morphologies of the as-deposited and annealed samples were investigated using optical and scanning electron microscopy. An optical micrograph of sample A (as-deposited) is shown in Figure 6.1 below with the numbers indicated giving the horizontal (X), vertical (Y) and diagonal (D) dimensions in microns of the rectangle formed by the intersection of the four marker bars. Apart from a network of line features the surface is featureless. Figure 6.2 shows a SEM picture of the surface, which is composed of grain-like features ~100nm across. Cross-sectional TEM results reported later in this chapter show that the PST consists of columnar grains, ~100nm across, of the pyrochlore phase which extend through the depth of the PST with the features seen on the SEM picture being the tops of these grains. Line features observed optically were not seen by SEM, suggesting that they are not micro-cracks.

Figure 6.1: Optical picture of sample A (as-deposited). (*Original in colour*)

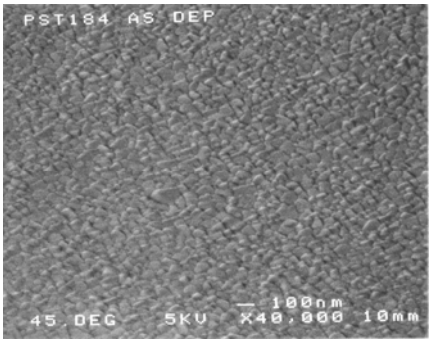

Figure 6.2: SEM picture of sample A (as-deposited).

Optical and SEM pictures of sample B (650°C RTP, 30s) are shown in Figures 6.3 and 6.4. The optical picture shows light coloured regions ~3-4μm across while in the SEM picture there are corresponding regions with observable contrast at the borders of the features. It is postulated that the lighter coloured features are perovskite grains in a sea of pyrochlore, the colour difference being produced by a small refractive index difference between the two phases. This explanation is supported by evidence from cross-sectional TEM analysis presented later in this chapter.

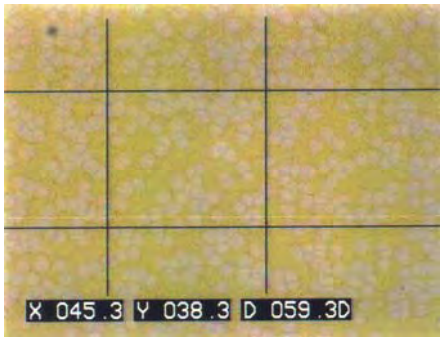

Figure 6.3: SEM picture of sample B (650°C RTP, 30s). (*Original in colour*)

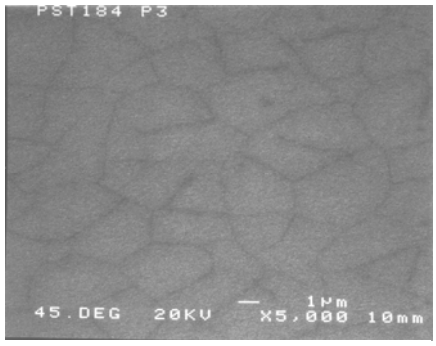

Figure 6.4: SEM picture of sample B (650°C RTP, 30s).

Figures 6.5 and 6.6 below show optical and SEM pictures of sample C (750°C RTP). The optical picture shows a crazy paving structure, with feature size ~3μm, which is a recognised feature of perovskite PST on platinised silicon substrates. These features are also visible in the SEM picture and it is thought that they are grains of perovskite.

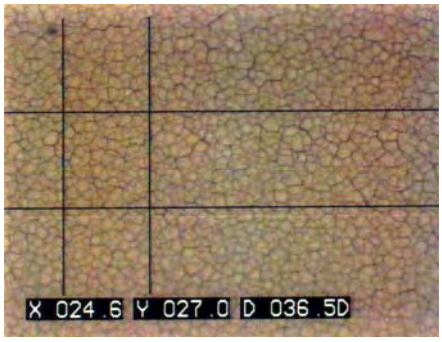

Figure 6.5: Optical picture of sample C (750°C RTP, 30s). (*Original in colour*)

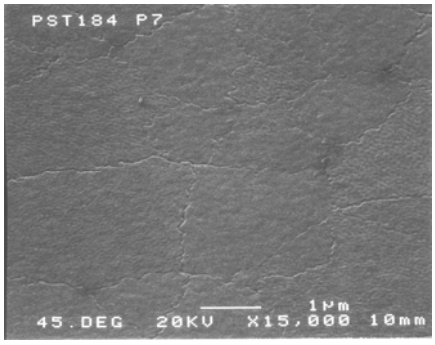

Figure 6.6: SEM picture of sample C (750°C RTP, 30s).

Optical and SEM pictures of sample D (850°C RTP, 30s) are shown in Figures 6.7 and 6.8 below. As for sample C the optical picture shows a network of crazy paving with a feature size of ~5μm, though more mottled in appearance. The SEM picture shows grain-like features with distinct boundaries and a pitted surface with the latter corresponding to voids in the PST, as will be shown in the TEM analysis presented later.

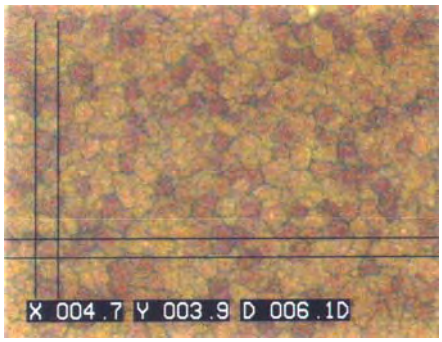

Figure 6.7: Optical picture of sample D (850°C RTP, 30s). (*Original in colour*)

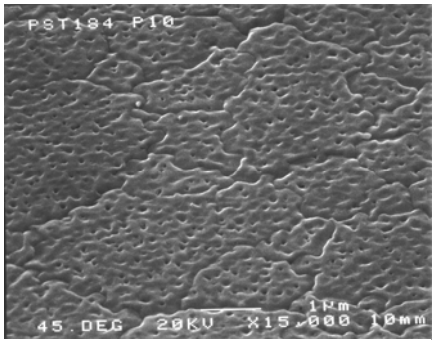

Figure 6.8: SEM picture of sample D (850°C RTP, 30s).

6.3.1.3 X-Ray Diffraction Analysis

XRD θ-2θ scans in Bragg-Brentano geometry, as well as rocking curves, were measured for all samples and used to determine the cytsalline structure of the PST thin films. In the case of θ-2θ scans all data was normalised to the as-deposited sample using the platinum (111) reflection. For the rocking curves, all data was normalised to the integrated intensity of the peak intensity of the platinum (111) rocking curve of the as-deposited sample.

A θ-2θ scan for the as-deposited sample is shown in Figure 6.9 below. The underlying platinum is seen to be (111) textured and the reflections due to PST are from the pyrochlore phase only [62]. The pyrochlore is (222) textured with lower intensity (400) and (440) reflections with the absence of odd-numbered reflections indicating that it is of the defect fluorite type [9, 12]. Compared with the pyrochlore reflections of the 300°C deposited PST reported in the previous chapter the intensities are very strong, suggesting a better formed crystalline structure.

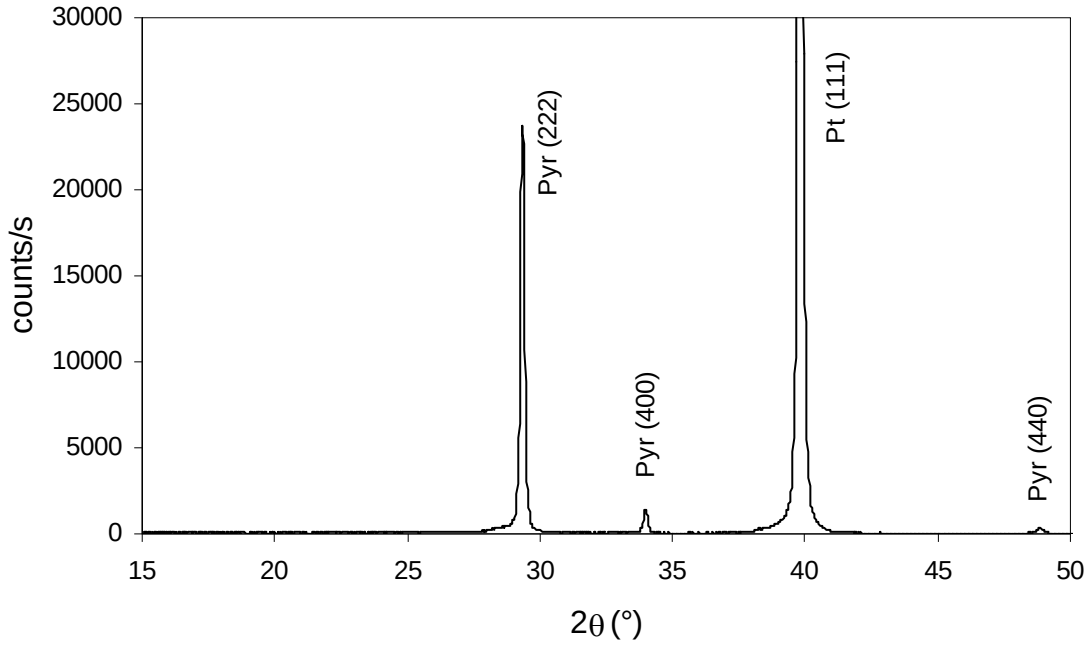

Figure 6.9: θ-2θ scan for sample A (as-deposited). *Pyr* denotes pyrochlore.

Figures 6.10 (log scale) and 6.11 (linear scale) below show the θ-2θ scans for the as-deposited and RTP annealed material. Both plots show that upon annealing the intensity of the pyrochlore reflections are successively reduced to zero whist perovskite reflections appear and increase in intensity with increasing anneal temperature. Sample B (650°C RTP, 30s) is seen to be mixed phase with both pyrochlore and perovskite reflections present which shows that the annealing conditions used were insufficient for complete conversion of the pyrochlore to perovskite, although the pyrochlore (222) reflection has decreased in intensity by over a factor of ten. A small peak that appeared on the low-angle shoulder of the pyrochlore (222) peak has been indexed as the orthorhombic phase of lead oxide [110]. The perovskite that has grown is (222) textured, following the underlying platinum, with additional low intensity (200), (220) and (400) reflections present although no (111) superlattice reflection at 2θ ~ 18.9°C is seen, indicating that the perovskite formed is not of the ordered type. It is interesting to note that the platinum (111) reflection has shifted to a higher angle, indicating an alteration of the stress in the sample in the tensile direction – as observed in Chapter 5.

The θ-2θ scan for sample C (750°C RTP, 30s) shows that the PST has almost completely converted to perovkite with a very low intensity residual pyrochlore (222) reflection. As for

sample B the perosvkite is (222) textured and there are low intensity (200), (220) and (400) reflections although in contrast to sample B (650°C RTP, 30s) there is evidence of ordering of the B-site cations in the PST with the appearance of a small (111) superlattice reflection. The θ-2θ scan for sample D, RTP annealed at the highest temperature – 850°C for 30s, shows complete conversion to perovskite with no pyrochlore reflections visible. The orientation distribution of the PST perovskite is similar to that of samples B and C with (222) being dominant and, as for sample C, the (111) superlattice peak is observed indicating ordering of the scandium and tantalum cations on the B-sites. The intensity of this peak is almost a factor of six greater than for sample C indicating a greater amount of ordering with the increased anneal temperature. Also the shift of the peaks to higher angles is greater suggesting a larger stress alteration in the platinum and PST layers.

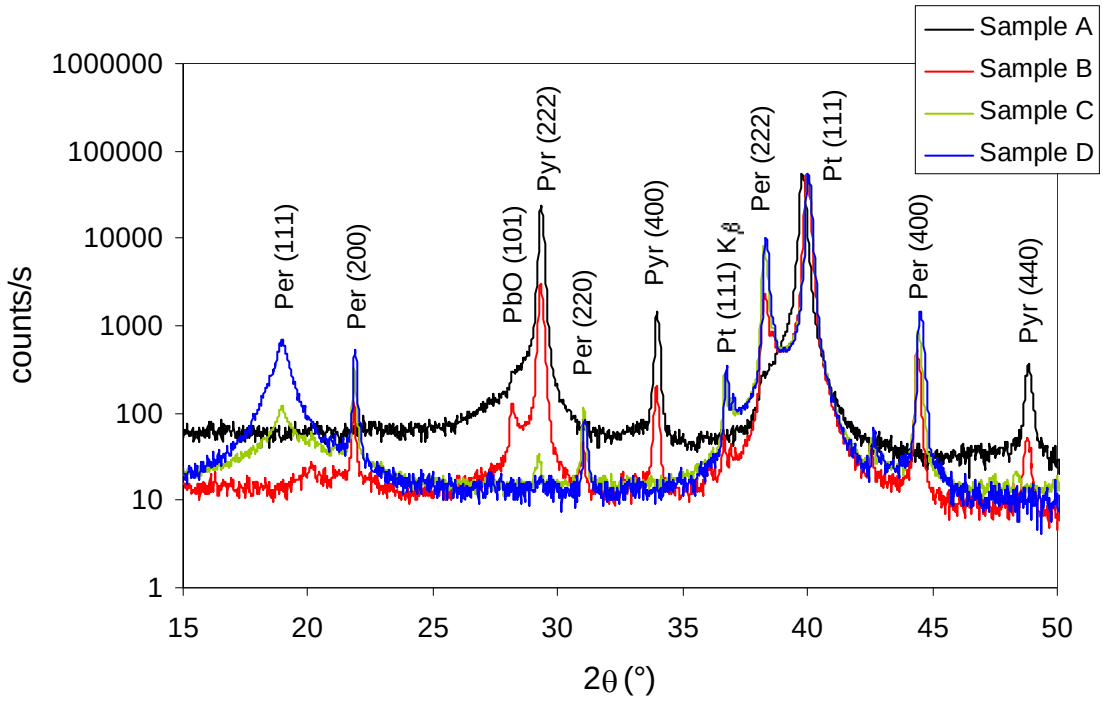

Figure 6.10: θ-2θ scans for samples A (as-deposited), B (650°C RTP), C (750°C RTP) and D (850°C RTP). *Pyr* and *Per* denote pyrochlore and perovskite respectively. (*Original in colour*)

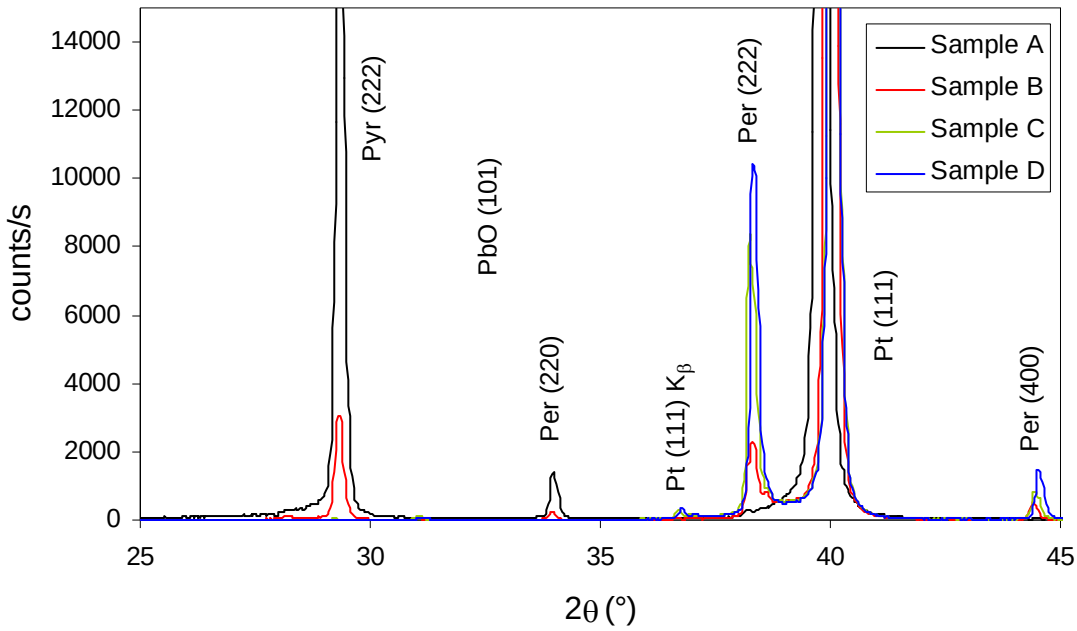

Figure 6.11: θ-2θ scans for samples A (as-deposited), B (650°C RTP), C (750°C RTP) and D (850°C RTP). *Pyr* and *Per* denote pyrochlore and perovskite respectively. (*Original in colour*)

The rocking curves for the platinum (111) and PST pyrochlore (222) reflections are shown in Figure 6.12 below. Figure 6.13 shows the perovskite (222) rocking curves for the RTP annealed samples and Table 6.6 summarises the salient information from Figures 6.12 and 6.13. The platinum is fibre textured with only a small spread about the preferred orientation, as indicated by the fwhm of 1.9°. PST pyrochlore that has grown on top of the platinum has a much larger spread about the preferred orientation with a fwhm of 10.6°. In contrast the fwhm of the perovskite (222) reflection is ~2° which suggests an epitaxial relationship between the platinum and the perovskite that grows on top of it. The perovskite (222) reflection rocking curve integrated intensity, taken as an indication of perovskite content, increases successively with increasing anneal temperature – see Table 6.6.

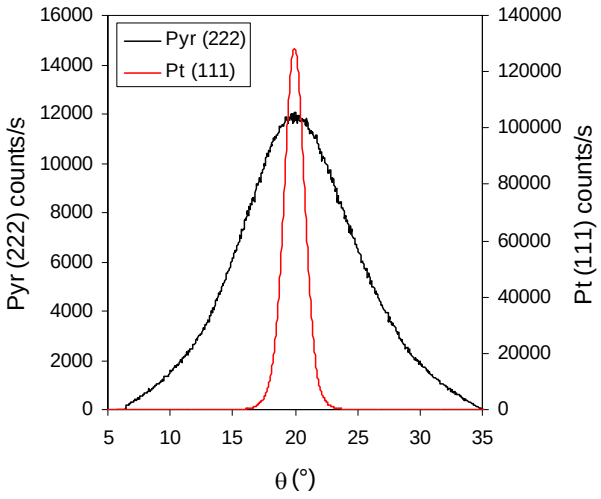

Figure 6.12: Rocking curves for sample A (as-deposited) pyrochlore (222) and platinum (111) reflections.
(*Original in colour*)

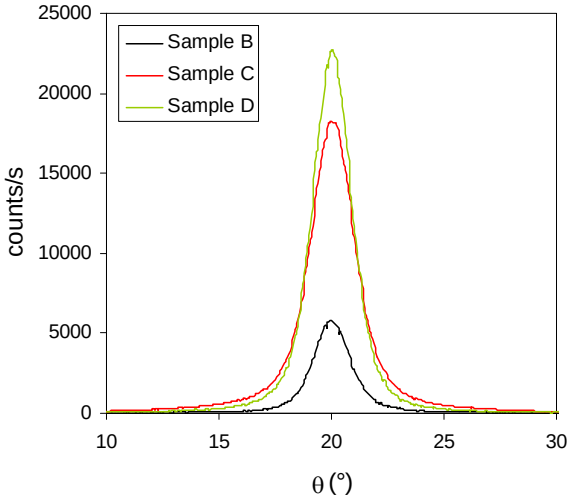

Figure 6.13: Perovskite (222) rocking curves for samples B (650°C RTP), C (750°C RTP) and D (850°C RTP).
(*Original in colour*)

Sample	Anneal	Reflection	Fwhm (°)	Integrated Intensity (counts°/s)
A	–	Pt (111)	1.9°	–
		Pyrochlore (222)	10.6°	–
B	650°C RTP, 30s	Perovskite (222)	1.9°	14248
C	750°C RTP, 30s	Perovskite (222)	2.3°	55338
D	850°C RTP, 30s	Perovskite (222)	2.0°	56170

Table 6.6: Summary of rocking curve data for samples A to D.

6.3.1.4 Transmission Electron Microscopy

To determine the detailed microstructure of the samples, both as-deposited and after annealing, cross-sectional TEM analysis was performed courtesy of Dr. D.A. Wallis of DERA. The lamellae used for this were formed using the focussed ion beam technique which was described in detail in Chapter 3. All images presented are bright field. Figure 6.14 below shows a cross-section of the as-deposited PST, with the underlying platinum and protective tungsten capping layer left from the FIB processing clearly visible. The PST is seen to be composed of well formed columnar pyrochlore grains of ~0.1μm diameter extending up from the platinum to the PST top surface and is reminiscent of the structure of the thin film PST deposited directly into the perovskite phase, a picture of which is shown

in Appendix A2. This columnar grained pyrochlore structure is different from that observed in the 300°C deposited PST described in the previous chapter which had a diffuse structure of faint vertical striations composed of a nano-crystalline pyrochlore phase. This shows that deposition of PST at 450°C results in a very well formed pyrochlore phase with a dense columnar grained structure with (222) texture, as shown by XRD.

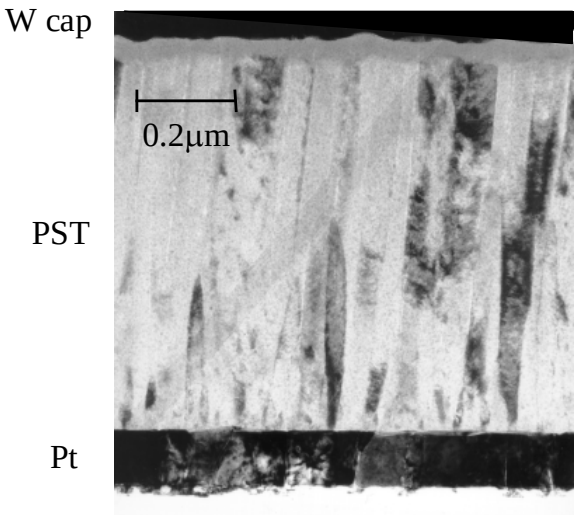

Figure 6.14: TEM cross-section of sample A (as-deposited) showing Columnar grained pyrochlore.

Figure 6.15 shows a cross-sectional TEM picture of sample B which was RTP annealed at 650°C for 30s. The PST is incompletely transformed with a large perovskite grain, of the order of several microns lateral dimension, growing up from the underlying platinum and consuming the pyrochlore matrix. Faint striations corresponding to the original pyrochlore grain boundaries can be seen within the perovksite grain, see Figure 6.16 for an expanded view. These islands of perovskite in a 'sea' of pyrochlore correspond well to the regions of discolouration observed under the optical microscope - see Figure 6.3 of section 6.3.1.2. This growth pattern is symptomatic of a low nucleation density of the perovskite phase on the platinum and is unlike that of PZT perovskite formed under similar conditions, see Chapter 8 section 8.3.4 Figure 8.28, which forms a dense film of columnar perosvkite grains. Small area electron diffraction (SAED) has shown that the perovskite is well crystallised with no observable residual pyrochlore within it.

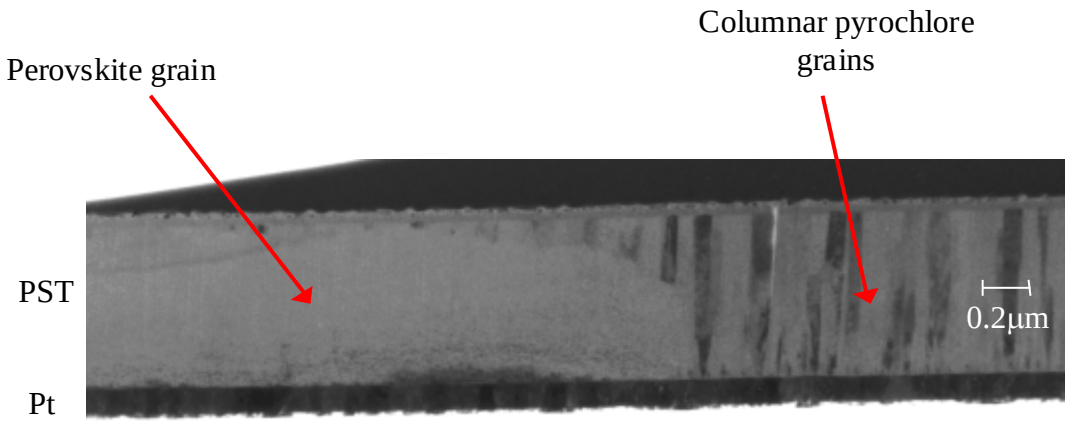

Figure 6.15: TEM cross-section of sample B (RTP at 650°C for 30s) showing perovskite grain growing into columnar grained pyrochlore matrix. (*Original in colour*)

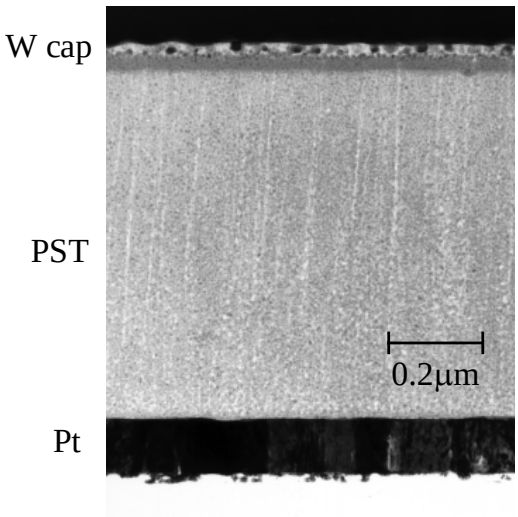

Figure 6.16: TEM cross-section of perovskite grain in sample B (RTP at 650°C for 30s).

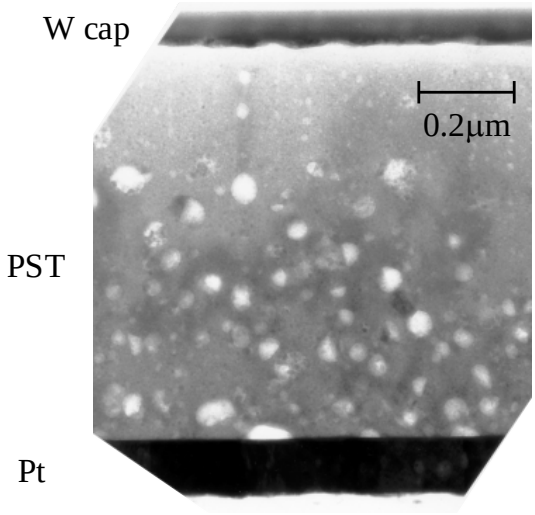

Figure 6.17: TEM cross-section of sample C (RTP at 750°C for 30s).

Figure 6.17 shows a picture of the TEM cross-section for sample C, RTP annealed at 750°C for 30s. No evidence of the original columnar grained pyrochlore structure was observed and SAED showed that the film was perovskite. As for the 300°C deposited PST followed by RTP annealing discussed in the previous chapter, the PST is characterised by voiding. This voiding has also been observed in sol-gel deposited PST thin films [83], but is not a characteristic of PST thin films deposited directly into the perovskite phase [86], and is most likely due to volume shrinkage on conversion from pyrochlore to perovskite as well as loss of some of the initial excess lead. The TEM cross-section for sample D, RTP annealed

at 850°C for 30s, is shown in Figure 6.18 below. As for sample C, the film is characterised by voiding. The two large regions of missing material, one at the PST/platinum interface and the other at the upper right of the picture, are thought to be artifacts from the FIB processing. Unlike the 300°C deposited PST reported in Chapter 5 the high temperature annealing did not result in lead rich inclusions in the SiO_2 layer, although at the higher anneal temperature the tianium adhesion layer is not visible and has presumably been dispersed by upwards diffusion along the platinum grain boundaries [99]. This lack of lead diffusion is understandable since the as-deposited PST is in a stable pyrochlore form, as opposed to the poorly crystallised pyrochlore/amorphous form of Chapter 5, and so there is little free lead oxide available for diffusion.

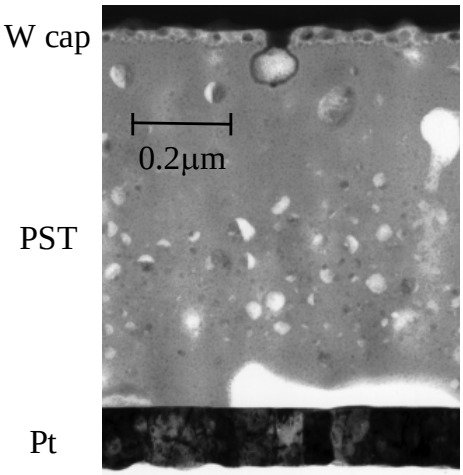

Figure 6.18: TEM cross-section of sample D (850°C RTP, 30s)

6.3.2 Electrical Characterisation of 450°C Deposited PST

Upon RTP annealing, the 450°C deposited PST samples showed varying degrees of transformation from the as-deposited pyrochlore phase to perovskite. Sample B (650°C, 30s) was incompletely transformed, as shown by XRD and TEM analysis, and electrical characterisation revealed PST of low permittivity and high loss – symptomatic of pyrochlore. Samples C (750°C RTP, 30s) and D (850°C RTP, 30s) were transformed to perovskite, with sample C showing a very low intensity trace of pyrochlore by XRD. Sample D was the most promising electrically and this section will concentrate on the results from this.

Figure 6.19 shows the dielectric properties of sample D as a function of temperature and measurement frequency. The maximum relative permittivity is 3346±194 (120Hz) at 35°C and is much higher than the correspondingly annealed film deposited by single RF magnetron sputtering discussed in the previous chapter (ε_r = 2277±155 at 120Hz and 25°C). The permittivity peak shows only slight dispersion with frequency and is relatively sharp with a diffuseness parameter (δ) value of 54, compared with a δ value of 78 for the similarly annealed single magnetron deposited PST reported in Chapter 5. This suggests that the phase transition of the PST is becoming less diffuse, as might be expected due to the observation of the superlattice perovskite (111) reflection in the XRD θ-2θ scan.

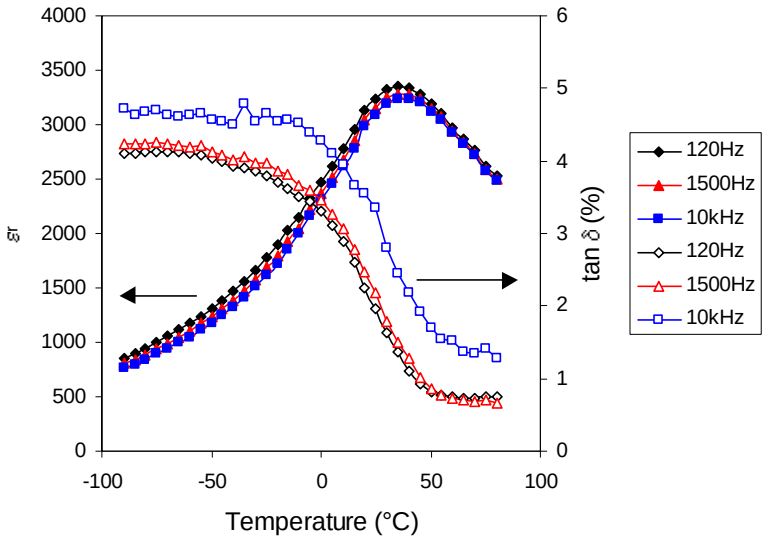

Figure 6.19: Dielectric properties of sample E (850°C RTP, 30s) as a function of temperature and frequency. (*Original in colour*)

Figure 6.20 below shows the behaviour of ε_r and tanδ (both 120Hz) with applied field at 35°C and 54°C. Both quantities can be seen to be suppressed by the application of a field in a positive (wrt the top electrode) sense. The breakdown strength of the PST was low with the sample only withstanding applied fields of 1.9V/μm and 1.3V/μm at 35°C and 54°C respectively. As for the PST films discussed in the previous chapter ε_r and tanδ peak at negative applied fields in the region of –1.5 to –2V/μm, suggesting an effective internal bias field of this magnitude.

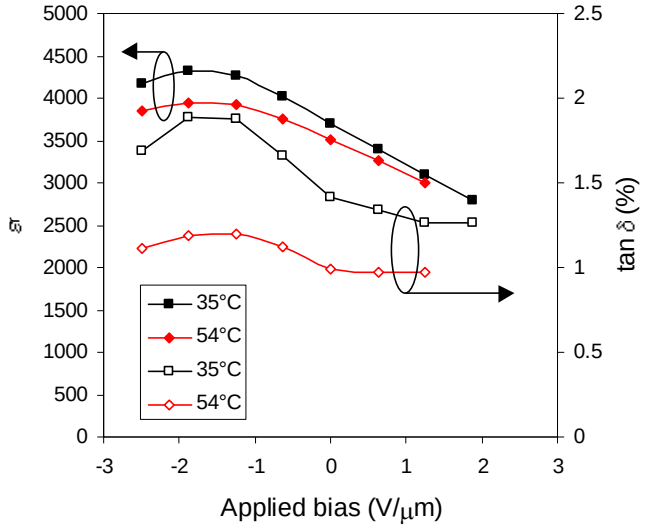

Figure 6.20: Relative permittivity of sample E (850°C RTP, 30s) as a function of applied bias and temperature. (*Original in colour*)

Figures 6.21 and 6.22 show the pyroelectric coefficient and materials merit figure as a function of applied bias. The relatively sharp permittivity curve results in a high induced pyroelectric coefficient at 35°C of 916±46μC/m^{2}K at a modest applied field of 1.9V/μm. In addition there is a high zero field pyroelectric coefficient of 582±29μC/m^{2}K at 35°C, presumably largely a result of the internal bias as well as a conventional pyroelectric component due to the persistence of the polar state to temperatures well in excess of the temperature of the dielectric maximum in relaxor type materials[22]. As for the material discussed in Chapter 5 it was possible to reduce the pyroelectric coefficient to zero and reverse its sign by the application of a negative bias with the field at which the pyroelectric coefficient became zero corresponding approximately to that at which the dielectric properties peak. Maximum merit figures for this sample were 1.9±0.2×10^{-5}Pa$^{-1/2}$ (1.9V/μm) at 35°C and 1.9±0.2×10^{-5}Pa$^{-1/2}$ (1.3V/μm) at 54°C.

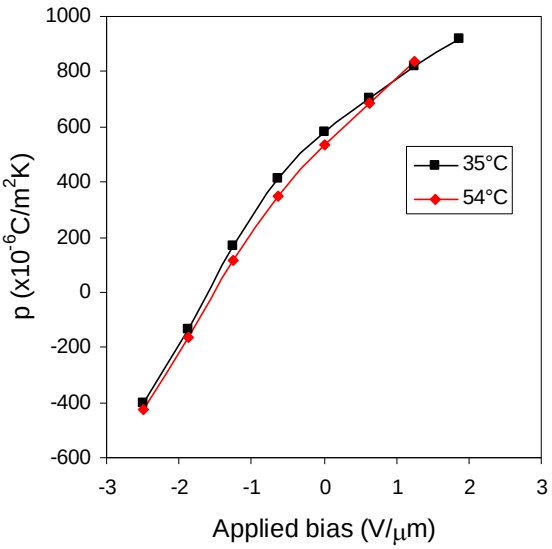

Figure 6.21: Pyroelectric coefficient of sample E (850°C RTP, 30s).

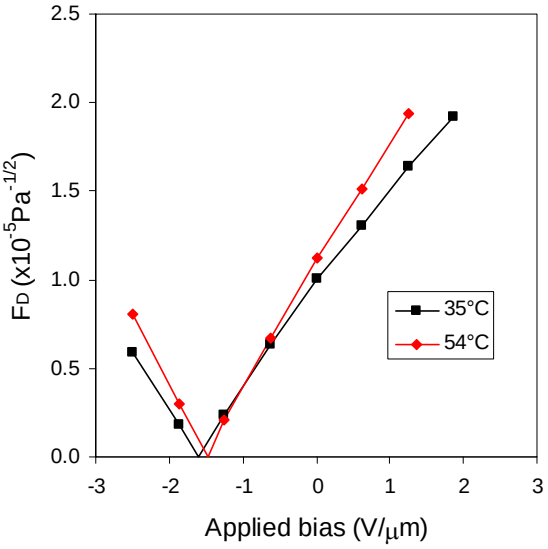

Figure 6.22: Materials merit figure of sample E (850°C RTP, 30s).

6.4 Discussion: 450°C Deposited PST

As mentioned in Chapter 5 the structure of ferroelectric mixed oxides is dependent on the deposition temperature, with a progression through the amorphous, pyrochlore and perovskite phases as the temperature is increased. Due to a lack of a comprehensive phase diagram for PST it was not known what the form of PST deposited at 450°C would be, although it was thought that a pyrochlore phase was likely since deposition at 525°C is on the border between pyrochlore and perovskite, with excess lead being required for perovskite [4, 5, 96]. In the event the PST was pyrochlore but of a form not previously reported and distinctly different from that reported in Chapter 5 for 300°C single magnetron deposition. The starting material was roughly stoichiometric in scandium and tantalum with a slight lead excess (~10-15%) which was intended to compensate for lead loss during annealing and promote perovskite formation [103]. Optically the film had a slightly crazed surface, in contrast to the to the largely featureless surface of the 300°C deposited material reported in Chapter 5. The PST microstructure consisted of a densely packed arrangement of columnar pyrochlore grains, of ~100nm diameter, with a (222) texture, although the apparent absence of superlattice reflections suggests that the structure is defect fluorite [12].

In order to investigate whether this starting material could be transformed into the required perovskite the technique of RTP annealing in an oxygen ambient was used, drawing upon

the experience gained from the results reported in Chapter 5. Annealing at different temperatures resulted in samples with different physical and crystallographic structures. A 650°C RTP anneal in oxygen resulted in only partial conversion of the as-deposited pyrochlore to perovskite. Although encouraging this ruled out the use of this material in a fully integrated device structure. We should recall that the results of Chapter 4 showed that the ROIC was not capable of withstanding this temperature regime, with 600°C for 30s being the practical limit. Optically the appearance of this film was comparable to that of the similarly annealed material reported in Chapter 5, with a granular bi-coloured appearance. The explanation put forward for this is, again, that the regions of different colour are areas of either predominantly pyrochlore or perovskite phase with the colour difference being due to small refractive index variation between the two phases. TEM cross-sectional analysis supports this explanation since the microstructure of the part converted film consisted of large perovskite grains, growing up from the PST/platinum interface, separated by regions of the as-deposited pyrochlore. The size of the perovskite grains and their separation suggests that, as for the single magnetron deposited material, there is a low nucleation density of the perovskite on the platinum. XRD showed that the PST perovskite rocking curve fwhm (~2°) was very close to that of the underlying platinum (~1.9°), a common trait in all of the annealed samples, indicating that the platinum had a strong influence on the growth of the PST. Upon RTP annealing at 650°C for 30s in O_2 (sample B) this PST pyrochlore was able to be converted to perovskite, with a small amount of lead being lost but there still being an excess of ~9%. The PST perovskite formed was (222) textured with rocking curve fwhm of ~2° which corresponded closely to the underlying platinum.

Higher temperature RTP annealing in oxygen at 750°C and 850°C, both for 30 seconds, resulted in virtually complete conversion of the starting material to perovskite with the same (222) texture as found in the 650°C annealed material. In contrast to the 650°C anneal, (111) superlattice peaks were evident which indicates occurrence of ordering of the scandium and tantalum cations on the perovskite B-sites. The intensity of this reflection was around six times higher in the 850°C annealed material than the 750°C, indicating a greater degree of ordering. The PST film was composed of large interlocking grains of the order of a few microns across, with surface pitting due to voiding observed in the 850°C annealed sample. As discussed in Chapter 5 these voids are primarily due to the volume change (~9%) on conversion from pyrochlore to perovskite, with additional shrinkage caused by loss of some of the excess lead. In these films, as for those discussed in Chapter

5, the volume reduction is taken up by voiding, rather than a significant thickness change of the PST layer – confirmed by film thickness measurements before and after annealing.

Electrical properties were measured to assess the suitability of the annealed PST for incorporation into uncooled IR detectors. Detailed results were presented for the highest anneal temperature – 850°C RTP, this sample giving the best performance. The 650°C RTP for 30s was insufficient to fully convert the as-deposited pyrochlore PST to perovskite, resulting in a low permittivity film with high loss which would be unsuitable for detector fabrication. Dielectric properties of the 850°C annealed material were good with high maximum ε_r (ε_r^{max}) of 3346±194 (120Hz) at 35°C (T_{max}) which was relatively sharply peaked. This compares with a value of ε_r = 2277±155 (120Hz) at 25°C for the similarly annealed single magnetron 300°C deposited film reported in Chapter 5 but is still much lower than for PST bulk ceramic[6] (ε_r~9000). Use was made of the Smolenski quadratic model [21, 106], discussed in Chapter 2, for classifying the nature of the ε_r (versus T) peak and indicating its sharpness via the diffuseness parameter δ. The sharpness of the peak is important since in dielectric bolometer mode operation the induced pyroelectric coefficient is proportional to $\partial\varepsilon_r/\partial T$. Although the plots of ε_r and tanδ versus temperature showed only slight dispersion with frequency the curves were still diffuse compared with those for bulk ceramic PST, a plot of $\varepsilon_r^{max}/\varepsilon_r$ versus $(T-T_{max})^2$ (see Appendix A3) yielded a good straight line – indicating relaxor behaviour. The resulting δ value of 54 was high compared with bulk ceramic (δ=11) and PST on sapphire (δ=34) but lower (indicating a sharper peak) than the best value reported in Chapter 5 of δ=78 for the 850°C RTP annealed material. The sharpening and increased magnitude of the permittivity peak and reduced dispersion with frequency are a consequence of the onset of ordering in the material, as found by Setter and Cross for PST bulk ceramic[13]. At zero applied bias the film had a very high pyroelectric coefficient of 582±28μC/m^{2}K which is symptomatic of the action of an internal bias field [45], as was observed for the annealed PST reported in Chapter 5, and probably due to some extent the persistence of the ferroelectric state to temperatures in excess of the dielectric maximum. The internal bias field hypothesis is reinforced by the fact that both ε_r and tanδ peaked at negative applied fields of ~ -1.5 to –2V/μm. In terms of breakdown strength this PST was poor with maximum sustainable applied fields of 1.9V/μm and 1.3V/μm at 35°C and 54°C respectively. Despite this the performance was good (for low applied fields) with maximum pyroelectric coefficients of 916±44μC/m^{2}K (35°C, 1.9V/μm) and

840±40μC/m^{2}K (54°C, 1.3V/μm) and is due to a combination of high zero field pyroelectric response and the sharpness of the permittivity peak (high $\partial\varepsilon_r/\partial T$). In conjunction with suppression of ε_r (not so much of tanδ) this yielded F_D values of $1.9\pm0.2\times10^{-5}Pa^{-1/2}$ (1.9V/μm) and $1.9\pm0.2\times10^{-5}Pa^{-1/2}$ (1.3V/μm) at 35°C and 54°C respectively – very good values for such low bias voltages but with performance limited by low breakdown strength.

The reported work has shown that PST deposited at 450°C can be successfully converted to perovskite by RTP annealing in oxygen. Electrical properties were symptomatic of a relaxor ferroelectric although the onset of ordering resulted in a sharpening of the dielectric properties. As discussed in Chapter 5 the route to high performance in relaxor PST is directly linked to the ability to apply a high bias field in order to suppress ε_r and tanδ which in conjunction with moderate pyroelectric coefficients (relative to PST bulk ceramics[6], p~6mC/m^{2}K) can yield reasonable F_D values (relative to PST bulk ceramic[6], $F_D\sim16\times10^{-5}Pa^{-1/2}$ at 5V/μm). In the material reported, low breakdown strength limited the performance which was comparable with that obtained from PZT ($F_D\sim2\times10^{-5}Pa^{-1/2}$ [109]) and PST deposited directly into the perovskite phase at 525°C ($F_D\sim2\times10^{-5}Pa^{-1/2}$ [5]). Other samples from the similar starting material, not reported here, have on annealing shown poor breakdown strength – for as yet undetermined reasons. This indicates that PST deposited at 450°C into a well formed polycrystalline pyrochlore phase may not be a good starting point for perovskite formation by annealing.

6.5 Results: 300°C Deposited PST

6.5.1 Materials Characterisation of 300°C Deposited PST

6.5.1.1 Compositional Analysis by Energy Dispersive Spectroscopy

As for the 450°C deposited PST thin films the composition of those deposited at 300°C was determined using EDS. Analysis conditions used were the same as for the 450°C films i.e. a 15KeV accelerating voltage and single element standards. The composition of the samples, expressed as a ratio to scandium, is given in Table 6.7, with the Ta/Sc and Pb/Sc ratios being subject to an experimental error of ±3%.

As can be seen from the table, the as-deposited samples are close in composition. Of the annealed series those pieces taken from the wafer PST285 were on average slightly

deficient in tantalum, and with a lead excess of ~9% while the PST315 and PST316 pieces were on the slightly excess tantalum side of stoichiometric, with a lead excess of between ~ 4-10%. All of the annealed samples have lost lead to some extent. Lead loss is more severe in the oven annealed samples (H, I and J) with the lead ratio being below stoichiometry in the two higher temperature oven annealed samples, i.e. I (750°C, 1 hour) and J (800°C, 1 hour). Care must be taken in interpreting these results since, as discussed in Chapter 3, the PST is not sampled uniformly with depth by the EDS method. The 'pear' type shape of the X-Ray generation volume means that for the analysis conditions used (15KeV SEM acceleration voltage) a lower effective weighting is applied to the PST towards the surface than to that in the body of the thin film. The importance of this will become clear in section 6.3.3.4 dealing with TEM analysis where EDS revealed severe lead loss from the surface of the oven annealed films. Sample K (combined RTP/Oven annealed) and sample L (RTP annealed) have not lost lead to the extent of the straight oven annealed samples, with neither showing a lead deficiency wrt the B-site components.

To within experimental error the high temperature RTP annealed samples have the same composition before and after annealing.

Sample	Sc:Ta:Pb As-deposited	Sc:Ta:Pb After annealing
F	1:1.04:2.35	–
G	1:0.91:2.17	–
H	–	1:0.94:1.94
I	–	1:0.93:1.76
J	–	1:0.89:1.68
K	–	1:0.92:1.93
L	–	1:0.95:2.15
M	1:1.00:2.19	–
N	1:1.06:2.21	1:1.07:2.13
O	1:1.02:2.07	1:0.95:1.95

Table 6.7: EDS compositional analysis results of 300°C Deposited PST.

6.5.1.2 Optical and Scanning Electron Microscope Analysis

As for the 450°C deposited PST, optical and SEM microscopy was used to investigate the surface morphology of PST deposited at the lower temperature of 300°C. Figures 6.23 and

6.24 below show optical and SEM pictures of sample M (as-deposited). The optical picture reveals a featureless surface apart from occasional dark spots, shown by EDS analysis to be similar in composition to the surrounding PST, suggesting that they are regions of enhanced growth caused either by defects on the substrate or particulates generated in the sputtering process. The SEM picture shows a gently undulating surface with no particular structure.

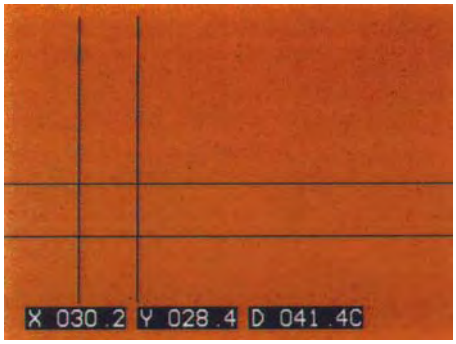

Figure 6.23: Optical picture of sample M (as-deposited). (*Original in colour*)

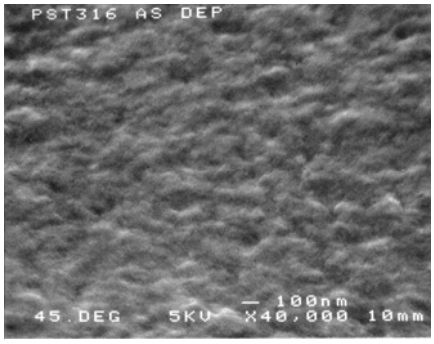

Figure 6.24: SEM picture of sample M (as-deposited).

Figures 6.25 to 6.34 below show optical and SEM pictures of the surfaces of the oven-only annealed samples. Optically the samples are similar with irregular crazy-paving of feature size ~4-8μm. Additionally the optical picture of sample J (Oven, 800°C) shows one of the large cracks, ~3μm wide, which were observed on all of the oven-only annealed samples but not on combined RTP/oven and RTP-only annealed material – as seen in Chapter 5. By SEM the surface morphology is similar with large rosettes of perovskite PST surrounded by pyrochlore PST (shown by TEM later).

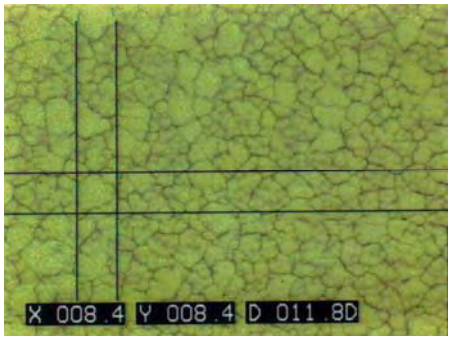

Figure 6.25: Optical picture of sample H (Oven, 700°C). (*Original in colour*)

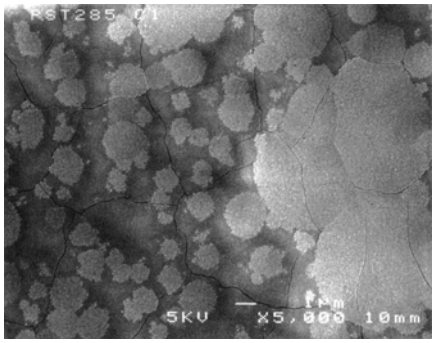

Figure 6.26: SEM picture of sample H (Oven, 700°C).

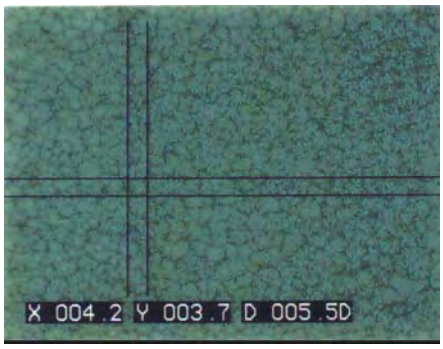

Figure 6.27: Optical picture of sample I (Oven, 750°C). (*Original in colour*)

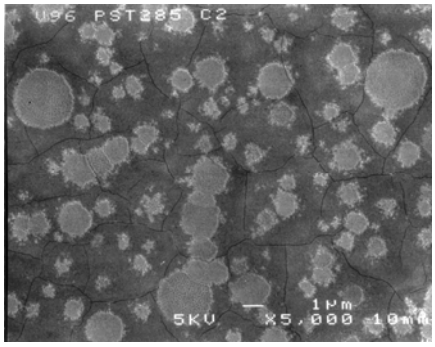

Figure 6.28: SEM picture of sample I (Oven, 750°C).

Figure 6.29: Optical picture of sample J (Oven, 800°C). (*Original in colour*)

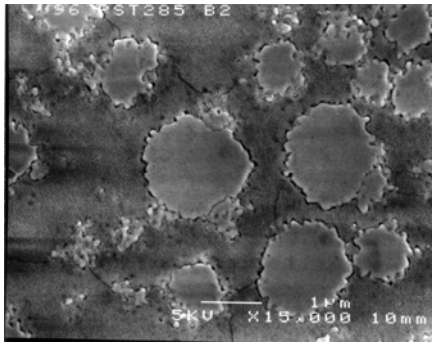

Figure 6.30: SEM picture of sample J (Oven, 800°C).

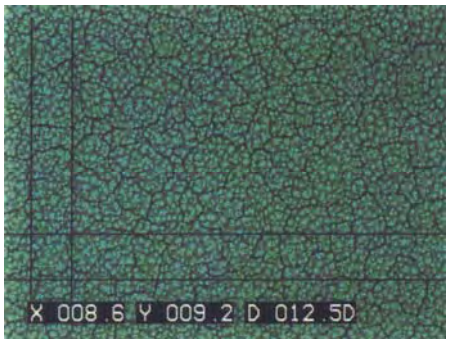

Figure 6.31: Optical picture of sample K (700°C RTP/800°C oven). (*Original in colour*)

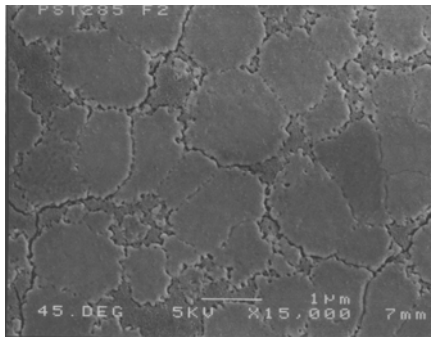

Figure 6.32: SEM picture of sample K (700°C RTP/800°C oven).

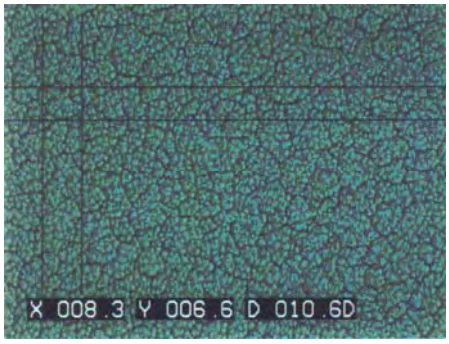

Figure 6.33: Optical picture of sample L (700°C RTP, 600s). (*Original in colour*)

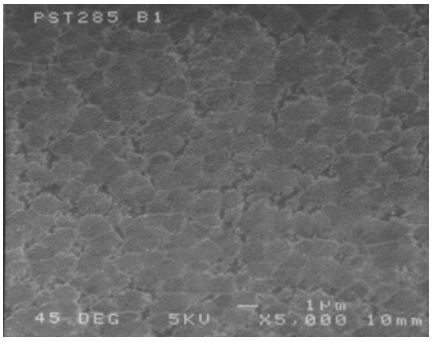

Figure 6.34: SEM picture of sample L (700°C RTP, 600s).

Optically samples L (700°C RTP) and K (700°C RTP/800°C oven) look similar with small grain like features ring fenced by larger scale crazy-paving with a feature size of ~8µm. The SEM picture reveals differences, with sample L having a continuous surface with a mosaic pattern of feature size ~1-2µm. Edges of the individual 'tiles' making up the mosaic are brighter indicating charging due these regions being relatively more insulating. Sample K's SEM picture on the other hand reveals a mosaic with similar feature size but with distinct boundaries between the 'tiles'. A possible interpretation of this is that the tiles of the mosaic are individual perovskite grains and that upon conversion from the as-deposited state, by RTP, excess lead is left at the grain boundaries forming a PbO rich layer. Upon oven annealing after RTP (sample K) this PbO either evaporates or diffuses through the platinum underlayer leaving distinct grain boundaries, in contrast to the RTP-only case. This view is corroborated by the EDS evidence which shows that sample K is roughly stoichiometric, having lost lead compared to the as-deposited material, whereas oven annealing only at 800°C resulted in lead deficiency (sample J) – showing that RTP has "locked-in" the lead required for perovskite PST.

Pictures of the high temperature RTP annealed material are shown in Figures 6.35 to 6.38 below. Optically sample N (850°C RTP, 30s) exhibits a 'standard' crazy paving pattern of feature size ~6µm while the SEM picture reveals a pattern of interlocking perovskite grains (shown by XRD in the next section) with variable sizes between ~1-3µm. Small pits on the surface are interpreted as voids in the PST which are remnants of the volume change upon conversion to perovskite which were also observed in similarly annealed material discussed in Chapter 5. Figure 6.37 shows an optical picture of sample O (850°C RTP, 120s). A

crazy paving pattern is visible but unlike sample N some 'slabs' are relatively featureless whereas others are heavily mottled. The SEM picture, Figure 6.38, shows variable sized interlocking grains with pitting of the surface in a similar manner to sample N.

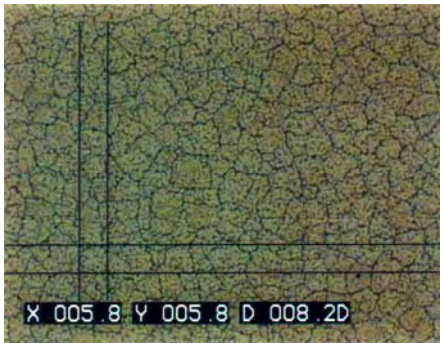

Figure 6.35: Optical picture of sample N (850°C RTP, 30s). (*Original in colour*)

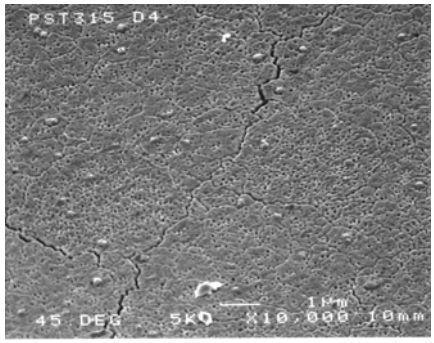

Figure 6.36: SEM picture of sample N (850°C RTP, 30s).

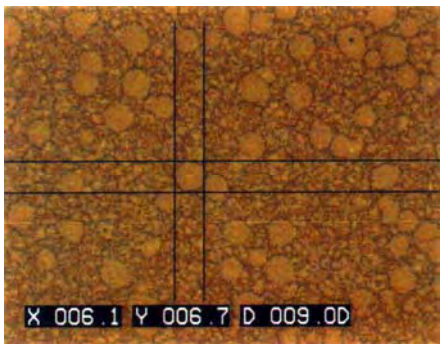

Figure 6.37: Optical picture of sample O (850°C RTP, 120s). (*Original in colour*)

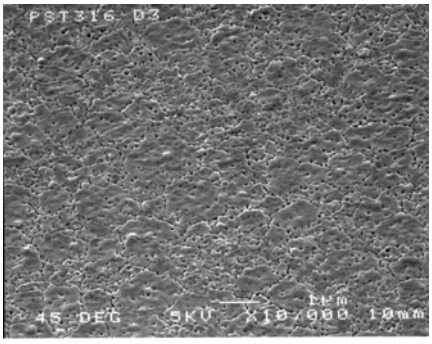

Figure 6.38: SEM picture of sample O (850°C RTP, 120s).

6.5.1.3 X-Ray Diffraction Analysis

XRD θ-2θ scans in Bragg-Brentano geometry were taken for all samples in order to determine the crystalline structure of the PST. As for the 450°C deposited material the θ-2θ data has been normalised to platinum (111) intensity from the appropriate as deposited sample, i.e. samples H to O (PST285 series) were normalised using sample G – the as-deposited PST285 sample etc. Rocking curves were similarly normalised using the integrated intensity of the platinum (111) reflection rocking curve.

Figure 6.39 below shows the θ-2θ scan for sample G, as-deposited at 300°C. The underlying platinum was (111) textured while the PST exhibited only pyrochlore phase

reflections [62] with (222) as the dominant reflection although the intensity is relatively weak in comparison with that observed in the 450°C deposited material discussed earlier in this chapter. The presence of the (311) superlattice reflection indicates that the structure is of a true pyrochlore, as opposed to a defect fluorite pyrochlore [12], and possibly due to the slight tantalum deficiency in this series of samples. No perovskite reflections are observed.

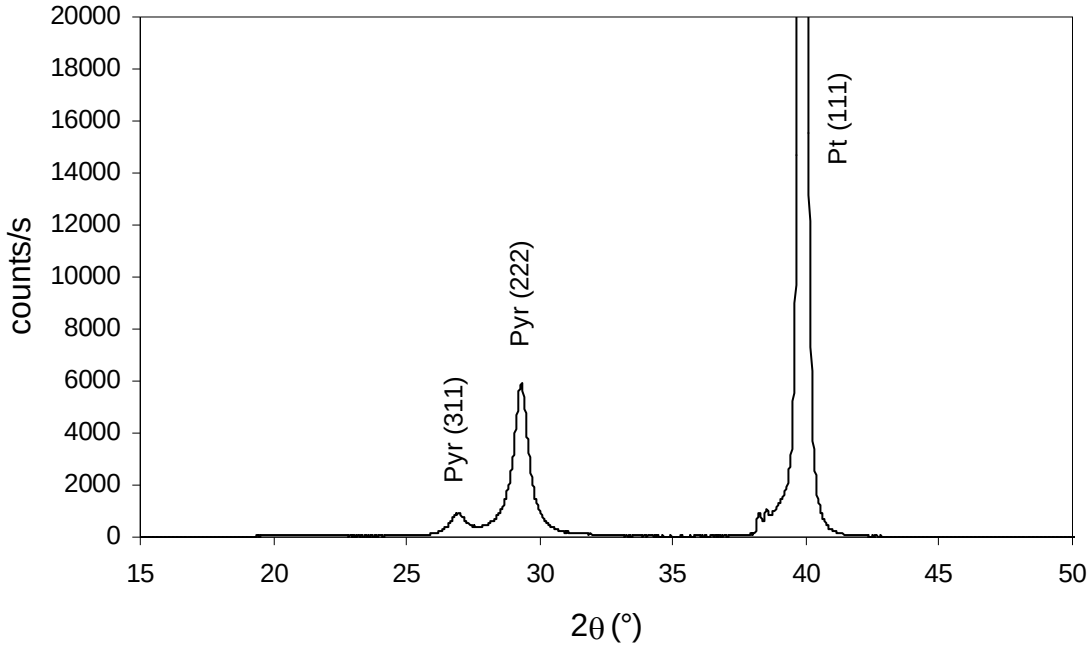

Figure 6.39: θ-2θ scan for sample G (as-deposited). *Pyr* denotes pyrochlore.

θ-2θ scans for the oven annealed samples are shown in Figure 6.40 with all samples showing evidence of conversion to perovskite with (222) as the dominant orientation and low intensity (200), (220) and (400) reflections also present. The perovskite (222) reflection peak intensity is 18633 counts/s, 20050 counts/s and 22967 counts/s for samples H (700°C), I (750°C) and J (800°C). The higher temperature annealed samples, I and J, also exhibit a perovskite (111) superlattice peak indicating a degree of ordering of the B-site cations. All such oven annealed samples had residual pyrochlore reflections indicating incomplete conversion of the PST to perovskite, even at 800°C.

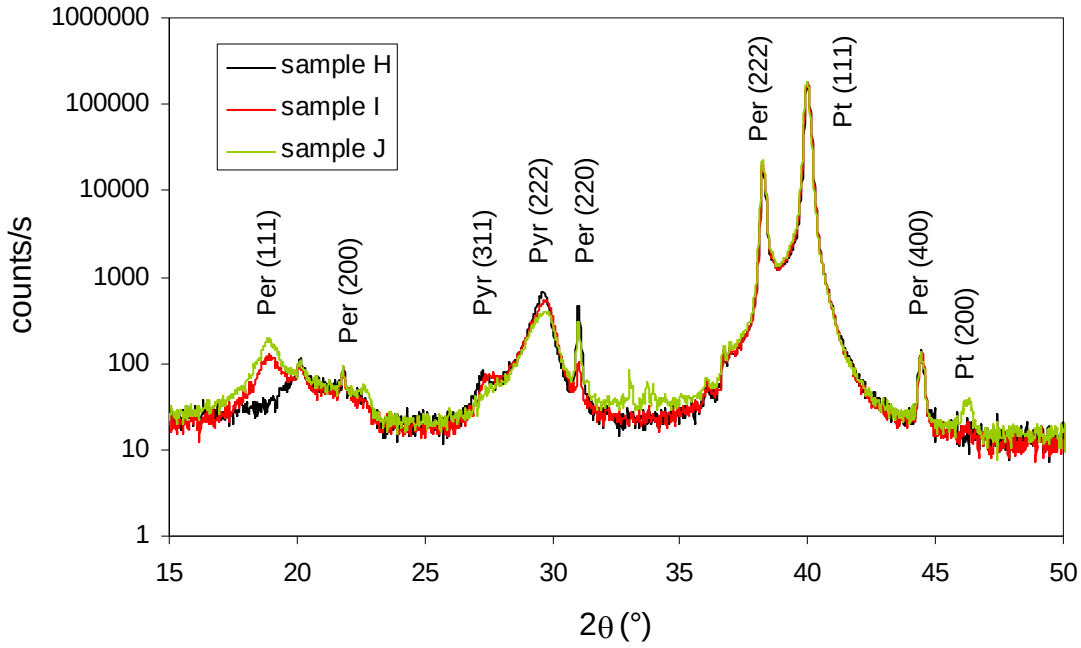

Figure 6.40: θ-2θ scans for samples H (Oven 700°C, 1hr), I (Oven 750°C, 1hr) and J (Oven 800°C, 1hr). *Pyr* denotes pyrochlore, *Per* denotes perovskite. (*Original in colour*)

Figure 6.41 shows the θ-2θ scans for samples K and L. Sample K was given a combined RTP/oven anneal with a 700°C/5 min RTP step followed by an 800°C/1 hour oven step whilst sample L was given the RTP step only. Both show evidence of conversion to perovskite with (222) being the dominant orientation with low intensity (200), (220) and (400) reflections. The intensity of the perovskite (222) peak is similar for samples K and L but only sample K exhibits a perovskite (111) superlattice peak. Residual pyrochlore is present in both samples as shown by the presence of the (222) reflection. In Figure 6.41 the θ-2θ scan for sample H exhibits a low intensity reflection at 2θ~20°. This reflection has been observed on a number of other samples and is thought to result from crystalline titanium oxide (TiO – JCPDS file 23-1078), formed by oxidation of the titanium adhesion layer underlying the platinum. Evidence from TEM of similar samples (not presented here) adds weight to this supposition. Table 6.8 summarises information from the rocking curve analysis. An integrated intensity ratio has been used to give an indication of the perovskite to pyrochlore ratio using the pyrochlore (222) and perovskite (222) reflection rocking curve integrated intensities, designated I_{pyr} and I_{per} respectively. This ratio is then defined as $I_{per}/(I_{pyr}+I_{per})$.

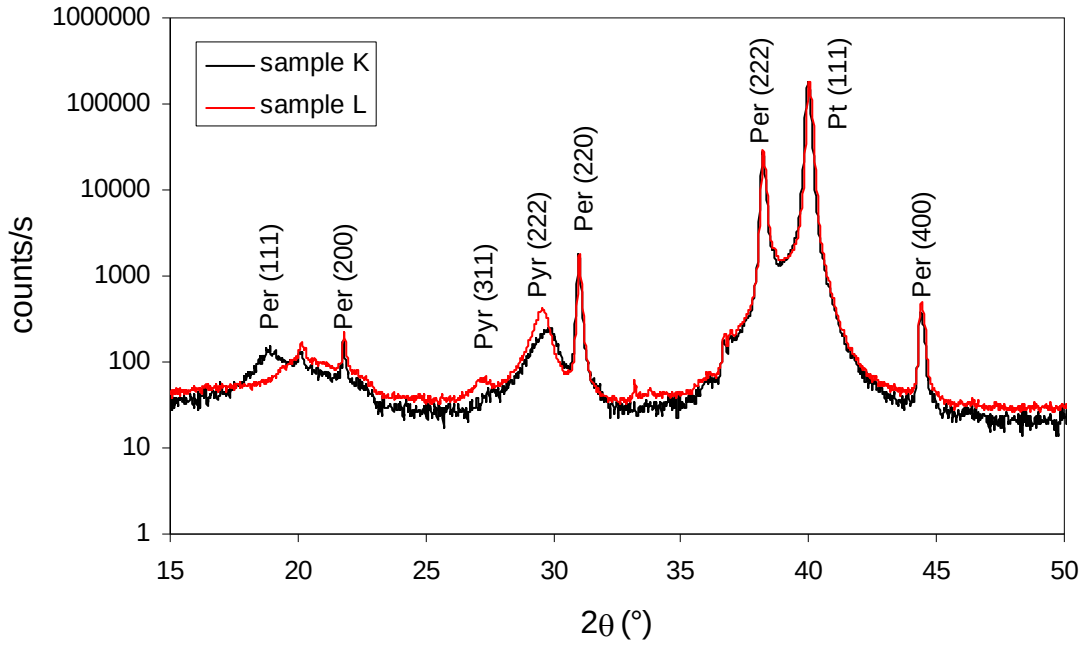

Figure 6.41: θ-2θ scans for samples K (RTP 700°C 600s/Oven 800°C 1hr) and L (RTP 700°C 600s). *Per* denotes perovskite, *Pyr* denotes pyrochlore. (*Original in colour*)

Sample	Anneal	Reflection	Fwhm (°)	Integrated Intensity (counts°/s)	$I_{per}/(I_{per}+I_{pyr})$ (%)
G	–	Pt (111)	1.7	351653	0
		Per (222)	–	0	
		Pyr (222)	12.5	78977	
H	Oven 700°C	Per (222)	2.2	57860	86
		Pyr (222)	10.8	9221	
I	Oven 750°C	Per (222)	2.0	62413	87
		Pyr (222)	11.0	8921	
J	Oven 800°C	Per (222)	2.0	64988	93
		Pyr (222)	10.8	5063	
K	RTP(700°C) +Oven (800°C)	Per (222)	2.6	59244	98
		Pyr (222)	10.7	1340	
L	RTP 700°C	Per (222)	2.5	60545	94
		Pyr (222)	10.4	3794	

Table 6.8: Summary of rocking curve data for samples G to L. Pt, Per and Pyr refer to platinum, pyrochlore and perovskite respectively. I_{per} and I_{pyr} refer to the integrated intensity of the pyrochlore (222) and perovskite (222) reflections respectively.

Figure 6.42 below shows the θ-2θ scan for sample M (as-deposited). The underlying platinum is (111) textured and the PST shows few reflections, with a very weak peak in the region of the pyrochlore (222) reflection – suggesting a very weak pyrochlore/amorphous

phase. Figure 6.43 shows the θ-2θ scans for samples N (850°C RTP, 30s) and O (850°C RTP, 120s). Both samples show strong PST perovskite reflections with no significant pyrochlore reflections. Unusually, among the samples reported in this thesis (as well as others which are not) the perovskite is not (222) textured but is multi-orientated with (400) being dominant. Sample O, given the longer anneal, exhibits a perovskite (111) superlattice peak indicating a degree of B-site ordering of the scandium and tantalum cations. The reason for the multi-orientation of the perovskite, in contrast to other reported samples, is not known. For sample O for example, there is nothing untoward in the rocking curves with the platinum (111) reflection fwhm being 1.2° and the perovskite (222) reflection fwhm being 1.7°. It has been found in the past that multi-orientated platinum, due to deposition problems or deposition onto a relatively rough surface, can induce multi-orientation in the overlying PST but this is not the cause in this case.

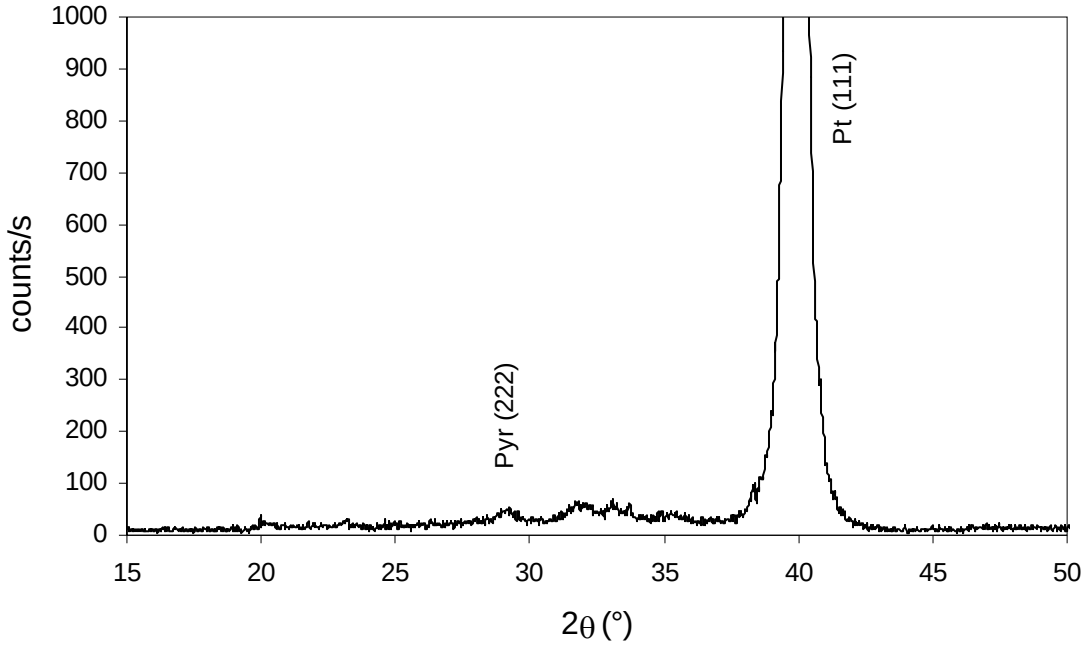

Figure 6.42: θ-2θ scan for sample M (as-deposited). *Pyr* denotes pyrochlore.

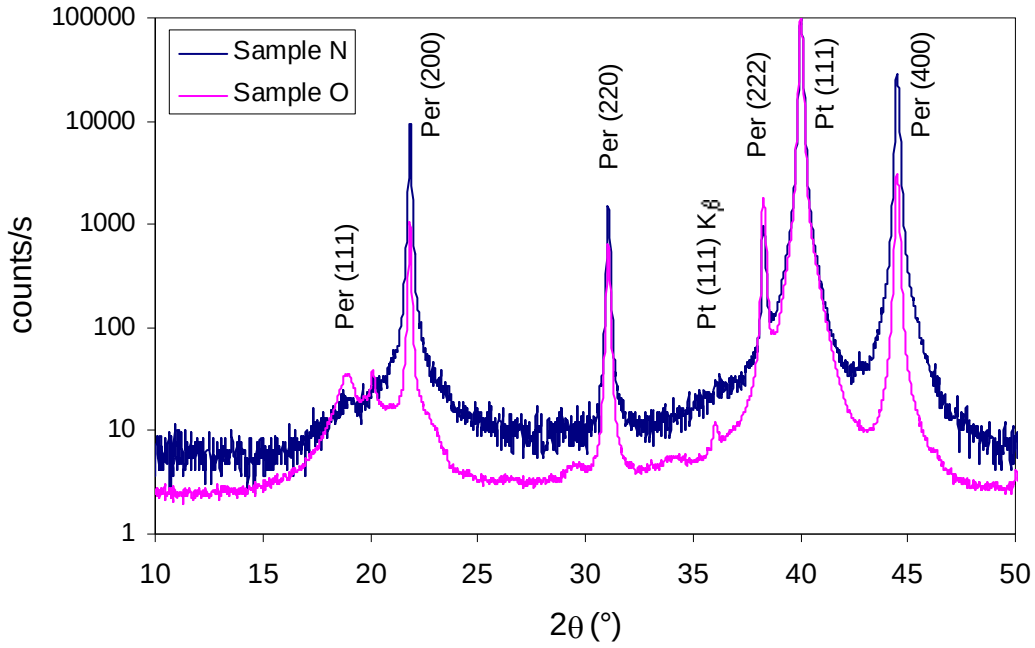

Figure 6.43: θ-2θ scans for samples N (850°C RTP, 30s) and O (850°C RTP, 120s). *Pyr* and *Per* denote pyrochlore and perovskite respectively.
(*Original in colour*)

6.5.1.4 Transmission Electron Microscopy

Cross-sectional and plan-view TEM analysis was carried out with sample preparation being via the conventional route (detailed in Chapter 3), as opposed to the FIB sample preparation method. TEM analysis and sample preparation was carried out by Dr. Z. Huang of Cranfield University.

Figure 6.44 shows a cross-sectional TEM picture of sample F, as-deposited. The PST is seen to have a filamentous structure on a fine scale with filaments ~10nm in diameter extending up through the film, this being very similar to the 300°C single RF magnetron deposited PST discussed in Chapter 5. Small area electron diffraction analysis (SAED) within a filament showed it to be composed of nanocrystalline pyrochlore grains rather than the filament itself being a single pyrochlore grain. PST deposited at 300°C therefore differs significantly in microstructure from that deposited at 450°C which was seen to be composed of a very well formed pyrochlore with a columnar grain structure. This shows that at 300°C the single RF magnetron and dual RF magnetron deposition methods, the latter using the novel ‘dwell time method’, produce PST with the same apparent microstructure.

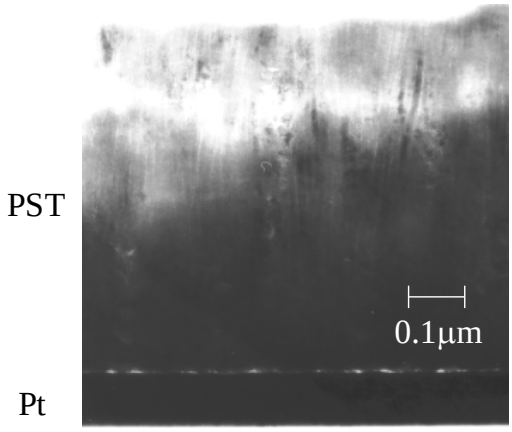

Figure 6.44: Cross-sectional TEM of sample F (as-deposited).

A TEM cross-section of sample I, oven annealed at 750°C for 1 hour, is shown in Figure 6.45 and is typical of the oven annealed samples with the PST being composed of two regions, identified by SAED. The lower region is perovskite, which has grown up from the PST/platinum interface, whilst the upper region contained regions of pyrochlore, shown bordered by the red lines. There are also inclusions in the silicon dioxide layer underneath the titanium-platinum layers which was identified by EDS analysis to be composed of lead and silicon. The slow heating rate in the oven has allowed lead to be lost from the as-deposited weak pyrochlore/amorphous PST prior to the transformation to perovskite. At least some of this lead has then diffused down through the platinum, probably between the grain boundaries, and reacted with the underlying SiO_2 to form a lead-silicon compound.

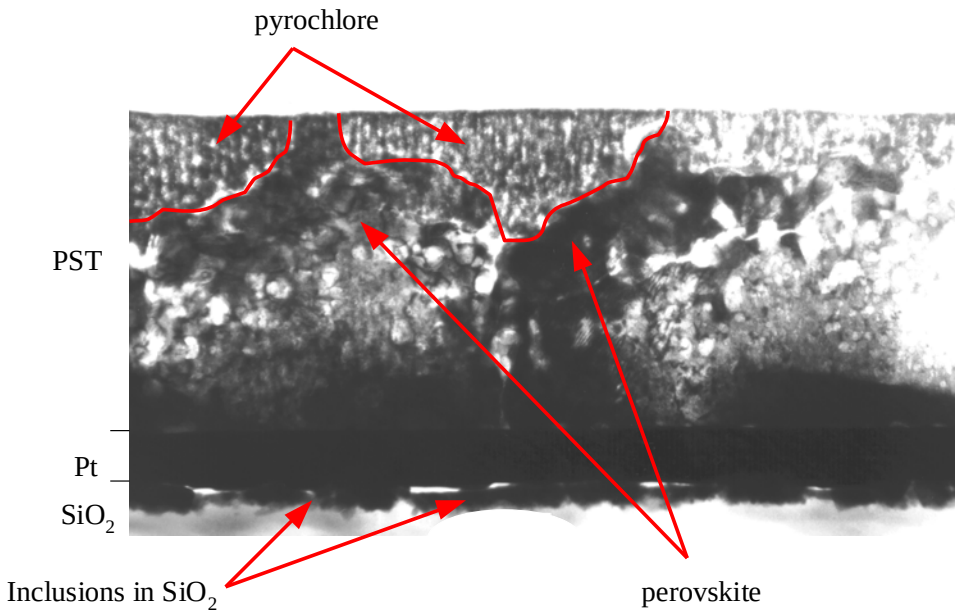

Figure 6.45: Cross-sectional TEM of sample I showing perovskite in the lower half of the film and pyrochlore (bounded by red) in the upper part.
(*Original in colour*)

Figure 6.46 shows a plan view TEM picture of sample I. The surface is characterised by rosette structures which can also be observed in SEM pictures for both this and the other oven annealed samples, see section 6.3.3.2. Also shown in the figure are SAED patterns collected from the regions indicated. Pattern (a) is taken from the region surrounding the rosettes and shows only the ring pattern associated with PST pyrochlore. Pattern (b), taken from a rosette, shows a spot pattern due to perovskite PST. Investigation of the composition of these different regions has revealed that while the scandium and tantalum content is similar the lead content is very different. The perovskite regions are stoichiometric while the regions identified as pyrochlore are deficient in lead by up to 50% from stoichiometric. These results are in general agreement with the EDS results (by SEM) for the oven annealed samples where lead deficiency was observed. This indicates that in oven annealing the slow ramp-up rate, compared to RTP, allows loss of the volatile lead component both down through the underlying platinum/titanium layer, with loss by evaporation from the top surface also being likely. Because of this lead loss the perovskite transformation front progresses up from the platinum interface until it reaches a point where there is no longer enough lead to allow further transformation with the top portions of the film forming into a lead deficient pyrochlore phase.

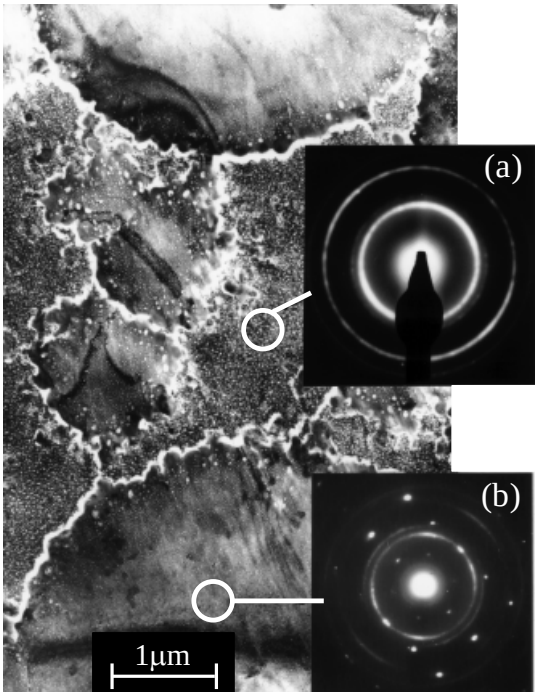

Figure 6.46: Plan view TEM of sample I showing SAED patterns from pyrochlore (a) and perovskite (b) regions.

A cross-sectional TEM picture of the combined RTP/Oven anneal sample is shown in Figure 6.47 below. Only the PST layer is detailed in the picture and can be seen to have voids but these are less numerous than for other samples presented in this thesis. Unlike the oven annealed samples there are no large inclusions of pyrochlore close to the surface with the absence of these presumably a consequence of the RTP method converting the PST quickly and 'locking in' the lead before it can escape from the as-deposited film, either from the top surface by evaporation or from the bottom surface by diffusion through the platinum. Combined RTP/Oven anneal was deliberately carried out to achieve this, in the light of the results from the oven-only annealing.

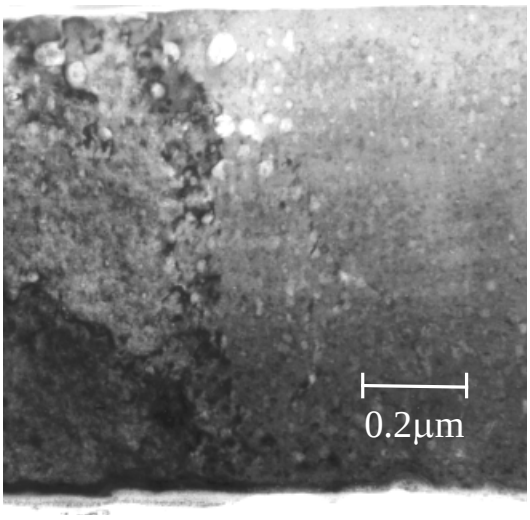

Figure 6.47: Cross-sectional TEM of sample K (RTP 700°C/Oven 800°C) showing PST layer only.

TEM analysis of samples N (850°C RTP, 30s) and O (850°C RTP, 120s) showed PST with a voided structure very similar the 850°C RTP annealed PST reported in Chapter 5, the picture of which the reader is referred to. As for that material the titanium adhesion layer was no longer clearly visible and there were also lead and tantalum rich inclusions in the silicon dioxide layer. As discussed in Chapter 5 the electrode structure is not optimised for high temperature annealing with the result that interdiffusion has taken place by diffusion along the grain boundaries of the columnar grained platinum, in a similar fashion to that observed by Maeder et al for the PZT system [99]. Although no adhesion or electrical problems were encountered it may be wise to consider optimising the electrode structure for high temperature annealing to minimise any potential problems (such as delamination) that may occur during device fabrication – assuming that high temperature anneals are used.

6.5.2 Electrical Characterisation of 300°C Deposited PST

Electrical characterisation of the annealed PST samples comprised dielectric properties and pyroelectric coefficient measurements. Measurement of the dielectric properties (ε_r and $\tan\delta$) with temperature and frequency allowed the nature of the ferroelectricity of the PST thin films to be determined whilst the measurement of the dielectric properties and the pyroelectric coefficient as a function of applied bias field enabled the calculation of a merit figure for IR detection, F_D. For brevity the electrical properties of the oven and low temperature RTP (700°C) samples (H, I, J and L) are presented in tabular form only. Data

for the better performing samples, combined oven-RTP annealing (sample K) and high temperature RTP annealing (samples N and O) are presented in graphical form.

6.5.2.1 Oven and Low Temperature RTP Annealing

The electrical properties of the oven annealed samples (H, I and J) and 700°C RTP annealed sample (L) are summarised in Table 6.9 below. For the oven annealed samples it can be seen that as the annealing temperature is increased, the maximum value of ε_r (zero applied field) increased successively from 362±21 for the 700°C anneal to 1759±102 for the 800°C anneal. The temperature at which this maximum (T_{max}) occurred also increased from –25°C for the 700°C anneal to –10°C for the 800°C anneal.

Samples I (750°C Oven) and J (800°C) showed dispersion of ε_r and tanδ with frequency indicating that the perovskite PST formed was predominantly relaxor in nature. Further evidence of this is given by the good fit of the zero field relative permittivity data to the Smolenski quadratic law for relaxor ferroelectrics, discussed in detail in Chapter 2, with straight line fits of $\varepsilon_r^{max}/\varepsilon_r$ versus $(T-T_{max})^2$, where ε_r^{max} is the maximum value of ε_r occurring at temperature T_{max}, being shown in Appendix A3. Good fits can be made for the data for both samples. Appendix A3 also shows the same plot for the dielectric data for sample H (700°C Oven) and K (700°C RTP). Neither sample exhibited obvious relaxor behaviour in their dielectric properties although ε_r versus temperature for both did exhibit a single broad peak, accounting for the low but non-zero induced pyroelectric coefficients (Table 6.9). A straight line could not be fitted to the data of sample H indicating that the PST is not relaxor, whilst for sample K a reasonable straight line fit was obtained (Appendix A3).

Sample	Anneal	ε_r^{max}	δ	p_{max} ($\mu C/m^2K$)	F_D^{max} ($\times 10^{-5} Pa^{-1/2}$)
H	Oven 700°C	357±21 (-25°C)	–	215±11 (35°C, 10V/μm)	0.9±0.1 (35°C, 10V/μm)
I	Oven 750°C	1020±59 (-15°C)	124	396±20 (35°C, 8V/μm)	1.5±0.1 (35°C, 8V/μm)
J	Oven 800°C	1731±100 (-10°C)	107	339±17 (35°C, 2V/μm)	0.8±0.1 (35°C, 2V/μm)
L	RTP 700°C	284±16 (-15°C)	208	160±8 (35°C, 9.4V/μm)	0.9±0.1 (35°C, 9.4V/μm)

Table 6.9: Summary of electrical properties of oven annealed and low temperature RTP annealed samples. p_{max}, F_D^{max} and ε_r^{max} are the maximum values of the pyroelectric coefficient, materials merit figure and zero field relative permittivity respectively (all 120Hz), while δ is the diffuseness parameter.

6.5.2.2 Combined RTP/Oven Annealing

This section presents the electrical measurements for sample G which was annealed using a combined RTP and oven approach, with a 700°C 5 minute RTP anneal performed prior to a 800°C 1 hour oven anneal. As mentioned previously the purpose of the RTP step was to prevent excessive lead loss prior to the oven anneal. XRD analysis, see section 6.3.3.3, showed the PST to be mainly perovskite with a small pyrochlore trace. Figure 6.48 below shows the zero field dielectric properties as a function of temperature and frequency. The broadness of the peaks in ε_r and tanδ and their shift to higher temperatures with increasing frequency, especially tanδ, show that the PST is behaving as a relaxor ferroelectric[13, 17, 22]. This was anticipated from the XRD measurements, which revealed the presence of only a weak superlattice peak. At 120Hz ε_r peaks at 1803±97 between –15°C and –10°C while tanδ peaks at between –95°C and –90°C. A plot of $\varepsilon_r^{max}/\varepsilon_r$ versus $(T-T_{max})^2$ yielded a good straight line (see Appendix A3), as should be the case for a relaxor material, with a diffuseness parameter value of 107. Figure 6.49 shows the temperature dependence of ε_r and tanδ (at 120Hz) as a function of applied bias field (top electrode positive). Both quantities are suppressed with increasing field although at the higher temperatures and fields there is an upturn in tanδ which is attributed to dc leakage.

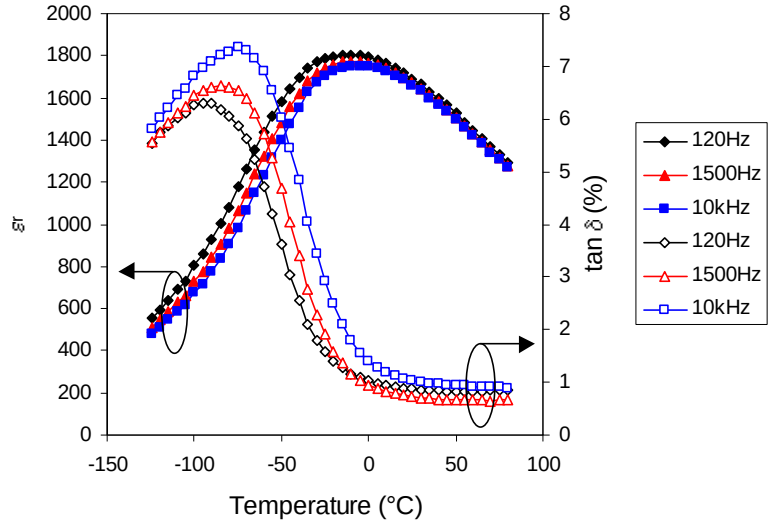

Figure 6.48: Dielectric properties of sample L (RTP/Oven) as a function of temperature and frequency. (*Original in colour*)

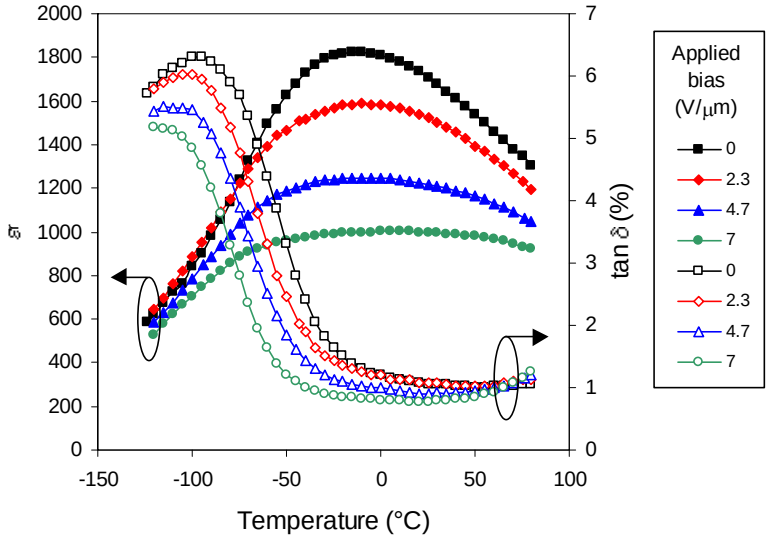

Figure 6.49: Dielectric properties of sample K (RTP/Oven) at 120Hz as a function of temperature and applied bias. (*Original in colour*)

Figures 6.50 shows a plot of ε_r and tanδ versus applied field at temperatures of 37°C and 50°C – temperatures in the likely range of device operation in a thermal imager. Application of positive applied field suppressed ε_r while tanδ rose initially and then depressed at higher fields. It is interesting to note that ε_r peaks at between –0.6V/μm and –1.2V/μm, - suggesting the presence of an internal bias field.

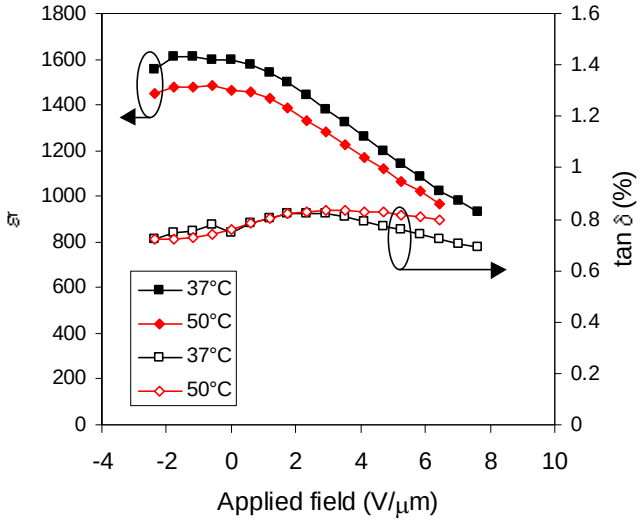

Figure 6.50: Dielectric properties of sample K (RTP/Oven) as a function of applied bias and temperature. (*Original in colour*)

The measured pyroelectric coefficient as function of applied bias at 37°C and 50°C is shown in Figure 6.51. At zero applied field the pyroelectric coefficient is non zero at both temperatures with p = 74±4μC/m^{2}K at 37°C and 81±4μC/m^{2}K at 50°C. Application of a field in a negative sense brought the pyroelectric coefficient to zero at –0.8V/μm (37°C) and –0.6V/μm (50°C) – approximately the same region as the peak in ε_r, suggesting that the applied field has counteracted any internal bias. The maximum pyroelectric coefficients (breakdown limited) were 505±23μC/m^{2}K (7.6V/μm) at 37°C and 480±22μC/m^{2}K (6.5V/μm) at 50°C. Using the data of Figures 6.50 and 6.51, as well as the PST bulk ceramic heat capacity, the materials merit figure, F_D, was calculated for the two measurement temperatures and is shown in Figure 6.52. As with the pyroelectric coefficient the F_D values are virtually unchanged between 37°C and 50°C with values of 2.5±0.3×10^{-5}Pa$^{-1/2}$ at 7.6V/μm (37°C) and 2.2±0.2×10^{-5}Pa$^{-1/2}$ at 6.5V/μm (50°C).

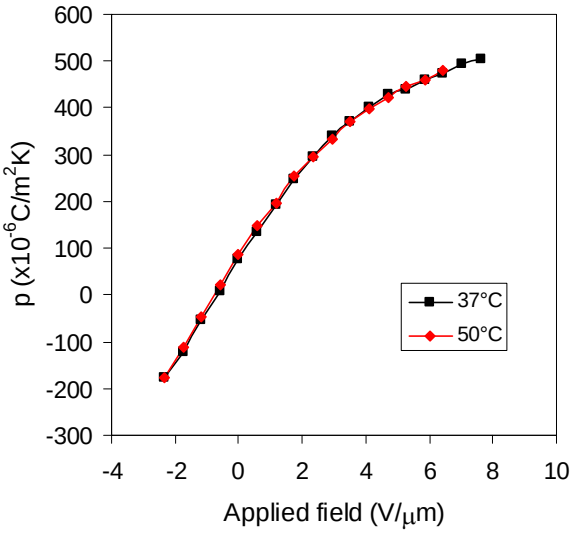

Figure 6.51: Pyroelectric coefficient of sample K (850°C RTP, 30s). (*Original in colour*)

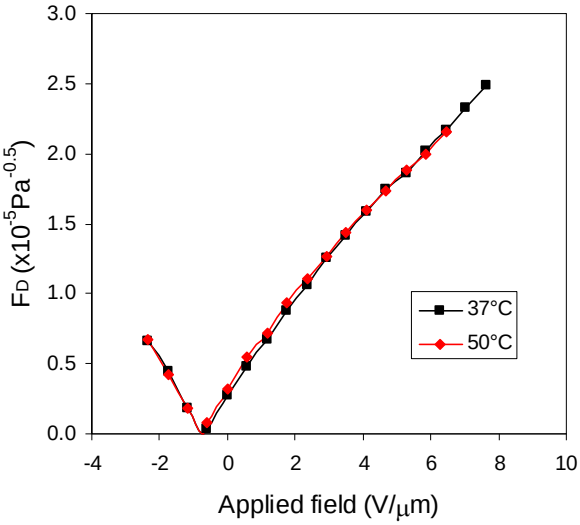

Figure 6.52: Materials merit figure of sample K (850°C RTP, 30s). (*Original in colour*)

6.5.2.3 High Temperature RTP Annealing

Electrical measurements for the high temperature RTP annealed samples – sample N (850°C RTP, 30s) and sample O (850°C RTP, 120s) – are presented in this section. XRD of these samples showed only perovskite reflections with sample O exhibiting a low intensity perovskite (111) superlattice reflection, see section 6.3.3.3 Figure 6.53.

The dielectric properties of sample N as a function of temperature and frequency are shown in Figure 6.54. A broad peak in ε_r is observed with some dispersion with frequency, indicating relaxor behaviour, with a peak value of 2875±239 at 10°C (120Hz). Relaxor behaviour was confirmed by fitting the zero field ε_r data above the dielectric maximum to the Smolenski quadratic model discussed previously in this chapter and in more detail in Chapter 2 and appendix A3. A plot of $\varepsilon_r^{max}/\varepsilon_r$ versus $(T-T_{max})^2$ yielded a good straight line with a diffuseness parameter value of 65. Within the temperature range of the measurement (-80°C to 86°C) no peak in tanδ was observed. Figure 6.54 shows the temperature dependence of ε_r and tanδ (at 120Hz) as a function of applied bias field. Application of a negative voltage results in the highest ε_r value of 3219±241 at 5°C. Increasing the applied bias in the positive sense results in suppression of ε_r and tanδ. As the applied field increases the peak in ε_r shifts to higher temperatures, as expected for a ferroelectric but the first of the

films reported in this thesis to clearly exhibit this effect, with peaks occurring at ~25°C (2.2V/μm) and ~60°C (4.4V/μm).

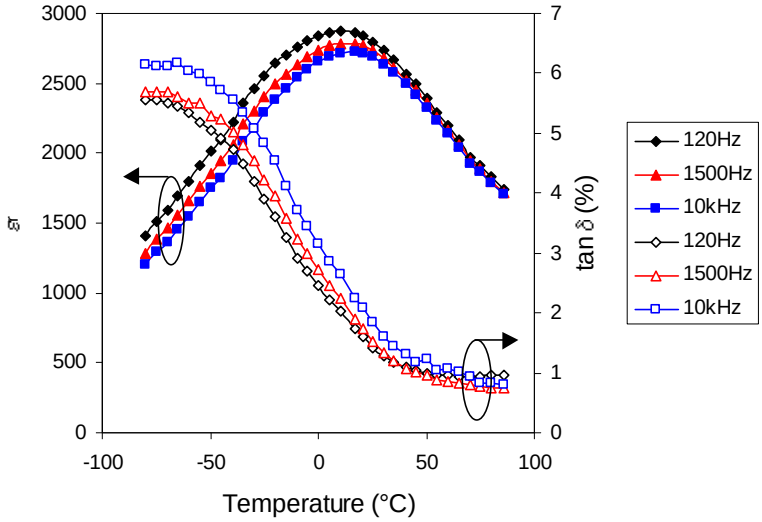

Figure 6.53: Zero applied field dielectric properties of sample N (850°C RTP, 30s) as a function of temperature and frequency.
(*Original in colour*)

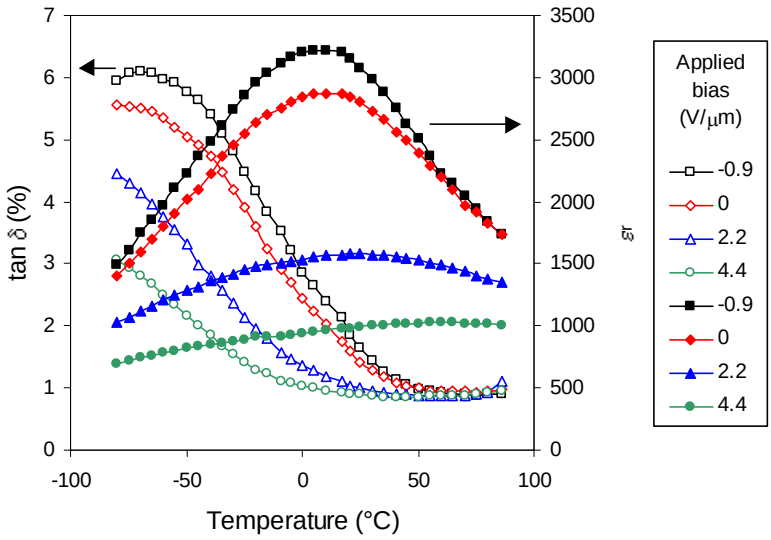

Figure 6.54: Dielectric properties of sample N (850°C RTP, 30s) at 120Hz as a function of temperature and applied bias.
(*Original in colour*)

The variation of ε_r and tanδ for sample N as a function of applied bias field at 35°C and 50°C is shown in Figure 6.55. Both quantities are suppressed markedly with a field applied in the positive sense (bottom electrode earthed) with ε_r suppressed by a factor of four (35°C) between zero applied field and 9.5V/μm and tanδ~0.6% (37°C, 9.5V/μm). As with other PST samples reported in this thesis ε_r and tanδ peak at negative applied fields,

between –0.5V/μm and –1V/μm in this case, which again indicates the presence of an effective internal bias field.

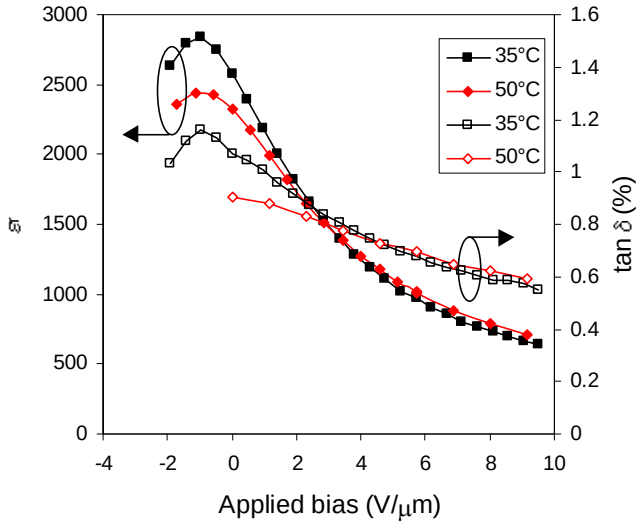

Figure 6.55: Dielectric properties of sample N (850°C RTP, 30s) as a function of applied bias and temperature. (*Original in colour*)

The measured pyroelectric coefficient of sample N as a function of applied bias at 35°C and 50°C is shown in Figure 6.56. At zero applied field the pyroelectric coefficient is non-zero at both temperatures with values of 379±30μC/m^{2}K (35°C) and 271±22μC/m^{2}K (50°C). Application of an applied bias field in a negative sense brought the pyroelectric coefficient to zero at –1V/μm (35°C). As the applied field is increased in the positive sense the pyroelectric coefficient is seen to increase to a maximum value and then decrease again. At 35°C there is a broad maximum of ~790μC/m^{2}K (at ~4.3V/μm) while at 50°C the maximum is ~800μC/m^{2}K (at ~5.7V/μm). This can be understood in terms of the dielectric bolometer effect, described in detail in Chapter 2, where the induced pyroelectric coefficient depends on the integral up to the applied field (E) of $(\partial\varepsilon_r/\partial T)_E$, where T is the sample temperature. Figure 6.54 shows that as the applied field is increased the peak in ε_r shifts to higher temperatures. If the peak in ε_r is below the operating temperature then $(\partial\varepsilon_r/\partial T)_E$ is negative, as is the induced pyroelectric coefficient (Figure 6.56 actually shows a plot of –p). When the applied field is increased such that the peak in ε_r moves above the measurement temperature then $(\partial\varepsilon_r/\partial T)_E$ becomes positive with the integral over applied field of this quantity, and hence the induced pyroelectric coefficient, being reduced. The induced pyroelectric coefficient should then peak at higher applied fields as the sample temperature

is increased, as is seen in Figure 6.56. This point is illustrated very well by Watton in his consideration of the second order ferroelectric Barium Strontium Titanate in bulk ceramic form [39].

Using the measured data of Figures 6.55 and 6.56 the materials merit figure F_D was calculated at both sample temperatures as a function of applied field, Figure 6.57. There can be seen to very little difference in the F_D values at the two temperatures with maximum values obtained of $4.8\pm0.8\times10^{-5}Pa^{-1/2}$ at 35°C (9.5V/μm) and $4.6\pm0.7\times10^{-5}Pa^{-1/2}$ at 50°C (9.1V/μm).

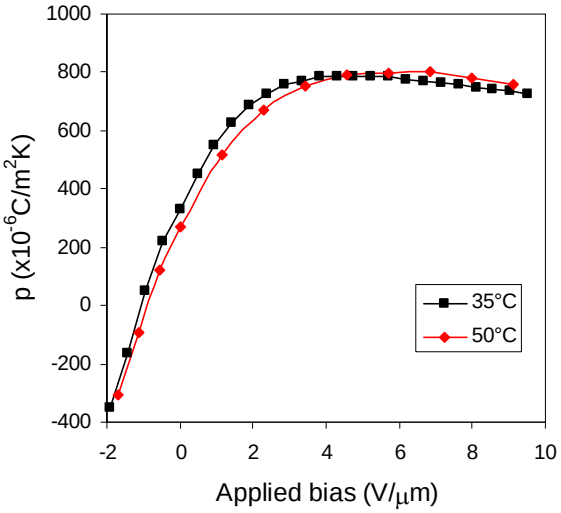

Figure 6.56: Pyroelectric coefficient of sample N (850°C RTP, 30s). (*Original in colour*)

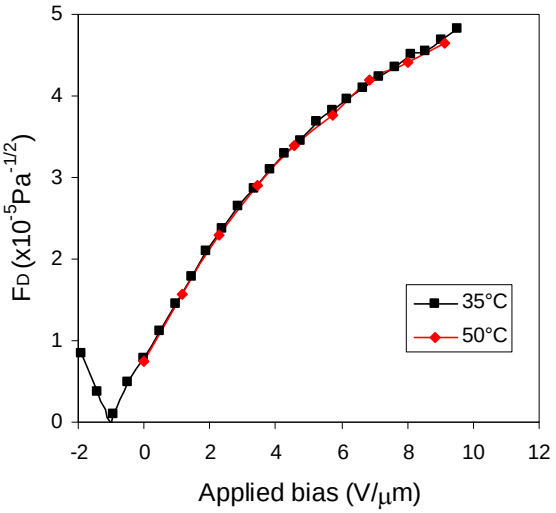

Figure 6.57: Materials merit figure of sample N (850°C RTP, 30s). (*Original in colour*)

The electrical properties of sample O, RTP annealed at 850°C for 120s, were a further improvement on those of sample N. Figure 6.58 shows the zero field dielectric properties as a function of temperature and frequency. The material exhibits some relaxor like-properties, but less clearly than with the other 300°C deposited samples discussed in this chapter, with clear frequency dispersion of the peak in tanδ but only slight dispersion of the peak in ε_r. At 120Hz ε_r peaks at 3625±272 (19.5°C), whilst tanδ peaks at –70°C. A plot of $\varepsilon_r^{max}/\varepsilon_r$ versus $(T-T_{max})^2$ for the zero applied field ε_r data (120Hz) can be found in Appendix A3. A good straight line can only be fitted to the points within 25°C of the dielectric maximum with the data diverging at higher temperatures in a manner similar to high temperature annealed PST on sapphire substrates and PST bulk ceramic. The calculated diffuseness parameter (δ) value of 47 is the lowest reported in this thesis and is a result of

the sharpest zero applied field dielectric peak. This represents a move away from relaxor properties towards the first order ones obtained in ordered PST. Figure 6.59 illustrates the effect of an applied bias field on ε_r and tanδ (both 120Hz). As for sample N both quantities are suppressed as the applied field is increased, with the peak in ε_r shifting to higher temperatures.

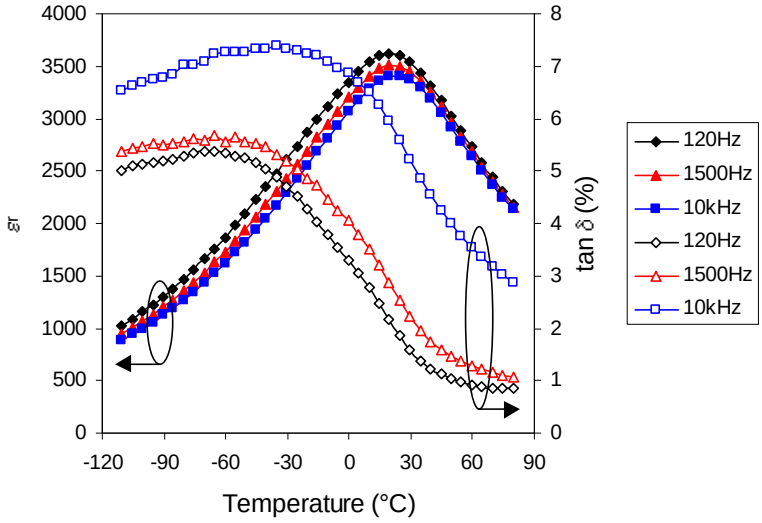

Figure 6.58: Zero applied field dielectric properties of sample O (850°C RTP, 120s) as a function of temperature and frequency.
(*Original in colour*)

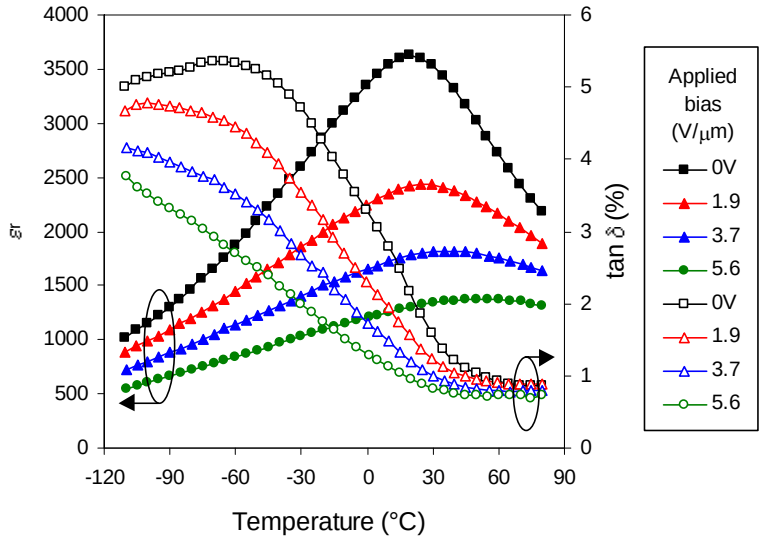

Figure 6.59: Dielectric properties of sample O (850°C RTP, 120s) at 120Hz as a function of temperature and applied bias.
(*Original in colour*)

The behaviour of ε_r and tanδ (both 120Hz) of sample O as a function of applied bias field at 35°C and 49°C is shown in Figure 6.60. Again, as with other samples reported, both

quantities are suppressed with increasing positive applied field with tanδ being 0.52±0.05% (35°C) and 0.49±0.05% (49°C) at 9.3V/μm. Both ε_r and tanδ (120Hz) peaked at negative applied fields of between –0.5V/μm and –0.9V/μm.

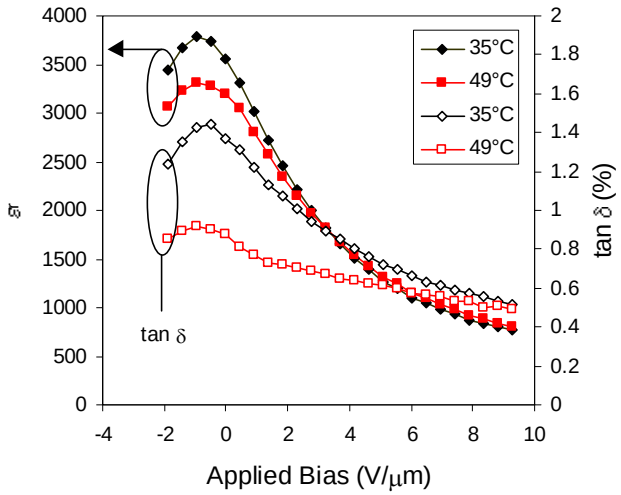

Figure 6.60: Dielectric properties of sample O (850°C RTP, 120s) as a function of applied bias and temperature. (*Original in colour*)

The measured pyroelectric coefficient of sample O at 35°C and 49°C as a function of applied bias field is shown in Figure 6.61. At zero applied bias the pyroelectric coefficient is high at 393±29μC/m^{2}K (35°C) and 357±26μC/m^{2}K (49°C) with a negative applied field of ~0.9V/μm required to bring p to zero. As with sample N, p is seen to increase to a maximum value and then decrease with further increase of the applied field. The values are higher than for sample N, reflecting the sharper peak in ε_r, with peak values of 1002±73μC/m^{2}K at 35°C (4.2V/μm) and 1041±76μC/m^{2}K at 49°C (4.7V/μm). These are the highest reported in this thesis and were anticipated due to the sharp zero applied field dielectric peak. Using the data of Figures 6.60 and 6.61 F_D was calculated as a function of applied field at both measurement temperatures, Figure 6.62, and had peak values at 9.3V/μm of 5.2±0.8×10^{-5}Pa$^{-1/2}$ (35°C) and 5.8±0.9×10^{-5}Pa$^{-1/2}$ (49°C). The 49°C F_D value is the highest known reported value for PST on silicon. It is interesting to note that neither measurement was limited by breakdown of the PST and therefore higher F_D values could possibly be obtained by further increasing the applied field, although there is a law of diminishing returns since ε_r and tanδ are starting to level out at the higher fields while p is reducing.

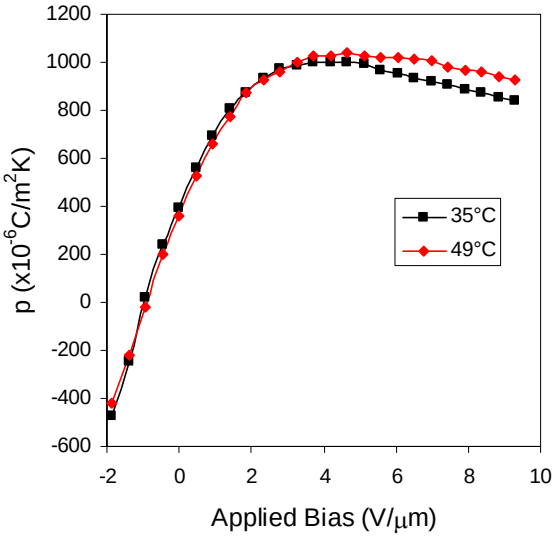

Figure 6.61: Pyroelectric coefficient of sample O (850°C RTP, 120s). (*Original in colour*)

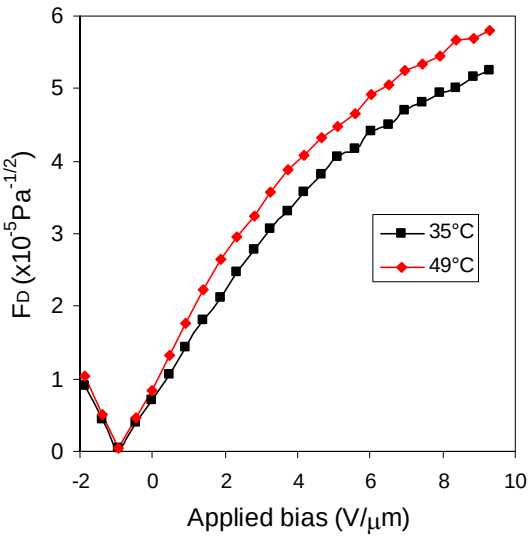

Figure 6.62: Materials merit figure of sample O (850°C RTP, 120s). (*Original in colour*)

6.6 Discussion: 300°C Deposited PST

The 300°C deposited PST described in this chapter is different from that described in Chapter 5 in that a dual magnetron deposition system was used and, additionally, the system was operated using the new 'dwell time' method for controlling the composition. These differences make this deposition-annealing method more suitable for productionisation by allowing more uniform coating of large area (4") substrates and a higher degree of compositional control. Questions about the use of this technique were: Firstly what was the nature of the as-deposited PST, more specifically had the deposition of the constituent atomic species in layers had any effect on the nature of the PST as compared to 300°C deposited PST using the single magnetron technique? Secondly, could this PST be transformed into the required perovskite phase with good physical properties (e.g. no cracking) by using elevated temperature annealing? Lastly, did this annealed material have electrical properties suitable for device operation? To attempt to answer these questions two annealing techniques were tried, RTP and furnace annealing which were used both separately and in conjunction with each other.

The as-deposited starting material for the annealing studies was roughly stoichiometric in scandium and tantalum content. In general there was a lead excess in the as-deposited PST which, as in previously discussed samples, was intended to compensate for lead loss during

annealing and also promote perovskite formation. As-deposited, the PST was shown by XRD to exhibit a very weak pyrochlore reflection and no perovskite reflections. The slightly tantalum deficient material gave slightly stronger pyrochlore reflections which indicated a (222) texture in this phase plus the presence of the (311) superlattice reflection suggesting a true pyrochlore structure[12]. As for the 450°C deposited PST discussed in this chapter the pyrochlore (222) rocking curve was broad with a fwhm ~13° compared with 1.7° for the platinum (111) reflection. This was not unexpected given the large lattice mismatch between the two. The XRD results thus show the material to have a poorly crystallised pyrochlore/amorphous structure. The PST surface was featureless apart from an undulating morphology and was very similar to the 300°C single RF magnetron material reported in Chapter 5. Analysis of the film microstructure showed that the PST had a filamentous structure, with each filament extending up from the platinum/PST interface to the PST surface. Each filament was not a pyrochlore grain, as might be expected, but was composed of a nanocrystalline pyrochlore phase. The conclusion of the analysis of the as-deposited PST is that its structure is very similar to the 300°C deposited material deposited using the single RF magnetron technique. This is good since it indicates that at 300°C, the use of the two target deposition system in the dwell time mode (with the lead, scandium and tantalum components being deposited in discrete layers) produces PST with the same structure as that obtained from the single RF magnetron deposition technique, where the constituent atoms are deposited as an intimate mixture. In addition the use of the lower deposition temperature of 300°C has avoided the formation of the well crystallised pyrochlore phase that was obtained at 450°C.

To investigate whether this starting material could be converted into the required perovskite phase both RTP and oven annealing in an oxygen ambient were carried out. One of the samples was annealed using a combination of RTP and oven annealing. As mentioned briefly previously, combined oven/RTP annealing was performed in response to the problem of lead loss in the oven annealed samples and is discussed in more detail below. The principle difference between the oven and RTP techniques is the heating and cooling rates which are ~50°C/s and ~30°C/s respectively for the RTP and ~7.5°C and ~1°C/min respectively for the oven. Also oven-annealed samples were given longer anneal times to try and increase ordering.

Oven-only annealing at 700°C, 750°C and 800°C for 1 hour in oxygen was successful at partially converting the as-deposited PST to perovskite, as determined by XRD analysis, which was encouraging since it showed that conversion was at least possible. The perovskite that formed had a (222) fibre texture with a narrow rocking curve fwhm of ~2°, matching closely that of the platinum (111) reflection of ~1.7° - suggesting that the perovskite has nucleated on the platinum and had its crystal structure influence by it. At annealing temperatures of 750°C and 800°C low intensity perovskite (111) reflections were recorded, indicating that a degree of B-site cation ordering was attained in the perovskite structure. All of the oven-only annealed samples showed residual pyrochlore reflections in their XRD spectra, with the intensity of these decreasing only slightly with increasing anneal temperature. This point is illustrated in Figure 6.63 where a simple ratio of the perovskite and pyrochlore (222) rocking curve integrated intensities has been used to give an indication of the differences in relative perovskite/pyrochlore content between samples. Compositional analysis revealed that the oven annealed samples had lost lead, with the material annealed at 750°C and 850°C dropping below stoichiometric, as shown in Figure 6.64. The effect of this lead loss on the microstructure was that some regions adjacent to the PST top surface were pyrochlore with full thickness perovskite in between. More specifically this pyrochlore region was the cause of the general lead deficiency of the PST, with a lead content down to a level of half that of perovskite PST. This is possible since, as mentioned in Chapter 2, it is known that pyrochlore can exist with a large range of compositions. These areas of pyrochlore were easily visible in the SEM as rosettes on the sample surface. In addition to this problem there were also extensive lead inclusions in the silicon dioxide layer underneath the platinum. From these results a mechanism for lead loss and the PST microstructure resulting from annealing can be proposed. Since the as-deposited material was a poorly crystallised pyrochlore/amorphous mixture then there would be a proportion of free lead, most probably in the form of lead oxide. In the slow heat up process of the oven annealing this lead oxide would be free to diffuse so long as it was not bound into a stable crystal structure. On diffusing to the surface the lead oxide would be free to evaporate, having a high vapour pressure at elevated temperatures. As well as diffusing upwards the lead could also diffuse downwards through the platinum, most likely along grain boundaries, and into the silicon dioxide layer where it would react to form a lead-silicate compound. At a sufficiently high temperature the perovskite phase would start to form, possibly via a metastable pyrochlore phase, starting at the PST/platinum interface and growing upwards. The upward advance of the perovskite would be halted

before conversion of the entire film due to a lack of lead, thus leaving unconvertible material at the surface in the form of a lead deficient pyrochlore. Morphologically the oven annealed samples were relatively poor compared with the RTP annealed samples discussed shortly. As was seen in Chapter 5 there was extensive cracking of the PST surface, although unlike the material reported in Chapter 5 this did not prevent measurement of the electrical properties. Using the XRD results a ratio of the perovskite and pyrochlore (222) rocking curve integrated intensities has been used to give an indication of the differences in relative perovskite/pyrochlore 'content' between samples, Figure 6.63 below. For the oven annealed samples the perovskite content can be seen to increase with anneal temperature, not quite reaching 100% even at 800°C – for reasons discussed above.

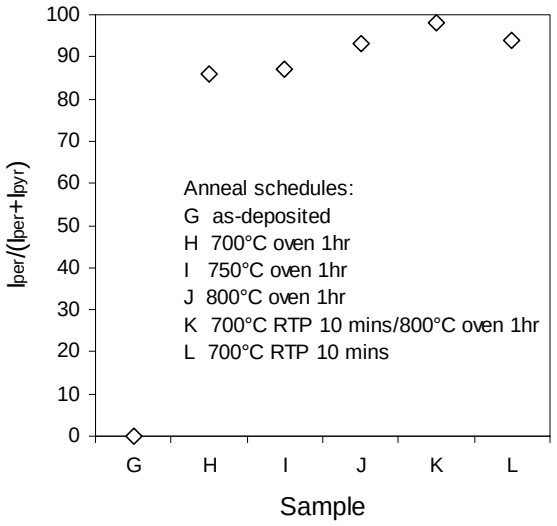

Figure 6.63: Perovskite to pyrochlore ratio for annealed samples G to L.

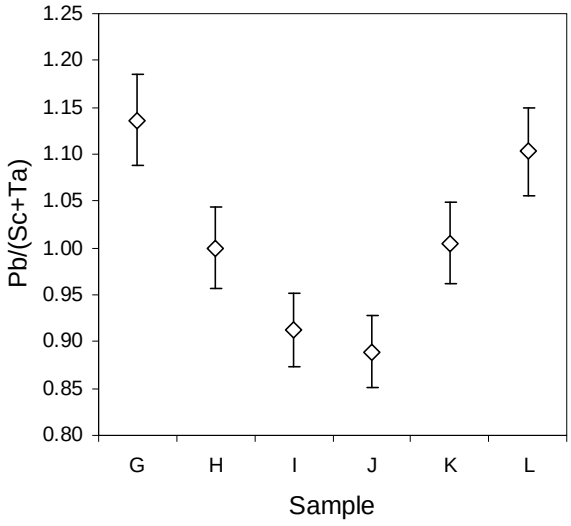

Figure 6.64: Lead composition of annealed samples G to L.

With lead loss obviously being a problem in the oven anneal samples, due to the slow heating rate, it was decided to try RTP annealing both on its own and in conjunction with oven annealing. The reasoning behind this was that with the very fast heating rate compared with oven annealing (50°C/s c.f. 7.5°C/min), severe lead loss would be prevented due to the lead component being quickly bound into a stable crystalline form, as was observed for the single RF magnetron material reported in Chapter 5. RTP-only, in an oxygen ambient, was performed at 700°C for 10 minutes as well as at 850°C for both 30 seconds and 120 seconds. The two anneals at 850°C were performed as a result of the experience gained from the annealing studies of the single RF magnetron deposited PST reported in Chapter 5, where the best electrical performance was obtained after an anneal at

this temperature. In addition to this a RTP annealed sample (700°C, 10 minutes, O_2) was oven annealed at 800°C, to compare with the oven-only technique.

RTP annealing at 700°C for 10 minutes was successful for converting the as-deposited material into the required perovskite phase. As can be seen from Figure 6.64 the PST has a higher perovskite content than for the 800°C oven-annealed sample but still had residual pyrochlore. In terms of structure the perovskite was (222) textured (no ordering), with a rocking curve fwhm ~2° as for oven annealing, whilst the intensity of the original pyrochlore peaks was markedly reduced. Within the experimental error of the EDS technique the lead content was unchanged from the as deposited value. The combination of this RTP with a further oven anneal at 800°C for 1 hour in an oxygen ambient can be seen from Figure 6.63 to have resulted in further perovskite conversion, with the PST being almost entirely perovskite. Also a small (111) superlattice peak was observed, indicating the onset of B-site cation ordering. Importantly the lead content, Figure 6.64, is seen to have reduced to around perovskite PST stoichiometry and not below, with the initial RTP step having bound in the lead and thereby prevented excessive loss during the oven anneal. Structurally the RTP (700°C) and combined RTP/oven annealed samples were much improved over those given an oven-only anneal. There were no pyrochlore rosettes at the surface and no gross cracking of the PST, with a clearly defined grain structure (grain size ~1-2μm) being observed. Absence of cracking in combined RTP/oven annealing supports the hypothesis of Chapter 5 that it is the formation of a metastable pyrochlore phase, during the slow heat-up in the oven, that is instrumental in the development of cracks in the PST – due to volume shrinkage upon conversion to perovskite. Another possibility is that lead loss leads to shrinkage, resulting in stress in the PST film which is relieved by cracking. Detailed investigation of the microstructure of the combined RTP/oven annealed sample showed the PST to be perovskite throughout its thickness, with no near-surface lead deficient pyrochlore regions (hence the absence of rosettes) or any significant lead diffusion through the platinum and into the silicon dioxide – a result of the RTP binding-in the lead. Voids were present in the PST but they were both smaller and fewer in number than those observed in the annealed material reported in Chapter 5 and the 450°C deposited PST reported earlier in this chapter.

The extension of RTP-only annealing in oxygen to 850°C, for both 30 seconds and 120 seconds, resulted in PST films which were morphologically similar to the 850°C RTP

annealed single magnetron deposited PST reported in Chapter 5. Optically the surface had a crazy-paving structure with SEM revealing a network of large interlocking grains with sizes between ~1-3μm. , This grain size is over an order of magnitude greater than that observed in PST deposited directly into the perovskite phase at 525°C, indicating a low nucleation density of the perovskite phase on the platinum. Additionally the surface was pitted, in contrast to the 700°C RTP annealed sample, which as discussed previously is symptomatic of voids in the PST breaking the surface. XRD analysis of this material showed only perovskite reflections, suggesting complete conversion. Interestingly both the 30s and 120s samples were multi-orientated perovskite with (400) being the dominant reflection, which is different to similarly annealed PST reported elsewhere in this thesis. The only evidence of B-site ordering was a small (111) reflection observed in the XRD θ-2θ scan of the PST given a 120s duration anneal. Despite the multi-orientated nature of the polycrystalline PST of both samples, no other odd indexed reflections (a result of ordering) were observed. The author has in the past observed that either a broad platinum rocking curve width or muti-orientated platinum (due to substrate roughness) can result in multi-orientation of the overlying PST, although in this case the platinum has neither of these characteristics. Within experimental error the Lead content of both the 30s and 120s duration anneal samples was stoichoimetric, with Pb/(Sc+Ta) ratios of 1.03±0.04 and 1.00±0.04 for the 30s and 120s duration anneals respectively.

Where possible, comprehensive electrical measurements were made in order to ascertain the ferroelectric nature of the annealed PST and assess its suitability for incorporation into uncooled IR detectors. Table 6.10 below gives a summary of the electrical properties of the samples analysed, where δ is the Smolenski diffuseness parameter. Oven-only annealed material was characterised by generally low merit figures. This was the result of either low breakdown strength or low pyroelectric response. Additionally a low electrical yield was also found, due to the gross cracking observed in the PST and the consequent shorting between the top and bottom electrodes. A consequence of oven annealing at successively higher temperatures was an increase in the both the maximum value of, and the temperature of occurrence of, the peak permittivity. This is consistent with increasing perovskite 'content' as indicated by the XRD measurements discussed earlier. Good fits to the Smolenski model, see Appendix A3, as well as frequency dispersion of the dielectric properties demonstrate that the 750°C and 800°C oven annealed PST behaves as a relaxor ferroelectric. In general the higher the oven anneal temperature the sharper permittivity

peak, as shown by a reduction in δ. Since the induced pyroelectric coefficient is proportional to $\partial\varepsilon_r/\partial T$ this resulted in better performance for a given applied field. However, another feature of higher temperature annealing was lower breakdown strength. A consequence of this was that although the 800°C annealed material performed best, the higher breakdown strength of the 750°C annealed material resulted in it having the highest F_D value ($1.5\pm0.1\times10^{-5}Pa^{-1/2}$) which was still only moderate, being comparable with that of PZT ($F_D\sim2\times10^{-5}Pa^{-1/2}$ [109]) and 525°C deposited PST (perovskite directly, $F_D\sim2\times10^{-5}Pa^{-1/2}$ [5]).

Sample	Anneal	ε_r^{max} (T_{max})	δ	p_{max} ($\mu C/m_2K$)	F_D^{max} ($\times10^{-5}Pa^{-1/2}$)
H	Oven 700°C for 1 hr	357±21 (-25°C)	–	215±11 (35°C, 10V/μm)	0.9±0.1 (35°C, 10V/μm)
I	Oven 750°C for 1 hr	1020±59 (-15°C)	124	396±20 (35°C, 8V/μm)	1.5±0.1 (35°C, 8V/μm)
J	Oven 800°C for 1 hr	1731±100 (-10°C)	107	339±17 (35°C, 2V/μm)	0.8±0.1 (35°C, 2V/μm)
K	RTP 700°C For 10 mins & Oven 800°C for 1hr	1803±97 (-10°C)	107	505±23 (37°C, 7.6V/μm)	2.5±0.3 (37°C, 7.6V/μm)
L	RTP 700°C for 10 mins	284±16 (-15°C)	208	160±8 (35°C, 9.4V/μm)	0.9±0.1 (35°C, 9.4V/μm)
N	RTP 850°C for 30s	2875±240 (10°C)	65	803±64 (50°C, 7.2V/μm)	4.8±0.8 (35°C, 9.5Vμ/m)
O	RTP 850°C, for 120s	3625±272 (20°C)	47	1041±76 (49°C, 4.7V/μm)	5.8±0.9 (49°C, 9.3V/μm)

Table 6.10: Summary of the electrical properties of oven, combined RTP/oven and RTP annealed samples. F_D^{max}, p_{max} and ε_r^{max} are the maximum values of the materials merit figure, pyroelectric coefficient and zero field relative permittivity respectively (all 120Hz). T_{max} and δ are the temperature at which ε_r^{max} occurs and the diffuseness parameter (120Hz) respectively.

The 700°C RTP annealed (10 minutes) material was electrically very similar to that given a 700°C oven anneal (1 hour), being characterised by low permittivity which was not sharply peaked (high δ) which exhibited some frequency relaxation indicating relaxor behaviour. As a result this sample gave a low pyroelectric coefficient, even at high bias fields, yielding a maximum merit figure of $0.9\pm0.1\times10^{-5}Pa^{-1/2}$. This relatively moderate performance is not

entirely surprising since 650°C RTP annealed PST reported in this chapter and in Chapter 5 was seen to be incompletely converted. The combined oven/RTP annealed PST (sample K) was electrically very similar to the PST given the oven anneal only (sample J). Both exhibited relaxor properties and good fits to the Smolenski quadratic law, see Appendix A3. A marked difference between the two though was the breakdown strength, with the combined RTP/oven annealed material withstanding an applied field of 7.6V/μm compared with 2V/μm in the oven-only annealed, thereby yielding an F_D of $2.5\pm0.3\times10^{-5}Pa^{-1/2}$ compared with a maximum value of $0.8\pm0.1\times10^{-5}Pa^{-1/2}$ for the oven-only anneal. The major physical difference between the two is the presence in the oven-only annealed PST of the lead deficient pyrochlore phase which may be limiting the breakdown strength.

A single RTP at 850°C of 30 seconds and 120 seconds duration (sample N and O respectively) resulted in the perovskite PST with very good electrical performance, the best reported in this thesis with the 120s duration annealed sample in particular giving (to the authors knowledge) the best reported F_D values in the literature for thin film PST on silicon substrates. Both samples had relatively high permittivities. Frequency dispersion was evident in the dielectric properties of both samples, but with the 120s duration annealed PST only showing a very slight frequency dependence. This was evident when the data was fitted to the Smolenski model, see Appendix A3. Sample N fitted well, yielding a δ value of 65, while sample O could only be fitted for a narrow temperature range just above the dielectric maximum, yielding a δ value of 47. For sample N this difficulty in fitting to the Smolenski model suggests that the PST is becoming less relaxor in nature. Certainly the low δ value, which compares with values of 11 and 34 for bulk ceramic PST and thin film PST on sapphire respectively, shows that the peak in ε_r is becoming less diffuse. The higher pyroelectric coefficient for sample O compared to sample N reflects the sharper permittivity peak. In common with other annealed PST reported in this thesis, these samples had appreciable pyroelectric coefficients at zero applied field which in conjunction with peaks in ε_r and tanδ occurring at negative applied fields suggests the presence in the PST of an effective internal bias field. The combination of the relatively high pyroelectric coefficients, a high breakdown strength and the suppression of ε_r and tanδ under field yielded good F_D values of $4.8\pm0.8\times10^{-5}Pa^{-1/2}$ and $5.8\pm0.9\times10^{-5}Pa^{-1/2}$ for sample N and O respectively. With such high merit figures it would be possible, in a final device, to trade off some performance for a lower applied field with these samples giving F_D values of

~$4\times10^{-5}Pa^{-1/2}$ at 5-6V/μm. To set these merit figures in context the reader is referred to Appendix A7 which gives a plot of detector NETD versus F_D for a hypothetical detector structure.

All of the annealing schemes reported for the 300°C deposited PST are obviously well beyond the temperature limitations of a fully integrated detector fabrication process and would therefore depend on the composite wafer route. The best performing PST has been obtained by performing an RTP anneal at 850°C for 120s, which should be within the thermal budget of the composite wafer. Of all of the samples reported in this chapter none have exhibited very sharp first order type properties, i.e. high $\partial\varepsilon_r/\partial T$ and low δ in the region of the dielectric maximum, although the higher temperature RTP annealed material is beginning approaching them. As discussed in Chapter 5 the consequence of this is that even the highest reported the pyroelectric coefficients are still around a factor of six lower than for bulk ceramic PST [6], suggesting that there is still a way to go in performance terms for thin film PST on silicon substrates.

6.7 Summary

Thin film PST deposited by dual RF magnetron sputtering at a substrate temperature of 450°C results in a novel, very well crystallised pyrochlore phase. Upon RTP annealing this pyrochlore phase can be converted to perovskite although an RTP anneal at 650°C for 30 seconds is insufficient to complete this conversion. This rules out the use of this PST in a fully integrated detector fabrication process since the conditions for complete conversion are beyond the survivability limits for the ROIC, determined in Chapter 4 to be 600°C for 30 seconds. RTP at the higher temperatures of 750°C and 850°C, both for 30 seconds, resulted in virtually complete conversion with some ordering of the B-site cations observed at both anneal temperatures. In all cases the polycrystalline perovskite resulting from conversion was (222) textured, reflecting the influence of the underlying platinum. The surface morphology of the samples was good with no gross cracking, as observed in conventional oven annealed PST thin films reported in this thesis. As for the single RF magnetron sputtered PST reported in Chapter 5 a low nucleation density of the perovskite phase on the underlying platinum resulted in relatively large perovskite grains up to several microns across. Volume shrinkage of the PST upon conversion from pyrochlore to perovskite was manifested as voiding, as observed in Chapter 5. Electrically the

performance of the 850°C RTP annealed material was very good but limited by a low breakdown strength. The material was characterised by high permittivity (ε_r = 3346±194 at 35°C) which was relatively sharply peaked (δ = 54). This resulted in high pyroelectric coefficients, compared with the similarly annealed 300°C deposited PST reported in Chapter 5, and a maximum F_D value of $1.9\pm0.2\times10^{-5}Pa^{-1/2}$ (54°C, 1.25V/μm) which is comparable with the best values from the conventional pyroelectric material PZT and from 525°C deposited (perovskite directly, no anneal) PST. Conversion of this 450°C well crystallised PST results in material with poorer electrical performance than that converted from the 300°C starting point. On this basis this deposition/annealing route can be ruled out as the best for incorporation into a detector fabrication process.

It has been shown in this chapter that PST deposited as single metal component layers at 300°C, using the novel 'dwell time' method of operating a dual RF magnetron deposition system, can be converted to the required perovskite phase by a post deposition anneal. In contrast to the 450°C deposited PST, that deposited at 300°C did not form a very well crystallised pyrochlore phase but a pyrochlore/amorphous mix with a filamentous structure composed of nanocrystalline pyrochlore – very similar to the single RF magnetron deposited PST where there is a more intimate mixture of the elemental components. Conversion to perovskite was accomplished by using oven-only, combined oven/RTP and RTP-only techniques. Oven-only annealed films at temperatures between 700°C and 800°C, all for 1 hour, were characterised by incomplete conversion to perovskite, loss of lead to levels below perovskite stoichiometry and poor surface morphology with gross cracking and pyrochlore rosette structures. Lead loss was shown to have occurred via diffusion through the underlying platinum and reaction with the underlying silicon dioxide layer to form a lead-silicate compound, as well as evaporation from the top surface and is probably a result of the slow heat up rate (7.5°C/min). This resulted in a lead-deficient unconvertible pyrochlore layer at the surface. Electrical properties of the oven-only annealed films improved with increasing anneal temperature but were ultimately limited by low breakdown strength. The best F_D value was measured from the 750°C annealed film at $1.5\pm0.1\times10^{-5}Pa^{-1/2}$ (35°C, 8V/μm). Overall the oven annealing technique, in the form reported, would seem to offer only disadvantages compared to the RTP technique and can therefore be ruled out as a way forward.

RTP annealing of 300°C deposited PST at 700°C for 10 minutes was also able to convert the material to perovskite, but not completely. A combined RTP (700°C, 10 mins)/oven (800°C, 1 hour) anneal resulted in more complete conversion, although incomplete removal of pyrochlore. Lead loss below perovskite stoichiometry was not observed, even in the oven annealed sample, which leads to the conclusion that RTP binds-in the lead component. The surface morphology was improved over oven-only annealing with no gross-cracking and grain sizes of ~1-2μm. Electrically the 700°C RTP-only sample was relatively poor, being very similar to the 700°C oven-only annealed material with a maximum F_D value of $0.9\pm0.1\times10^{-5}Pa^{-1/2}$ (35°C, 9.4V/μm). The 800°C oven anneal after RTP improved the electrical properties to a level comparable with the 800°C oven-only annealed sample. Improved breakdown strength over the 800°C oven annealed sample resulted in a maximum F_D value of $2.5\pm0.3\times10^{-5}Pa^{-1/2}$ (37°C, 7.6V/μm), which is higher than for PZT (F_D~$2\times10^{-5}Pa^{-1/2}$ [109]) and 525°C deposited PST (F_D~$2\times10^{-5}Pa^{-1/2}$ [5]).

A single, 850°C RTP anneal produced the best perovskite films from 300°C deposited PST. Two anneal times of 30 seconds and 120 seconds were investigated with XRD spectra showing only perovskite reflections and a degree of B-site ordering at the longer anneal time. The perovskite formed upon annealing was multi-orientated with (400) as the dominant orientation, in contrast to all other PST thin films reported in this thesis which were (222) textured. Lead content after RTP annealing was found to be close to stoichiometric (perovskite) and the surface morphology was good with none of the rosette features or gross cracking observed in oven-only annealing. Electrical properties of these films were good with high and relatively sharp ε_r peaks, with the 120s annealed sample having a maximum ε_r of 3625±272 (20°C) and a δ value of 47. Breakdown strength was high, compared to the similarly annealed 450°C deposited PST, with no sign of breakdown at applied fields up to 10V/μm). The dielectric properties are the most sharply peaked reported in this thesis, although the phase transitions are still relatively diffuse, and resulted in the highest pyroelectric coefficient of $1041\pm76\mu C/m^2K$ (35°C, 4.7V/μm). Maximum F_D values of $4.8\pm0.8\times10^{-5}Pa^{-1/2}$ (35°C, 9.5V/μm) and $5.8\pm0.9\times10^{-5}Pa^{-1/2}$ (49°C, 9.3V/μm) for the 30s and 120s duration anneals respectively. These values are, to the authors knowledge, the highest reported values for PST thin films on silicon substrates with the 120s F_D value being around a factor of three better than for PZT thin films and 525°C deposited PST thin films.

In summary the PST thin film deposition/annealing regimes reported are capable of producing perovskite phase material with good electrical properties – thus satisfying the main aim of the chapter. The temperatures and times involved are such that they are not compatible with a fully integrated detector fabrication process and therefore would rely on the composite detector approach, described in Chapter 2, in conjunction with a high temperature stable sacrificial layer. On balance the best deposition/annealing scheme is a 300°C deposition followed by an 850°C RTP anneal which produces PST thin films with good morphological properties, high breakdown strength and high merit figures for IR detection. This temperature may seem high but is within the limits of the interconnect wafer technology, although interdiffusion and interface disruption of the underlying electrode layers suggest that stabilisation of these layers may be necessary in order to avoid any potential problems during device processing. When allied to a high performance thermal structure such as the XAC design this PST gives the possibility of high performance uncooled IR detectors.

Chapter 7:

Excimer Laser Annealing: Experimental Design and Thermal Modeling.

7.1. Introduction

In an integrated IR detector fabrication process, a method of preferentially heating the ferroelectric layer whilst keeping other sensitive layers relatively cool would be highly advantageous. The ferroelectric layer could then be deposited at a low temperature into a pyrochlore or amorphous phase and subsequently annealed into the required perovskite phase. As identified in previous chapters, the sensitive layers of interest are those comprising the active readout circuitry, although it may be desirable to keep other layers relatively cool to prevent interdiffusion between sacrificial, barrier and electrode layers. The possibility of such a method exists in pulsed laser annealing. If the laser wavelength is chosen so that the ferroelectric layer is strongly absorbing and the pulse length is kept sufficiently short, to prevent excessive heat diffusion, then this layer can be heated preferentially, limiting the temperature rise in underlying layers.

Very few papers currently exist on the topic of laser annealing of ferroelectric thin films. Matsui et al [111] describe the annealing of lead titanate thin films using a cw CO_2 laser with induced temperature rises in the lead titanate layer of up to 1400°C. Being a cw technique the temperature rise in the underlying layers would also be considerable. Lin et al [112] describe very low fluence (0.01-0.2mJ/cm^2) excimer laser annealing of lead zirconate titanate thin films. No supporting X-Ray diffraction was presented to confirm the presence of PZT perovskite although FTIR data did indicate the presence of the B-O_6 octahedra stretching mode that is associated with this phase. Varshney et al describe the use of an excimer laser to cystallise PZT thin films [113, 114]. The discussion centered on PZT for Ferroelectric Random Access Memory (FeRAM) applications, although the problems are very similar to those for integrated IR detectors, namely a heat sensitive underlying active circuitry layer. In this application excimer laser annealing was able to crystallise sol-gel deposited PZT into a perovskite phase with the promise of improved aging and fatigue characteristics of the resulting FeRAM.

An area where pulsed laser annealing has had a high degree of success is in the crystallisation of poly-silicon (poly-Si) used as the gate contact of thin film transistors (TFT's) for use in active matrix liquid crystal displays [115, 116, 117, 118, 119, 120, 121, 122]. Poly-Si based TFT's have superior performance to their amorphous silicon counterparts [121] but require higher processing temperatures, 600-1000°C as opposed to 200-300°C for amorphous silicon [122]. By using an excimer laser, which has a short pulse length - typically around 25ns, an amorphous silicon surface layer is preferentially heated with respect to the underlying glass substrate, which remains relatively cool at less than 500°C. The amorphous silicon melts and upon cooling crystallises as poly-Si. Keeping the temperature experienced by the substrate less than 500°C allows inexpensive glass to be used, thereby reducing process costs as compared with furnace annealing, where an expensive high-temperature tolerant substrate is needed. The problem addressed by excimer laser annealing of poly-Si based TFT's is both different and similar to that of laser annealing of ferroelectric thin films. Similarities occur in that the objective is to heat a surface layer while limiting the temperature rise of a thermally sensitive underlayer. The problem is different since the objective in the TFT process is to cause melting of the surface layer whereas in the ferroelectric case the objective is to supply sufficient heat to transform the layer to perovskite without causing ablation and/or chemical decomposition. The thermal and optical properties of silicon are also different from either PST or PZT. Even with these differences, a study of the literature concerned with poly-Si for TFT's was still very useful. Information on basic laser annealing experimental setups was obtained as well as insight into the laser light absorption and heat diffusion problem, the solution of which was necessary to both give confidence that the technique was appropriate and also to give basic operating parameter information, e.g. the laser fluence level.

The work reported in this chapter deals with the design of an experiment to investigate the excimer laser annealing of low temperature deposited PST and PZT layers into the perovskite phase for fully integrated device processing. A major part of this included the modelling of the temperature profiles developed in integrated detector layer stack under laser irradiation. Also included are measurements of the optical properties of thin film PST and PZT, required as inputs to the model. A standard commercial excimer laser was used for experimental purposes. This type of laser has the advantage of short pulse length and high pulse energy. A novel aspect of the work presented is that thermal modeling indicated that better annealing conditions would be attained if the laser pulse was lengthened. To this

end a bespoke temporal "pulse-extender" was commissioned and incorporated into the annealing system.

7.2. Theory

UV laser energy is absorbed in a solid by electronic excitations which decay in the order of picoseconds by energy exchange between the lattice and free electrons [123, 124], resulting in localised heating of the material. The heat thus generated spreads throughout the material by thermal conduction. This process is described by the heat diffusion equation with the addition of a source term driven by the absorption of laser radiation. If the beam is spatially uniform then away from the edges of the irradiated area any temperature variation will occur only along the axis perpendicular to the sample surface. This simplifies the problem, which then becomes unidimensional and is described by equation (1) below

$$\frac{\partial T}{\partial t} = \frac{\alpha}{\rho c_p} I(z,t) + \frac{1}{\rho c_p} \frac{\partial}{\partial z}\left(\kappa \frac{\partial T}{\partial z}\right) \tag{7.1}$$

where T is the temperature at time t and depth z, α is the optical absorption coefficient of the illuminated material or specific heat capacity c_p and density ρ, κ is the thermal conductivity and I is the laser power density in the specimen. Equation (1) assumes that heat loss from the surface of sample due to radiative transfer is negligible - confirmed by simple calculations. The power density at depth z and time t is given by

$$I(z,t) = I_0(t)\left[1 - R\right]\exp\left[-\alpha z\right] \tag{7.2}$$

where I_0 is the power density at the surface and R is the reflectivity of the illuminated material. The absorption coefficient is given by

$$\alpha = \frac{4\pi k}{\lambda} \tag{7.3}$$

where k is the extinction coefficient at the laser wavelength λ. The reflectivity of the surface is given by,

$$R = \frac{\left[n-1\right]^2 + k^2}{\left[n+1\right]^2 + k^2} \tag{7.4}$$

where n is the refractive index at the laser wavelength.

The diffusion equation as given in equation (7.1) can only be solved analytically for special cases [125, 126, 127, 128, 129, 130], which are

(i) No temperature dependence of the optical and thermal parameters.

(ii) No phase change induced by the laser pulse.

(iii) No inhomogeneity through the depth of the sample.

(iv) Constant laser power.

(v) Infinite sample thickness.

This is a very restrictive set of conditions which do not lend themselves to the sample structures considered in this study, i.e. PST or PZT (0.5-1μm)/Pt(1000∑)/Ti(100∑)/SiO_2(1000∑)/Cr(1μm)/SiO_2(0.8μm)/Si – the basic layers of the RAB device (neglecting the titanium top electrode which would be deposited after annealing) - and PST or PZT (0.5-1μm)/Pt(1000∑)/Ti(100∑)/SiO_2(0.8μm)/Si – the experimental thin film structure. In view of these restrictions a numerical method has been employed to solve equation (7.1) and is an adaptation of the forward time finite difference approach used by Baeri et al [123, 125] and Wood et al [131].

To solve for the temperatures the sample is divided up into slices of thickness Δz and time is discretised into units of duration Δt. The temperature of each slice is calculated from the energy deposited into it by absorption of laser light and heat transfer in or out by diffusion. The proportion of the laser power density that will propagate into the sample is given by

$$I = I_0(t)(1-R) \tag{7.5}$$

The power density reaching the jth slice (the top surface slice is j = 1) is given by

$$I_j = I_{j-1}\exp(-\alpha_{j-1}\Delta z) \tag{7.6}$$

where α_{j-1} is the absorption coefficient of the (j-1)th slice. The amount of laser energy absorbed in the jth slice during the time interval Δt is given by

$$\Delta Q_{abs} = I_j\left\{1-\exp\left(-\alpha_j\Delta z\right)\right\}\Delta t \tag{7.7}$$

The amount of energy transferred from the nearest neighbour slices by thermal diffusion in a time interval is given by

$$\Delta Q_{diff} = \left| \kappa_{-} \frac{T_{j-1}^{b} - T_{j}^{b}}{\Delta z} + \kappa_{+} \frac{T_{j+1}^{b} - T_{j}^{b}}{\Delta z} \right| \Delta t \tag{7.8}$$

where T^b donates the current temperature; κ_+ and κ_- are the average thermal conductivities at the upper and lower boundaries of the slice respectively, and are given by

$$\kappa_{-} = \frac{\kappa_{j-1} + \kappa_{j}}{2} \tag{7.9}$$

and

$$\kappa_{+} = \frac{\kappa_{j+1} + \kappa_{j}}{2} \tag{7.10}$$

The new temperature, T^a, of each slice at time $t+\Delta t$ is given by

$$T_{j}^{a} = T_{j}^{b} + \frac{\left(\Delta Q_{abs} + \Delta Q_{diff}\right)}{c_{p} \rho \Delta z} \tag{7.11}$$

Equation (7.1) is a parabolic partial differential equation and convergence of the numerical method used to solve it requires that a stability criterion be met [132], which is

$$\frac{\kappa \Delta t}{c_{p} \rho \Delta z^{2}} < \frac{1}{2} \tag{7.12}$$

Physically the stability criterion corresponds to the diffusion length during a time step being less than the slice thickness. In effect the numerical method is stable if the only significant thermal diffusion component is between next nearest neighbours – as might be expected from the formulation.

The solution is subject to boundary conditions, which are:

(i) the temperature distribution in the sample at zero time,

(ii) heat is not lost from the illuminated surface,

(iii) $\lim_{z \to \infty} T$ = constant at all times.

For assumption (ii) to be true then both radiative heat transfer and heat exchanged with the surrounding gaseous medium must be negligible. Simple calculations showed that in the timescales involved heat loss from the surface by radiative heat transfer and convection were negligible compared to that lost through downwards diffusion. Radiative heat transfer calculations were made assuming a surface emissivity of 1. A paper by Marinova et al [23] reported measurements of the optical properties of single crystal pyrochlore PST, $Pb_2Sc_{0.5}Ta_{1.5}O_{6.5}$, suggesting that the emissivity in the wavelength range 1.6→7.3μm, corresponding to surface temperatures 1800→400°C, was low. This further supports the omission of radiative heat transfer.

To solve for the temperature distributions in illuminated samples it was necessary to have information about the optical properties of the materials involved, as well as thermal properties. The use of a numerical method allows temperature variations of the thermal properties to be taken into account, as well as temporal variations of the intensity of beam during the pulse.

7.3. Experiment

7.3.1. Measurement of Materials Optical Properties

In order to model the temperature profiles that develop in thin film layer stacks during laser irradiation it is necessary to know the material optical properties at the laser wavelength. The optical properties in question are the extinction coefficient and either one of the refractive index or the reflectivity. As this data was not available in the literature it was measured for both PST and PZT thin films deposited onto platinised silicon.

The refractive index and extinction coefficient were measured using the technique of Ellipsometry [133], by Dr. J Russell of DERA Malvern. Samples were analysed using a Sopra Spectroscopic Ellipsometer with the angle of incidence of the linearly polarised input beam set to 75°. Although the samples were multilayer stacks of the form PST or PZT(0.5-0.8μm)/Pt(1000∑)/Ti(100∑)/SiO_2(0.8μm)/Si, the n and k values were extracted from the data by assuming that the reflected beam was influenced only by the PST (or PZT). Reflectivity measurements, discussed later, show this to be a valid assumption.

Sample reflectivity was measured using a Cary Hemispherical Directional Reflectometer. This instrument uses an integrating sphere to determine the total reflectivity i.e. both specular and diffuse components. The input beam was set to 6° off the sample surface normal (the minimum allowable) and measurements were made between 200nm and 2.5μm at 1nm intervals.

7.3.2. Laser Annealing System

A Lambda Physik LPX210i excimer laser was used for the experimental studies and was operated with a KrF gas mixture giving a principle operating wavelength of 248nm and a nominal pulse width of 25ns (fwhm). The nominal maximum energy per pulse was 700mJ and the maximum repetition rate was 100Hz, sufficiently slow for the temperature rise due to each pulse to be independent of the following or preceding pulse – as will be discussed below. Figure 7.1 shows a schematic diagram of the complete system. The other major components were the annealing chamber, pulse extender, beam homogeniser and analytical equipment used to monitor the beam energy, spatial and temporal profiles. These equipments are described in the sections below.

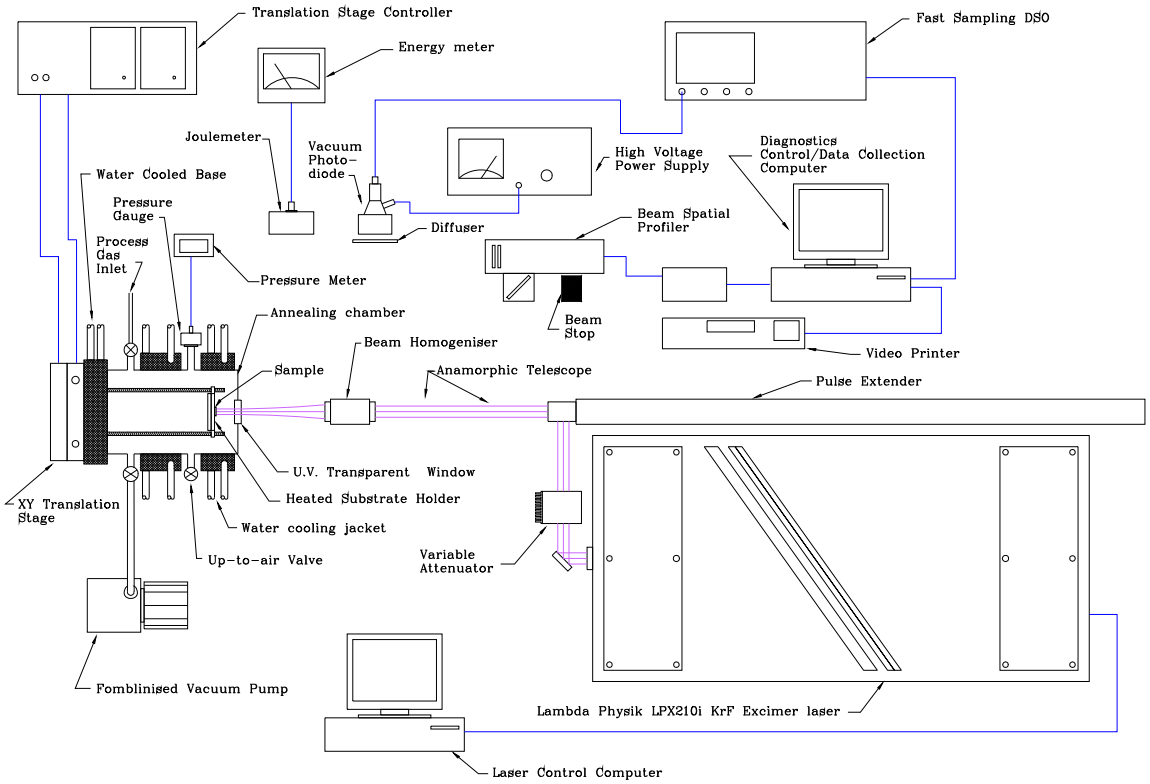

Figure 7.1: Schematic diagram of laser annealing apparatus.
(*Original in colour*)

7.3.3. Annealing Chamber

The annealing chamber was constructed from standard vacuum components modified to accommodate the experimental requirements. The basis of the chamber were two ISO-KF cylinders, each with two KF ports, and two ISO flanges. A schematic cross sectional view of the chamber is shown in Figure 7.2. The base flange was attached to a water cooled plate, itself fixed to an Ealing x-y translation stage. On the upper side of the base flange a thin stainless steel substrate holder was clamped onto three pillar supports. A resistive heating element was fixed to the underside of the substrate holder, allowing the temperature to be varied up to 590°C. The temperature was sensed by a stainless steel shrouded K-type thermocouple inserted into a hole drilled into the substrate holder and controlled by a West 6100 PID controller and associated circuitry. To prevent excessive heating of the chamber walls during high temperature operation a number of cooling jackets were clamped to the side of the chamber with thermally conductive paste ensuring a good thermal contact. These jackets were made of aluminium and encased water cooling copper tubes. A fused silica AR-coated laser window was clamped into the lid, see Figure 7.2. Viton o-rings were

used throughout in case of problems during extended operation at elevated temperatures. A fomblinised Edwards E2M8 rotary vacuum pump was connected to the chamber allowing operation with oxygen. Process gas was fed into the chamber via a needle valve and the pressure monitored by an Edwards EPS10 (0-1000mbar) sensor and EMV251 gauge.

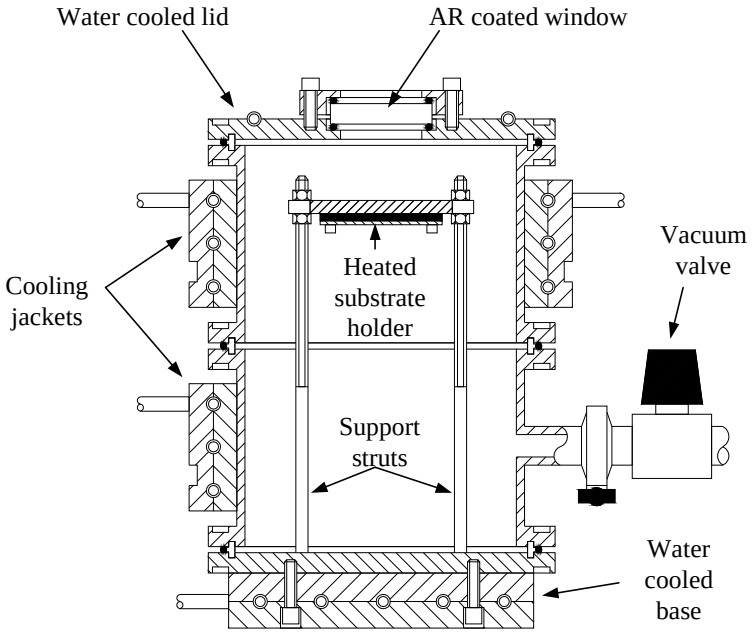

Figure 7.2: Schematic cross-section of annealing chamber.

7.3.4. Pulse Extender

Modelling studies of the temperature distributions developed in the samples during laser illumination, discussed in detail below, showed that a standard excimer laser pulse resulted in very high surface temperatures and poor heat transport into the depth of the ferroelectric layer. One solution to this was to temporally extend the pulse so as to slow down the rate of energy delivery to the ferroelectric layer. As a result of this a bespoke pulse extender was commissioned. A schematic diagram of the equipment, built by Exitech Ltd., is shown in Figure 7.3.

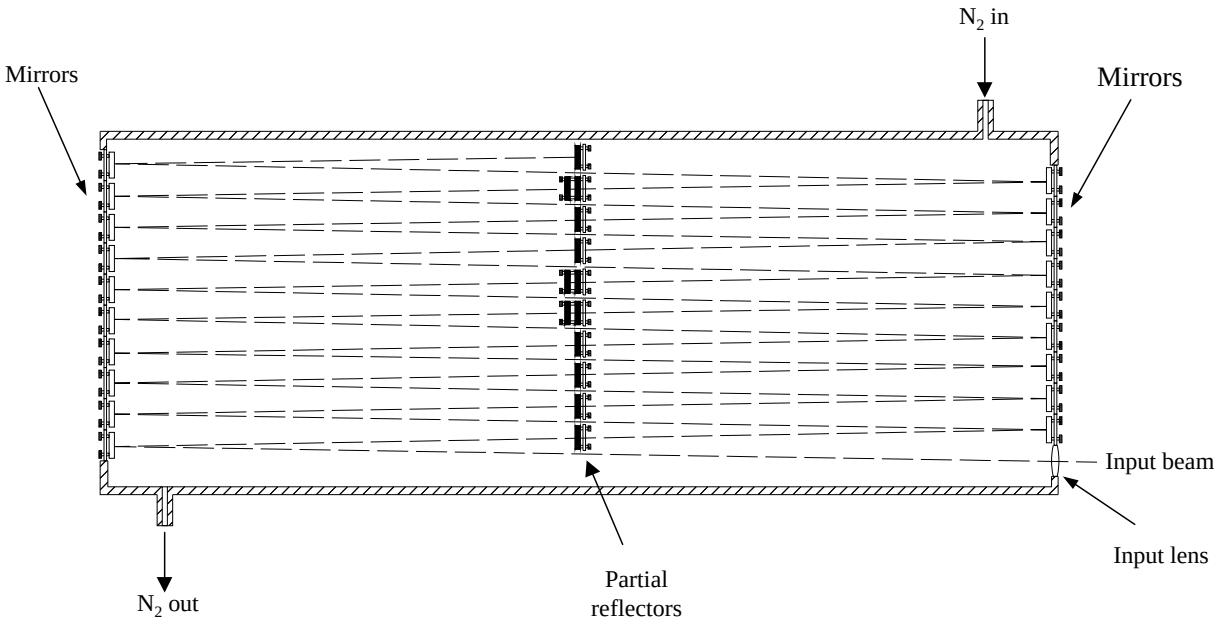

Figure 7.3: Schematic illustration of temporal pulse extender.

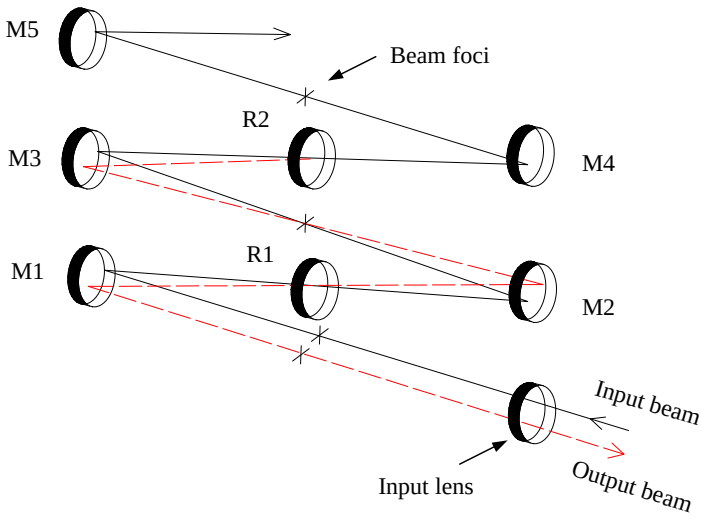

Figure 7.4: Pulse extender action.
(*Original in colour*)

The pulse extention action is due to path length delay of reflected components of a forward propagating beam. As can be seen from the diagram, at each end of the extender are two banks of high reflectivity dielectric mirrors. In the centre is a bank of nine partial reflectors with a total reflector at the top of the of the stack. A schematic view of the operation of the pulse extender is shown in Figure 7.4. The beam enters the extender via the input lens, which keeps the input and output divergences equal, and propagates to the mirror M1. The reflected beam then passes through the partial reflector R1, upon which 10% of the energy

is reflected back towards the input. The beam then propagates forward, hitting the mirror M2, and then passes through the second partial reflector R2, upon which 11.1% of the remaining beam energy (corresponding to 10% of the input energy) is reflected back towards the input. This continues until the forward propagating beam reaches the total reflector at the top of the central stack, upon which it is back reflected and propagates back down the mirror/partial reflector stacks until it leaves the system. The operation of the extender results in ten back reflected components, each with 10% of the original pulse energy, seperated by the time for the beam to traverse four lengths of the cavity (distance between left and right banks of mirrors). In practice each component has slightly less than 10% due to losses resulting from back propagating beam components having to pass through the partial reflectors. With a cavity length of 2.8m the delay between emerging output pulses is 35ns, giving a total effective output pulse length of 350ns. During operation, nitrogen is flowed through the extender to prevent excessive energy loss due to the break down of atmospheric oxygen by the beam – which is focused on each second traverse of the cavity. If the system has been well aligned then the efficiency is around 50%.

7.3.5. Beam Homogeniser

A well aligned excimer laser has a rectangular shaped beam which is gaussian in the short direction and gaussian with a flat top in the long direction. By using a Microlas beam homogeniser this was changed into a square profile of uniform intensity. The homogeniser, shown schematically in Figure 7.5, consists of two 9×9 arrays of square microlenses and an ouput lens. These microlens arrays split the input beam up, with the resulting components being expanded and overlaid at a common plane. If properly aligned then the beam in this plane is square and of uniform intensity.

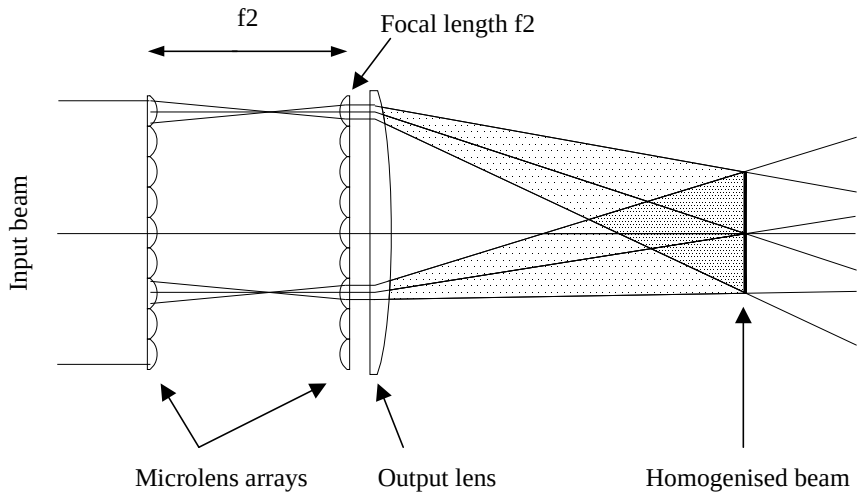

Figure 7.5: Beam Homogeniser.

7.3.6. Measurement of Beam Temporal and Spatial Profiles

The spatial intensity profile of the beam at the sample plane was monitored, so as to maintain uniform illumination, using an Exitech P256C Laser Beam Analysis System. This used a beam splitter to direct a small portion of the beam onto a windowless ccd camera, via a variable attenuator, the ouput from which is displayed on a pc.

The temporal profile of the beam was measured and used for modelling purposes. This was accomplished using a planar cathode vacuum photodiode, with an MgF_2 window for UV operation, supplied by ITL Ltd. This was connected to a Gould 4096 8-bit digital storage oscilloscope (DSO) which was operated at its maximum speed of 800 mega-samples per second, giving one sample every 1.25ns which meant that the DSO output was at either 0.2ns (non-extended pulse) or 1ns (extended pulse), the "missing" data being filled in by linear interpolation. The true sample time was significantly longer than the 12ps rise time of the photodiode. Captured data was downloaded to a pc via GPIB and a simple program written in Visual Basic.

7.4. Results

7.4.1 PST and PZT Optical Properties

The optical properties of three thin film samples were measured at room temperature. These were single RF magnetron deposited PST (deposition temperature = 300°C), dual RF

magnetron deposited PST (deposition temperature = 450°C) and sol-gel spin deposited PZT (dried at 400°C). The thickness of the samples was 0.6µm, 1µm and 0.5µm respectively. The measured reflectance for the PST samples is shown in Figure 7.6 below. Interference fringes due to reflection of incident light off the underlying platinum are evident and disappear below ~350nm. This is consistent with the samples becoming strongly absorbing and corresponds to a photon energy of 3.5eV and is in good agreement with the general value for the bandgap of similar materials in perovskite form of 3-4eV, quoted by Lines and Glass [34]. The reflectance at the 248nm, the laser wavelength, is 17.8% for 300°C deposited PST and 18.6% for 450°C deposited PST.

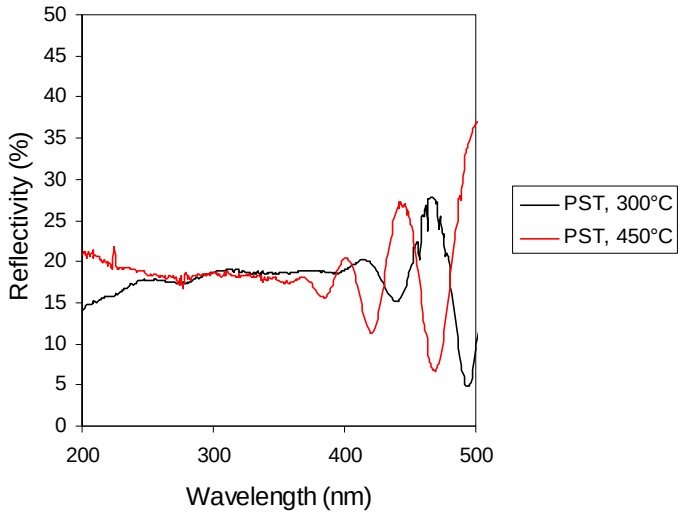

Figure 7.6: Measured reflectance for 300°C and 450°C deposited PST.
(*Original in colour*)

Shown in Figure 7.7 is the measured reflectance of the PZT sample. The interference fringes disappear at ~320nm, corresponding to a photon energy of 3.9eV, and the reflectance at 248nm is 24.9%.

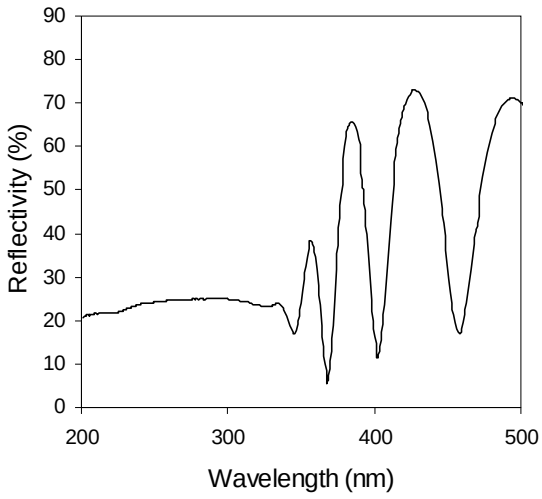

Figure 7.7: Measured reflectance for 300°C deposited PZT.

The refractive index and extinction coefficient of each of the samples were measured between 240nm and 280nm (where the samples are optically thick – as shown by the reflectivity data) and are shown in Figure 7.8. There is little variation between the samples with the refractive indices lying between 2 and 2.5 and the extinction coefficients between 0.7 and 1.3. These values are in good general agreement with data for the similar materials barium titanate ($BaTiO_3$) and strontium titanate ($SrTiO_3$) given by Palik [134].

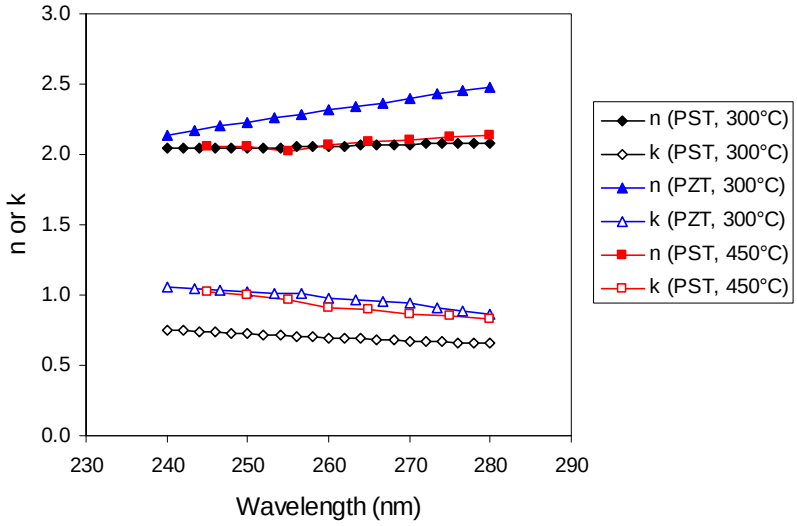

Figure 7.8: Measured n and k for 300°C deposited PST and PZT and 450°C deposited PST.
(*Original in colour*)

The values of the extinction coefficients are very high, indicating that the PST and PZT are highly absorbing at these wavelengths. Absorption lengths are shown in Figure 7.9 and are very short compared to the film thickness. A summary of the optical properties at the laser wavelength is given in Table 7.1.

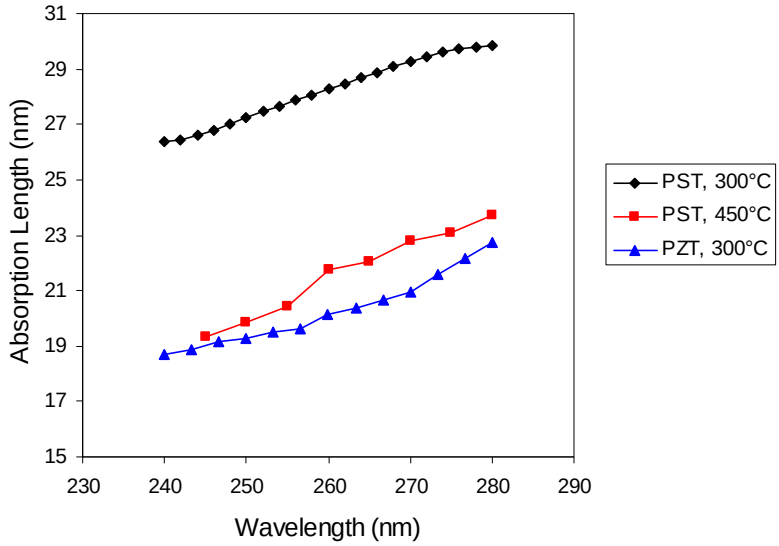

Figure 7.9: Absorption lengths for the different materials considered. (*Original in colour*)

Material	Deposition Temperature (°C)	n	k	Absorption Coefficient (m^{-1})	Absorption Length (nm)	Reflectance (%)
PST	300	2.0	0.7	3.7×10^{7}	27.0	17.8
PZT	300	2.2	1.0	5.1×10^{7}	19.5	24.9
PST	450	2.1	1.1	5.4×10^{7}	18.7	18.6

Table 7.1: Summary of optical properties, at 248nm, of materials considered.

It is worth noting that the optical measurements reported were taken at room temperature. It is likely that these will change at elevated temperatures and under conditions of very intense illumination, due to alteration of the phonon distribution and band gap shifts [125].

7.4.2 Beam Spatial Profile

A typical spatial profile of the homogenised beam in the sample plane is shown in Figure 7.10 below. The beam is square and away from the edges has a uniform energy distribution. Slight non-uniformities can be observed and are attributed to divergence incompatibilities between the homogeniser and the laser-pulse extender combination.

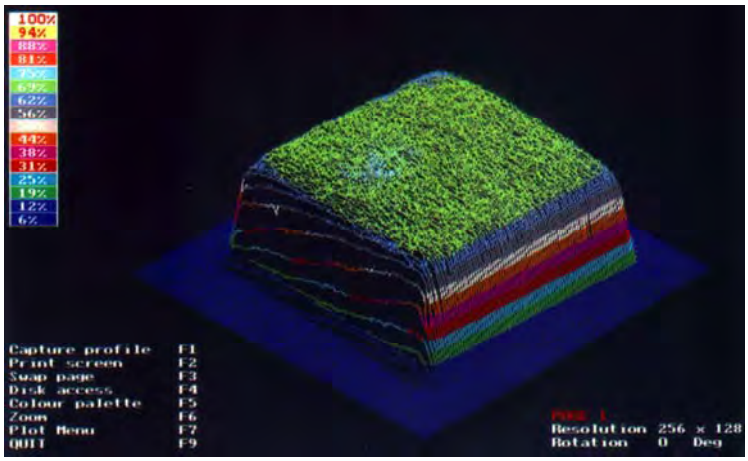

Figure 7.10: Spatial profile of the homogenised beam.
(*Original in colour*)

7.4.3 Beam Temporal Profiles

The temporal profile of the pulse obtained from the excimer laser is shown, at a number of energy levels, in Figure 7.11. The general shape of profiles is in good agreement with that in the Lambda Physik literature, with the fwhm being around 25ns, and does not change significantly with laser operating voltage.

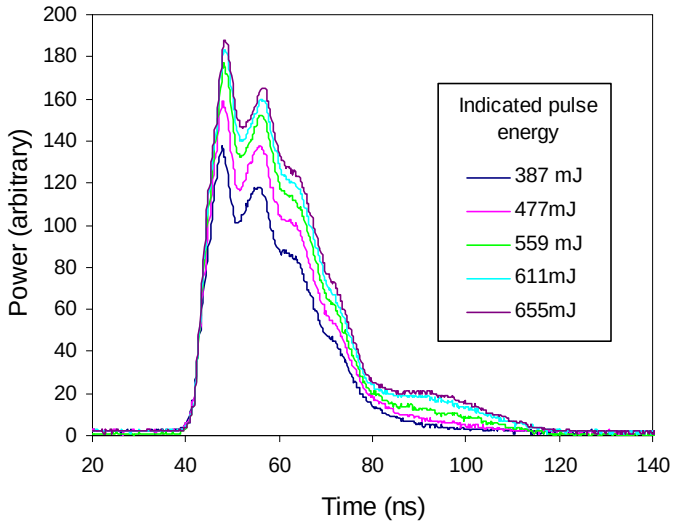

Figure 7.11: Measured laser pulse temporal profiles.
(*Original in colour*)

A measured extended pulse is shown in Figure 7.12 below. There are ten main components, which comprise the main pulse extension action with following subsidiary components due to back-reflections caused by the backward propagating (exitting) beam having to pass through the partial reflectors.

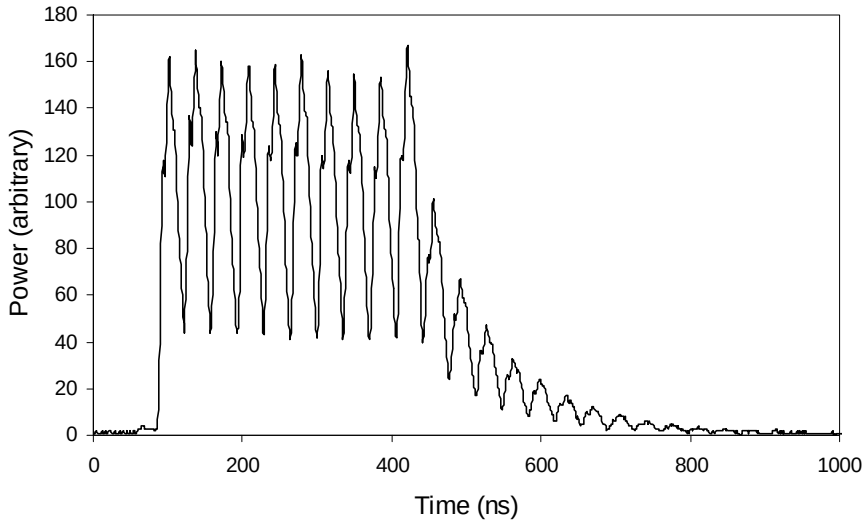

Figure 7.12: Measured extended laser pulse temporal profile.

7.4.4 Predicted Temperature Profiles

In order to establish initial operating parameters for the laser annealing studies it was necessary to predict the temperature profiles that would develop in samples during laser illumination. Results of the modeling also served to give an indication of the viability of

this annealing technique. The modeling encompassed the basic RAB layer structure (neglecting any structure in the silicon due to readout circuitry) and also the experimental thin film structure of the ferroelectric layer deposited onto platinised silicon. The ferroelectric materials considered were both PST and PZT.

As discussed in section 2, the use of a numerical method was necessary to solve the heat diffusion equation. The method of solution involved splitting up the sample structure into finite slices of thickness 50nm, and splitting time into finite periods of duration 25ps. These values were chosen to give a good depth resolution and also comply with the stability criterion for the numerical method given in equation 12. The use of 50nm thick slices does mean that with absorption lengths in PST and PZT ≈ 30nm then almost all of the laser energy is absorbed in the first slice. Temporal pulse data was not available at this resolution so a cubic spline interpolation, using Matlab, was employed to fill in the missing points. Thermal data for the layers used was obtained from Kaye and Laby [73] and the CRC Handbook of Chemistry and Physics [135], except for data on PST and PZT which was taken from bulk ceramic (perovskite) values reported by BAE Systems Caswell [105, 136]. The layers considered were sufficiently thick for bulk thermal properties to be used, further discussion on this topic can be found in appendix A4. Data was interpolated to 1°C intervals using either cubic spline interpolation or curve fitting for modeling purposes. Further information on the thermal properties, and also the stability criteria can be found in appendix A5. A summary of the thermal properties, at 300°C, of the materials involved is given in Table 7.2. The materials can be segregated into fast diffusers, i.e. Pt, Cr and Si, and very poor diffusers, i.e. PST, PZT and SiO_2.

Material	κ (W/mK)	c_p (J/kgK)	D (m^2/s)
PST	1.43	324	4.85×10^{-7}
PZT	1.52	364	5.14×10^{-7}
SiO_2	1.72	1020	6.36×10^{-7}
Pt	73	141	2.41×10^{-5}
Cr	82	527	2.16×10^{-5}
Si	65	850	3.28×10^{-5}

Table 7.2: Summary of thermal properties of materials considered, at 300°C.

For the RAB structure the layering would be n×PST (or PZT) slices, 2×Pt slices, 2×SiO_2 slices, 20×Cr slices, 16×SiO_2 slices and 1200×Si slices. The number of silicon substrate slices is high to satisfy the boundary condition $\lim_{z\to:}T$= constant at all times, as discussed in section 2, and hence to prevent the downwards propagating thermal wave from encountering zero thermal impedance at the bottom silicon slice – whose temperature was set constant. The titanium adhesion layer underlying the platinum was neglected but in any case was very thin at ≈100∑. Optical absorption lengths for PZT and PST, Figure 7.9 and Table 7.1, were so short that a thickness corresponding to only four of these slices was sufficient for the whole structure to be treated as an optically homogeneous medium.

To model the temperature profiles in the layer stack a program was written in Pascal and run on a DEC Alpha AXP workstation. Temporal pulse profiles, both extended and non-extended, obtained experimentally were input along with the laser fluence, although the program could also run with a "top hat" temporal profile. The thermal data was in 1°C increments and the program altered the thermal parameters of each of the slices according to the temperature of the slice. At each time step the temperature of each slice was calculated, i.e. every 25ps, but data was output to file only every nanosecond during the pulse and every ten nanoseconds after the pulse. To check the validity of the method and the program, a run with a "top hat" profile pulse and with the optical and thermal parameters for all slices set to those for silicon. Results were compared to the analytical solution for this special case, see appendix A6, which confirmed that the method and the program were valid. After each run the temperature of the bottom forty silicon slices at the final solution time were checked to make sure that the thermal wave had not penetrated to the bottom thermally clamped slice.

A number of scenarios were modelled, including PST and PZT based structures both with and without chromium sacrificial and SiO_2 barrier layers. Optical properties of 300°C deposited PST and PZT have been used to generate the graphs. Figure 7.13 below shows the predicted temperature distribution through a 1μm thick PST layer during and after illumination with a non-extended pulse with a fluence of 0.1J/cm^2. The ambient temperature has been set to 450°C, easily achievable with the substrate heater described in sections 3.2 and 3.3. Underneath the PST are Pt(1000∑), SiO_2(1000∑), Cr(1μm), SiO_2(0.8μm) and silicon. There are twenty curves, PST1→PST20, which represent the

mean temperatures of the 50nm thick slices with PST1 being at the illuminated surface and PST20 adjacent to the platinum. The maximum surface temperature of the PST is very high, at 2016°C, with poor propagation of heat into the depth of the film and consequently the maximum temperature of the bottom PST layer is 512°C. It is worth noting that without substrate heating the laser fluence would have to have been significantly higher to achieve this temperature, which would have resulted in even higher surface temperatures.

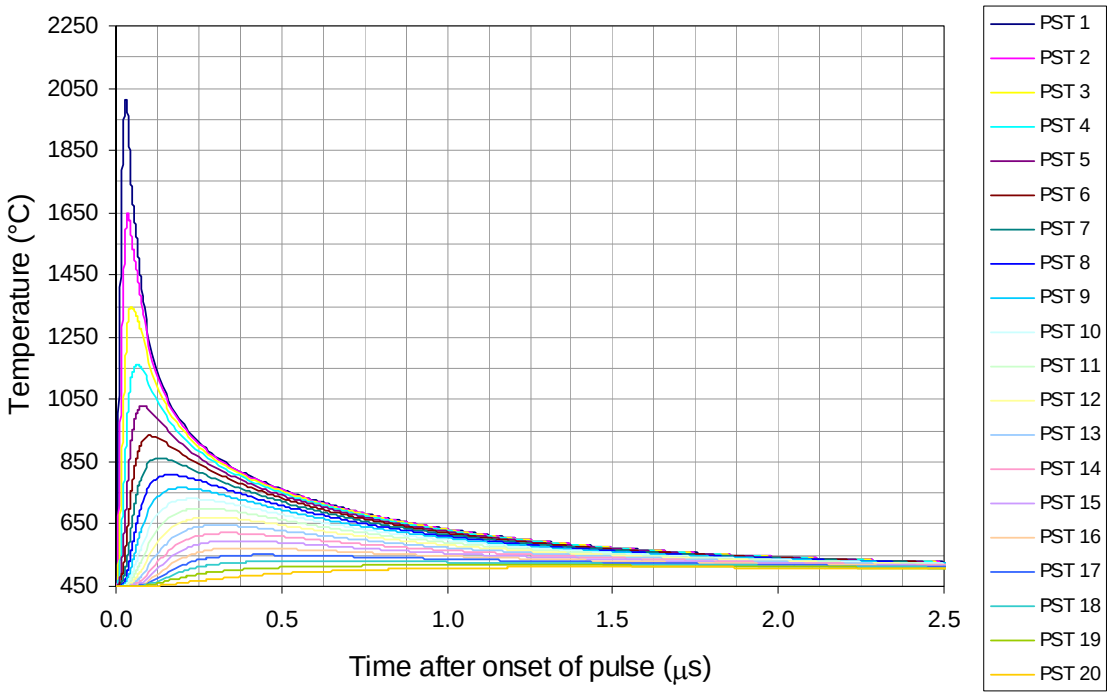

Figure 7.13: Temperature profiles through 1μm thick PST layer, underlying sacrificial layer, 450°C substrate temperature and non-extended pulse (0.1J/cm^2).
(*Original in colour*)

Figure 7.14 below shows the temperatures developed through the structure to a depth of 5μm, with the extent of the component materials marked. The graph represents snapshots of the temperature distributions at 29ns, 1.3μs, 1.59μs, 3μs, 6μs and 9μs after the onset of the laser pulse with the first three times being when the maximum temperatures are developed in the top PST (PST1), bottom PST (PST20) and the top silicon slices respectively - the latter giving an indication of the temperature that would be experienced by the ROIC in a real device. A high thermal gradient develops in the PST, as shown by the 29ns curve, which is not surprising given its poor thermal diffusivity - see Table 7.2. Being a good diffuser of heat the chromium sacrificial layer has only a small temperature gradient

across it. It may be noted that temperature of the uppermost silicon slice rises only 18°C above the 450°C ambient.

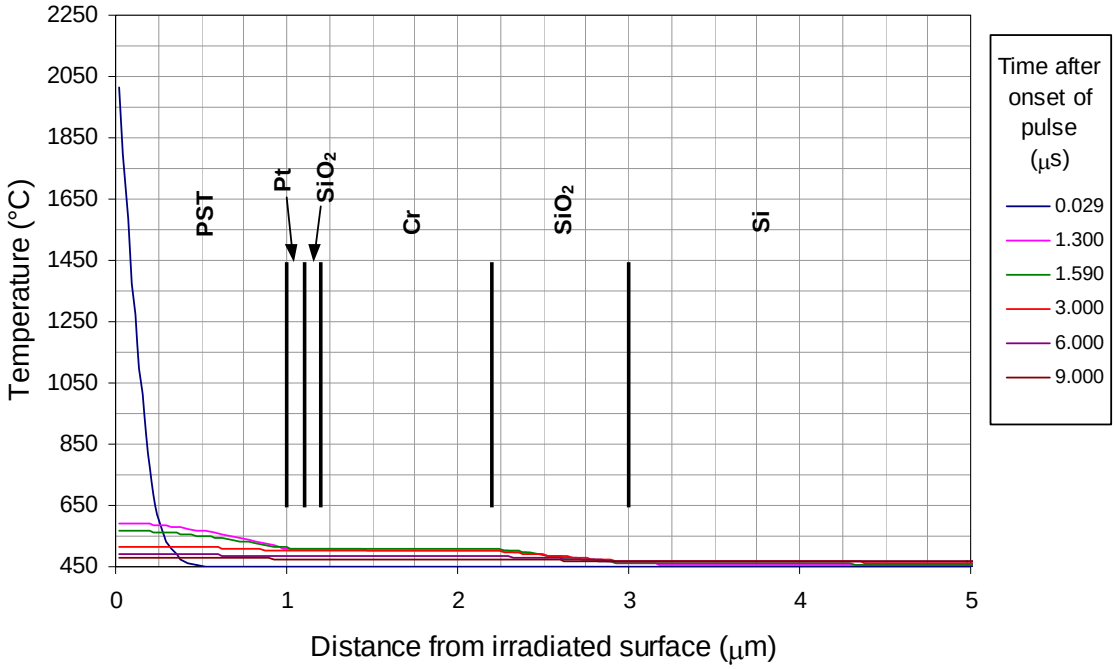

Figure 7.14: Temperature profiles through device layer stack, 1μm of PST, 450°C substrate temperature and non-extended pulse (0.1J/cm^2).
(*Original in colour*)

Figures 7.15 and 7.16 show the temperatures developed in the same structure when illuminated with an extended pulse at a fluence of 0.2J/cm^2, again with the ambient temperature set to 450°C. Compared with the non-extended case a more even temperature distribution is seen in the PST, Figure 7.15, with the maximum surface temperature being 1642°C and the maximum temperature of the bottom PST slice being 572°C. The temperature distribution with depth, Figure 7.16, shows that the maximum temperature of the topmost silicon slice is 488°C. This is obviously kept down by the action of the overlying SiO_2, which being a poor diffuser of heat is acting as a thermal barrier layer. Another interesting point is that the induced temperature rise decays away in the order of 10μs, which indicates that extended pulses from the excimer laser used (maximum rep rate 100Hz) can be considered independently of each other.

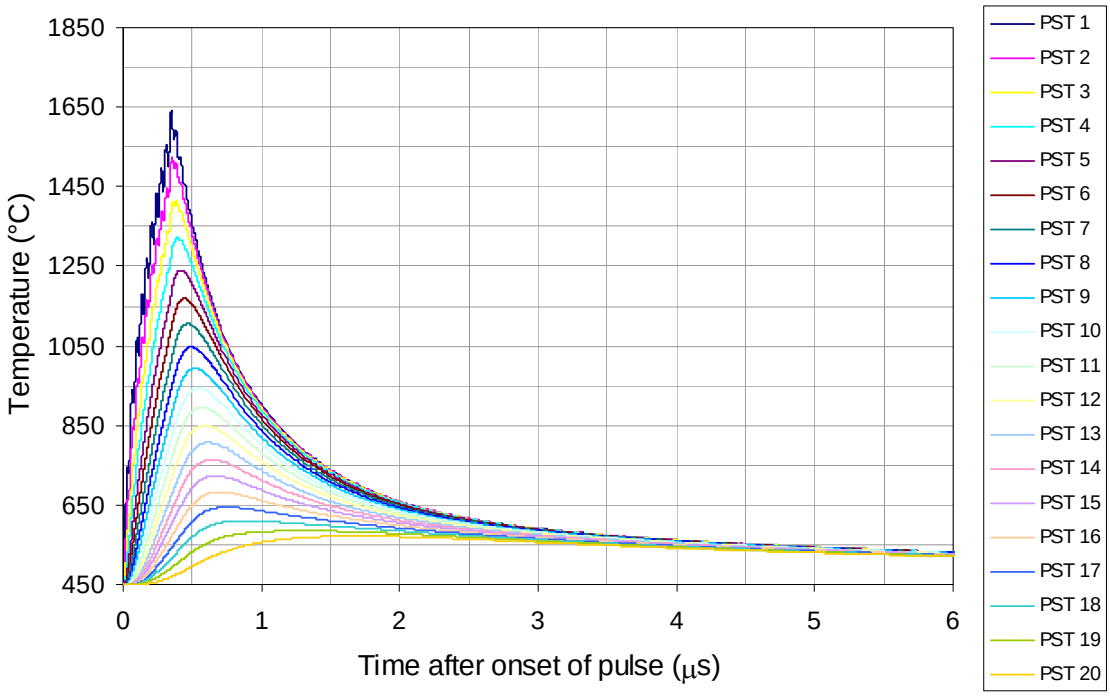

Figure 7.15: Temperature profiles through 1μm thick PST layer, underlying sacrificial layer, 450°C substrate temperature and extended pulse (0.2J/cm^2).
(*Original in colour*)

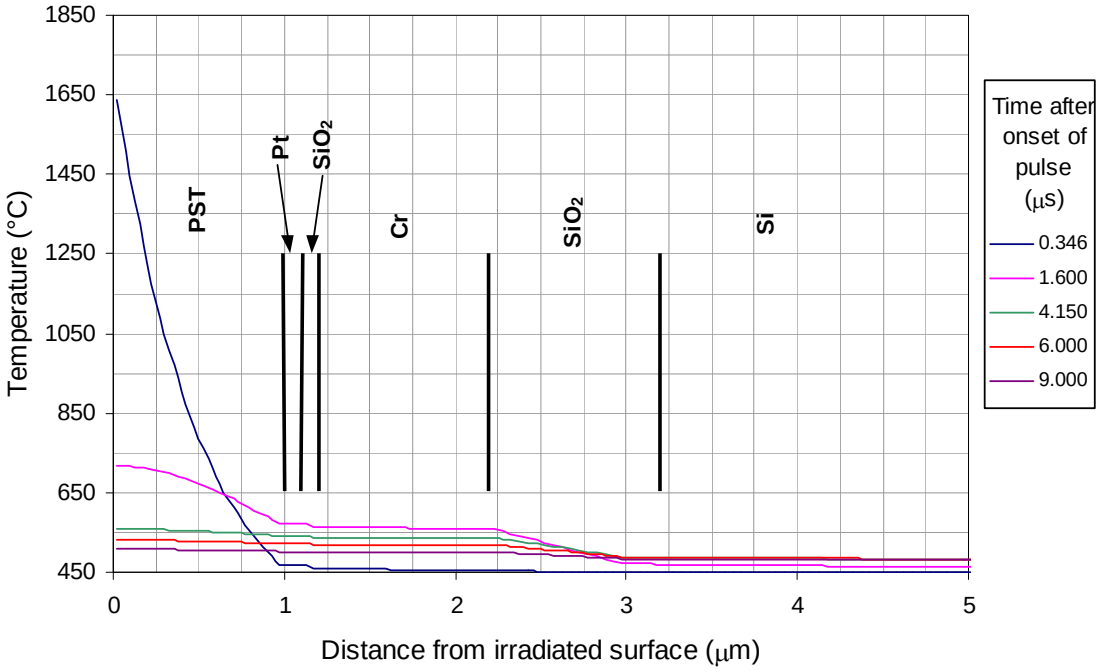

Figure 7.16: Temperature profiles through device layer stack, 1μm of PST, 450°C substrate temperature and extended pulse (0.2J/cm^2).
(*Original in colour*)

The effect of reducing the thickness of the PST thin film to 0.5μm was investigated. Figure 7.17 shows the temperatures in the PST, again with PST1 being the topmost slice, as a result of illumination with an extended pulse of fluence 0.15J/cm^2. For approximately the same maximum temperature of the bottom PST slice, 583°C c.f. 572°C for 1μm of PST, the maximum surface temperature has been reduced markedly from 1642°C to 1270°C.

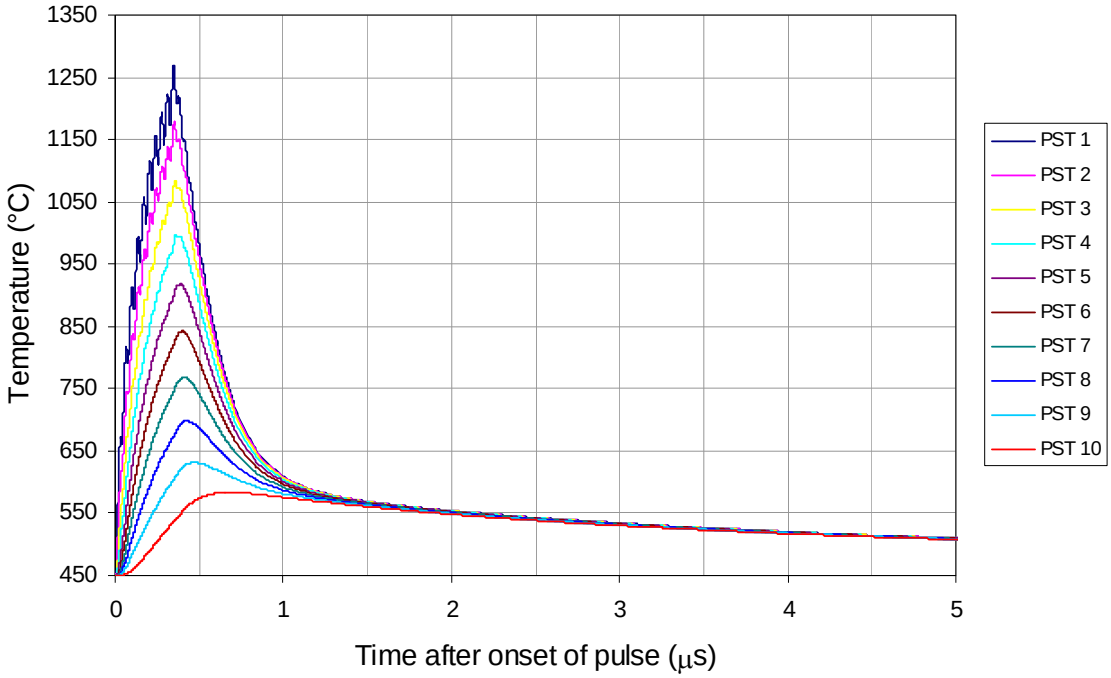

Figure 7.17: Temperature profiles through 0.5μm thick PST layer, underlying sacrificial layer, 450°C substrate temperature and extended pulse (0.15J/cm^2).
(*Original in colour*)

The temperature distribution with depth, Figure 7.18, shows that the topmost silicon slice experiences a maximum temperature of 482°C. Again the thermal barrier action of the overlying SiO_2 layer helps to keep this low.

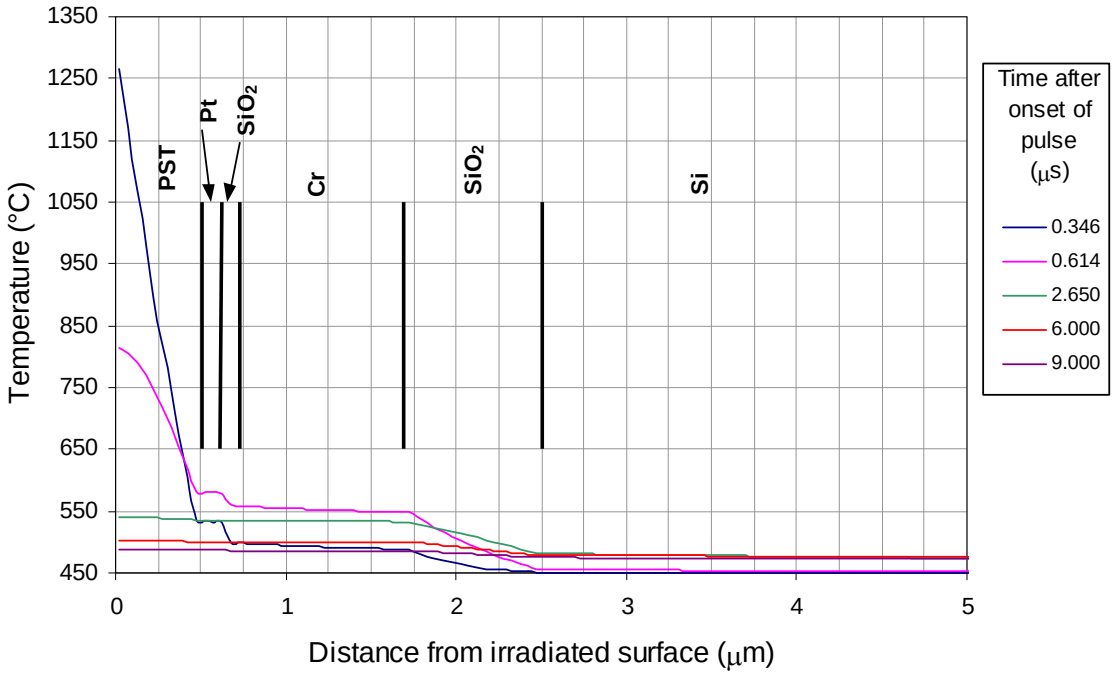

Figure 7.18: Temperature profiles through device layer stack, 0.5μm of PST, 450°C substrate temperature and extended pulse (0.15J/cm^2).
(*Original in colour*)

For a non-extended pulse the switch to 0.5μm thick PST is beneficial in terms of lowering the maximum surface temperature, Figure 7.19, which reaches 1624°C. The temperature profiles through the structure, Figure 7.20, show that the uppermost silicon slice experiences hardly any temperature rise above the 450°C ambient, reaching only 465°C.

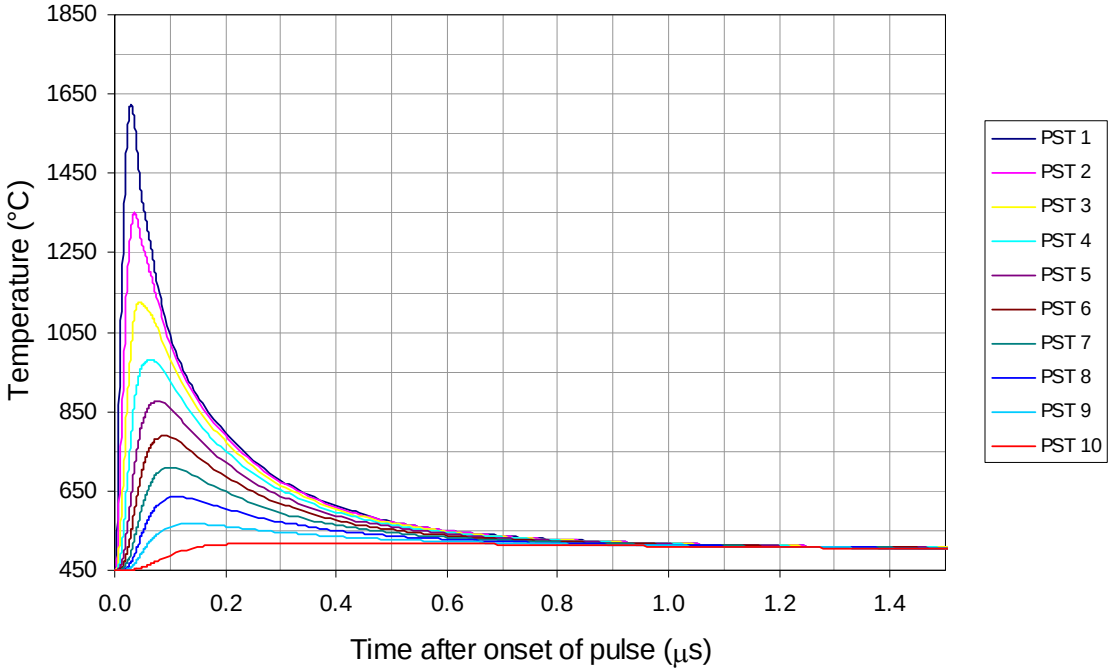

Figure 7.19: Temperature profiles through 0.5μm thick PST layer, underlying sacrificial layer, 450°C substrate temperature and non-extended pulse (0.75J/cm^2).
(*Original in colour*)

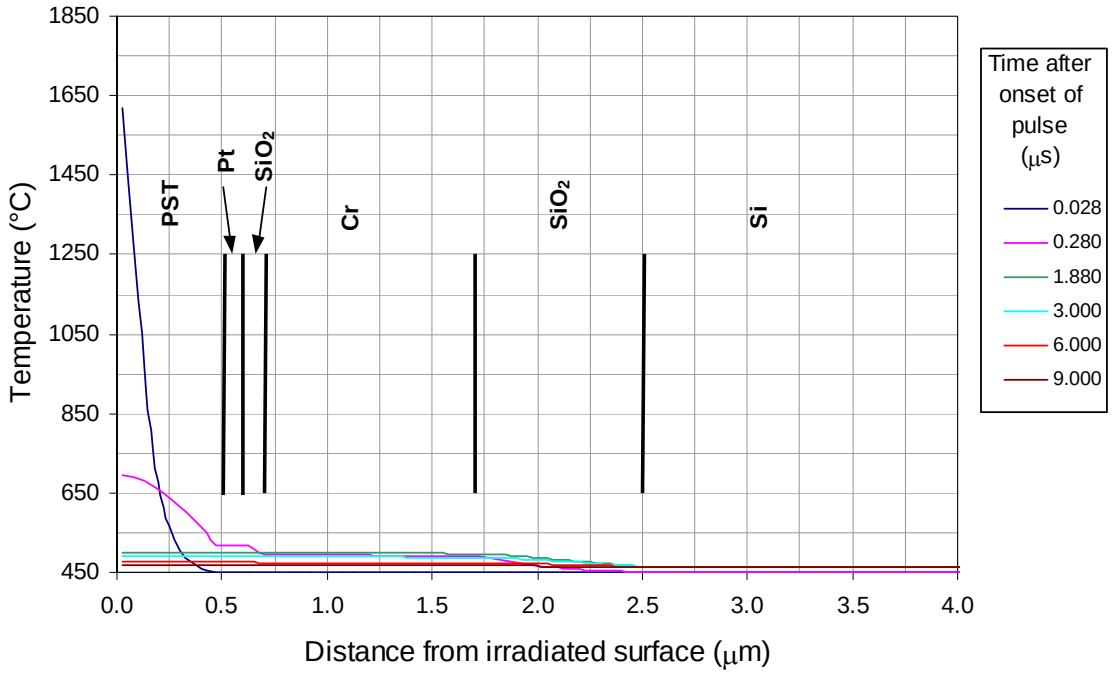

Figure 7.20: Temperature profiles through device layer stack, 0.5μm of PST, 450°C substrate temperature and non-extended pulse (0.075J/cm^2).
(*Original in colour*)

In referring to the figures above, three specific temperatures have been used to compare different annealing conditions. These are the maximum surface temperature (i.e. the

temperature of the topmost PST slice – PST1), the maximum temperature of the bottom PST slice (i.e. the PST slice adjacent to the platinum – either PST20 for a 1μm thickness of PST or PST10 for a 0.5μm thickness of PST), and the maximum temperature of the uppermost silicon slice. The model has been run for a number of sample structures and beam conditions and the results summarised in Table 7.3 in terms of the these three temperatures, which have been designated as $T_{surface}$, $T_{interface}$ and $T_{silicon}$ respectively.

Thickness (μm)	Sacrificial & barrier layers	Fluence (mJ/cm^2)	Extended pulse	$T_{substrate}$ (°C)	$T_{surface}$ (°C)	$T_{interface}$ (°C)	$T_{silicon}$ (°C)
1	SiO_2/Cr	200	Yes	450	1646	571	487
1	none	200	Yes	450	1646	618	501
1	SiO_2/Cr	100	No	450	2056	511	468
1	none	100	No	450	2056	538	479
0.5	SiO_2/Cr	150	Yes	450	1275	582	481
0.5	none	150	Yes	450	1285	657	498
0.5	SiO_2/Cr	75	No	450	1654	519	465
0.5	none	75	No	450	1654	561	473
1	SiO_2/Cr	200	Yes	450	1642	572	488
1	none	200	Yes	450	1642	620	501
1	SiO_2/Cr	100	No	450	2016	512	468
1	none	100	No	450	2016	538	475
0.5	SiO_2/Cr	150	Yes	450	1270	583	482
0.5	none	150	Yes	450	1280	659	499
0.5	SiO_2/Cr	75	No	450	1624	520	465
0.5	none	75	No	450	1624	562	473

Table 7.3: Predicted anneal temperatures for PST.

The modelled temperature profiles in layer stacks with PZT as the topmost layer have a similar form to those shown for PST in Figures 7.13 to 7.20 with the characteristic temperatures $T_{surface}$, $T_{interface}$ and $T_{silicon}$ given for a range of PZT thicknesses and annealing conditions in Table 7.4. Since PZT has a slightly higher diffusivity than PST ($5.14\times10^{-7}m^2/s$ cf $4.85\times10^{-7}m^2/s$) the predicted values of $T_{surface}$, for the same annealing conditions, are lower while $T_{interface}$ and $T_{silicon}$ are comparable. The predicted results for a substrate temperature of 300°C relate to experimental work reported in Chapter 8. The general conclusion for PZT films is the same as that for PST with the advantages of pulse extension being clear, i.e. lower peak surface temperatures and improved heat penetration into the PZT thin film whilst still keeping the underlying silicon well below the damage threshold levels identified in Chapter 4.

Thickness (μm)	Sacrificial & barrier layers	Fluence (mJ/cm^2)	Extended pulse	$T_{substrate}$ (°C)	$T_{surface}$ (°C)	$T_{interface}$ (°C)	$T_{silicon}$ (°C)
1	SiO_2/Cr	200	Yes	450	1536	562	484
1	none	200	Yes	450	1536	604	497
1	SiO_2/Cr	100	No	450	1908	507	467
1	none	100	No	450	1908	531	472
0.5	SiO_2/Cr	150	Yes	450	1196	573	479
0.5	none	150	Yes	450	1206	642	494
0.5	SiO_2/Cr	75	No	450	1543	515	464
0.5	none	75	No	450	1543	553	471
0.5	SiO_2/Cr	100	Yes	300	798	387	317
0.5	none	100	Yes	300	805	438	324
0.5	SiO_2/Cr	100	No	300	1758	390	317
0.5	none	100	No	300	1758	444	324

Table 7.4: Predicted anneal temperatures for PZT.

7.5. Discussion

Problems with uniformly heating the PST or PZT thin films result from their very short absorption lengths, <30nm, and very low thermal diffusivities. These two factors combined mean that illumination using a very short (standard) excimer laser pulse result in very high surface temperatures and poor heating of the PST/PZT film down towards the interface with the platinum bottom electrode, even with substrate heating. The possibility of high surface temperatures is a potential problem from the point of view of ablation of material from the illuminated surface and chemical decomposition due to loss of one or more of the constituent atomic species. Depending on the form of the ferroelectric layer, i.e. amorphous or polycrystalline pyrochlore, the possible effects may be varied. If the materials are in an amorphous form then the most volatile constituent will be lead oxide (PbO), (assuming all components are fully oxidised) which has a melting temperature of 890°C [73, 135], and a very high vapour pressure, making lead loss a distinct possibility. Melting points of other oxides of interest are Sc_2O_3 at 2845°C, Ta_2O_5 at 1780°C, ZrO_2 at 2710°C and TiO_2 at 1843°C [73]. Modelling indicates that illumination of 1μm thick PST with a standard pulse at a fluence of 0.1J/cm^2, Figure 7.13 and Table 7.3, results in surface temperatures of the order of 2000°C. This is hot enough not only to affect the lead content but also tantalum in amorphous compositions. For PZT with the same annealing conditions the peak surface temperatures

are are slightly lower but still above the TiO_2 melting temperature. The is a question of what would happen to the lead at temperatures well above the lead oxide melting temperature, and whether it would be "locked" into the stable perovskite structure or just evaporate – or some combination of the two! Thinning of the PST layer to 0.5μm results in reduced surface temperatures of the order of 1600°C at a fluence of 75mJ/cm^2, Figure 7.17 and Table 7.3. The effect of very high surface temperatures on pyrochlore compositions may be to chemically decompose and ablate the materials either in conjuction with or instead of transformation to the perovskite phase. The relatively low temperatures developed near the platinum interface is a cause for concern in that for the non pulse extended case it may not be possible to convert a 0.5μm thickness of PST or PZT to perovskite, let alone 1μm.

The use of a temporal pulse extender, such as the one described, effectively slows down the rate of delivery of laser energy to the surface. For an increase in the fwhm of the pulse from 25ns to ~375ns this results in a factor of four increase in the diffusion length, resulting in improved heat penetration into the ferroelectric layer. For a 1μm thick PST layer, exposure to an extended pulse at a fluence of 200mJ/cm^2, results in surface temperatures of ~1600°C and temperatures at the ferroelectric/platinum interface of ~570°C. These represent both a lower upper-surface temperature and a higher lower-surface temperature than for the non-extended case. Interestingly, for both PST and PZT the temperature of the lower reaches of the ferroelectric layer, i.e. near the interface with the platinum, are above the lower range of temperatures at which PST[4, 5, 96, 137] and PZT[24, 89, 92, 138] can be grown when nucleated on platinum, although the time spent at these temperatures is only of the order of microseconds for each pulse. Thinning the ferroelectric layer to 0.5μm again, as for the non-extended case, results in a further improvement in the temperature distribution. For the case of PST a fluence of 150mJ/cm^2 results in a maximum surface temperature of ~1250°C, with the maximum temperature at the ferroelectric-platinum interface temperature being ~580°C. It may be noted that in both non-extended and extended pulse cases, for PST and PZT, that the temperature of the platinum electrode, silicon dioxide barrier and chrome sacrificial layers is kept below 650°C, for a substrate heater temperature of 450°C, thereby reducing the likelyhood of interdiffusion between these layers.

The temperature distributions predicted by the modelling give an indication of the timescales over which the PST or PZT layers remain hot enough for nucleation and growth

of the perovksite to take place. Since the highest temperatures are developed at the surface it is anticipated that nucleation will occur here and a growth front will propagate down towards the interface with the platinum. For both extended and non-extended pulses the ferroelectric layer remains signficantly hot for times on the order of microseconds. This suggests that a large number of pulses would be required for complete conversion to perovskite – as alluded to by Varshney et al [113]. As was seen in Chapters 5 and 6 a thirty second RTP anneal was insufficient to completely transform a 0.6μm and 0.8μm thicknesses of PST, although it was sufficient for 0.5μm of PZT. In the case of the laser, the top slices of material are very much hotter than this, while the lower slices (in the pulse-extended case) are of this order, and so the process might be expected to progress faster than RTP. Even so, ten thousand pulses would only be equivalent to a few tens of milliseconds of effective annealing time.

The predicted temperature distributions show that the SiO_2 in the sample structures effectively acts as a thermal barrier layer. This layer acts to supress the temperature rise of the underlying silicon by slowing the rate of downwards diffusion of heat. The high thermal diffusivity of silicon also helps to restrict its temperature rise. Silicon dioxide layers are included in the structures only as barrier or buffer layers and were not intended as a thermal buffer layer, unlike Kuriyama et al [119], who did make use of 1.5μm of SiO_2 as a thermal buffer layer in order to suppress the temperature rise of the glass substrate in poly-Si TFT annealing studies.

7.6. Summary

An experimental setup for the excimer laser annealing of thin films has been described in conjunction with a theoretical modelling study of the temperature distributions developed in PST and PZT thin film structures during laser illumination. The modelling study was used both to investigate the viability and also to establish initial operating parameters for the experiment. Several important points came out of the modelling which significantly influenced the form of the laser annealing system. To keep the illuminated surface temperatures down and also bring the temperature of all of the PST (and PZT) thin films up to useful levels it was found that substrate heating and also temporal extension of the laser pulse proved very beneficial. Use of the latter is considered to be a novel approach to the problem and has resulted in a patent application [139]. Modelling has shown that laser annealing is, in theory, capable of preferentially heating the ferroelectric layer whilst not

raising the temperature of the underlying silicon above 500°C. In Chapter 4 it was shown that active readout circuitry can withstand temperatures of that order for extended periods without damage. The problem does however appear to be more tractable for thinner (0.5μm) PST and PZT layers. Reducing the ferroelectric thickness results in a significant reduction of the absorption in an RAB device structure, but is far less significant in a XAC structure where the majority of the absorption is in the resonant gap between microbridge and substrate.

Chapter 8:

Pulse-Extended Excimer Laser Annealing.

8.1 Introduction

Work reported in this chapter describes the results of annealing experiments carried out using the laser annealing apparatus described in Chapter 7. The experimental conditions used were in accordance with the modelling studies described in the previous chapter. Since the modelling showed the clear advantages of extending the duration of the excimer laser pulse, only samples annealed with the extended pulse will be presented. Most initial success has been gained with PZT thin films and these will form the basis of the work presented in this chapter.

8.2 Experiment

8.2.1 Starting Material

The material used for the experiments was thin film PZT 30/70 ($PbZr_{0.3}Ti_{0.7}O_3$), wafer designation AP#510, supplied to the author by Dr. Anil Patel of BAE Systems. This had been deposited onto a platinised silicon substrate using a sol-gel spin deposition technique [57, 58] described in Chapter 3. The substrates had been prepared by sputter depositing a ~100∑ thick titanium adhesion layer onto a thermally oxidised 6" silicon wafer, followed by the sputter deposition of a ~1000∑ thick platinum layer. Both the titanium and platinum were deposited in the same Nordiko NM2000 deposition system. The starting sol included a 10% Pb excess which in the standard spin and fire process aids crystallisation and compensates for lead loss during firing [103]. Five layers were spin deposited and pyrolysed at 300°C to remove the organic components with the thickness of the final film being ~0.46-0.5μm.

8.2.2 Annealing Conditions

All samples were annealed in an ambient of oxygen at a pressure of 800mbar. The ambient temperature was set to 300°C using the substrate heater. This temperature was chosen partly as a result of the modelling studies discussed in Chapter 7 and partly to prevent

nucleation of perovskite PZT at the PZT/platinum interface. The latter would lead to confusion when trying to determine whether the laser or the substrate heater had caused the PZT to convert to perovskite. The output lens on the beam homogeniser was chosen to give a uniform square beam profile of side 7.5mm. This was sufficiently large for materials characterisation purposes and sufficiently small to ensure that the required fluence levels from the laser were easily obtainable. In all cases the laser was operated at a repetition rate of 10Hz. Table 8.1 below gives the annealing conditions used for the samples. The beam energy level at the sample plane was determined as the average of 100 pulses recorded using a Gentec ED500 Joulemeter used in conjunction with a Gentec Sun series energy meter. The size of the homogenised beam at the sample plane was determined using laser burn paper and a travelling microscope.

Sample	Identifier	Fluence (mJ/cm^2)	Number of pulses
AP#510 piece R5	Sample R5	80	1
AP#510 piece R6	Sample R6	80	10^2
AP#510 piece R7	Sample R7	80	10^3
AP#510 piece L7	Sample L7	80	10^4
AP#510 piece R10	Sample R10	80	16×10^4
AP#510 piece R9	Sample R9	90	10^4
AP#510 piece R8	Sample R8	80/90	$10^4/10^4$
AP#510 piece L8	Sample L8	80/100	$10^4/10^4$
AP#510 piece L10	Sample L10	100	10^4
AP#510 piece L4	Sample L4	117	10^2
AP#510 piece L3	Sample L3	200	1
AP#510 piece L2	Sample L2	200	10^2
AP#510 piece L1	Sample L1	200	10^3

Table 8.1: Annealing conditions.

For samples R8 and L8 a combination of two fluence levels was used. The purpose of this was to investigate whether the near surface PZT could be crystallised with a lower fluence into the stable perovskite phase which would then withstand a higher fluence aimed at driving the crystallisation front further into the material. As a control to ensure that the material could actually be crystallised into the perovskite phase, a piece was RTP annealed at 650°C for 30s in flowing O_2 – a regime known to transform this type of material [31, 32, 64, 88, 89, 90, 92].

8.3 Results

8.3.1 Compositional Analysis by Energy Dispersive Spectroscopy

Energy dispersive spectroscopy was used to determine the composition of the PZT thin films. As for PST films in the preceding chapters quantitative analysis was performed using single element standards. It will become clear below that due to the nature of the heating induced by the laser, the samples have a graded structure from the top surface down. The nature of EDS is that the X-Ray fluorescence occurs in the X-Ray volume. We recall from Chapter 3 that in PZT of mean density 8.14kgm^{-3} (perovskite bulk ceramic) the X-Ray ranges (R) for Pb M_α, Zr L_α and Ti K_α radiation are 0.71μm, 0.7μm and 0.64μm respectively at an acceleration voltage of 15KeV. For a 0.5μm thick film analysed at an incident angle of 45°, giving an effective thickness of 0.71μm, this means that the X-Ray volume extends down to the platinum, especially in the case of zirconium. This is problematic since there is an overlap between the Zr L_α (2.04KeV) and Pt $M_{\alpha1}$ (2.05KeV) and the EDS system can have difficulty separating the two contributions. A simple solution to this problem is to analyse at an accelerating voltage of 10KeV where the X-Ray ranges for Pb Mα, Zr Lα and Ti Kα are 0.34μm, 0.35μm and 0.28μm respectively thereby avoiding excitation of the troublesome platinum $M_{\alpha1}$ peak. The known composition of the starting sol and composition by EDS of the as-deposited material were used as the control.

Table 8.2 below gives the EDS compositional analysis results for some of the samples. For one of the 200mJ/cm^2 illuminated samples, L1 – 10^3 pulses, the platinum $M_{\alpha1}$ and silicon $K_{\alpha1}$ peaks were more prominent. Also sample L2, 10^2 pulses, showed a more prominent Zr Lα peak. The fits for samples L2 and L1 were poor without the inclusion of platinum, and platinum and silicon respectively. Even with these elements included the fits were still poor relative to the other samples. This suggest that these films were thinned, at least in places – a fact confirmed by SEM inspection, section 8.3.2 below, resulting in X-Ray generation in the underlying layers.

Sample	$\frac{Zr}{Zr+Ti} : \frac{Ti}{Zr+Ti} : \frac{Pb}{Zr+Ti}$	
	Annealed area	Non-annealed area
As-deposited	-	0.33:0.67:1.12
R5	0.30:0.70:1.12	0.32:0.68:1.14
R6	0.31:0.69:1.13	0.31:0.69:1.12
R7	0.30:0.70:1.07	0.30:0.70:1.13
L7	0.33:0.67:1.14	0.32:0.68:1.09
L4	0.31:0.69:1.12	0.31:0.69:1.08
L3	0.31:0.69:1.13	0.33:0.67:1.14
L2 (no Pt)	0.38:0.62:1.03	0.32:0.68:1.12
L2 (with Pt)	0.15:0.85:1.39	-
L1 (no Pt or Si)	0.74:0.26:0.59	0.31:0.69:1.18
L1 (with Pt & Si)	0.00:1.00:2.19	-

Table 8.2: Sample composition by EDS before and after annealing.

The general trend in the samples is to give a slight zirconium excess and titanium deficiency than might be expected from the starting sol composition. In general the lead ratio is slightly higher than the 10% excess expected from the sol. Analysis of similar samples using X-Ray Photoelectron Spectroscopy by Impey et al [140] did indicate compositional fluctuations with zirconium and lead excess and titanium deficiency at the layer interfaces. This may partially account for the observed compositions since the X-Ray interaction volumes at 10KeV may result in the preferential sampling of layer boundary regions. With the exception of samples L2 and L1 the composition after annealing can be seen to be largely unchanged. The results for L2 and L1 illustrate the difficulty for the system in decoupling the X-Ray contributions from platinum and zirconium.

8.3.2 Optical and Scanning Electron Microscope Analysis

The effect of laser irradiation on the surface morphology of the samples was ascertained qualitatively using optical microscopy and SEM. Pictures of the surfaces of the samples are shown in Figures 8.1 to 8.18 below

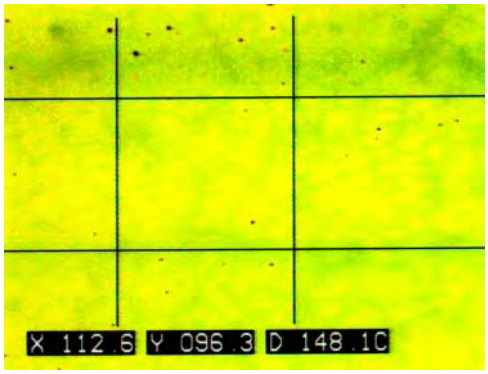

Figure 8.1: Optical picture of sample L7. (*Original in colour*)

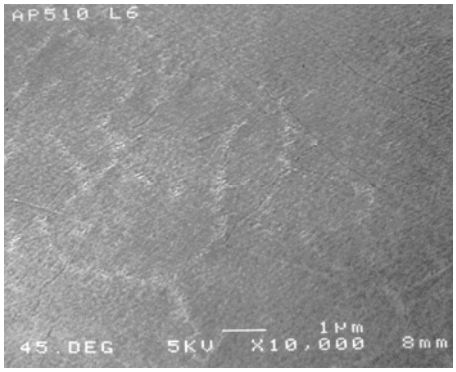

Figure 8.2: SEM picture of sample L7.

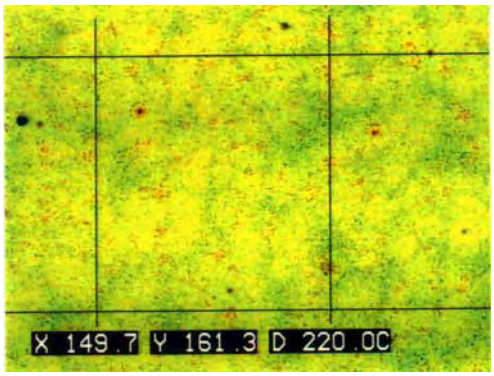

Figure 8.3: Optical picture of sample R10. (*Original in colour*)

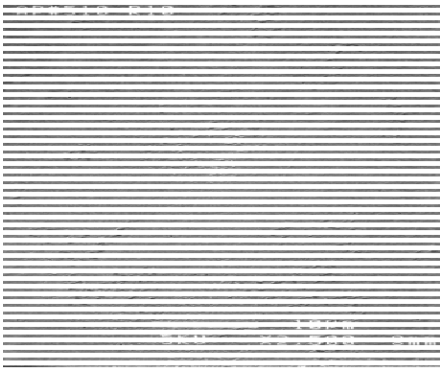

Figure 8.4: SEM picture of sample R10.

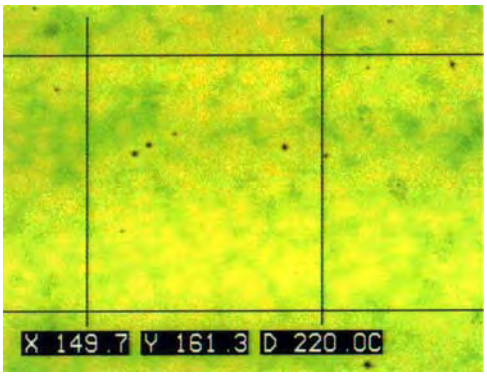

Figure 8.5: Optical picture of sample R9. (*Original in colour*)

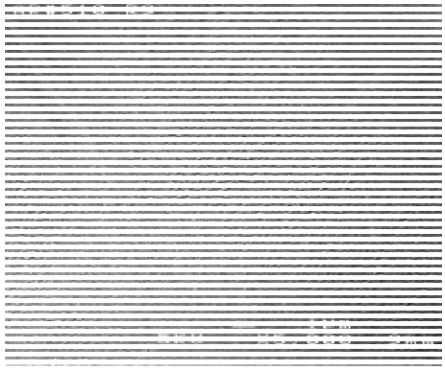

Figure 8.6: SEM picture of sample R9.

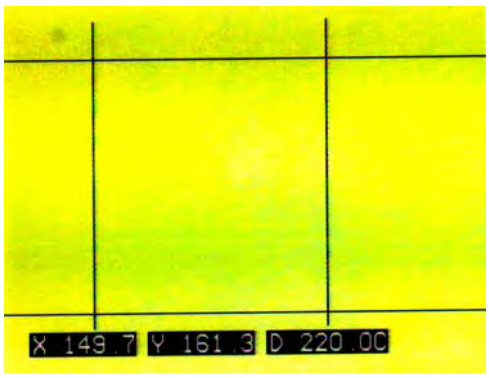

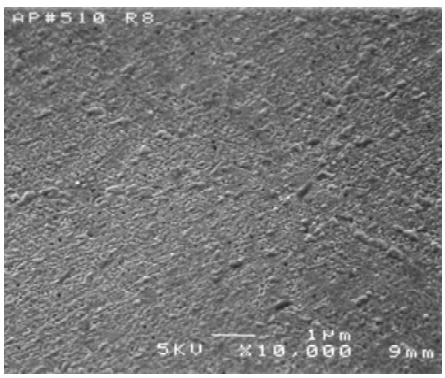

Figure 8.7: Optical picture of sample R8. (*Original in colour*)

Figure 8.8: SEM picture of sample R8.

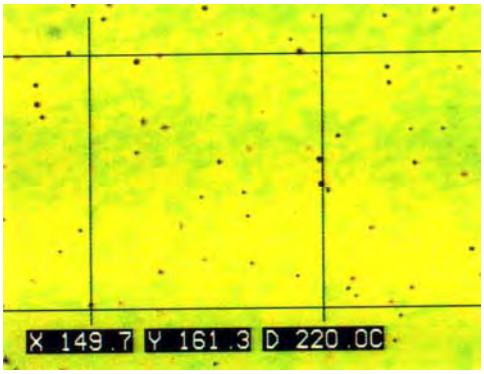

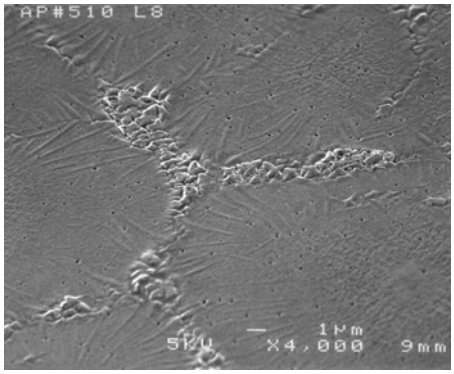

Figure 8.9: Optical picture of sample L8. (*Original in colour*)

Figure 8.10: SEM picture of sample L8.

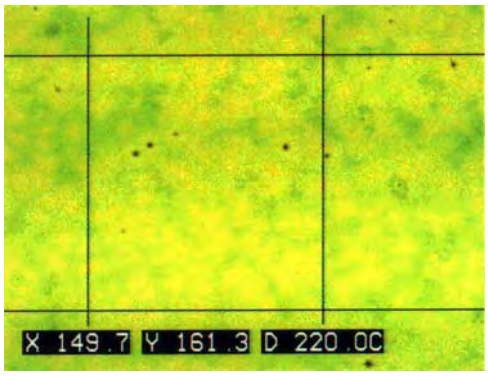

Figure 8.11: Optical picture of sample L10. (*Original in colour*)

Figure 8.12: SEM picture of sample L10.

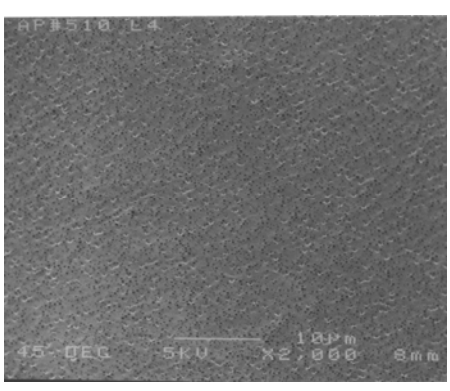

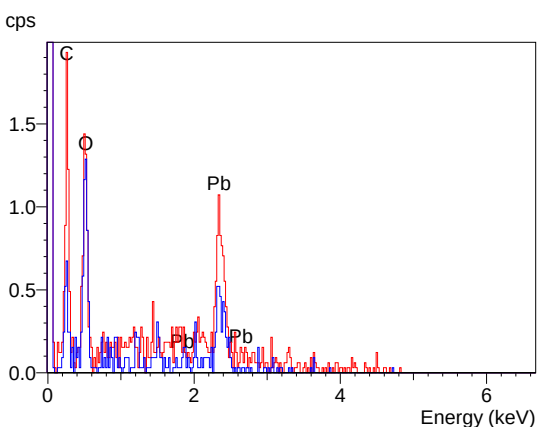

Figure 8.13: SEM picture of sample L4.

Figure 8.14: EDS spectra from black spot (red) and general area (blue). (*Original in colour*)

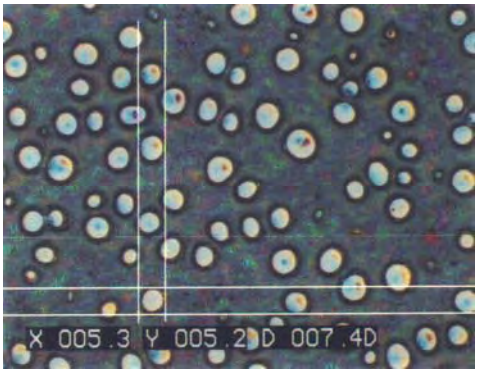

Figure 8.15: Optical picture of sample L2. (*Original in colour*)

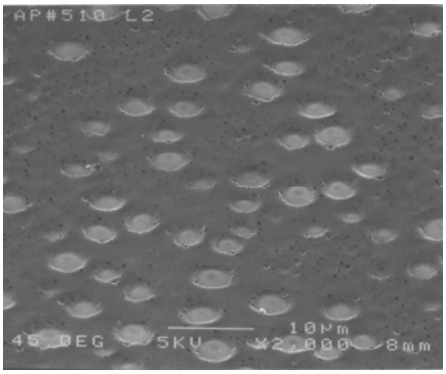

Figure 8.16: SEM picture of sample L2.

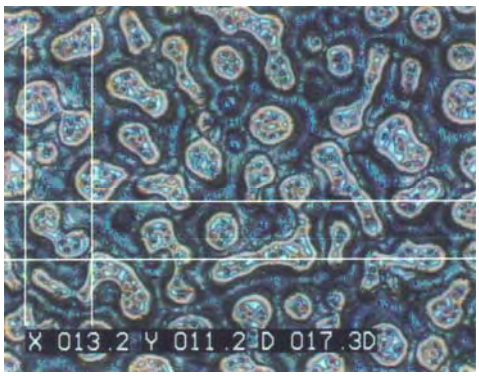

Figure 8.17: Optical picture of sample L1. (*Original in colour*)

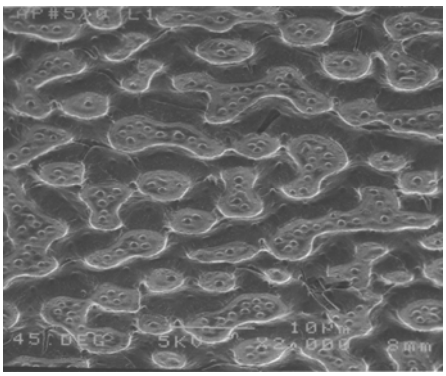

Figure 8.18: SEM picture of sample L1.

Samples irradiated at a fluence of 80mJ/cm^2 only, L7 and R10 and Figures 8.2 and 8.4, show relatively featureless surfaces with no obvious beam induced damage. Sample R9, 90mJ/cm^2 for 10^4 pulses – Figure 8.6, has a more structured surface with grain-like features occurring in patches and some small scale pitting of the surface. Sample R8, 80mJ/cm^2 for 10^4 pulses followed by 90mJ/cm^2 for 10^4 pulses – Figure 8.8, has a similar surface to sample R9 except that the grain like features are uniformly distributed. Again pitting of the surface on a fine scale can be observed. An increase in the laser fluence resulted in more

striking surface features. Sample L8 also had a two step anneal, 80mJ/cm^2 for 10^4 pulses followed by 100mJ/cm^2 for 10^4 pulses – Figure 8.10. There is what appears to be a network of grains arranged into linear features surrounding smoother regions with pronounced pitting of the surface.

Sample L10 was given a single energy anneal using a fluence of 100mJ/cm^2 for 10^4 pulses. The SEM picture shown in Figure 8.12 shows that there has been significant surface modification. Smooth regions are interspersed with areas having rough surfaces comprising regular linear features which are similar to the so-called laser induced periodic surface structures (LIPSS) reported for laser annealing of other materials[141]. LIPSS arise due to scattering of part of the incident beam across the sample surface. Interaction of this scattered part of the beam with the normal incident part of the beam results in an interference pattern which can melt the surface resulting in a periodic ripple pattern[141]. Again there is pitting of the surface. Sample L4 was annealed at a slightly higher fluence, 117mJ/cm^2 for 100 pulses, and the surface morphology is shown in Figure 8.13. The SEM picture shows a heavily pitted surface with a high density of black spots approximately a quarter of a micron across which originate from relatively conducting regions acting as sinks for the beam current. Figure 8.14 shows EDS spectra taken from a general region and a spot, using a JOEL JSM6400F SEM in conjunction with an Oxford Link windowless EDS system, and shows that spectrum for the spot has a high carbon count in comparison to non-spotty regions of the PZT. This carbon would have originated from the original sol and indicates that the pyrolysis at 400°C did not entirely remove all of the organic components. Pitting on other samples could be the result of explosive evolution of carbon from the film in gaseous form, i.e. CO or CO_2.

Figures 8.15 to 8.18 show the surfaces resulting from annealing using a high fluence beam of 200mJ/cm^2. They are highly disrupted in a fashion indicative of melting and reflow with the resulting variable thickness of the PZT explaining the appearance of silicon in the EDS spectra collected from these samples.

8.3.3 X-Ray Diffraction Analysis

XRD analysis of the annealed samples was performed using a Siemens D5005 high resolution diffractometer in Bragg-Brentano geometry with the data collected by Dr J.C. Jones of DERA using a Seimens D5005 high resolution diffractometer with the beam

stopped down to give an illuminated area on the sample of ~2mm×2mm. Each sample was analysed both within and outside the annealed region. The θ-2θ scan for the as-deposited sample, Figure 8.19, shows the underlying platinum to be (111) textured with the PZT exhibiting a weak broad peak ~29.5°[64] symptomatic of an amorphous/poorly crystallised pyrochlore structure.

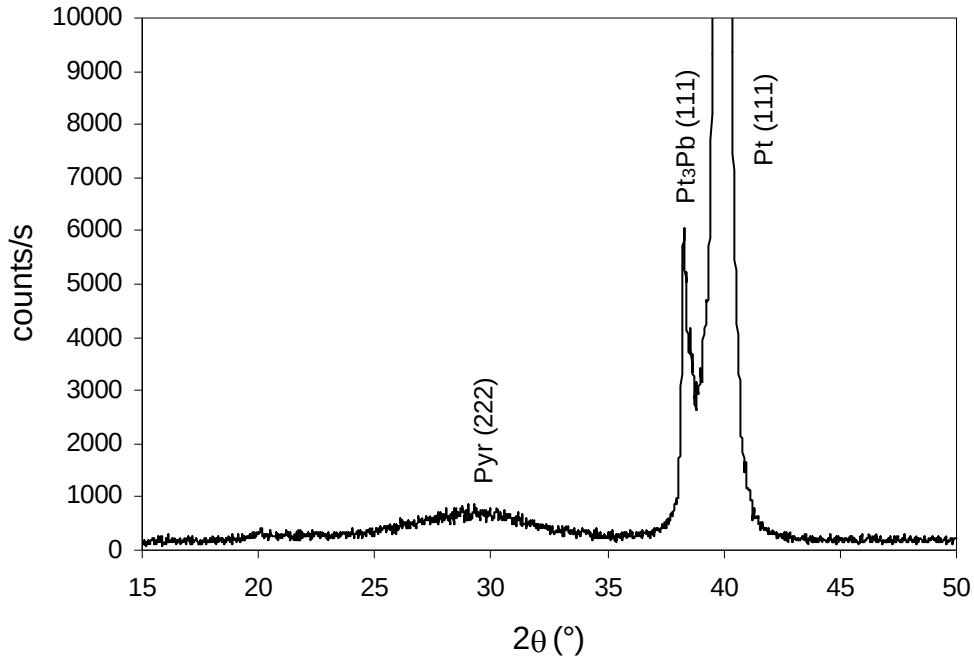

Figure 8.19: XRD θ-2θ scan of as-deposited material. *Pyr* indicates pyrochlore reflections.

As mentioned previously a sample was RTP annealed as a control to check that the starting material could be crystallised. Figure 8.20 shows the θ-2θ scan for this sample. Only PZT perovskite reflections were observed with the broad peak at ~29° seen on the as-deposited sample having disappeared, indicating complete transformation. The perovskite can be seen to be (111) textured, following the underlying platinum, with relatively low intensity (100) and (200) reflections.

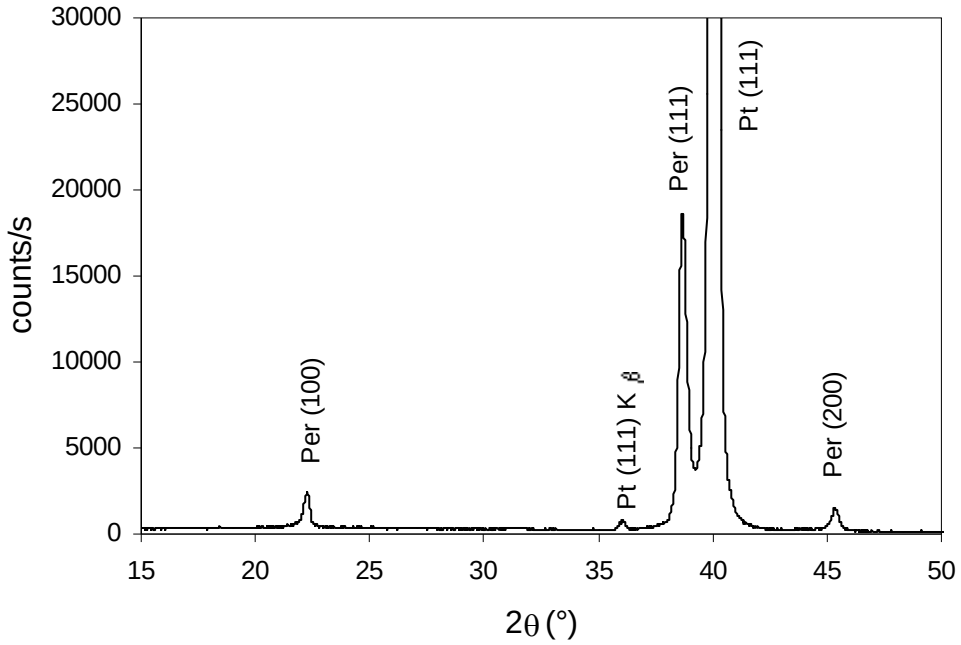

Figure 8.20: XRD θ-2θ scan of RTP annealed material. *Per* indicates perovskite reflections.

Samples R5 and R6, fluence of 80mJ/cm^2 for 1 and 100 pulses respectively, showed no evidence by XRD of conversion with θ-2θ scans similar to the as-deposited sample. XRD θ-2θ scans for samples R7, L7 and R10 are shown in Figure 8.21. The scan for sample R7 (80mJ/cm^2, 10^3 pulses) shows a pyrochlore (222) reflection with no perovskite reflections. This pyrochlore is a metastable phase formed prior to perovskite - given that PZT converts from an amorphous phase to perovskite via a metastable pyrochlore phase [32]. Scans for samples L7 and R10 (80mJ/cm^2 for 10^4 and 16×10^4 pulses respectively) show that there has been some conversion to perovskite with (100), (110) and (200) reflections observed with the (100) being dominant. Absence of the (111) reflection suggests that the underlying platinum has not influenced the perovskite growth. The relative intensity of the reflections suggests that the perovskite grains are not randomly orientated, as in the case of PZT ceramic [142, 143] where the (110) reflection is dominant. Incomplete conversion is indicated by the presence of a pyrochlore (222) reflection. XRD θ-2θ scans for the laser annealed samples R8, R9, L8 and L10 shown in Figure 8.22 and again reveal mixed orientation perovskite with some pyrochlore.

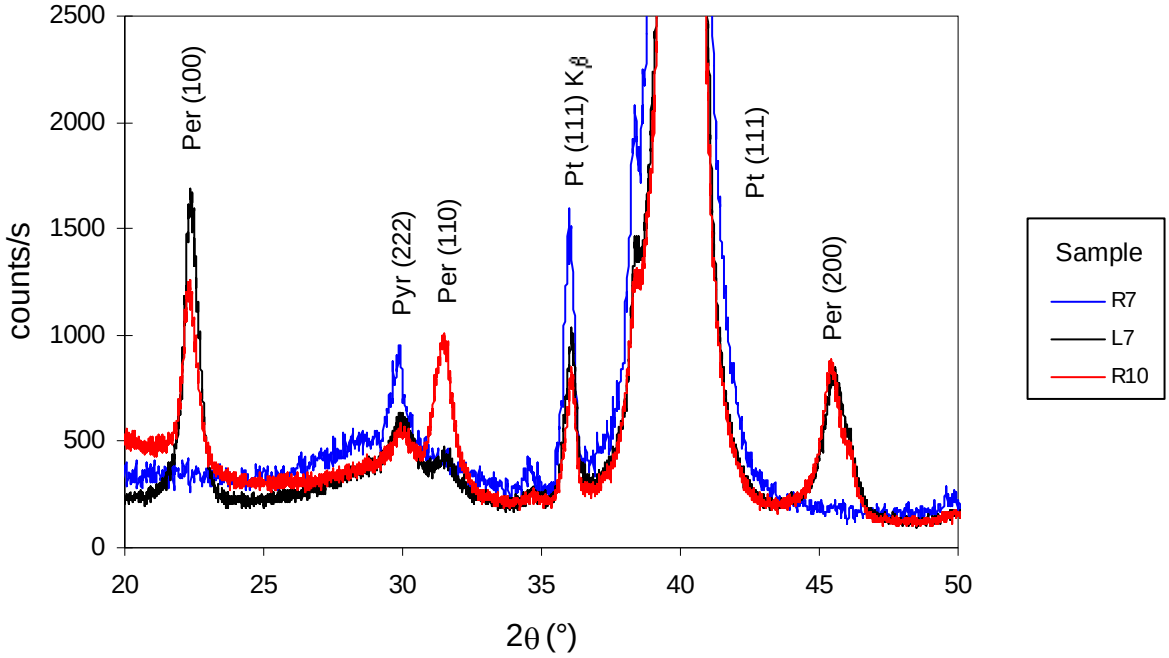

Figure 8.21: XRD θ-2θ scan of samples R7,L7 and R10.
(*Original in colour*)

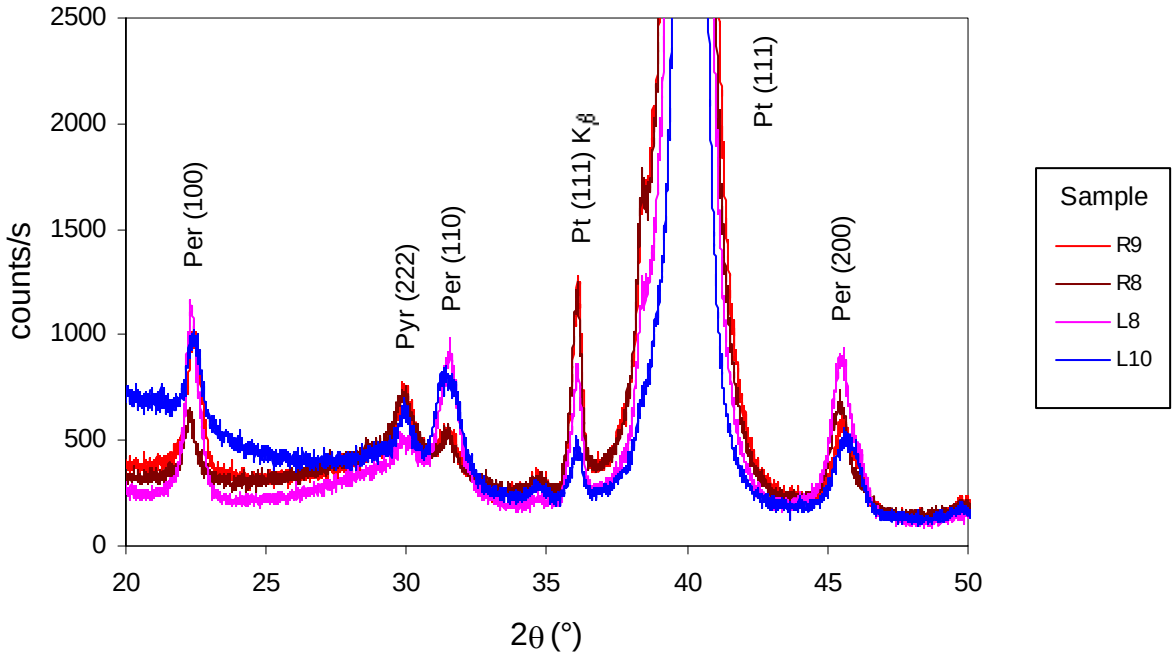

Figure 8.22: XRD θ-2θ scan of samples R8, R9, L8 and L10.
(*Original in colour*)

θ-2θ scans for the >100mJ/cm^2 fluence annealed samples are shown in Figures 8.23 and 8.24 below. Only sample L1 shows evidence of conversion to perovskite, even though the SEM picture of the surface shows the PZT to be highly disrupted, with the distribution of orientations being similar to other partially converted samples except that the pyrochlore peak at ~29° is relatively strong.

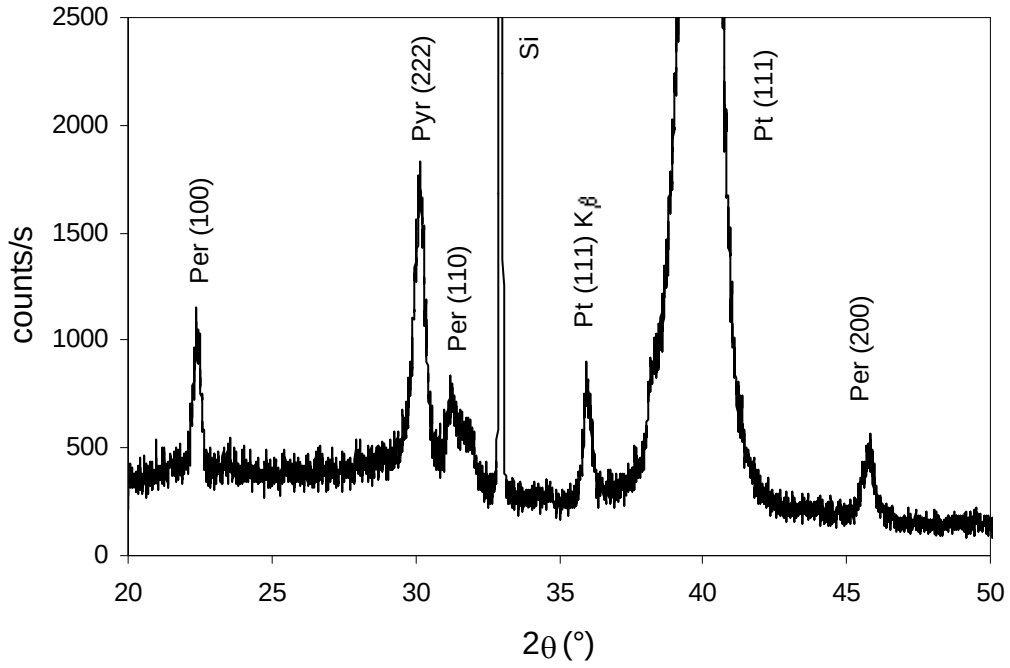

Figure 8.23: XRD θ-2θ scan of sample L1.

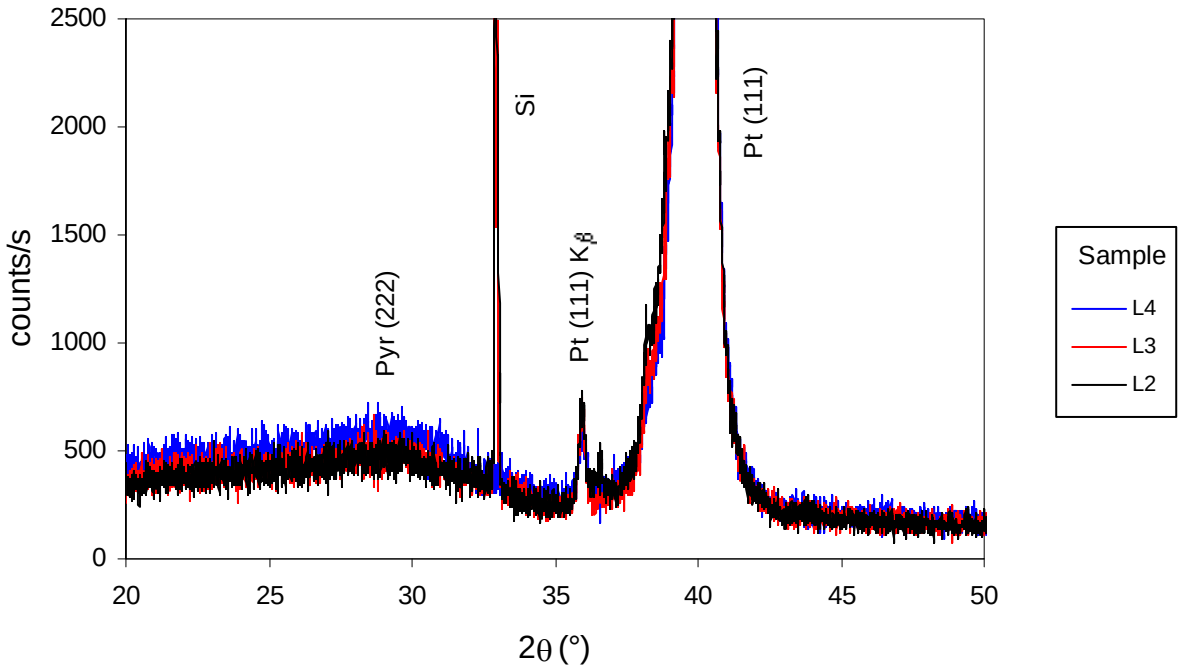

Figure 8.24: XRD θ-2θ scans of samples L2, L3 and L4.

(*Original in colour*)

Given that the pyrochlore phase is cubic [31], the lattice parameter calculated from the (222) reflection is 10.29∑. The perovskite phase of PZT 30/70 is tetragonal at room temperature (see the phase diagram, Chapter 2 section 2.4). Calculation of the lattice parameters using the (200) and (211) reflections gives a and c as 3.995∑ and 4.110∑ respectively.

8.3.4 Transmission Electron Microscopy

TEM analysis was performed on a number of the samples in order to determine the nature of the cyrstallisation to perovskite revealed by the XRD analysis. This was carried out both at DERA and at Cranfield University by Dr. D.J. Wallis and Dr. Z. Huang respectively. TEM cross sections of samples L7 (80mJ/cm^2, 10^4 pulses), R10 (80mJ/cm^2, 16×10^4 pulses) and L8 (80mJ/cm^2 for 10^4 pulses followed by 100mJ/cm^2 for 10^4 pulses) are shown in Figures 8.25-8.27. The lamella for sample L7 was prepared using the FIB technique described in Chapter 3, while those of samples R10 and L8 were prepared using conventional techniques (also described in Chapter 3).

Figure 8.25 shows the cross section for sample L7 with the PZT and platinum thin films clearly visible. The PZT shows a graded structure from the top surface downwards. Close to the irradiated surface are large perovskite grains. This indicates that perovskite has crystallised in the absence of a nucleating surface in a fashion akin to the case for bulk ceramic. Underneath this is a region of PZT which has been partially crystallised into perovskite but is mostly pyrochlore. The lower region of the PZT is seen to be amorphous and has not been modified by the beam. A line is clearly visible about 0.1μm up from the PZT/Pt interface. This is probably caused by diffraction contrast resulting from compositional variation due to elemental segregation at the PZT layer boundaries, as was observed by Impey et al for similar material [140]. It is interesting to note that there has been no crystallisation of perovskite at the PZT/Pt interface, as is observed in hotplate annealing [140] at 460°C – 515°C, suggesting that this interface has not moved far from the 300°C ambient temperature of the substrate heater. Also repeated laser pulses have not caused the sample temperature to generally rise to a level at which perovskite would nucleate at the PZT/platinum interface.

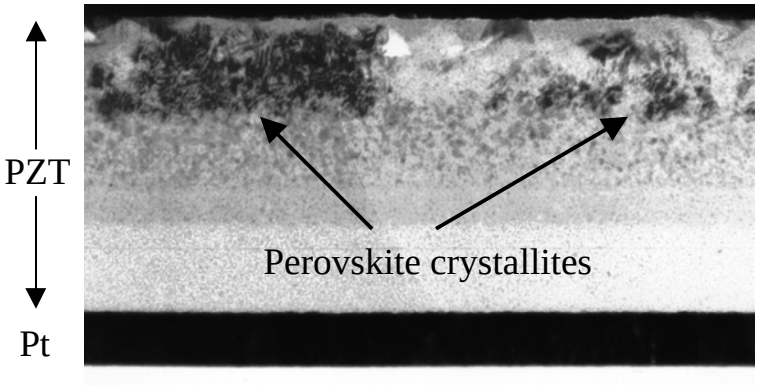

Figure 8.25: Sample L6 TEM cross-section showing crystallisation from the top surface down.

The TEM cross-section for sample R10 is shown in Figure 8.26 below. Despite the larger number of pulses compared to sample L7 the structure of the PZT looks very similar. Small area electron diffraction (SAED) patterns were taken from three areas shown approximately by the numbered circles. Area 1, at the top of the film shows spots due to perovskite and is well crystallised. Area 2 shows weak spots amongst pyrochlore rings with very weak spots due to perovskite, and is therefore predominantly pyrochlore. Area 3, that furthest from the irradiated surface shows no crystal structure and is therefore still amorphous.

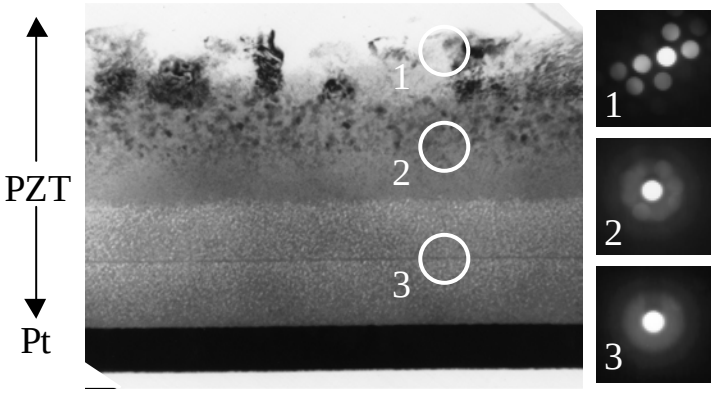

Figure 8.26: Sample R10 TEM cross-section and SAED patterns showing extent of crystallisation.

Figure 8.27 below shows a TEM cross-section for sample L10. Again the top of the film is well crystallised. In contrast to SEM observations the top surface of the TEM sample is very uneven and suggests some loss of material during sample preparation.

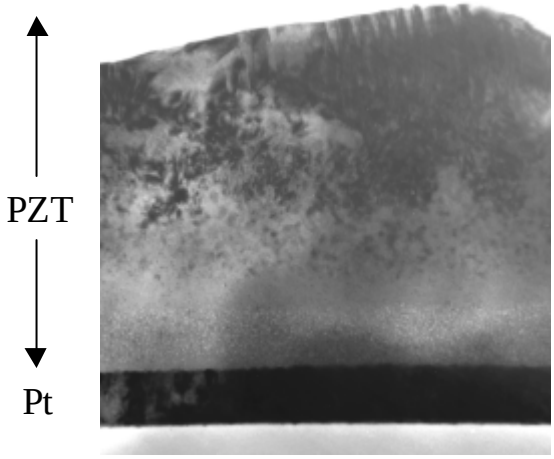

Figure 8.27: AP#510 L10 TEM cross-section showing crystallisation from the top surface downwards.

For some of the TEM cross-sections it was possible to estimate the thicknesses of perovskite, pyrochlore and amorphous material, Table 8.2. The FIB prepared sample has a total PZT thickness of 485nm, as expected, with the other conventionally prepared samples being slightly thinner. The TEM pictures of these samples show rough surfaces, see Figure 8.27 above for sample L10, which is not reflected in the optical microscope and SEM observations of section 8.3.2. It is not unreasonable to assume the top portions of the samples (towards the original PZT surface) may have been lost in the sample preparation. Table 8.3 gives the approximate perovskite, pyrochlore and amorphous region thicknesses with the thickness of the perovskite region adjusted to make the total film thickness 485nm, in agreement with the FIB sample. This involves the simplification that volume changes due to transformation leave the total film thicknesses similar to the FIB prepared sample, L7. Using the lattice parameters calculated in section 8.3.3 the change in unit cell volume on conversion to perovskite is –3.8%. This value is in good agreement with the value of –5.7% found by Kwok and Desu[64] using TEM methods. In the absence of voiding and cracking this volume shrinkage will be taken up as a reduction in film thickness[31]. The nature of the starting film is not entirely certain with the XRD data suggesting a weak pyrochlore/amorphous structure. In this case any amorphous material would expand to form pyrochlore, as observed by observed by Swartz et al for PMN[144], compensating for shrinkage due to perovskite formation from pyrochlore.

Sample	Annealing Conditions	Perovskite Region Thickness (nm)	Pyrochlore Region Thickness (nm)	Amorphous Region Thickness (nm)	Total Thickness (nm)
L5	RTP at 650°C for 30s	465	-	-	465
L7	10^4 pulses at 80mJ/cm^2	157	107	221	485
R10	16×10^4 pulses at 80mJ/cm^2	150	100	231	481
L8	10^4 pulses at 80mJ/cm^2, 10^4 pulses at 100mJ/cm^2	174	99	144	417
L10	10^4 pulses at 100mJ/cm^2	258	81	114	463

Table 8.2: Thickness of perovskite, pyrochlore and amorphous regions in some of the annealed samples.

Sample	Annealing Conditions	Perovskite Region Thickness (nm)	Pyrochlore Region Thickness (nm)	Amorphous Region Thickness (nm)
L7	10^4 pulses at 80mJ/cm^2	157	107	221
R10	16×10^4 pulses at 80mJ/cm^2	154	100	231
L8	10^4 pulses at 80mJ/cm^2, 10^4 pulses at 100mJ/cm^2	242	99	144
L10	10^4 pulses at 100mJ/cm^2	280	81	114

Table 8.3: Thickness as for table 8.2 but with the perovskite region thickness adjusted to make the total film thickness 485nm.

Figure 8.28 below shows the FIB prepared TEM cross section of the RTP annealed sample. The PZT is seen to be well crystallised with columnar perovskite grains ~0.1μm in diameter extending up from the platinum. The work of Patel and Beanland et al [145], using the same PZT sol system, showed that the perovskite nucleates at the PZT/platinum interface and grows upwards consuming untransformed material as it goes. In marked contrast to the low temperature deposited PST annealed in a similar fashion, and discussed in Chapters 5 and 6, the PZT perovskite is dense and the grains have a relatively small diameter. Film structure is very similar to that of PST deposited directly into the perovskite phase at 525°C, a cross-sectional TEM picture of which can be found in Appendix A2.

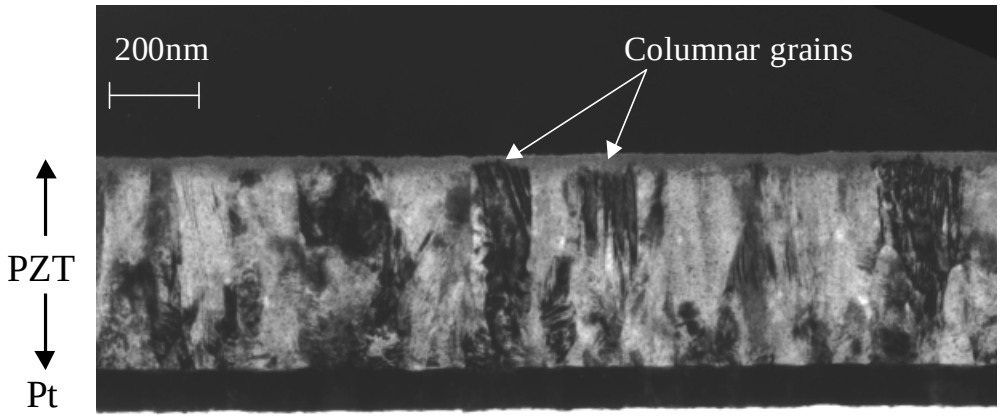

Figure 8.28: AP#510 L5, RTP annealed sample TEM cross section.

8.4 Discussion

Experimental results show that by using laser induced heating a 0.5μm thick PZT layer can be partially crystallised into the perovskite phase without gross disruption of the PZT surface using fluence levels of [100mJ/cm^2. The crystallisation observed was from the top surface downwards, as might be expected from the modelled temperature profiles presented in Chapter 7. Small area electron diffraction analysis in the TEM showed the perovskite regions to be well crystallised. XRD analysis showed that without the influence of the underling platinum the PZT perovskite did not take on a (111) texture, as has been observed for the same material when hotplate [140] and RTP annealed, but was multi-orientated with the dominant orientation being (100), as in the ceramic form [142, 143]. The orientation distribution was not random, as in the ceramic, with the (111) reflection not present. Of all of the samples annealed with a fluence of ≥117mJ/cm^2 only L1 (200mJ/cm^2, 10^3 pulses) showed any evidence, by XRD, of conversion – this being despite gross disruption of the sample surface by the high fluence beam.

Measurements of the thicknesses of the perovskite regions showed that between ~160→280nm of the starting material could be converted with the conditions used. At a fluence of 80mJ/cm^2 the thickness converted was ~155nm for both 10^4 and 16×10^4 pulses. The fact that the extra pulses made no significant difference to the amount of material converted to perovskite suggests that the activation energy for conversion is such that the time required to convert further material is well in excess of that represented by the extra 15×10^4 pulses. A study by Huang et al [101] into the crystallisation kinetics of a similar PZT

30/70 sol-gel system showed that to crystallise a ~200nm thickness of PZT at 440°C took over four hours. The calculations presented in Chapter 7, and in Figure 8.29 below, showed that temperatures of this order would be achieved in the lower half of a 500nm thick PZT film for times of the order of a microsecond. This means that to transform the lower regions of the film would require ~10^{10} pulses! Sample L8, annealed at fluence levels 80mJ/cm^2 for 10^4 pulses followed by 100mJ/cm^2 for a further 10^4 pulses, showed a conversion thickness of ~242nm – half the as-deposited thickness. Sample L10, annealed at a fluence of 100mJ/cm^2 for 10^4 pulses, showed a conversion thickness of ~280nm, over half the original film thickness. Compared to L10 optical and SEM pictures of L8 showed evidence of some beam induced damage in some areas of the annealed region. All other samples annealed at fluences of 80-100mJ/cm^2 did not show signs of surface damage. The use of a dual fluence scheme 80mJ/cm^2 for 10^4 pulses followed by 100mJ/cm^2 for 10^4 pulses was no more effective than 100mJ/cm^2 for 10^4 pulses.

Observation of the surfaces of the samples after annealing has revealed that the PZT is very sensitive to the laser fluence used and that there is a maximum pulse energy above which surface damage is induced. At a fluence of 80-100mJ/cm^2 the surface of the annealed samples showed no damage, with only slight modification at high pulse counts. At the higher fluence level of 117mJ/cm^2 the sample surface exhibited pitting and concentrations of carbon, presumably due to outgassing of residual carbon left over from the starting sol. Severe surface disruption occurred at a fluence level of 200mJ/cm^2 with surface features characteristic of melting and re-solidification. In order to understand why this might be, the model used in Chapter 7 has been employed to give an indication of the temperature profiles in the PZT under the fluence levels used. The temperature in the PZT has been solved for finite slices 50nm thick, giving ten slices for a 0.5μm thick film, with the calculated temperatures representing the average for each slice.

Figure 8.29 shows the temperature distribution in the PZT during and after irradiation of the sample with an extended pulse of fluence 80mJ/cm^2. The slices in the PZT are numbered 1 to 10 with PZT 1 representing the top surface slice and PZT 10 representing the slice adjacent to the underlying platinum. PZT1 and PZT 10 are termed the surface and interface slices respectively. Figure 8.30 shows a plot of the maximum temperatures reached by each slice. Also shown is the melting temperature of lead oxide (indicated by the red line at 886°C), the lowest melting point component in the starting material. The model indicates

that at this fluence level the temperatures reached in the PZT are well below the lead oxide melting temperature, with the maximum surface and interface temperatures being 704°C and 411°C respectively.

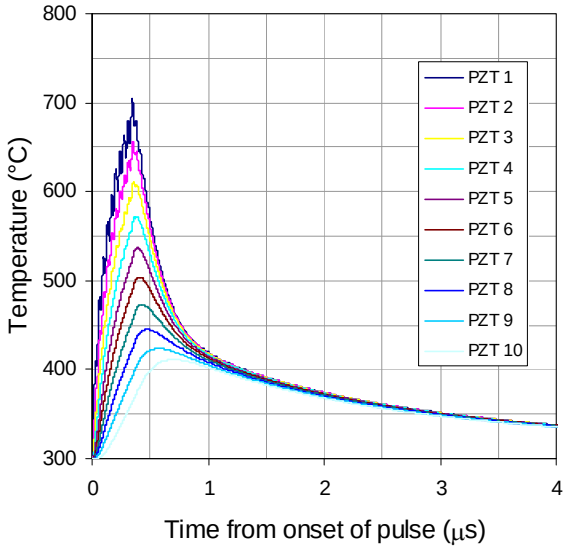

Figure 8.29: PZT temperature profiles, 80mJ/cm^2.
(*Original in colour*)

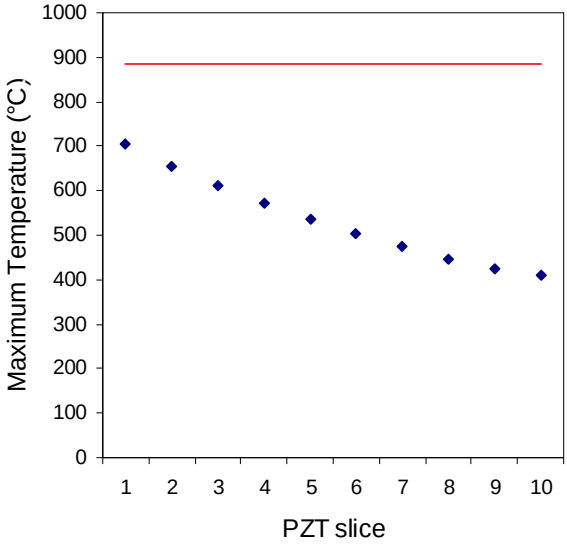

Figure 8.30: PZT slice maximum temperatures, 80mJ/cm^2 (PbO melting temperature in red).
(*Original in colour*)

The temperature distribution in the PZT due to irradiation with an extended pulse of fluence 117mJ/cm^2 is shown in Figure 8.31 with the corresponding maximum temperatures reached by each slice are shown in Figure 8.32. It can be seen that the maximum temperature of the surface slice reaches 891°C, just above the lead oxide melting point, indicating that the slight surface disruption may be due to the melting of lead oxide.

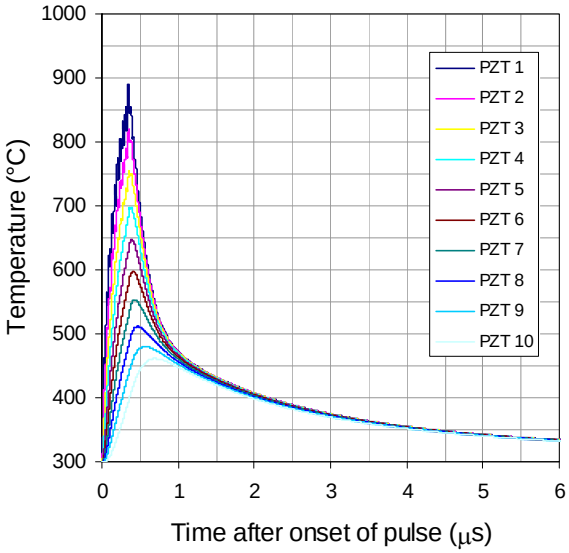

Figure 8.31: PZT temperature profiles, 117mJ/cm^2.
(*Original in colour*)

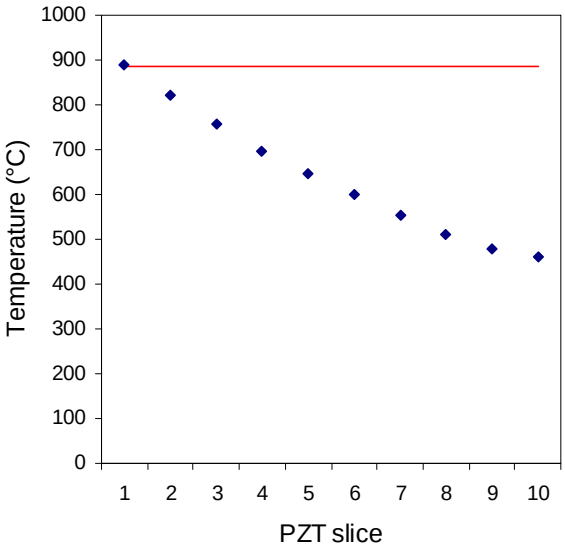

Figure 8.32: PZT slice maximum temperatures, 117mJ/cm^2 (PbO melting temperature in red).
(*Original in colour*)

Figure 8.33 shows the temperature distribution in the PZT due to a pulse of fluence 200mJ/cm^2. The maximum temperature reached by each slice is shown in Figure 8.34. The model indicates that the maximum temperatures reached by the top five slices are above the lead oxide melting temperature. This would explain the gross surface disruption observed in the annealed samples. It is worth noting that the model does not include the process of melting and evaporation and so above the lead oxide melting point the calculated temperatures are only roughly indicative. On this basis the concern expressed in Chapter 7 about the melting of the lead oxide component would appear to be justified.

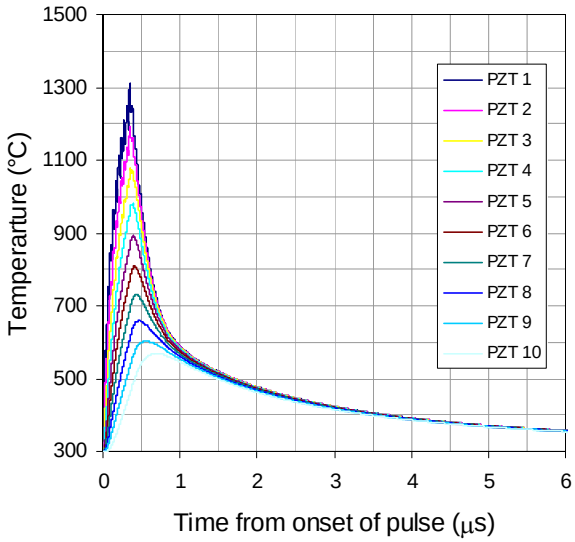

Figure 8.33: PZT temperature profiles, 200mJ/cm^2.
(*Original in colour*)

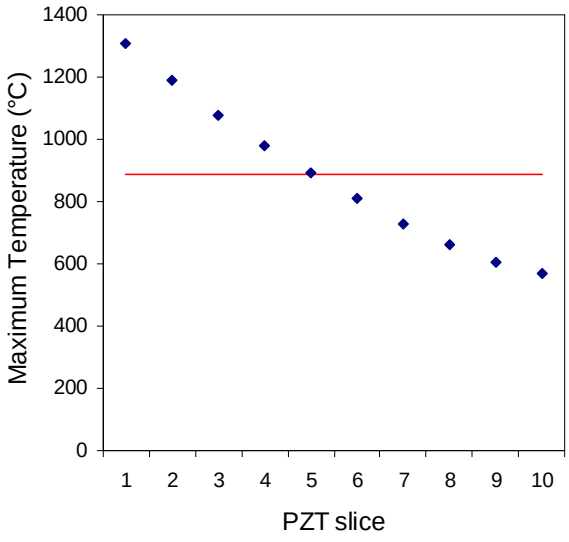

Figure 8.34: PZT slice maximum temperatures, 200mJ/cm^2 (PbO melting temperature in red).
(*Original in colour*)

8.5 Summary

The work presented in this chapter shows that new technique of pulse-extended laser annealing of ferroelectric thin films can, with the conditions used, partially transform a 0.5μm PZT into the required perovskite phase. A fluence of 100mJ/cm^2 for 10^4 pulses resulted in a perovskite layer ~280nm deep, i.e. over half the as-deposited PZT film thickness, with minimal damage to the PZT top surface. TEM cross-sections showed that the crystallisation of perovskite had taken place from the top surface of the film downwards with a graded perovskite-pyrochlore-amorphous structure following the temperature profiles presented in Chapter 7. The depth of perovskite formation would appear to be limited by the activation energy for conversion from pyrochlore to perovskite with 16×10^4 pulses at a fluence of 80mJ/cm^2 being no more effective than 10^4 pulses. XRD analysis showed that without the influence of the underlying platinum the PZT did not crystallise into a preferred (111) orientation – as was observed in an RTP annealed control sample – but was mixed orientation. The Pulse count used may seem high but the excimer laser used is able to operate at a repetition rate of 100Hz thereby delivering 10^4 pulses in 100s.

Samples annealed with fluences of ≥117mJ/cm^2 exhibited evidence of surface disruption which became severe at a fluence of 200mJ/cm^2 – even at low pulse counts. The model

described in Chapter 7 was used to give an indication of the temperatures developed in the PZT. This suggested that surface disruption occurred when the temperature of the as-deposited PZT rose above the melting temperature of PbO. As a result of this the thickness of PZT that can be converted will be limited due to the constraint on the surface temperature. This may result in problems for the conversion of PST which requires a higher temperature to form the perovskite phase than in PZT. An avenue of research not explored in the work presented would be to form a PZT perovskite layer without surface damage at 100mJ/cm^2 and then attempt to drive the crystallisation front further into the PZT with a fluence of 117-200mJ/cm^2 or greater - although there are limitations to the temperature that even the perovskite phase can withstand. Hontzopoulos and Damigos found that with high fluence excimer laser treatment of perovskite phase bulk ceramic the surface of the material begins to decompose with the loss of the constituent elemental components, especially oxygen[146].

8.6 Conclusions of Chapter

The pulse-extended excimer laser annealing technique has been found to be capable of crystallising into perovskite ~0.28μm of a low temperature deposited 0.5μm thick PZT film. Unfortunately this is insufficient for the device structures under consideration. This conclusion can be extended to PST thin films, which are in any case likely to be more difficult to convert using this technique in view of the RTP studies in this thesis showing that PST perovskite requires higher temperatures (or longer times) than PZT perovskite and also the problem of lead oxide melting. The thicknesses converted in the samples reported in this chapter are more compatible with those used in the fields of memory films, i.e. FeRAMs and DRAMs (where similar temperature compatibility problems with active circuitry arise), than for uncooled IR detector designs requiring PZT thickness ⁄0.3μm. For a detector design requiring ferroelectric thicknesses of around this level then the technique may be suitable. Such a thickness (250-300nm) of ferroelectric material is being investigated by Raytheon TI [70] in the United States using a transparent conducting oxide bottom electrode and IR absorption utilising a resonant gap underneath each element. The laser annealing technique described may eleviate any temperature compatibility problems that may exist in their process. An alternative scheme for thicker ferroelectric layers would be to either have deposition/anneal cycles or combined deposition and annealing in the same chamber.

Chapter 9:

Conclusions and Further Work

9.1 Conclusions

In this thesis research work into several topics related to the development of thin film ferroelectric-based uncooled IR detectors primarily for military applications has been presented. The detectors in question are of the microbridge type and are formed from a thin film layer stack using surface micromachining techniques. This type of detector structure offers advantages over the current generation of hybrid detectors in terms of processing cost and performance. In hybrid detectors, the detector elements are formed from a thin slice of ferroelectric bulk ceramic and are flip-chip bonded to the ROIC, whereas the conventional method of making microbridge detectors uses an integrated approach whereby the required thin film layers are deposited directly onto the ROIC. This is potentially problematic since the thermal budget available for the crystallisation of the ferroelectric layer is limited to that of the ROIC. A large proportion of the work presented is concerned with this fabrication route. Recently, however, another method of fabricating this type of detector became available which uses an interconnect wafer, containing no heat sensitive circuitry, on which the microbridges are formed. Using a flip-chip technique, similar to that used for hybrid detectors, this is then bonded to a ROIC wafer to form the completed detector. This so-called 'composite' approach has advantages over the integrated approach which include an extension of the thermal budget available for ferroelectrics processing. Some of the work presented in this thesis has taken advantage of this to investigate the potential performance gains of high temperature processed ferroelectric material. The ferroelectric materials investigated were PST and PZT, both of which need to be in their perovskite phase in order to realise their ferroelectric properties.

In Chapter 4 a study was carried out into the thermal budget limitations of a typical ROIC with standard aluminium-based CMOS metallisation. Two thermal treatments were investigated which corresponded to deposition of the ferroelectric material directly into the required perovskite phase and also the deposition of the ferroelectric material at a temperature below that at which perovskite is formed followed by a high temperature anneal

to convert the material to this phase. The direct-to-perovskite route requires temperatures in excess of 500°C for PST deposited by sputtering. To assess the survivability of the ROIC at these temperatures a series of simulated sputtering trials were carried out in an ambient atmosphere of 5mTorr of Ar/10% O_2 using a bespoke vacuum annealer. Electrical assessment showed that the ROIC functionality was unaffected for 4 hour anneals at temperatures up to 575°C, although signs of deterioration of the metallisation were observed. At 550°C for 4 hours however, complete electrical functionality was accompanied by absence of any observed metallisation deterioration and was taken to be the thermal budget for direct to perovskite deposition by sputtering. Interestingly, a corresponding anneal in air at stp resulted in catastrophic electrical failure of the ROIC. This was attributed to oxidation of the metallisation at elevated temperature and indicates that the partial pressure of oxygen is very important in determining the ROIC survivability at elevated temperatures. The second thermal regime investigated in Chapter 4 corresponded to low temperature deposition of the ferroelectric layer followed by a high temperature crystallisation step using RTP. Using RTP anneals in argon, in view of the sensitivity to oxygen, the ROIC's electrical functionality and physical structure were found to be unaffected at 600°C for up to 30s, which was taken to be the thermal budget of this processing route. Markedly decreased electrical functionality was found at temperatures and times in excess of this but was accompanied by thermally induced alteration and damage to the metallisation. The main electrical failure mode was shorting, indicating that the likely failure mechanism was spiking and hillocking of the aluminium. One way of extending this thermal budget is to use copper metallisation, which is being investigated to increase processor speeds. A literature review revealed, however, that for foundries to realise the full benefits of copper it will be used in conjunction with low-k dielectrics which restrict the maximum process temperature to ~450°C, thereby increasing rather than reducing the temperature restrictions. If copper metallisation is adopted generally then intermediate wafer based detector fabrication route then becomes desirable, unless bespoke fabrication facilities are used.

Chapter 5 reported a study of the deposition by single RF magnetron sputtering of PST onto platinised silicon at 300°C followed by annealing to realise the required perovskite phase. Low temperature deposition has distinct benefits for the sputtering method which include ease of compositional control, especially of the volatile lead component, and improved deposition system reliability. The main annealing technique used was RTP in oxygen, with

RTP in argon and conventional oven annealing in oxygen performed for comparison. As-deposited PST had a poorly crystallised pyrochlore/amorphous structure with no evidence of the required perovskite phase. Upon RTP annealing in an oxygen ambient it was possible to convert this to highly (222) textured perovskite, with a large grain size (>1μm) which indicated a low nucleation density of this phase on the underlying platinum. Unlike direct-to-perovskite PST or similarly annealed PZT the RTP annealed material was characterised by voiding, resulting primarily from volume shrinkage on conversion from pyrochlore to perovskite. An RTP anneal at 650°C for 30s was insufficient to fully convert the PST film to perovskite, showing that this processing route is incompatible with the integrated processing route. Higher temperature RTP (700°C for 5 minutes; 750°C and 850°C both for 30s) did achieve complete conversion, however no B-site cation ordering was observed even at the highest anneal temperatures. Electrically the annealed PST exhibited broad, relatively low magnitude (compared with bulk) permittivity peaks with frequency dispersion characteristic of a relaxor ferroelectric. Since PST is operated in dielectric bolometer mode the broadness of the permittivity peaks resulted in only moderate induced pyroelectric coefficients compared to those obtained from bulk, which is very sharply peaked. It was however possible to obtain good F_D values, up to $3.8\pm0.5\times10^{-5}Pa^{-1/2}$ for the 850°C RTP annealed material, through the application of a sufficiently high bias and the suppression of ε_r and $\tan\delta$ - this being the route to high performance in relaxor materials. In this way the performance of the PST is directly linked to its breakdown strength under applied bias.

Interdiffusion between the layers, especially diffusion of lead in the PST through the platinum, was evident after high temperature RTP and whilst it was not seen to cause a problem does indicate that stabilisation of the underlying electrode may be desirable. RTP annealing in argon (700°C for 5 minutes) resulted in conversion to (222) textured perovskite, which nucleated on and grew up from the PST/platinum interface. In addition there was a reaction between lead in the PST and the underlying platinum resulting in the formation of a Pt_3Pb intermetallic. Electrically this PST was very poor and unsuitable for incorporation into an uncooled IR detector. The PST annealed in a conventional oven was converted to (222) textured perovskite, again with evidence of lead-platinum interaction. Compared with the RTP annealed material the surface morphology of this PST was very poor, being characterised by gross cracking which resulted in zero electrical yield and the

ruling out of this method for detector processing. The work of Chapter 5 gave a proof of principle that low temperature deposited PST could, by RTP annealing in oxygen, be converted to perovskite capable of yielding good merit figures for IR detection. A characteristic of the converted PST was the presence of an apparent internal bias field, which was the primary cause of substantial non-zero pyroelectric coefficients above the temperature of the dielectric maximum, thought to be due to the action of defects. Although the best merit figures were low compared with bulk PST ($F_D \sim 16\times10^{-5}Pa^{-1/2}$) they are high compared with thin film PZT and 525°C direct-to-perovskite PST (both with $F_D \sim 2\times10^{-5}Pa^{-1/2}$) and should, when allied with a high performance detector structure and interconnect wafer processing, result in uncooled IR detectors with <100mK NETD.

A similar study of low temperature deposited PST was described in Chapter 6, this time using the technique of dual RF magnetron reactive sputtering where the lead and scandium/tantalum were on separate targets. Two deposition temperatures were investigated, 450°C and 300°C. At 450°C the deposition equipment was operated in standard mode where the ratios of the elements in the PST was controlled by varying the powers on the targets. The as-deposited PST was well crystallised (222) textured pyrochlore which had a columnar grain structure that extended through the thickness of the film. This is very different from materials such as PZT and the 300°C deposited PST of Chapter 5 which forms a nanocrystalline pyrochlore phase. Using RTP annealing in an oxygen ambient it was possible to convert this pyrochlore to the required perovskite phase with perovskite nucleating on and growing up from the PST/platinum interface. A 650°C RTP anneal of 30s duration was insufficient to induce complete conversion, thereby discounting the use of this deposition/annealing scheme in a fully integrated detector fabrication process. Higher temperature RTP anneals at 750°C and 850°C, both for 30s, did induce complete conversion of the as-deposited PST to (222) textured perovskite with a degree of B-site cation ordering at both temperatures. As for the 300°C deposited PST reported in Chapter 5 the grain size was large ($\exists$1μm diameter) and reflected a low nucleation density of the perovskite on the underlying platinum. Voiding was again observed in the converted material but was not perceived to be problematic. Electrical characterisation of the 850°C annealed PST revealed ferroelectric relaxor behaviour. A relatively sharp permittivity peak did however yield good pyroelectric coefficients with the result that F_D values of up to $1.9\pm0.2\times10^{-5}Pa^{-1/2}$ were realised at a bias fields as low as

1.3V/μm. Unfortunately, a characteristic of this material was a low breakdown strength which ultimately limited the performance to levels similar to that available from PZT and 525°C deposited direct-to-perovskite PST. It was therefore concluded that this well crystallised pyrochlore phase was not a good starting point for the fabrication of high performance uncooled IR detectors.

For the 300°C depositions a novel technique of PST compositional control was employed which involved operating the sputtering targets at voltage and power levels where the erosion rate was constant and oxygen poisoning not a problem. Lead, scandium and tantalum content of the PST was then controlled by varying the amount of time that the substrate spent over each target. In this way a the PST thin film was built up as a series of very fine layers. Obtaining the desired composition and maintaining it run to run were markedly easier with this technique compared to the power/voltage variation method. The PST deposited in this way was found to have a weak pyrochlore/amorphous structure very similar to the single RF magnetron deposited PST at the same temperature. Three annealing methods were tried which were conventional oven annealing, RTP annealing and combined RTP/oven annealing, all in oxygen ambients. The purpose of the oven annealing was to investigate whether ordering could be induced by extended time anneals at elevated temperature. Oven annealing at temperatures of 700°C, 750°C and 800°C for 1 hour was found to be capable of converting the as-deposited PST into (222) textured perovskite, although not completely, with the two higher temperatures inducing a degree of B-site cation ordering. This was nonetheless encouraging since it was not known whether conversion could be achieved after low temperature deposition using the 'dwell time' technique. The PST was characterised lead loss which manifested itself as a surface lead-deficient pyrochlore phase and large scale lead inclusions in the silicon dioxide under the platinum bottom electrode layer. Additionally there was gross cracking of the PST. These undesirable properties have been attributed in some measure to lead loss during the slow ramp-up rate of the oven to the annealing temperature, compared to RTP. Free lead oxide in the as-deposited PST is free to diffuse, both down through the underlying platinum and also to the PST surface where it can evaporate. Perovskite conversion proceeds from the PST/platinum interface until all of the convertible material is used up, leaving residual lead deficient material at the surface. The higher the oven anneal temperature the greater the perovskite content of the PST and the sharper the permittivity peak, although the material

was characteristically relaxor in nature. In terms of electrical performance the higher the anneal temperature the better the pyroelectric response but the lower the breakdown strength (probably related to the presence of the lead deficient pyrochlore phase) with the result that the best F_D value of $1.5\pm0.1\times10^{-5}Pa^{-1/2}$ was recorded from the 750°C anneal. In response to the problem of lead loss a combined RTP/oven anneal schedule was tried, with the assumption that the RTP anneal (with its relatively fast ramp-up rate compared to the oven) would bind in the lead component through fast conversion to the stable perovskite structure. This was found to be the case with the combined anneal (700°C RTP/800°C Oven) showing near stoichiometric lead composition and a greater perovskite content than the oven-only annealed material. Electrically this material exhibited relaxor characteristics and apart from an improved breakdown strength was very similar to the 800°C oven-only annealed PST, yielding a maximum F_D value of $2.5\pm0.3\times10^{-5}Pa^{-1/2}$ – slightly better than the value of $\sim2\times10^{-5}Pa^{-1/2}$ expected from PZT and 525°C deposited direct-to-perovskite PST. RTP-only annealing of the 300°C dual magnetron deposited PST was, as for the single RF magnetron deposited material, capable of being converted to perovskite. A 700°C anneal of 10 minute duration was insufficient to completely convert the PST thin film to perovskite, again ruling out integrated processing, and was reflected in the relatively poor electrical performance of this film which gave a maximum F_D value of only $0.9\pm0.1\times10^{-5}Pa^{-1/2}$. The higher temperature RTP anneals, at 850°C for 30s and 120s, did result in complete conversion but unlike all other PST reported in this thesis gave a multiorientated crystal structure with the (400) orientation being dominant. As for the single RF magnetron deposited PST this material was characterised by a large grain size ($\exists1\mu m$) and voiding, the latter primarily due to a volume shrinkage on conversion. Electrically these samples were very good and both the magnitude and sharpness (high $\partial\varepsilon_r/\partial T$) of the permittivity peaks is beginning to approach those of ordered PST thin films on sapphire substrates, although still well short of ordered bulk ceramic. Relaxor behaviour was still evident in these films but in the 120s duration anneal material departures from this behaviour towards first order type properties was observed. In terms of F_D values the 30s and 120s duration anneals yielded maximum values of $4.8\pm0.8\times10^{-5}Pa^{-1/2}$ and $5.8\pm0.9\times10^{-5}Pa^{-1/2}$ respectively, both figures over a factor of two greater than expected values for PZT or 525°C deposited direct-to-perovskite PST. Indeed with such high merit figures it would be possible in a device to trade off some performance for a lower operating applied bias field.

Summarising the overall picture from Chapters 4 to 6, it was found that PST deposited at 300°C and given a post deposition anneal could be converted into the perovskite phase required for IR detector applications. Using this processing scheme it was not possible to obtain PST of sufficient quality within the ROIC RTP survivability envelope, i.e. 600°C for 30s, thereby ruling out this approach for integrated device processing. High temperature RTP anneals made possible by the composite detector technology did show very good performance, but mainly at anneal temperatures of the order of 850°C. These films exhibited ferroelectric relaxor properties and as a consequence had only moderate pyroelectric properties in comparison with ordered bulk material. It was however possible to obtain good performance from such material by suppression of ε_r and tanδ through the application of moderately high bias fields. In this way the performance in this PST is directly linked to the breakdown strength under applied field. When allied to a good detector structure and using the composite processing route, the PST reported offers the real possibility of sub 100mK NETD performance uncooled IR detectors, and to this extent has fulfilled the main objective of this work.

In Chapters 7 and 8, a novel approach to annealing low temperature deposited PZT and PST within the integrated processing method was described. This made use of excimer laser annealing to preferentially heat the ferroelectric layer while not significantly affecting the temperature of the underlying layers, in particular the ROIC. Chapter 7 described the experimental apparatus, optical characterisation of low temperature deposited PST and PZT thin films and the results of modelling studies to investigate the temperatures developed in the thin film layer structure and help establish operating parameters such as laser fluence level and whether substrate heating was required. The optical characterisation showed that at the laser wavelength of 248nm (KrF excimer) the reflectivity of the films was low at ~20% and the absorption coefficient was very high, the latter giving absorption lengths of ~20nm. Combined with very poor thermal diffusivities in PST and PZT this resulted in good absorption of the laser energy and confinement of the heat generated in the ferroelectric layer, with no significant temperature rise in the region of the ROIC. The temperature profiles through the ferroelectric layer using a standard excimer laser pulse were characterised by high surface temperatures and poor heat penetration into films of thickness 0.5-1μm. This problem was overcome using a bespoke temporal pulse extender which lengthened the laser pulse from ~25ns to ~375ns, thereby slowing down the rate of

energy delivery to the ferroelectric layer and increasing the diffusion length by almost a factor of four. Predicted surface temperatures of the ferroelectric thin film were markedly reduced and heat penetration was improved, both without significantly affecting the temperature of the ROIC. Even with the pulse extension technique though, modelling temperature distributions suggested that the technique was unlikely to be able to crystallise a full micron of ferroelectric, with the problem being more tractable for thickness of □0.5μm.

The final experimental chapter, Chapter 8, described the application of the pulse-extended laser annealing technique to crystallise low temperature sol-gel deposited 0.5μm thick PZT thin films (on platinised silicon substrates) into the perovskite phase. Annealing studies were performed in an oxygen atmosphere at an ambient temperature of 300°C (well below the ROIC survival limit identified in Chapter 4). It was found to be possible to obtain perovskite PZT using this technique with minimal surface disruption using fluence levels of □100mJ/cm^2 with the maximum transformed depth being ~280nm. The transformation occurred from the top surface downwards with the PZT thin film having a perovskite/pyrochlore/amorphous graded structure which followed the predicted temperature gradient. The perovskite formed did not crystallise into a preferred orientation, as expected due to the lack of a template layer at the surface. Fluence levels ⁄117mJ/cm^2 were found to result in severe surface disruption of the PZT. Use of the model employed in Chapter 7 suggested that damage to the PZT film occurred when the temperature went above the lead oxide melting temperature. This places a limit on the usable fluence and hence the perovskite crystallisation depth. Overall it was found that excimer laser annealing with pulse extension was capable of converting PZT from a low temperature deposited amorphous phase to perovskite within the ROIC thermal budget. Unfortunately the depth convertible was short of the ~0.6-0.7μm thicknesses required for the IR detector structures being contemplated. The technique may be compatible with applications using thinner ferroelectric layers such as FeRAMs.

9.2 Further Work

There are many possible future directions for the work reported, a few of which will be outlined. It was found for PST thin films that relaxor properties were obtained for the time-

temperature schedules used in the RTP annealing, but as the anneal temperature was increased the phase transition became less diffuse with a sharpening of the permittivity peak. In bulk material this sharpening is observed and is due to ordering of the PST brought about by a combination of preparation conditions and annealing treatments. Certainly other authors have found that for the thin film form of PST temperature has played a very important role in the ordering process, although the exact method for ordering has not been studied in detail. The importance of ordering from an uncooled IR detector viewpoint is clear, with first order type properties being commensurate with a sharp permittivity peak and hence a high induced pyroelectric coefficient for dielectric bolometer mode operation. Higher performance from PST thin films on silicon substrates can be gained in one of two ways, either from higher bias operation in films with relaxor properties or from increasing the degree of ordering and sharpening the dielectric properties. In terms of long term performance it is preferable to operate at as low an applied bias field as possible, so the ordering route to high performance is desirable. To this end a study could be undertaken with the remit of obtaining highly ordered PST thin films on silicon substrates, as has been obtained by other authors for PST on sapphire, possibly investigating higher temperature or novel annealing schedules or even the use of dopants to induce order.

For low temperature deposited PST on platinised silicon there exists a gap in the understanding of the nucleation and grain growth of the perovskite phase. The work presented in this thesis highlighted that growth on annealing from a non-perovskite phase produced large grains with a degree of porosity, very different than for PZT prepared in a similar way and also 525°C direct-to-perovskite PST which both exhibit dense columnar grained microstructure. A rigorous study of nucleation and grain growth, including the development of features such as voids would add to the understanding of growth mechanisms of PST and possibly allow optimisation of materials properties for IR detection applications. Such a study would be aided by a better understanding of the pyrochlore phase of PST, another subject about which there is scant information in the literature. To this end the 450°C deposited PST reported in this thesis, with its well crystallised pyrochlore structure, would provide excellent subject matter.

From the point of view of the PST presented in this thesis the next logical step would be to investigate the properties of the material in a full device layer structure, using a high temperature sacrificial layer and any associated barrier layers with the eventual aim of

fabricating and assessing microbridge structures. Associated measurements from a device point of view are stability of the PST under the operating field for extended periods, both in terms of pyroelectric and dielectric properties. It was noticed in the course of the research presented that the stability of the platinum bottom electrode was a potential problem at the higher anneal temperatures. Although no difficulties were encountered it is possible that interface quality could be problematic in a device. Future work could involve the investigation of the stabilisation of the bottom electrode, especially against lead diffusion from the PST, via the use of high temperature stable barrier layers such as tantalum oxide or even the use of an oxide electrode such as YBCO or ruthenium oxide. An alternative is further investigation of lower temperature RTP anneals for longer times, with some results in the thesis indicating that this tradeoff could be made.

For the laser annealing work there are avenues of research that could be explored. A simple extension of the work performed with PZT would be to attempt to fully convert thinner films, say of ~0.3μm thickness, and measure the electrical properties. Certainly for thinner material the temperature distribution may be such that the temperature at the PZT/platinum interface would be sufficient to cause nucleation there. This may give a degree of orientational control due to the template effect of the platinum. A less straightforward experiment is use of a longer excimer wavelength, such as XeCl (308nm) or XeF (351nm), to take advantage of the greater penetration depth in PST and PZT as the band edge is approached. In this way it may be possible to convert a greater thickness of material to perosvkite. If the increase in penetration depth is such that the ROIC temperature reaches detrimental levels then the use of thermal barrier layers such silicon dioxide, the effectiveness of which was identified in the thesis, could be employed.

A novel use of the pulse extended excimer laser annealing technique could be in the further annealing of PST already in the perovskite form so as to induce ordering of the B-site cations. As was seen in this thesis the laser technique has the ability to generate high temperatues in the ferroelectric layer whilst leaving other components of the device layer structure relatively cool. In this way ordered material could be obtained without electrode stability problems that may occur at elevated temperatures.

Appendix A1:

Internal DERA Invention Report

Title of invention

Composition control of sputtered thin films

Authors

M.A. Todd, P.P Donohue & M.A.C. Harper

Summary of invention

A technique involving programmable control of substrate position and delay periods in a dual target sputtering system has demonstrated control of film composition for the ferroelectric material Lead Scandium Tantalate (Pb_2ScTaO_6). Individual control of the atomic ratio of the three metallic elements, Pb, Sc and Ta is obtained. This not only gives control over the average composition in the final film – it also allows grading of the composition through the film thickness. Graded composition films are becoming increasingly of interest due to the improved material properties obtained. This invention could be applied to a number of similar multi-component ferroelectric oxide materials, or more generally for any multi-component film in which composition control or graded composition are required. Applications for ferroelectric multi-component films include pyroelectric detectors for thermal imaging, intruder alarms, and fire-sensing; DRAM and FeRAM memories and thin film capacitors; piezoelectric resonators and filters and many more.

Background

Thermal imaging systems based on 2-dimensional arrays of ferroelectric detectors have become established as a low cost, lightweight, low power alternative to cooled semi-conductor detectors. In the UK the development of ferroelectric arrays has largely been based on a hybrid detector approach, where bulk ceramic ferroelectric material is bump-bonded to a multiplexed readout chip. The detector material chosen for these arrays is Lead Scandium Tantalate (Pb_2ScTaO_6).

The ultimate performance of hybrid thermal detector arrays is however limited due to unwanted thermal conduction mechanisms that reduce the temperature rise and hence the signal generated through the pyroelectric effect. In order to improve imaging performance, a low thermal conductance pixel structure is required. It is advantageous to couple this to a low pixel thermal capacitance in order to match the thermal time constant to the array readout. Both of these improvements can be achieved through the use of thin film materials, where the pixel is constructed by micro-fabrication techniques to be supported above a substrate by thin, narrow legs, in a structure known as a ferroelectric microbridge.

Sputter deposition of thin films

Work at DERA has been on-going to develop a process to grow thin film Lead Scandium Tantalate (PST) by a sputtering deposition technique. The sputtering process is a vacuum deposition process which involves bombardment of a voltage biased target by energetic ions (commonly Argon ions) in a plasma. Atoms from the surface of the target are removed and are deposited on surrounding surfaces. By mounting a substrate close to the target, a thin film of deposited material can be grown on the substrate.

Dual target sputtering

In order to grow a thin-film of PST, the required elements: Scandium (Sc), Tantalum (Ta) and Lead (Pb), must be contained on the target, whist Oxygen is contained in the sputtering gas (i.e. the sputtering gas is a mixture of Argon and Oxygen) which is reactively combined during the growth of the PST film (known as reactive sputtering).

Ceramic oxide PST can be used as the target, however the resulting film composition may differ from that of the target (for instance lead is often lost from the film at high temperatures) so that a number of oxide targets of different composition may be required before the desired film composition is obtained. For the same reason a new oxide target is required every time there is a change in the required film composition. For these reasons it is preferred in our work to use pure metals on the target. The sputtering yield of lead is significantly greater than either Sc or Ta so it is difficult to combine the three metals on the same sputtering target, unless relatively small lead areas are used. Although this can be

done, the lead is eroded more quickly leading to either a variation of lead content during the depositing or from run to run and/or the need to replace the lead at frequent intervals.

Instead, in our work, dual 8" magnetron sputter targets are used in a custom sputtering system made by Scientific Vacuum Services (see figure below). Lead is used on one target, while the other comprises large sectors of Sc and Ta. The substrate is held on a rotating plate above the magnetrons, and heated by quartz lamps. The heater and substrate plate assembly can be moved using a stepper motor to allow scanning between the two targets. The scan angle and scan speed can be set by front panel controls. The relative areas and positions of the Sc and Ta segments, combined with careful setting of the scan angle, allow the ratio of Sc and Ta to be set. The two targets have independent RF bias generators, so altering the bias to the Pb target can set the Pb ratio, for a certain scan routine. Scanning between targets thus builds up a fine-layered film with typically over 200 layers per micron of film thickness, each layer having the same average composition. The combination of rotation and oscillation results in excellent film uniformity.

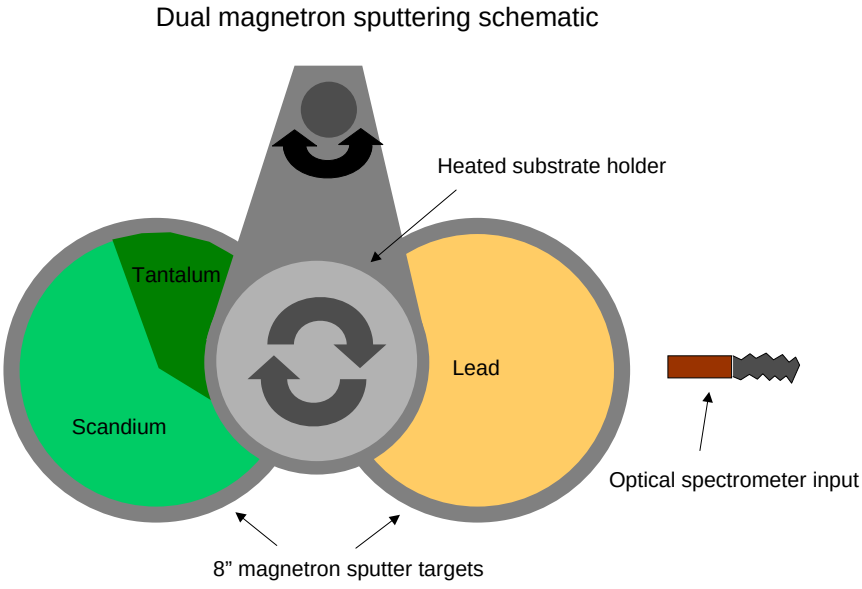

Figure A1.1
(*Original in colour*)

Basis of new invention

The dual magnetron system above, as designed by SVS, improves control of the average lead content in the film and film uniformity. However the Sc/Ta target is still 'fixed' to give a certain film composition. An additional problem comes due to oxidation of the metallic targets.

This can lead to difficulties in control and run-to-run repeatability, due to the conflicting processes of sputtering and oxidation. There is generally a window of sputtering powers which can be used which minimise oxidation effects - however these may not coincide with the powers needed to give the desired film composition.

In order to fabricate certain types of devices based on ferroelectric thin films, the ferroelectric is deposited on silicon which has been processed with integrated circuitry. An example of this is integrated pyroelectric detectors for thermal imaging. In this case it is desirable to process the ferroelectric at temperatures which are compatible with the silicon circuitry. It has been shown in our work that a lead excess in PST promotes the formation of a ferroelectric crystal phase at low temperatures i.e. easing substrate compatibilty problems. Having excess lead throughout the film, however, may compromise the electrical and/or structural properties of the films. If it is possible, therefore, to introduce a lead excess at the beginning of the deposition to promote formation of a ferroelectric crystal phase, and reduce the lead excess for the duration of the deposition, then this may result in low temperature growth combined with good electrical and structural properties.

Another - possibly related - observation, is that when films are deposited on Platinum electrodes it is possible to form a Lead-Platinum inter-metallic. Formation of the inter-metallic leads to preferred orientation of the ferroelectric film, which in turn influences the film properties. If a thin 'seeding' layer of lead, or lead-rich PST, could be deposited at the start of the deposition then there is potential to control the film orientation and therefore optimise electrical properties.

Compositionally graded ferroelectric thin films have recently been investigated - both experimentally and theoretically. Graded ferroelectric devices (GFDs) have shown novel properties - based on the inherent asymmetries provided by the internal self-biases created by compositional gradients. To date the material $Ba_{1-x}Sr_xTiO_3$ (BST) has been the most extensively studied. To obtain compositional gradients, sequential layers have been deposited by 'spin-and-fire' metalorganic deposition. A pre-requisite of the charge-pumping effect in GFDs is however that the change in composition must vary continuously and smoothly through the film thickness. This is achieved by annealing around 1000^oC after deposition, thus compromising the technique for direct-on-silicon integration. A lower temperature sputtering

process has been descibed which utilises dual magnetron sputtering from separate $BaTiO_3$ and $SrTiO_3$ targets. It is not known whether this technique uses the programmed substrate movement and delays of the present invention. Unlike the present invention, it cannot give independent control of all the metallic elements. It is not known at present whether GFDs based on compositionally graded PST will show enhanced or novel electrical properties.

The new invention uses the dual target sputter system described above but includes two new features:

1. A target consisting of half Sc, half Ta is used instead of uneven sectors and;

2. The constant speed scan between target positions is replaced by a computer-controlled movement - so that 'move-stop-delay-move' routines can be programmed in.

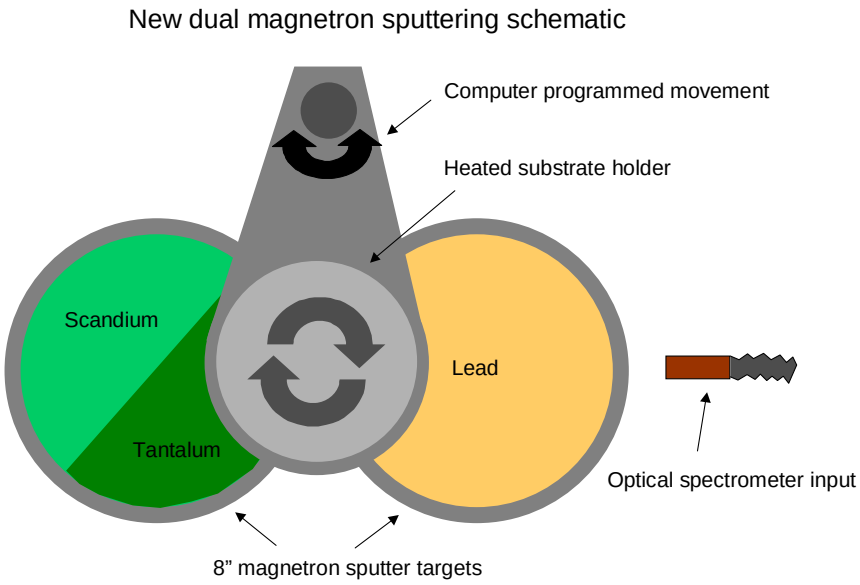

Figure A1.2
(*Original in colour*)

By programming in set positions e.g. over the Lead target and over the Sc and Ta areas of the other target, and programming in delays over each, a controlled film composition can be obtained. The following advantages are obtained:

1. The targets can be run at optimum bias power levels (i.e those which avoid target oxidation problems or the like)

2. The average film composition can then be controlled by setting the delays at each position. This allows changes to be made to the composition if required in a straight-forward way in the software. This is much simpler than the alternative of changing target areas and/or target powers, which are non-linear effects which can require extensive trials to optimise.

3. The film composition can be graded through the thickness by controlling the relative delays over certain positions e.g. a higher Sc/Ta ratio can be phased to an equal Sc/Ta ratio. The phasing can be linear, exponential or any variable function. This may provide the basis for Graded Ferroelectric Devices (GFDs).

4. The film can be deliberately 'seeded' with a composition at the start, or during the early stages of deposition, which is in a different proportion from the composition of the remainder of the film e.g. a thin lead film can be deposited at the start. This could help promote low temperature growth required for compatibility with deposition on active silicon circuitry. This may be by easing the nucleation of a preferred crystal phase and/or by controlling the crystal orientation to give a preferred orientation.

Appendix A2:

SEM and TEM of 525°C deposited PST.

Shown below are SEM and TEM pictures of single RF magnetron deposited PST on platinised silicon, courtesy of Mr. M.A. Todd of DERA Malvern. The deposition method was the same as that for the samples described in chapter 5 with the exception that the substrate temperature was 525°C, as opposed to 300°C. This increased temperature in conjunction with a lead excess of ≥10% results in formation of polycrystalline perovskite PST [4, 86, 98]. Figures A2.1 and A2.2 show the surface morphology of such films to consist of a dense array of pyramidal type structures – so called "sharks teeth" which are indicative of a columnar grain structure, as seen in the TEM cross section of figure A2.3.

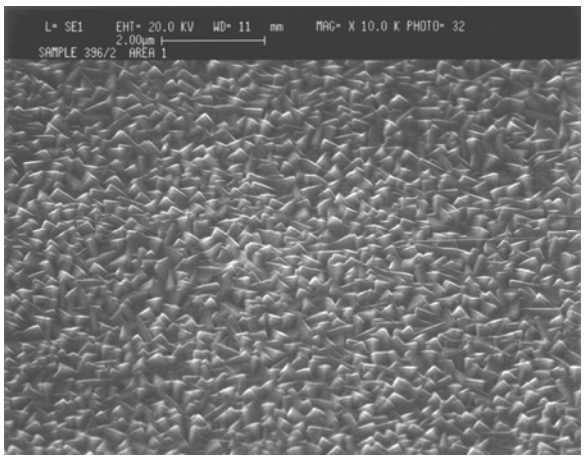

Figure A2.1: SEM picture showing surface morphology of a typical 525°C deposited PST sample.

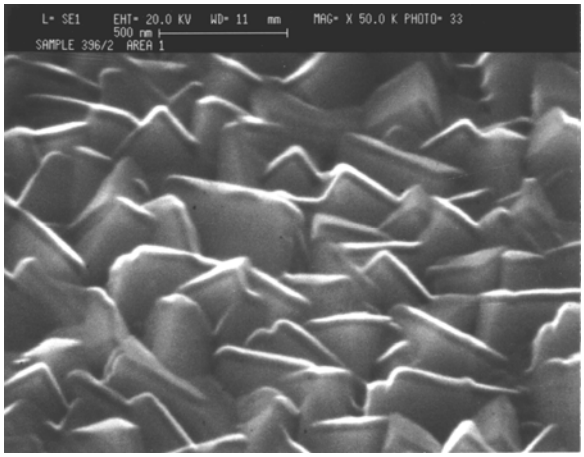

Figure A2.2: SEM picture showing "sharks teeth" surface morphology.

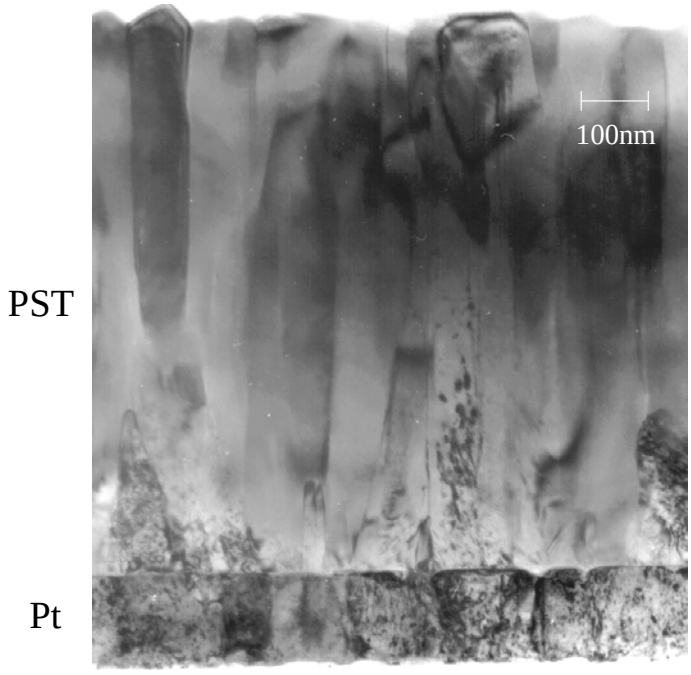

Figure A2.3: TEM cross-section of a typical 525°C deposited PST sample.

Figure A2.3 shows columnar perovskite PST grains growing up form the PST/platinum interface. The lateral dimension of the grains is of the order of 0.1μm. The PST can be seen to be dense with the pores and voids observed in the samples discussed in chapters 5 and 6 not present.

Appendix A3:

Comparison of PST Dielectric Properties.

The dielectric constants of some of the samples discussed in chapters 5 and 6 are compared with those for hot pressed ceramic PST, thin film PST sputtered onto sapphire substrates (sample PSTCH160) and thin film PST sputtered onto platinised silicon at 525°C (PSTCH351 piece 2). The data for ceramic PST was obtained for a BAE Systems Caswell sample designated KCE167H, courtesy of Dr. P.C. Osbond, and had been measured at 400Hz. The data for the thin film PST on sapphire and 525°C deposited PST on platinised silicon was obtained from DERA Malvern, courtesy of Mr. R. Watton and Mr. M.A. Todd.

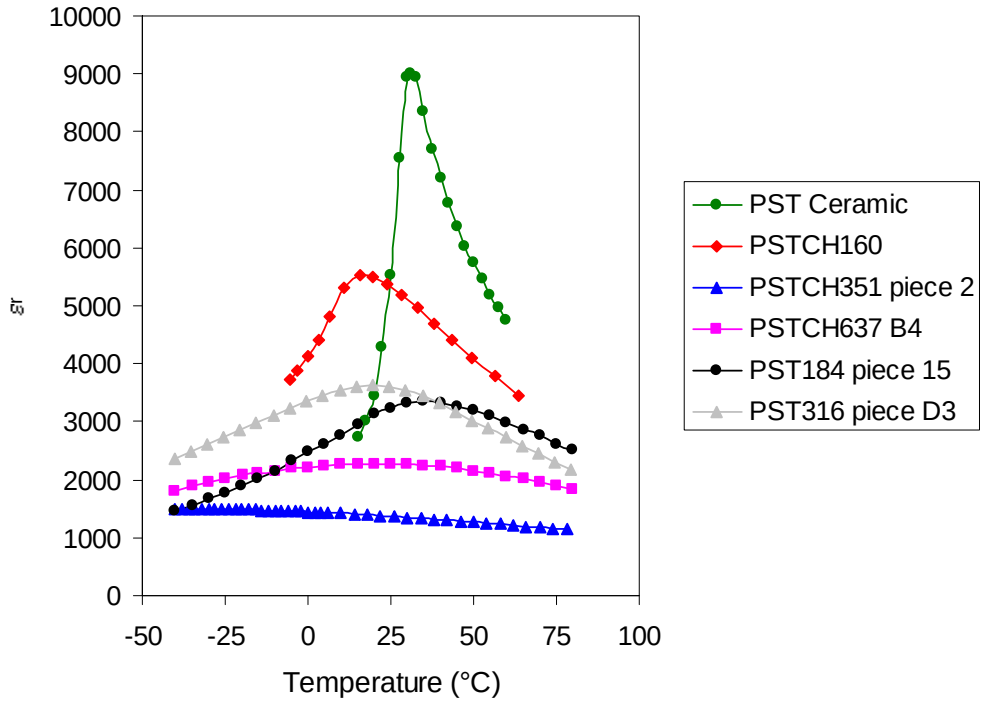

Figure A3.1: Comparison of ε_r for various PST samples.
(*Original in colour*)

The PST ceramic can be seen to be very sharply peaked with a maximum ε_r of 9000 occurring at 31°C. The thin film PST on sapphire is also sharply peaked, although less so than the ceramic, with a maximum ε_r of 5500 occurring at 16°C. The thin film samples on silicon substrates reported in this thesis are less sharply peaked and have lower dielectric

maxima, although some of the higher temperature RTP anneals result in dielectric properties that begin to approach those of PST ceramic and thin film PST on sapphire substrates.

Sample	Chapter	Identifier
PSTCH637 piece A4	5	Sample C
PSTCH637 piece B4	5	Sample D
PSTCH637 piece B5	5	Sample E
PST184 piece 15	6	Sample E
PST285 piece C1	6	Sample H
PST285 piece C2	6	Sample I
PST285 piece B2	6	Sample J
PST285 piece F2	6	Sample K
PST285 piece B1	6	Sample L
PST315 piece D4	6	Sample N
PST316 piece D3	6	Sample O

Table A3.1: Key to sample names and identifiers.

We may recall from chapter 2 that in relaxor ferroelectrics ε_r just above the temperature of the dielectric maximum, T_{max}, was described by a quadratic relation due to Smolenski [21] of the form

$$\frac{1}{\varepsilon_r(\upsilon,T)} = \frac{1}{\varepsilon_r^{max}(\upsilon)}\left(1+\frac{\left[T-T_{max}(\upsilon)\right]^2}{2\delta^2}\right) \qquad \text{(A3.1)}$$

where ν is the measurement frequency, T is the temperature, ε_r^{max} is the maximum dielectric constant, and δ is the diffuseness parameter. The value of δ is found from the slope of the straight line found in a plot of $\varepsilon_r^{max}/\varepsilon_r$ versus $(T-T_{max})^2$.

Using the zero field dielectric data, $\varepsilon_r^{max}/\varepsilon_r$ versus $(T-T_{max})^2$ have been plotted and δ values calculated from linear fits. Figure A3.2 below shows the plots for PSTCH637 pieces A4, B4 and B5 – all deposited at 300°C and subsequently annealed. The linear fits are good, indicating the relaxor nature of the dielectric properties. The calculated δ values are shown on the plot with pieces B4 (850°C RTP/30s) and B5 (700°C RTP/5 minutes) exhibiting the sharpest permittivity peaks.

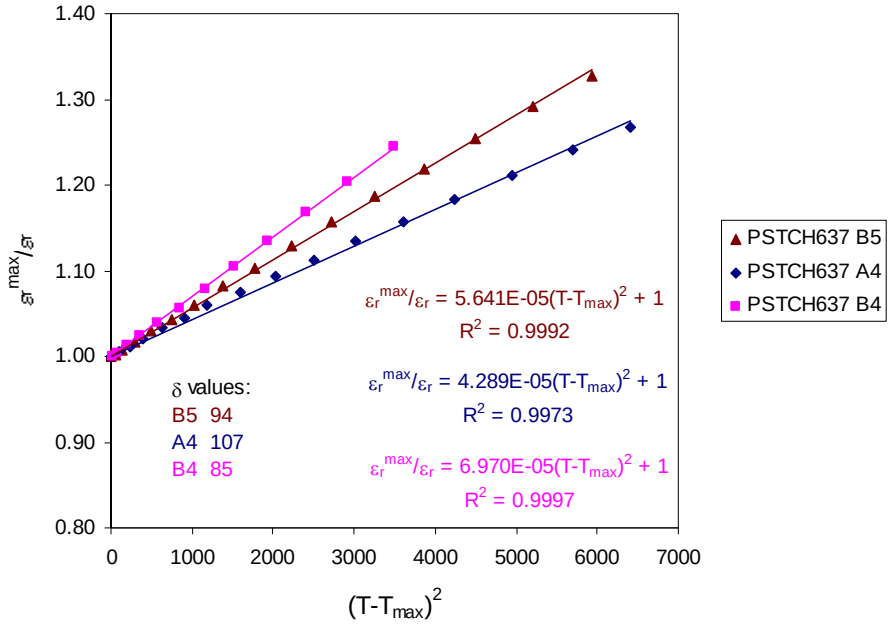

Figure A3.2: Plots of $\varepsilon_r^{max}/\varepsilon_r$ versus $(T-T_{max})^2$ for PSTCH637 pieces A4, B4 and B5. (*Original in colour*)

Figure A3.3 below shows a similar plot for PST184 piece 15 which was deposited at 450°C by dual RF magnetron sputtering and subsequently annealed. The calculated diffuseness parameter of 53 shows that this sample has a sharper permittivity peak than any of the PSTCH637 samples.

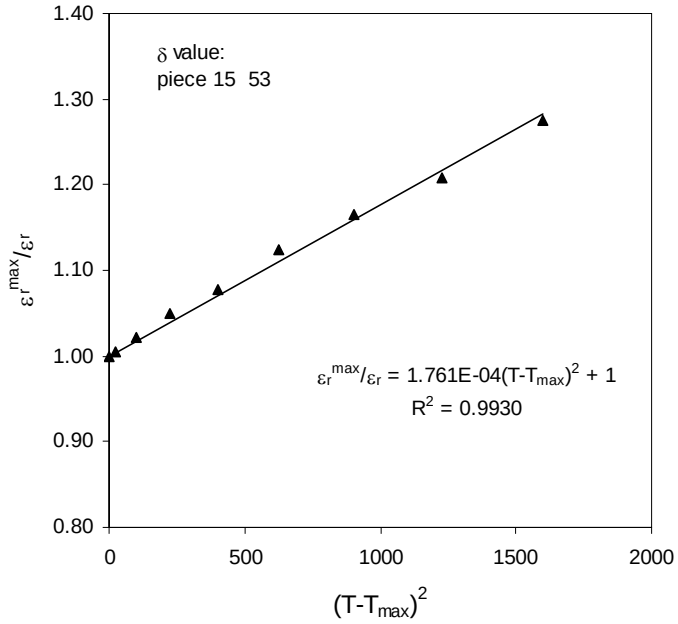

Figure A3.3: Plots of $\varepsilon_r^{max}/\varepsilon_r$ versus $(T\text{-}T_{max})^2$ for PST184 piece 15.

Shown in figure A3.4 below are plots of $\varepsilon_r^{max}/\varepsilon_r$ versus $(T\text{-}T_{max})^2$ for PST285 pieces B1 (700°C RTP), B2 (800°C Oven), C1 (700°C Oven) and C2 (750°C Oven) which were deposited at 300°C by dual RF magnetron sputtering and subsequently annealed. For the oven annealed samples (C1, C2 and B2) the higher the anneal temperature the lower the diffuseness parameter, i.e. the sharper the delectric peak. The exception to this was the lowest temperature oven annealed sample, piece C1, which did not fit well to the Smolenski model and hence no δ value is quoted. The $\varepsilon_r^{max}/\varepsilon_r$ versus $(T\text{-}T_{max})^2$ plot for PST285 piece F2, given a combined RTP/oven (700°C/800°C) anneal is shown in figure A3.5. The fit to the Smolenski law is very good, indicating relaxor behaviour, with a δ value of 107 – exactly the same as for piece B2 which received only the oven anneal at 800°C.

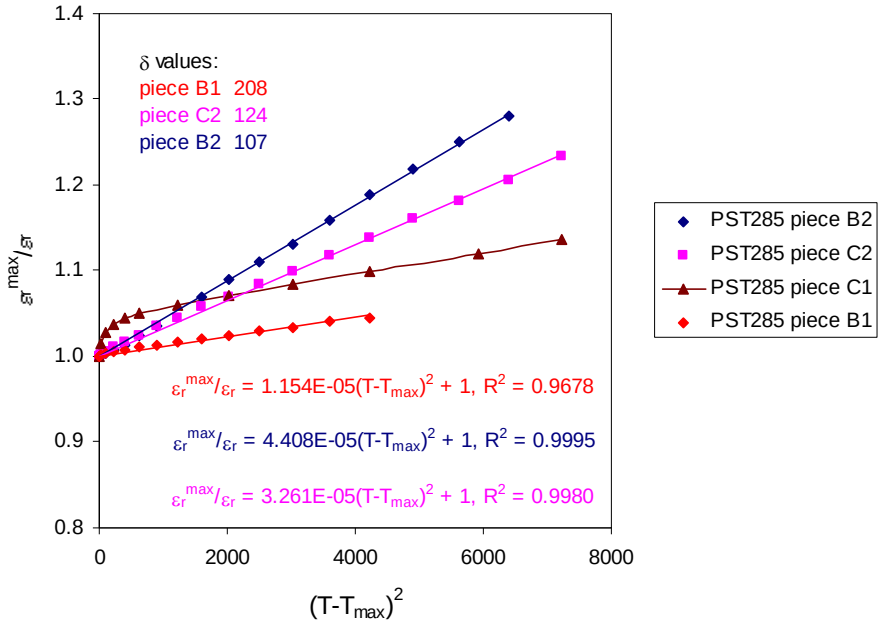

Figure A3.4: Plots of $\varepsilon_r^{max}/\varepsilon_r$ versus $(T-T_{max})^2$ for PST285 pieces B1, B2, C1, C2. (*Original in colour*)

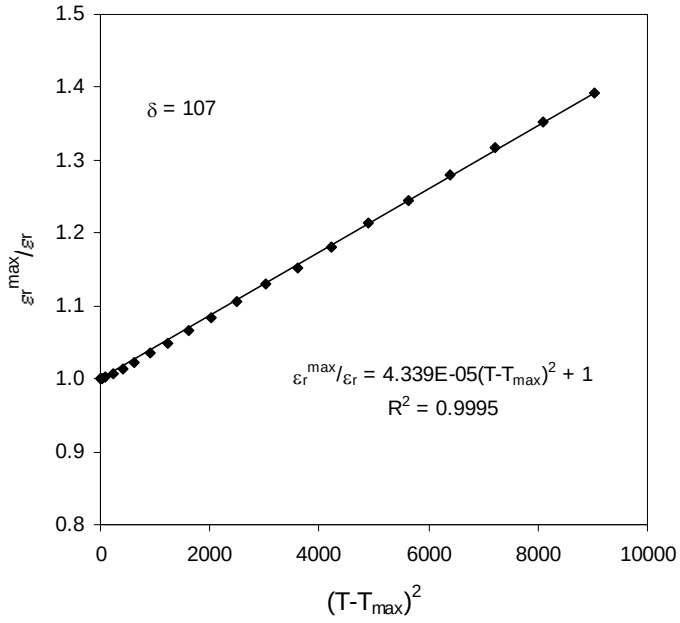

Figure A3.5: Plot of $\varepsilon_r^{max}/\varepsilon_r$ versus $(T-T_{max})^2$ for PST285 piece F2.

Figure A3.6 shows $\varepsilon_r^{max}/\varepsilon_r$ versus $(T-T_{max})^2$ plots for PST315 piece D4 and PST316 piece D3, both deposited at 300°C by dual RF magnetron sputtering at 300°C and subsequently RTP annealed. The zero field permittivity data for PST316 D3 (850°C RTP, 120s) did not fit well to the Smolenski law, indicating a departure from relaxor behaviour. A good straight line could, however, be fitted to the data up to five points above T_{max} giving a δ

value of 47, showing that this sample has the sharpest permittivity peak reported in this thesis. The permittivity data of PST315 D4 (850°C RTP, 30s) fitted well to the Smolenski law, indicating relaxor behaviour, yielding a δ value of 65.

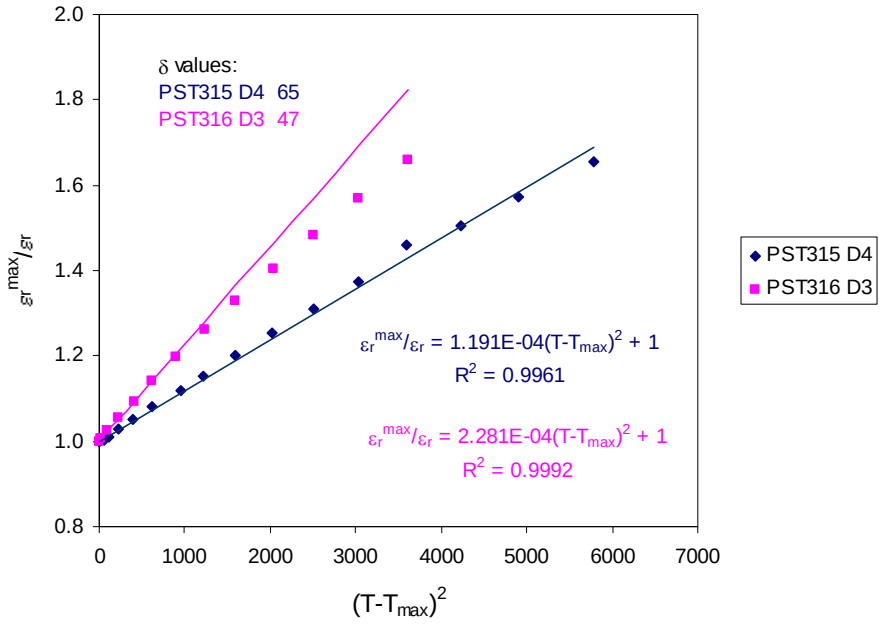

Figure A3.6: Plot of $\varepsilon_r^{max}/\varepsilon_r$ versus $(T-T_{max})^2$ for PST315 piece D4 and PST316 piece D3. (*Original in colour*)

Figure A3.7 below shows the plot of $\varepsilon_r^{max}/\varepsilon_r$ versus $(T-T_{max})^2$ for a typical sample of PST deposited onto platinised silicon by single rf magnetron sputtering at 525°C. Although this film was perovskite as-deposited the peak in ε_r was rather broad, as indicated by the high δ value of 132.

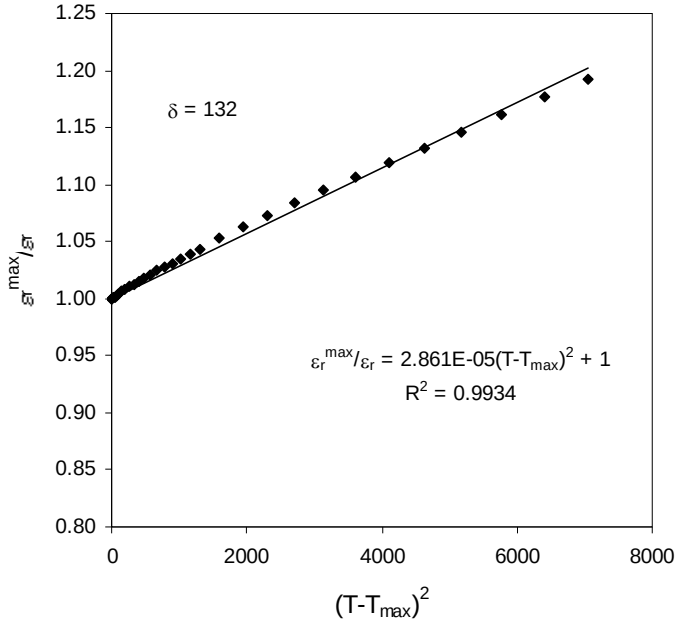

Figure A3.7: Plots of $\varepsilon_r^{max}/\varepsilon_r$ versus $(T-T_{max})^2$ for 525°C deposited PST.

Shown in figure A3.8 below are plots of $\varepsilon_r^{max}/\varepsilon_r$ versus $(T-T_{max})^2$ for a bulk ceramic PST sample and a PST thin film RF sputter deposited onto a sapphire substrate. Both samples exhibited first order-like properties and consequently the fit to the Smolenski model is poor. Values of the diffuseness parameter have, however, been gained by fitting a straight line to a few points just above T_{max}. These fits yield δ values of 11 and 34 for the ceramic and thin film respectively. As expected from the zero field ε_r values, the ceramic is very sharply peaked with the thin film on sapphire being slightly less sharp.

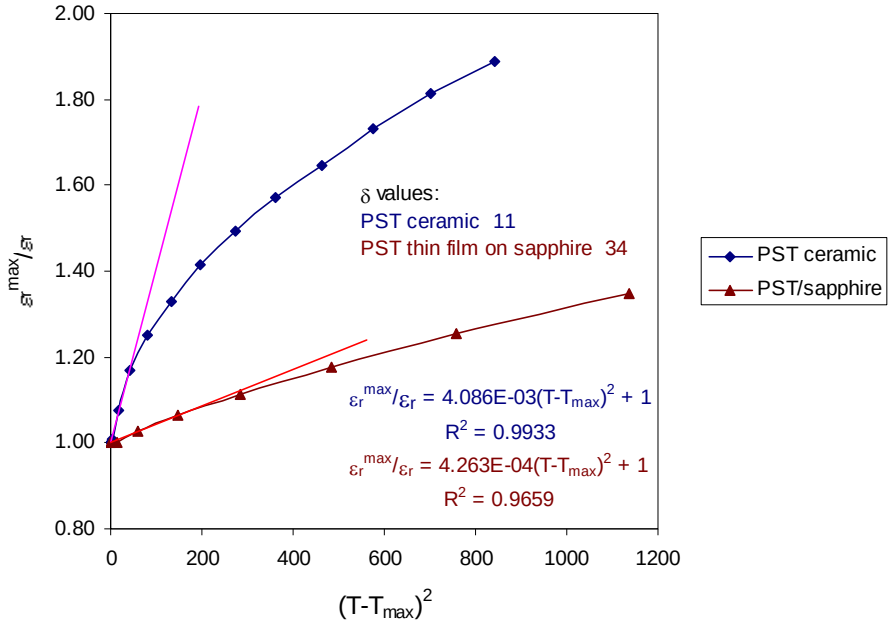

Figure A3.8: Plots of $\varepsilon_r^{max}/\varepsilon_r$ versus $(T-T_{max})^2$ for PST bulk ceramic and PST thin film deposited onto sapphire by RF sputtering.
(*Original in colour*)

Appendix A4:

Thermal Properties of Thin Films Considered in Thermal Modelling for Laser Annealing Studies.

In Chapter 7 the thermal modelling of the temperatures developed during laser irradiation assumed that the thermal properties of the thin films considered could be taken as those for the bulk materials. This requires justification since the thermal properties of materials in thin film from can be very different from those of bulk [147, 148, 149]. A further complication is the further dependence of the materials properties on both the method and the particular conditions of the deposition, as discussed by Thornton [95] and Wilson et al [68]. An insight into this variation can, for metals where the majority of heat transport is due to free electrons, be gained from the variation of the electrical resistivity with thickness and thin film structure. Wilson and Weiss, in a review of the properties of aluminium alloy films used for silicon device fabrication[68], discuss the factors affecting the resistivity. In polycrystalline thin films electron scattering is due to interaction with phonons, lattice defects, grain boundaries and also the film surface. The total resistivity of a thin polycrystalline film, ρ_f, is given by

$$\rho_f = \rho_0 \left(1 + \frac{\gamma^* L_0}{\overline{D}} + \frac{\gamma L_0}{d} \right) \qquad \text{(A4.1)}$$

where ρ_0 is the resistivity within a grain, $\overline{D}$ is the average grain diameter, d is the film thickness, L_0 is the electron mean free path in the material, and γ^* and γ quantify the scattering processes at grain boundaries and the surface respectively. For most metals the thermal and electrical conductivities (κ and σ respectively) are correlated by the well known Weidemann-Franz law (WFL) and variations of it such as the Smith-Palmer relation [150] which applies to alloys and takes into account residual thermal conductivity due to phonons. Powell [150] discusses the validity of the correlation between κ and σ . He concluded that for most pure metals the thermal conductivity can be predicted from the electrical conductivity using the WFL to within an accuracy of 5-10%. Platinum, one of the materials considered in Chapter 7, falls into this category. An exception to the WFL is chromium, the other metal considered in Chapter 7, where there is a high phonon component to the thermal

conductivity (~30% of the total). Powell does show a proportionality between κ and σ for chromium suggesting that a correlation could be described by a Smith-Palmer type relation with a modified Lorenz function and appropriate phonon component.

For the metal layers considered in the laser annealing modelling studies these relations are useful. Both the chromium and platinum (and titanium) are RF sputtered in argon at low pressure onto a thermally oxidised silicon surface which is heated to 300°C. In order to investigate whether the bulk value of κ is applicable for these thin chromium and platinum films the sheet resistivity was measured using a standard four terminal method. The equipment used was a Signatone four point probe and a Keithley 580 Micro-Ohmmeter with samples in the form of 3" wafers. The resistivity of several chrome films of thickness around 1μm are given in table 1 below:

Sample	Sputtering Pressure (mTorr)	RF Power (W)	Target Bias (V)	Thickness (μm)	ρ (Ωm)
V99 Cr 004	4	700	1100	0.65	1.44×10^{-7}
V99 Cr 005	4	650	1100	1.1	1.55×10^{-7}
V99 Cr 006	6	620	1100	0.82	1.37×10^{-7}
V99 Cr 007	4	650	1100	0.79	1.46×10^{-7}

Table A4.1: Measured electrical conductivity (in plane) of thin film chrome sputter deposited in argon onto thermally oxidised silicon.

For the thin film chromium the mean resistivity of the values given in table A4.1 is $1.46\times10^{-7}\Omega$m. The bulk resistivity of chromium is given by Kaye and Laby [73] as $1.27\times10^{-7}\Omega$m (0°C) and $1.61\times10^{-7}\Omega$m (100°C) with a value at room temperature of around $1.34\times10^{-7}\Omega$m. The thin film value is within 7% of this and would, on the basis of the Weidemann-Franz law, justify the use of bulk thermal properties for chromium in the calculations of Chapter 7.

The electrical resistivity of thin film platinum was also measured by the four point probe method. The platinum was sputter deposited onto a thin (100nm) titanium layer itself sputter deposited onto a 3" silicon wafer with a thermally oxidised surface. The thin titanium acts as an adhesion layer [50] since platinum does not form a reproducible oxide and hence adheres poorly to silicon dioxide. Table A4.2 below gives both the deposition conditions and the measured resistivity of a typical platinum film. The effect of the

titanium layer on the resistivity has been ignored since it is in the range where equation A4.1 predicts that the resistivity depends inversely on the thickness and would therefore have only a small effect when taken in parallel with the platinum.

Sample	Sputtering Pressure (mTorr)	RF Power (W) (Ti/Pt)	Substrate Bias (V) (Ti/Pt)	Thickness (∑) (Ti/Pt)	ρ (Ωm)
Pt/Ti 0567	9	150/300	100/1100	100/1000	1.10×10^{-7}

Table A4.2: Measured electrical conductivity (in plane) of thin film Pt (with a very thin Ti adhesion layer) sputter deposited in argon onto thermally oxidised silicon.

The measured value of the resistivity of $1.1\times10^{-7}\Omega$m compares with the values given in Kaye and Laby of $0.986\times10^{-7}\Omega$m (0°C) and $1.61\times10^{-7}\Omega$m (100°C) with a room temperature value of around $1.06\times10^{-7}\Omega$m. These two values agree well and support use of the bulk thermal properties of platinum in the calculations of Chapter 7.

It is worth noting that the measured resistivities for the chrome and platinum thin films are in-plane measurements, with the probe current flowing perpendicular to the columnar grain boundaries. Heat transport in the thin film layer stack considered in Chapter 7 occurs parallel to the grain boundaries. The comparison of the thin film properties with those of bulk assumes that the in-plane properties of the films are the not significantly different to the perpendicular properties.

The thermal conductivity of thin film silicon dioxide, the other material in the layer stack underlying the PST/PZT, have been measured by Kleiner et al [151] using specially fabricated microstructures. Thin films reported were in the thickness range 0.6-2.5μm and were deposited by a number of techniques, including PECVD and other techniques such as spin-on glass and APCVD. Measured κ values were only 20-30% below those of bulk fused quartz, whose temperature dependence they followed. Paul et al [152] reported measurements of the thermal conductivity of the thin film components of the complete Austria Mikro Systeme (AMS) 1.2μm CMOS process [153]. As for the paper by Kleiner, κ was measured using specially designed microstructures. For silicon dioxide κ was found to be between 0% and 16% lower than, and to follow the temperature dependence of, bulk fused silica.

The reported thermal conductivity values reported for thin film silicon dioxide are very close to those of bulk. Since variations in κ may be expected due to different deposition techniques and conditions (due to variation in film density for example), the bulk values of the thermal conductivity of silicon dioxide have been used in Chapter 7.

Appendix A5:

Materials Thermal Properties Used in Laser Annealing Thermal Modelling.

1. Introduction

The predicted temperature profiles for the laser annealing experiments described in Chapter 7 were modelled by solving the heat diffusion equation with the thermal properties for the materials composing the layers exposed to laser radiation. The situations modelled were PZT and PST layer stacks both with and without a chromium sacrificial layer, i.e. PST[or PZT](0.5-1μm)/Pt(1000∑)/SiO_2(1000∑)/Cr(1μm)/SiO_2(0.8μm)/Si(500μm) and PST[or PZT](0.5-1μm)/Pt(1000∑)/SiO_2(0.8μm)/Si(500μm). The modelling required the input of both the specific heat capacity and thermal conductivity for all of the materials involved. Data for PST and PZT bulk ceramic was taken from Marconi Caswell [105, 136]. Data for the other materials were taken from standard reference books [73, 135]. In order to incorporate the temperature variation of thermal properties with temperature this data was interpolated using the cubic spline facility of Matlab. The original data and interpolated points for each material considered are given in the sections below.

2. Thermal Properties

2.1 PST

The thermal properties of PST were taken from those for perovskite phase bulk ceramic [105], which were assumed to be representative of thin film PST – in both perovskite and pyrochlore/amorphous forms. The data available were the specific heat capacity (c_p) and the diffusivity (D). The specific heat capacity above the transition is given in table A5.1 below. The values at 277°C and 327°C are extrapolated values and were set constant at 324$Jkg^{-1}K^{-1}$.

Temperature (°C)	c_p ($Jkg^{-1}K^{-1}$)
63	312
127	316
177	320
227	322
277	324
327	324

Table A5.1: PST specific heat capacity.

For use in the modelling studies c_p was required at 1°C intervals. To accomplish this a 6th order polynomial, equation (A5.1), was fitted to the c_p values in the table.

$$c_p(T) = \sum_{n=1}^{5} p_n T^{5-n} \qquad \text{(A5.1)}$$

Where T is the reduced temperature {actual temperature(°C)/25}. The coefficients p_n are given in table A5.2 below.

Coefficient	Value
p_1	4.7012×10^{-9}
p_2	-4.5974×10^{-6}
p_3	1.3962×10^{-3}
p_4	-9.8894×10^{-2}
p_5	3.1429×10^{2}

Table A5.2: Coefficients for polynomial fit to specific heat capacity of PST.

Figure A5.1 below shows the c_p data and the polynomial fit. At 300°C and above the value of c_p was set constant at $324.23 Jkg^{-1}K^{-1}$.

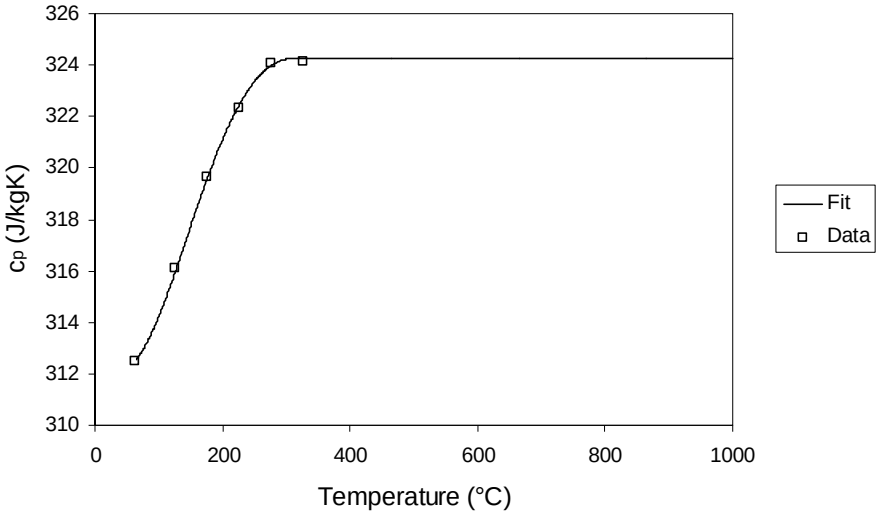

Figure A5.1: Specific heat capacity of PST, data and polynomial fit.

Diffusivity (D) data for bulk ceramic PST is given in table A5.3 below

Temperature (°C)	Diffusivity ($\times 10^{-6} m^2 s^{-1}$)	Temperature (°C)	Diffusivity ($\times 10^{-6} m^2 s^{-1}$)
40	0.416	248	0.480
53	0.426	276	0.482
79	0.439	300	0.484
90	0.443	335	0.488
100	0.449	369	0.491
129	0.457	400	0.493
152	0.462	434	0.495
181	0.469	600	0.501
200	0.472	700	0.503
226	0.476		

Table A5.3: Diffusivity of PST.

For use in modelling studies D was required at 1°C intervals, from which the thermal conductivity could be calculated at this interval. To accomplish this a 6th order polynomial, equation (2), was fitted to the D values in the table.

$$D(T) = \sum_{n=1}^{7} q_n T^{7-n} \qquad \text{(A5.2)}$$

where T is the reduced temperature {actual temperature(°C)/25}. The coefficients q_n are given in table A5.4 below. Above 700°C D was set constant.

Coefficient	Value
q_1	-1.2933×10^{-9}
q_2	1.602×10^{-7}
q_3	-8.0782×10^{-6}
q_4	2.0604×10^{-4}
q_5	-2.936×10^{-3}
q_6	2.488×10^{-2}
q_7	3.8377×10^{-1}

Table A5.4: Coefficients for polynomial fit to PST diffusivity.

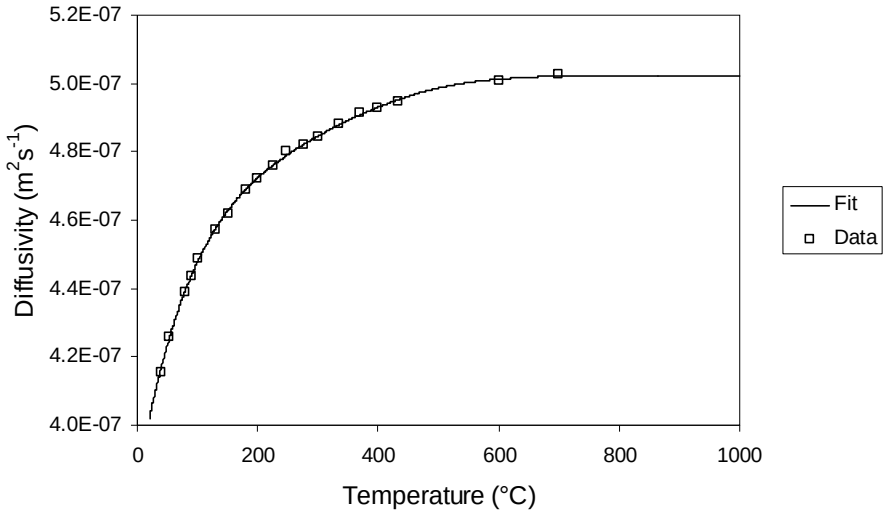

Figure A5.2: Diffusivity of PST, data and polynomial fit.

The thermal conductivity of bulk PST was calculated from the fitted specific heat capacity and diffusivity values using the definition,

$$\kappa = D\rho c_p \qquad \text{(A5.3)}$$

where ρ is the density and c_p the specific heat capacity. The density of PST was taken as the theoretical density calculated from the perovskite unit cell data in the JCPDS database [53]. The total unit cell mass for disordered PST perovskite is 6.1195×10^{-25} kg. With a cubic unit cell of side 4.068∑ the density is 9090.2 kgm^{-3}. The resulting thermal conductivity values are plotted in figure A5.3 below.

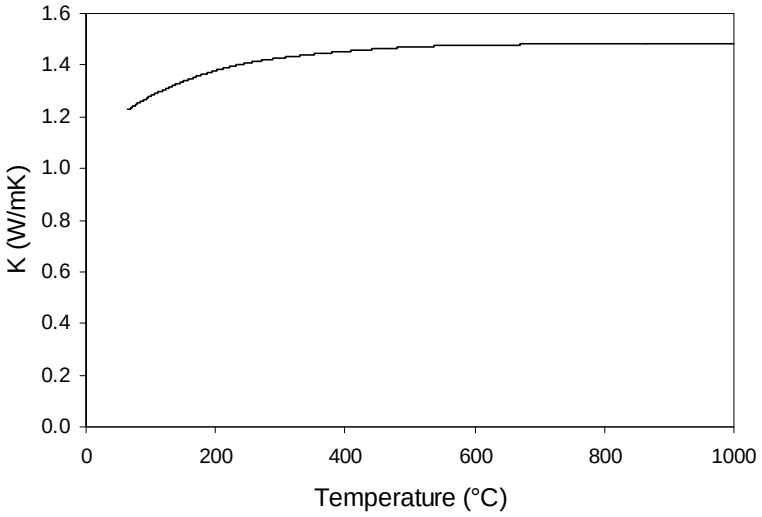

Figure A5.3: Fitted thermal conductivity of PST.

2.2 PZT

The thermal properties of PZT were taken from those for MIRL Caswell RM200 perovskite bulk ceramic [136] which, as in the case for PST, were assumed to be applicable to thin film PZT – in both perovskite and pyrochlore/amorphous forms. Table A5.5 below gives measured values of the specific heat capacity between –53.2°C and 276.9°C. Figure A5.4 shows a plot of this data with c_p peaking at the Curie temperature – around 220°C.

Temperature (°C)	c_p (J/kgK)	Temperature (°C)	c_p (J/kgK)
-53.2	288.7	116.9	353.8
-43.2	293.6	126.9	357.5
-33.2	297.3	136.9	361.2
-23.2	303.4	146.9	363.6
-13.2	308.4	156.9	367.3
-3.2	310.8	166.9	369.8
6.9	314.5	176.9	375.9
16.9	319.4	186.9	380.8
26.9	323.1	196.9	387
36.9	326.8	206.9	398
46.9	330.5	216.9	406.6
56.9	334.2	226.9	388.2
66.9	337.8	236.9	372.2
76.9	341.5	246.9	368.6
86.9	344	256.9	364.9
96.9	346.4	266.9	363.6
106.9	351.4	276.9	363.6

Table A5.5: Specific heat capacity of PZT.

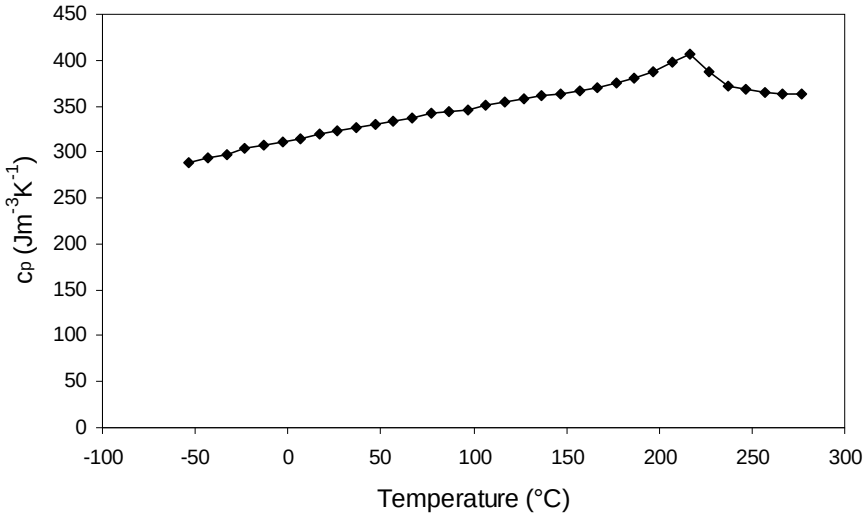

Figure A5.4: Specific heat capacity of PZT.

The diffusivity of PZT between 40°C and 300°C is given in table A5.6 below. The data is plotted in figure A5.5. As with the specific heat capacity there is an anomaly around the Curie temperature, above which the diffusivity rises rapidly before levelling off at 300°C.

Temperature (°C)	Diffusivity ($\times 10^{-7} m^2 s^{-1}$)	Temperature (°C)	Diffusivity ($\times 10^{-7} m^2 s^{-1}$)
40	4.37	217	4.58
67	4.42	226	4.57
90	4.42	235	4.74
116	4.43	244	4.84
141	4.44	255	4.96
166	4.46	281	5.10
191	4.48	300	5.14
208	4.56		

Table A5.6: Diffusivity of PZT.

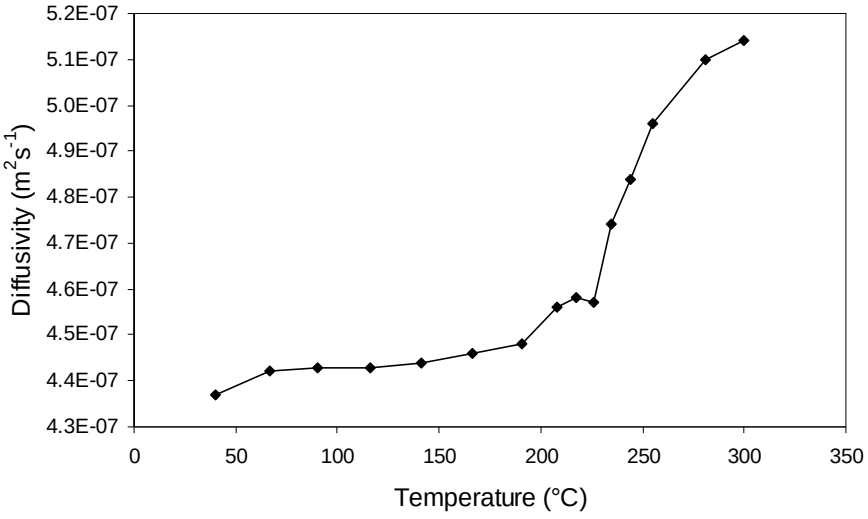

Figure A5.5: Diffusivity of PZT.

The specific heat capacity and diffusivity of PZT have been taken to be constant above the high temperature limits of the data, i.e. 363.6 J/kgK at 276.9°C and 5.14×10-7 m^2s^{-1} for c_p and D respectively. With a density of 8.14×10^3 kgm^{-3} this gives a high temperature thermal conductivity of 1.52 $Wm^{-1}K^{-1}$.

2.3 Platinum

Table A5.7 below gives specific heat capacity values for platinum, taken from Kaye and Laby [73]. Figure A5.6 shows a plot of these together with a spline interpolation, on a 1°C interval, performed using Matlab. Above 500°C c_p was set constant at 146 $Jkg^{-1}K^{-1}$. This is a reasonable assumption since the data shows c_p levelling off, as expected since the Debye temperature for platinum is –33°C [154].

Temperature (°C)	c_p ($Jkg^{-1}K^{-1}$)
-196.2	85
-100.5	123
-0.2	132
99.9	135
299.9	141
499.9	146

Table A5.7: Specific heat capacity of platinum.

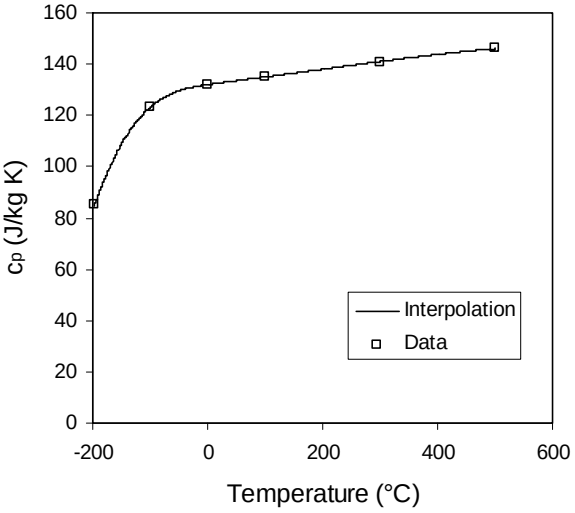

Figure A5.6: Specific heat capacity of platinum.

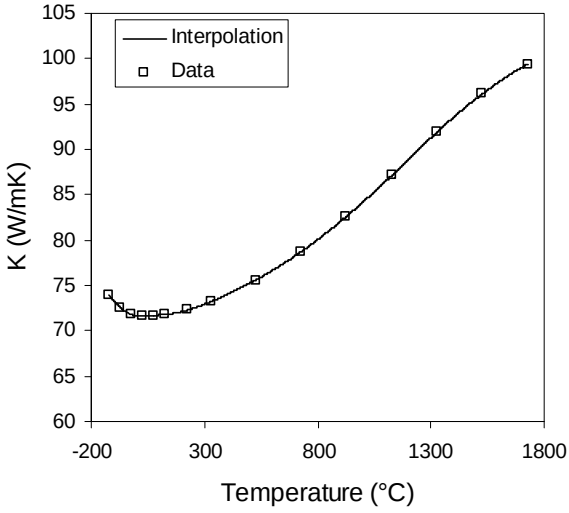

Figure A5.7: Thermal conductivity of platinum.

The thermal conductivity of platinum at various temperatures, taken from the CRC Handbook [135], is given in table A5.8 below. Figure A5.7 shows a plot of these together with a spline interpolation, on a 1°C interval.

Temperature (°C)	K (W/mK)	Temperature (°C)	K (W/mK)
-123.2	74	526.9	75.6
-73.2	72.6	726.9	78.7
-23.2	71.8	926.9	82.6
26.9	71.6	1126.9	87.1
76.9	71.7	1326.9	91.9
126.9	71.8	1526.9	96.1
226.9	72.3	1726.9	99.4
326.9	73.2		

Table A5.8: Thermal conductivity of platinum.

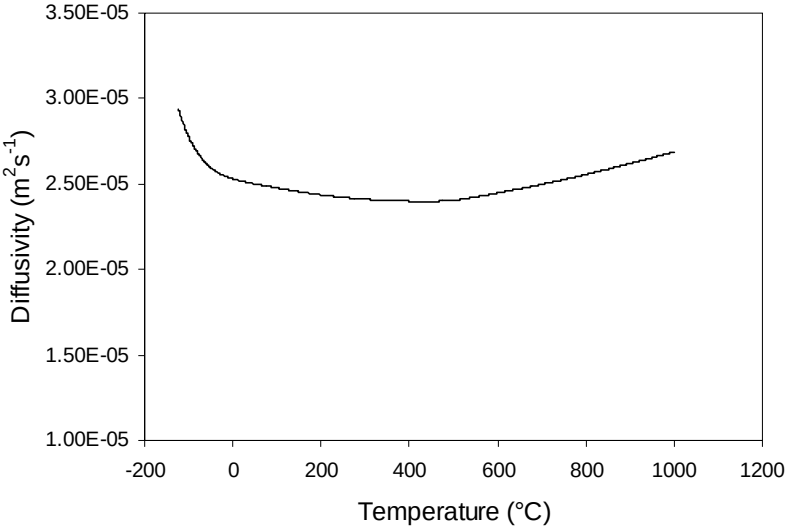

Figure A5.8: Diffusivity of platinum.

2.4 Silicon Dioxide

Table A5.9 below gives specific heat capacity values at various temperatures, taken from Kaye and Laby [73], for amorphous silicon dioxide. Above 500°C c_p was set constant at 1100 $Jkg^{-1}K^{-1}$. Figure A5.9 shows a plot of these together with a spline interpolation, on a 1°C interval.

Temperature (°C)	c_p ($Jkg^{-1}K^{-1}$)
-0.15	700
99.9	830
299.9	1020
499.9	1100

Table A5.9: Specific heat capacity of amorphous SiO_2.

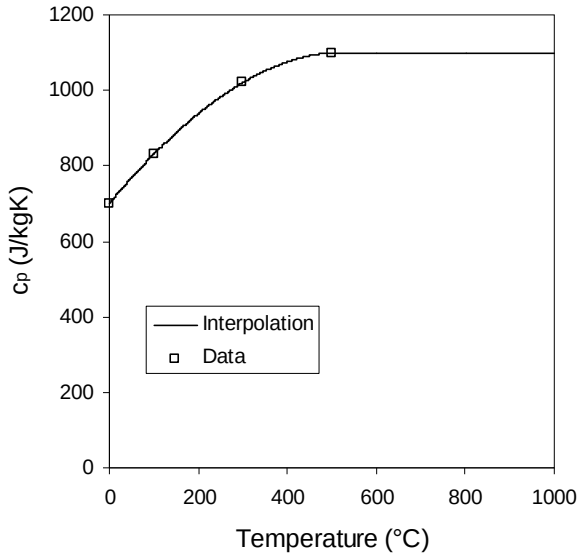

Figure A5.9: Specific heat capacity of amorphous SiO_2.

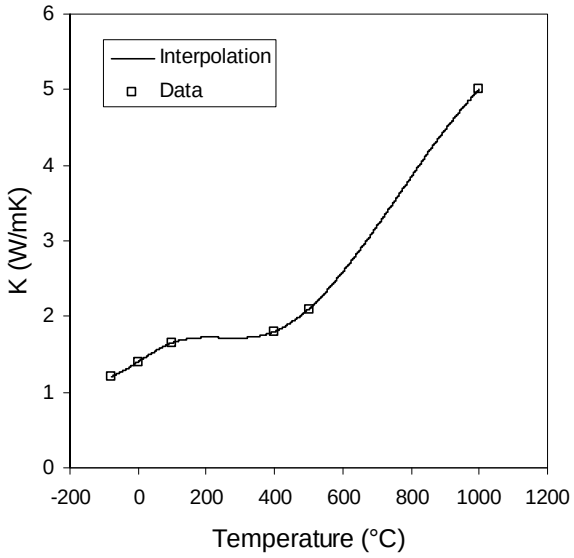

Figure A5.10: Thermal conductivity of amorphous SiO_2.

The thermal conductivity of silicon dioxide at various temperatures is given in table A5.10 below. The data is a combination of that from Kaye and Laby [73] and the CRC Handbook [135]. Figure A5.10 shows a plot of these together with a spline interpolation, on a 1°C interval.

Temperature (°C)	K (W/mK)
-79.2	1.2
-0.2	1.4
25	1.6
100	1.65
500	2.1
1000	5

Table A5.10: Thermal conductivity of silicon dioxide.

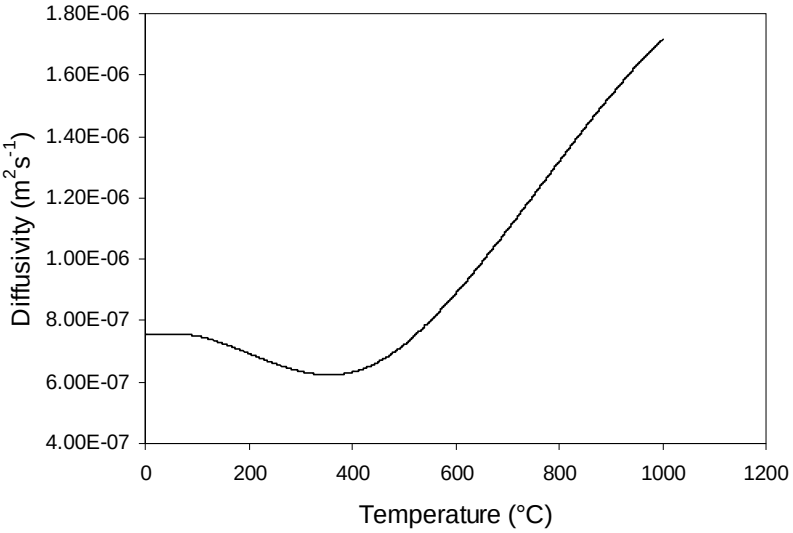

Figure A5.11: Diffusivity of silicon dioxide.

2.5 Chromium

Table A5.11 below gives specific heat capacity values at various temperatures, taken from Kaye and Laby [73], for chromium. A point was extrapolated to 880°C at which c_p was set to 580Jkg^{-1}K^{-1}, compared with a data value of 550Jkg^{-1}K^{-1} at 500°C. This upper temperature was sufficient for modelling purposes. Figure A5.12 shows a plot of these together with a spline interpolation, on a 1°C interval.

Temperature (°C)	c_p (Jkg^{-1}K^{-1})
-196.2	117
-100.2	351
-0.2	438
99.9	481
299.9	527
499.9	550
800*	580

Table A5.11: Specific heat capacity of chromium.

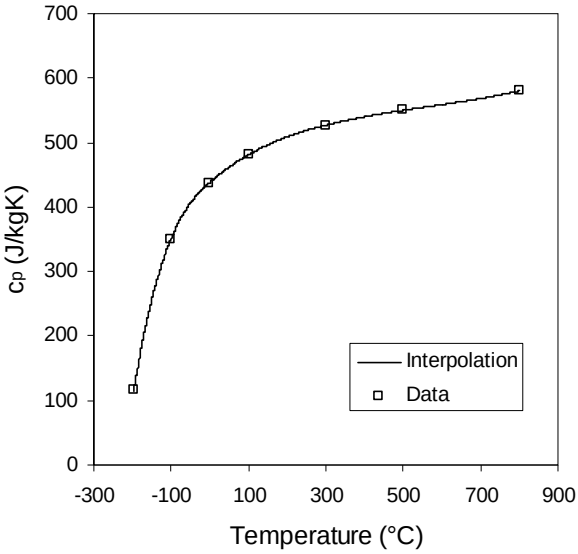

Figure A5.12: Specific heat capacity of chromium.

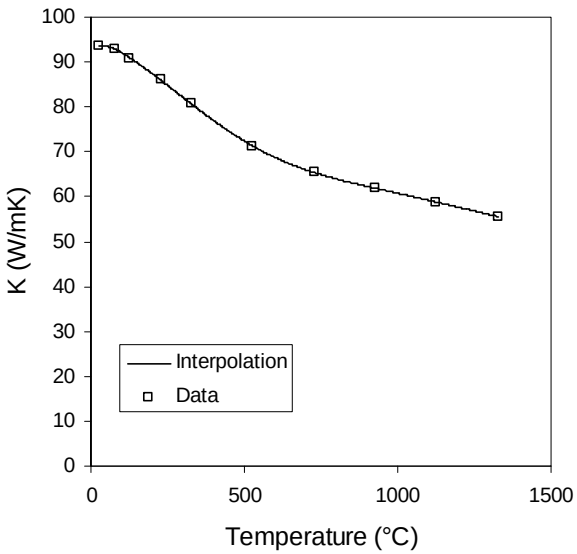

Figure A5.13: Thermal conductivity of chromium.

The thermal conductivity of chromium at various temperatures, taken from the CRC Handbook [135], is given in table A5.12 below. Figure A5.13 shows a plot of these together with a spline interpolation, on a 1°C interval.

Temperature (°C)	K (W/mK)	Temperature (°C)	K (W/mK)
-123.2	129	526.9	71.3
-73.2	111	726.9	65.4
-23.2	100	926.9	61.9
26.9	93.7	1126.9	58.8
76.9	92.9	1326.9	55.6
126.9	90.9	1526.9	52.6
226.9	86	1726.9	49.4
326.9	80.7		

Table A5.12: Thermal conductivity of chromium.

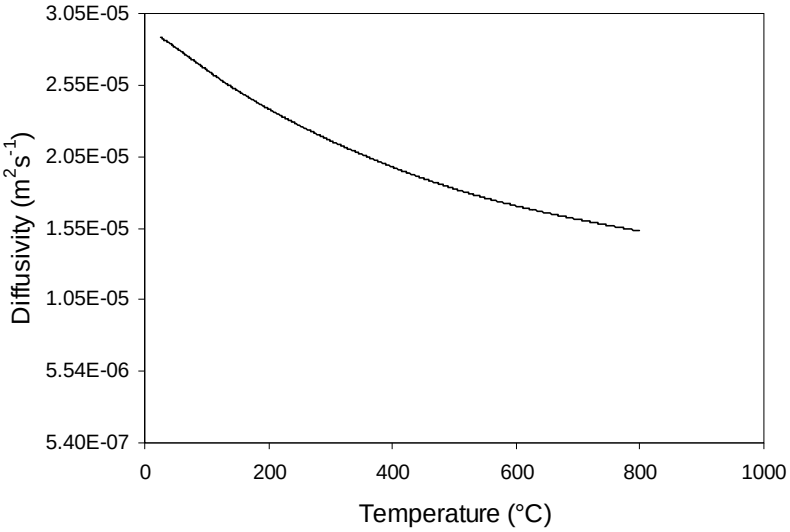

Figure A5.14: Diffusivity of chromium.

2.6 Silicon

Table A5.13 below gives specific heat capacity values at various temperatures, taken from the CRC Handbook [135], for silicon over a wide temperature range. Figure A5.14 shows a plot of these together with a spline interpolation, on a 1°C interval.

Temperature (°C)	c_p ($Jkg^{-1}K^{-1}$)	Temperature (°C)	c_p ($Jkg^{-1}K^{-1}$)
25	704.4	626.9	930.3
26.9	706.8	726.9	945.7
126.9	793.8	826.9	960.2
226.9	840.4	926.9	974
326.9	871.1	1026.9	987.3
426.9	894.3	1126.9	1000.4
526.9	912	1226.9	1013.1

Table A5.13: Specific heat capacity of silicon.

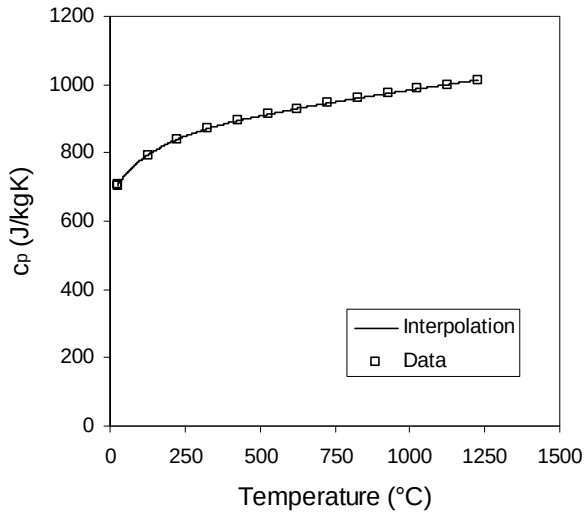

Figure A5.15: Specific heat capacity of silicon.

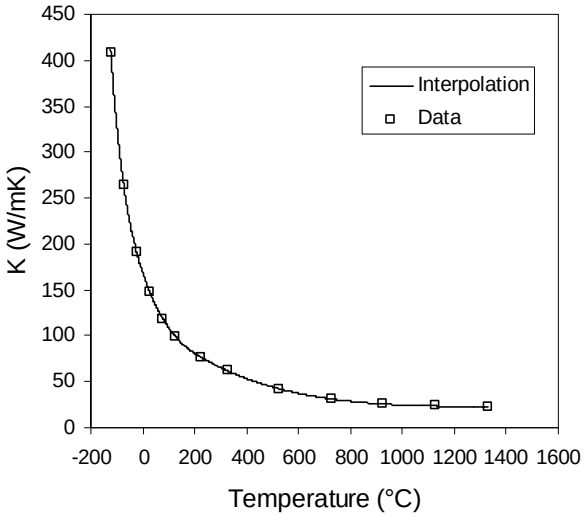

Figure A5.16: Thermal conductivity of silicon.

The thermal conductivity of silicon at various temperatures, taken from the CRC Handbook [135], is given in table A5.14 below. Figure A5.16 shows a plot of these together with a spline interpolation, on a 1°C interval.

Temperature (°C)	K (W/mK)	Temperature (°C)	K (W/mK)
-123.2	409	326.9	61.9
-73.2	264	526.9	42.2
-23.2	191	726.9	31.2
26.9	148	926.9	25.7
76.9	119	1126.9	23.5
126.9	98.9	1326.9	22.1
226.9	76.2		

Table A5.14: Thermal conductivity of silicon.

Figure A5.16: Thermal conductivity of chromium, actual data and interpolation.

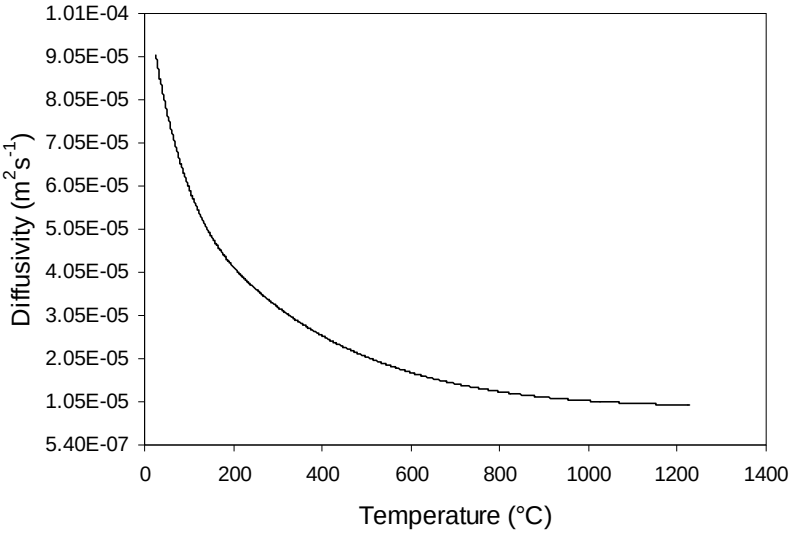

Figure A5.17: Diffusivity of silicon.

3. Stability Criteria

Using the thermal properties of the materials discussed it was possible to calculate the value of the stability parameter, discussed in Chapter 7, of the numerical method used to solve the heat diffusion equation. The stability criterion is given by

$$\frac{\kappa \Delta t}{c_p \rho \Delta z^2} < \frac{1}{2} \qquad \text{(A5.4)}$$

where the quantity on the left is the stability parameter and κ is the thermal conductivity, ρ is the density. Δt and Δz are the time step and layer thickness of the of the numerical method respectively. The stability parameters of platinum, silicon dioxide, chromium and silicon are shown in figure A5.18 below. Δt and Δz were 25ps and 50nm respectively.

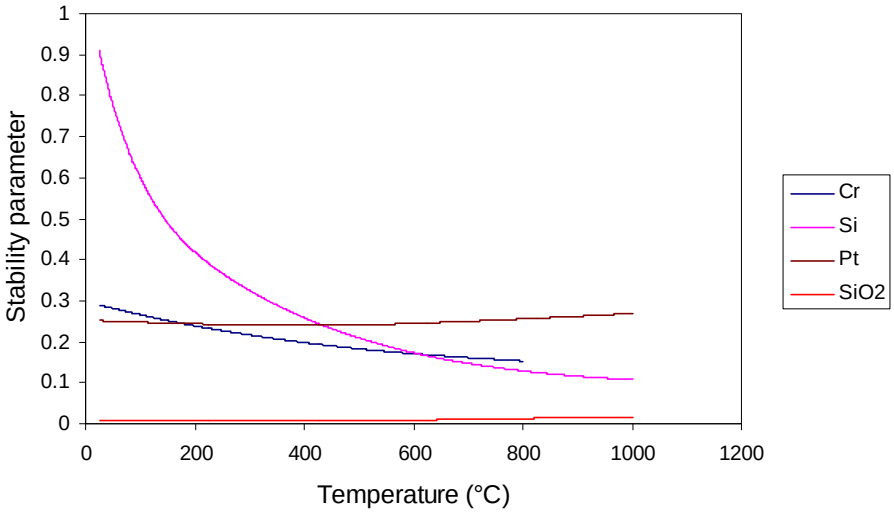

Figure A5.18: Stability parameter values for Pt, SiO_2, Cr and Si.
(*Original in colour*)

As can be seen from the figure, all materials are stable with the exception of silicon below 145°C. This was not a problem since no calculations were made at temperatures below this.

The stability parameter value for PST is shown in figure A5.19 below. As might be expected from such a poor diffuser the value is well below 0.5.

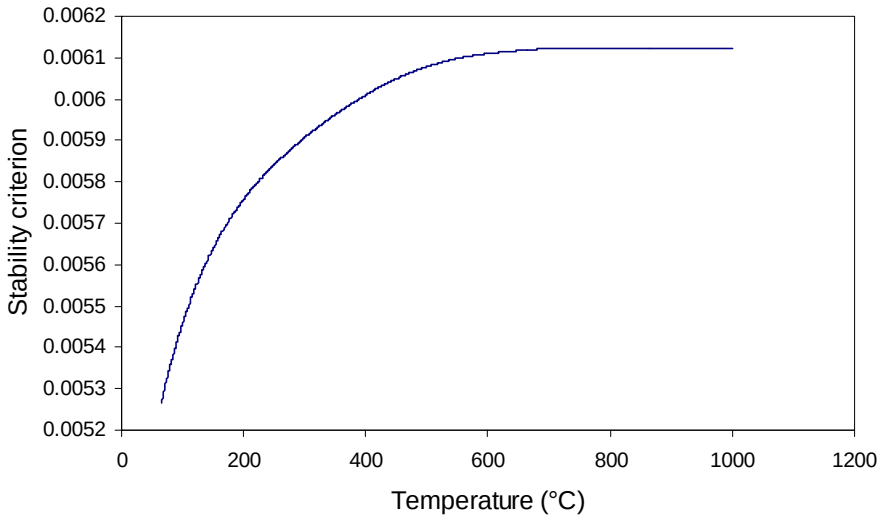

Figure A5.19: Stability parameter for PST.

The stability parameter value for PZT at 300°C and above is 0.0051, again very low due to the material being a very poor diffuser of heat.

Appendix A6:

Validation of the Numerical Method Used to Solve for the Temperature Distributions During Laser Annealing.

As a check of the numerical method used to solve the heat diffusion problem in the laser annealing experiment, the output from it has been compared to the analytical solution obtained using certain simplifying assumptions. As explained in Chapter 7, a unidimensional form of the heat equation, equation (A6.1) has been used to investigate the problem.

$$\frac{\partial T}{\partial t} = \frac{\alpha}{\rho c_p} I(z,t) + \frac{1}{\rho c_p} \frac{\partial}{\partial z}\left(\kappa \frac{\partial T}{\partial z}\right) \qquad \text{(A6.1)}$$

where T is the temperature, t is time, ρ is the density, c_p is the specific heat capacity, κ is the thermal conductivity and α is the absorption coefficient. I(z,t) is the power density of laser light at depth z and time t and for a homogeneous absorbing medium is given by

$$I(z,t) = I_0(t)(1-R)e^{-\alpha z} \qquad \text{(A6.2)}$$

where $I_0(t)$ is the laser output power density and R is the reflectivity of the top surface of the sample.

Equation (A6.1) can be solved analytically if a set of simplifying assumptions are imposed. These are:-

(i) The laser pulse does not induce a phase change in the material.

(ii) The optical (α,R) and thermal (κ,c_p) parameters of the material are not temperature dependent.

(iii) There is no inhomogeneity of the optical or thermal parameters of the material in the z direction.

(iv) The power output of the laser is constant.

(v) The sample is of infinite thickness.

Under these assumptions the solution to equation (A6.1) is given by[125, 126]

$$T(z,t)=\left\{\left(\frac{2I_0}{\kappa}\right)\sqrt{Dt}\;ierfc|\gamma|-\left(\frac{I_0}{\alpha\kappa}\right)e^{-\alpha z}+\left(\frac{I_0}{2\alpha\kappa}\right)e^{\alpha^2Dt-\alpha z}erfc|\phi|+\left(\frac{I_0}{2\alpha\kappa}\right)e^{\alpha^2Dt+\alpha z}erfc|\theta|\right\}(1-R))$$

(A6.3)

where D is the diffussivity given by

$$D=\frac{\kappa}{\rho c_p} \tag{A6.4}$$

and

$$\gamma=\frac{z}{2\sqrt{Dt}} \tag{A6.5},$$

$$\phi=\alpha\sqrt{Dt}-\gamma \tag{A6.6},$$

$$\theta=\alpha\sqrt{Dt}+\gamma \tag{A6.7},$$

$$erfc|x|=\frac{2}{\sqrt{\pi}}\int_x^\infty e^{-\varsigma^2}d\varsigma \tag{A6.8},$$

$$ierfc|x|=\frac{1}{\sqrt{\pi}}e^{-x^2}-xerfc|x| \tag{A6.9}.$$

If the optical absorption length (α-1) is much smaller than the heat diffusion length {$\sqrt{}$(Dt)} then the solution to equation (A6.1) can be simplified to

$$T(z,t)=\left[\frac{2I_0\sqrt{Dt}}{\kappa}\right]ierfc|\gamma|(1-R) \tag{A6.10}$$

As a test of the numerical method the output from the modeling program, described in chapter 7, has been compared with the solution using equation 10 above. A special case has been chosen so that the criteria for analytical solution are valid. The situation chosen is irradiation of silicon with 20ns pulse with a "top hat" temporal profile. The thermal properties were those at 300°C which give a diffusivity of $3.14\times10^{-5}m^2s^{-1}$ and a diffusion length during the pulse of 0.79μm. The optical properties for silicon were those at the laser wavelength, 248nm, taken from Palik [134], with the absorption length ($\lambda/4\pi k$) calculated from the quoted value of the extinction coefficient being 5.52nm. This is much less than the

diffusion length during the pulse and thus validates the use of the simplified analytical solution, equation A6.10. Table A6.1 below gives a summary of the properties of silicon used for the calculations.

ρ	2329 kg/m^3
D	3.14×10^{-5} m^{2}s^{-1}
κ	63.9 Wm^{-1}K^{-1}
α	1.81×10^{8} m^{-1}
R	0.66

Table A6.1: Thermal and optical properties of silicon used for calculations.

The temperature distribution during the pulse was solved numerically using the method described in detail in Chapter 7 with the silicon divided into finite layers of thickness 0.1μm and time discritised into finite periods of duration 0.1ns, with the temperature being output every 1ns. The substrate ambient temperature was set to 300°C and the thermal properties were held fixed at those for this temperature, with the fluence of the laser pulse being 0.5J/cm^2. Figure A6.1 below shows the numerical solution for the first ten layers into the silicon. These temperatures output from the model are interpreted as the average for each discrete layer and are taken to apply at the mid point of each layer, i.e. 0.05μm, 0.15μm… . Also shown on the graph are the analytical solutions for the temperature at positions corresponding to the mid point of each discrete layer.

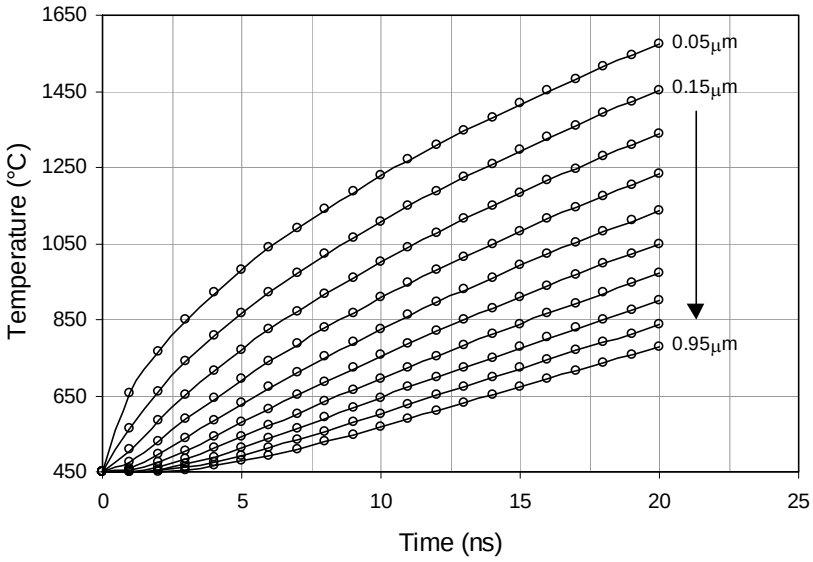

Figure A6.1: Analytical (—) and numerical (o) solutions.

As can be seen from the graph, there is very good agreement between the numerical and analytical solutions. This gives confidence that the numerical method and the program written to implement it are valid.

Appendix A7:

Relation Between Device Performance and Materials Merit Figure.

This appendix presents the results of modelling work carried out by Mr. R. Watton of DERA that gives an indication of the uncooled IR detector performance that can be expected from material with a certain F_D value. Performance is quantified in terms of the detectors noise equivalent temperature difference (NETD) which is the temperature difference in the scene which results in an output voltage from an IR detector element that is equal to the electrical noise output from that detector element. Figure A7.1 below shows a graph of NETD versus F_D which allows the PST merit figure values presented in Chapters 5 and 6 to be set in context. Modelling assumed a XAC detector structure (refer to Chapter 2) in composite (using an interconnect wafer – refer to Chapter 2) array of 300×400 detectors on a 40μm pitch, standard CMOS readout electronics, f/1 optics, short range imaging in the 8-14μm waveband.

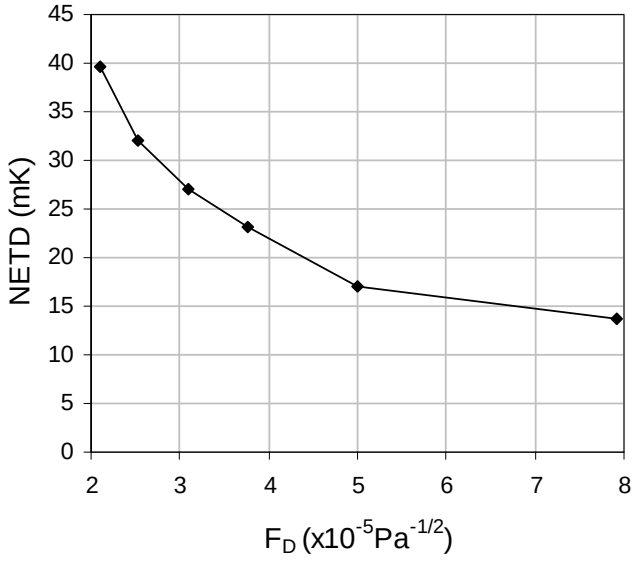

Figure A7.1: NETD-F_D correspondence.

Appendix A8

Publications

Deposition and Annealing of Lead Scandium Tantalate Thin Films for High Performance Thermal Detector Arrays.
M.A. Todd, P.P. Donohue, J.C. Jones, D.J. Wallis, M.J. Slater, M.A. Harper, R. Watton.
Integrated Ferroelectrics vol. 25, pp. 113-123, 1999.

Sputtered Lead Scandium Tantalate Thin Films for Dielectric Bolometer Mode Thermal Detector Arrays.
M.A. Todd, P.P. Donohue, M.A.C. Harper, J.C. Jones.
Submitted to *Integrated Ferroelectrics*, March 2000.

Pulse-Extended Excimer Laser Annealing of Lead Zirconate Titanate Thin Films.
P.P. Donohue, M.A. Todd.
Submitted to *Integrated Ferroelectrics*, March 2000.

Conference Presentations

Deposition and Annealing of Lead Scandium Tantalate Thin Films for High Performance Thermal Detector Arrays.
M.A. Todd, P.P. Donohue, J.C. Jones, D.J. Wallis, M.J. Slater, M.A. Harper, R. Watton.
International Symposium on Integrated Ferroelectrics, Colorado Springs, March 1999.

Sputtered Lead Scandium Tantalate Thin Films for Dielectric Bolometer Mode Thermal Detector Arrays.
M.A. Todd, P.P. Donohue, M.A.C. Harper, J.C. Jones.
International Symposium on Integrated Ferroelectrics, Aachen, March 2000.

Pulse-Extended Excimer Laser Annealing of Lead Zirconate Titanate Thin Films.
P.P. Donohue, M.A. Todd.
International Symposium on Integrated Ferroelectrics, Aachen, March 2000.

High Temperature Processing of Ferroelectric Thin Films Using Intermediate Wafer Technology.
P.P. Donohue, M.A. Todd, C.J. Anthony, A.G. Brown, M.A.C. Harper, R. Watton.
To be presented at the *International Symposium on Integrated Ferroelectrics*, Colorado Springs, March 2001.

List of References

[1] J.M. Lloyd. *Thermal Imaging Systems*. Plenum Press, 1975.

[2] W.D. Rogatto. *The Infrared and Electro-Optical Systems Handbook, Volume 3 Electro-Optical Components*. SPIE Optical Engineering Press, 1993.

[3] R.W. Whatmore, A. Patel, N.M. Shorrocks, F.W. Ainger. Ferroelectric Materials for Thermal IR Sensors State of the Art and Perspectives. *Ferroelectrics* vol. 104, pp. 269-283, 1990.

[4] R. Watton. Ferroelectric Materials and IR Bolometer Arrays: From Hybrid Arrays Towards Integration. *Integrated Ferroelectrics* vol. 4, pp.175-186, 1994.

[5] R. Watton, P.A. Manning, M.C.J. Perkins, J.P. Gillham and M.A.Todd. Uncooled IR Imaging: Hybrid and Integrated Bolometer Arrays. *SPIE* vol. 2744, pp. 486-499, 1996.

[6] N.M. Shorrocks, R.W. Whatmore, P.C. Osbond. Lead Scandium Tantalate for Thermal Detector Applications. *Ferroelectrics* vol. 106, pp. 387-392, 1990.

[7] R.Watton, M.A. Todd. Induced Pyroelectricity in Sputtered Lead Scandium Tantalate Films and their Merit for IR Detector Arrays. *Ferroelectrics* vol. 118, pp. 279-295, 1991.

[8] V.M. Goldschmidt. Geochemische Verteilungsgesetze der Elemente VII Die Gesetze der Krystallochemie. Skrifter Norske Videnskaps-Akad. Oslo, I. Mat.-Naturv. KI., No. 8, pp. 22-117, 1926.

[9] M.A. Subramanian, G. Aravamudan, G.V. Subba Rao. Oxide Pyrochlores – A Review. *Prog. Solid St. Chem*. vol. 15, pp. 55-143, 1983.

[10] R.A. McCauley. Structural Characteristics of Pyrochlore Formation. J. Appl. Phys. vol. 51, pp. 290-294, 1980.

[11] H.C. Ling, M.F. Yan, W.W. Rhodes. Phase stability in $Pb(B'^{3+}_{1/2}B''^{5+}_{1/2})O_3$ and $Pb(B'^{2+}_{1/3}B''^{5+}_{2/3})O_3$ Compositions. *Ferroelectrics* vol. 89, pp. 69-80, 1989.

[12] C.D.E. Lakeman, X. Zhengkui, D.A. Payne. On the Evolution of Structure and Composition in Sol-Gel derived Lead Zirconate Titanate Thin Layers. *J. Mater. Res* vol. 10, pp. 2042-2051, 1995.

[13] N. Setter, L.E. Cross. The role of B-site cation disorder in diffuse phase transition behaviour of perovskite ferroelectrics. *J. Appl. Phys.* vol. 51(8), pp. 4356-4360, 1980.

[14] C.G.F. Stenger, A.J. Burggraaf. Order-Disorder Reactions in the Ferroelectric Perovskites $PbSc_{1/2}Nb_{1/2}O_3$ and $PbSc_{1/2}Ta_{1/2}O_3$. *Phys. Stat. Sol. (a)* vol. 61, pp. 643-664, 1980.

[15] F.S. Galasso. *Structure, Properties and Preparation of Perovskite-Type Compounds*. Pergamon Press, 1969.

[16] H. Wang, W.A. Schulze. Order-Disorder Phenomenon in Lead Scandium Tantalate. *J. Am. Ceram. Soc* vol. 73(5), pp. 1228-1234, 1990.

[17] Z.C. Kang, C. Caranoni, I. Siny, G. Nihoul, C. Boulesteix. Study of the Ordering of Sc and Ta Atoms in PST by X-Ray Diffraction and High Resolution Electron Microscopy. *J. Solid State Chem* vol. 87, pp. 308-320, 1990.

[18] N. Setter, L.E. Cross. The Contribution of Structural Disorder to Diffuse Phase Transitions in Ferroelectrics. *J. Mat. Sci.* vol. 15, pp. 2478-2482, 1980.

[19] R.D. Shannon, C.T. Prewitt. Effective Ionic Radii in Oxides and Fluorides. *Acta. Cryst. B* vol. 25, pp. 925-946, 1969.

[20] F. Galasso, W. Darby. Ordering of the Octahedrally Coordinated Cation Position in the Perovskite Structure. *J. Phys. Chem.* vol. 66, pp. 131-132, 1962.

[21] G.A. Smolenski. Physical Phenomena in Ferroelectrics with Diffused Phase Transition. *J. Phys. Soc. Japan* vol. 28, pp. 26-37, 1970.

[22] L.E. Cross. Relaxor Ferroelectrics. *Ferroelectrics* vol. 76, pp. 241-267, 1987.

[23] V. Marinova, D. Petrova, M. Veleva. Optical Properties of Pyrochlore Lead Scandium Tantalate Crystals. *Cryst. Res. Technol*. vol. 33, No. 1, pp. 119-124, 1998.

[24] R.W. Whatmore, P. Kirby, A. Patel, N.M. Shorrocks, T. Bland, M. Walker. Integrated Thin Film PZT Pyroelectric Detector Arrays. *Proc. Nato. Conf. On Sci. and Tech. Of Electroceramic Films, E284*, pp. 383, 1994.

[25] A. Patel, D.A. Tossell, N.M. Shorrocks, R.W. Whatmore, R. Watton. Pyroelectric Properties of Lead Based Ferroelectric Thin Films. *Mat. Res. Soc. Symp. Proc.* vol. 310, pp. 53-58, 1993.

[26] Cao, L.E. Cross. The Ratio of Rhombohedral and Tetragonal Phases on the Morphotropic Phase Boundary in Lead Zirconate Titanate. *Jap. J. Appl. Phys. Pt. 1*, vol. 31, Iss. 5A, pp. 1399-1402, 1992.

[27] P.K. Larsen, G.J.M. Dormans, D.J. Taylor, P.J. van Veldhoven. Ferroelectric Properties and Fatigue of $PbZr_{0.51}Ti_{0.49}O_3$ Films of Varying Thickness. *J. Appl. Phys.* vol. 76(4), pp. 2405-2413, 1994.

[28] J.F. Scott, C.A. Araujo, B.M. Melnick, L.D. McMillan, R. Zuleeg. Quantitative Measurement of Space-Charge Effects in Lead-Zirconate-Titanate Memories. *J. Appl. Phys.* vol. 70(1), pp. 382-388, 1991.

[29] B.A. Tuttle, T.J. Headley, B.C. Bunker, R.W. Schwartz, T.J. Zender, C.L. Hernandez, D.C. Goodnow, R.J. Tissot, J. Michael. Microstructural Evolution of $Pb(ZrTi)O_3$ Thin Films Prepared by Hybrid Metallo-Organic Decomposition. *J. Mater. Res*. vol. 7(7), pp. 1876-1882, 1992.

[30] N.M. Shorrocks, A. Patel, M.J. Walker and A.D. Parsons. Integrated Thin Film PZT Pyroelectric Detector Arrays. Proceedings of EMIFI, Nijmegan, April 1995.

[31] J.A. Voigt, B.A. Tuttle, T.J. Headley, D.L. Lamppa. The Pyrochlore-to-Perovskite Transformation in Solution-Derived Lead Zirconate Titanate Thin Films. *Mat. Res. Soc. Symp. Proc.* vol. 361, pp. 395-402, 1995.

[32] K.G. Brooks, I.M. Reaney, R. Klissurska, Y. Huang, L. Bursill and N. Setter. Orientation of Rapid Thermally Annealed Lead Zirconate Titanate Thin Films on (111) Pt Substrates. *J. Mater. Res.* vol. 9(10), pp. 2540-2553, 1994.

[33] W.-P. Xu, Y. Chen, L. Zheng, M. Okuyama, C. Lin. Crystallisation of Thin PZT Films Deposited by Laser Ablation into Ferroelectric Perovskite Phase by Thermal Processing. *Phys. Stat. Sol. (a)* vol. 154, pp. 607-613, 1996.

[34] M.E. Lines and A.M. Glass. *Principles and Applications of Ferroelectrics and Related Materials.* pp. 8-9; Oxford University Press, 1996.

[35] D. Viehland, S.J. Jang, L.E. Cross, M. Wuttig. Freezing of the Polarisation Fluctuations in Lead Magnesium Niobate Relaxors. *J. Appl. Phys*. vol. 68(6), pp. 2916-2921, 1990.

[36] G.A. Smolenski, V.A. Isupov, A.I. Agranovskaya, S.N. Popov. Ferroelectrics with Diffuse Phase Transitions. *Soviet Physics - Solid State* vol. 2 (11), pp. 2584-2594, 1961.

[37] F. Chu, N. Setter, A.K. Tagantsev. The Spontaneous Relaxor-Ferroelectric Transition of $PbSc_{0.5}Ta_{0.5}O_3$. *J. Appl. Phys*. vol. 74(8), pp. 5129-5134, 1993.

[38] R.A. Hanel. Dielectric Bolometer: A New Type of Thermal Radiation Detector. *J. Opt. Soc. Am.* vol. 51(2), pp. 220-223, 1961.

[39] R. Watton. Ferroelectric Materials and Devices in Infrared Detection and Imaging. *Ferroelectrics* vol. 91, pp. 87-108, 1989.

[40] R. Watton, P.A. Manning. Ferroelectrics in Uncooled Thermal Imaging. SPIE vol. 3436, pp. 541-544, 1998.

[41] S.E. Stokowski. Temperature Noise and Dielectric Loss Noise in Pyroelectric Detectors. *Appl. Phys. Lett.* vol. 29(7), pp. 393-395, 1976.

[42] R.L. Kroes, D. Reiss. The Pyroelectric Properties of TGS for Application in Infrared Detection. *NASA Technical Memorandum* TM-82394, 1981.

[43] A.K. Jonscher. Low-Loss Dielectrics. *J. Mat. Sci.* vol. 34, pp. 3071-3082, 1999.

[44] T. Mitsui, I. Tatsuzaki, E. Nakamura. *Ferroelectricity and Related Phenomena Volume 1: An Introduction to the Physics of Ferroelectrics*. Gordon and Breach, 1976.

[45] G. Arlt, H. Neumann. Internal Bias in Ferroelectric Ceramics: Origin and Time Dependence. *Ferroelectrics* vol. 87, pp. 109-120, 1988.

[46] R. Watton, P.A. Manning. The Design of Low-Noise Arrays of MOSFETS for Pyroelectric Array Readout, (LAMPAR). *SPIE* vol. 807, pp. 98-105, 1987.

[47] S.G. Porter. A Brief Guide to Pyroelectric Detectors. *Ferroelectrics* vol. 33, pp. 193, 1981.

[48] C.Hilsum. Infrared Absorption of Thin Metal Films. *J. Opt. Soc. Am.* vol. 44(3), pp. 188-191, 1954.

[49] A.D. Parsons, D.J. Pedder. Thin Film Infrared Absorber Structures for Advanced Thermal Detectors. *J. Vac. Sci. Technol.* vol. 6(3), pp. 1686-1689, 1988.

[50] L.D. Madsen, L. Weaver, H. Ljungcrantz, A.J. Clarke. Analysis of the Stress and Interfacial Reactions in Pt/Ti/SiO_2/Si for Use with Ferroelectric Thin Films. *J. Elec. Mat.* vol. 27(5), pp. 418-426, 1998.

[51] P.D. Hren, H. Al-Shareef, S.H. Rou, A.I. Kingon, P. Buaud, E.A. Irene. Hillock Formation in Platinum Thin Films. *Mat. Res. Soc. Symp. Proc.* vol. 260, pp. 575-580, 1992.

[52] Pt XRD reference file. JCPDS file 4-802.

[53] PST pyrochlore XRD reference file. JCPDS file 45-554.

[54] M.A. Todd, P.P. Donohue, M.A.C. Harper, J.C. Jones. Sputtered Lead Scandium Tantalate Thin Films for Dielectric Bolometer Mode Thermal Detector Arrays. Submitted to *Integrated Ferroelectrics,* March 2000.

[55] M. Sayer. Fabrication and Application of Multi-Component Piezoelectric Thin Films. *Proc. 6th IEEE Int. Symp. App. Ferroelectrics,* pp. 560-568, 1986.

[56] A. Croteau, M. Sayer. Growth and Characterisation of PZT Films Deposited by Reactive Sputtering of Metal Targets. *Proc. 6th IEEE Int. Symp. App. Ferroelectrics,* pp. 606-609, 1986.

[57] Q. Zhang, R.W. Whatmore, M.E. Vickers, A. Patel. Characterisation of Particle Structure in PZT Sols. *J. Korean Physical Society* vol. 32, S572, 1998.

[58] A. Patel, J. Obhi. *GEC J. Res.* vol. 12, pp. 141, 1995.

[59] S.A. Campbell. *Computational Modeling in Semiconductor Processing, Chapter 6: Rapid Thermal Processing.* Artech House, 1995.

[60] J.J. Friel. X-Ray and Image Analysis in Electron Microscopy. Princeton Gamma Tech.

[61] J.I. Goldstein, D.E. Newbury, P. Echlin, D.C. Joy, C. Fiori, E. Lifshin. *Scanning Electron Microscopy and X-Ray Microanalysis.* Plenum Publishing Corporation, 1981.

[62] PST pyrochlore XRD reference file. JCPDS file 45-554.

[63] B.D. Cullity. *Elements of X-Ray Diffraction.* Addison-Wesley, 2nd Edition, 1959.

[64] C. K. Kwok, S.B. Desu. Pyrochlore to Perovskite Phase Transformation in Sol-Gel Derived Lead-Zirconate-Titanate Thin Films. *Appl. Phys. Lett.* vol. 60(12), pp. 1430-1432, 1992.

[65] D.B. Williams, C.B. Carter. *Transmission Electron Microscopy*. Plenum Publishing Corporation, 1996.

[66] R.L. Byer, C.B. Roundy. Pyroelectric Coefficient Direct Measurement Technique and Application to a NSEC Response Time Detector. *Ferroelectrics* vol. 3, pp. 333-338, 1972.

[67] A.G. Chynoweth. Dynamic Method for Measuring the Pyroelectric Effect with Special Reference to Barium Titanate. *J. Appl. Phys.* vol. 27(1), pp. 78-84, 1956.

[68] R.J. Wilson, B.L. Weiss. Invited Review: A Review of the Properties of Aluminium Alloy Films Used During Silicon Device Fabrication. *Vacuum* vol. 42(12), pp. 719-729, 1991.

[69] A.J. Griffin, F.R. Brotzen, C.F. Dunn. Mechanical Properties and Microstructures of Al-1%Si Thin Film Metallisations. *Thin Solid Films* vol. 150, pp. 237-244, 1987.

[70] C.M. Hanson, H.R. Beratan, J.F. Belcher, K.R. Udayakumar, K.L. Soch. Advances in Monolithic Ferroelectric IRFPA Technology. *SPIE* vol. 3379, pp. 60-68, 1998.

[71] S.M. Sze. *VLSI Technology, 2nd Edition.* McGraw-Hill International Editions, 1988.

[72] S.M. Sze. *Semiconductor Devices Physics and Technology.* John Wiley & Sons.

[73] G.W.C. Kaye and T.H. Laby. *Tables of Physical and Chemical Constants.* 15th Ed., Longman Scientific and Technical, 1993.

[74] F. Ericson, N. Kristensen, J-A. Schweitz, U. Smith. A Transmission Electron Microscopy Study of Hillocks in Thin Aluminium Films. *J. Vac. Sci. Technol.* B9(1), pp. 58-63, 1991.

[75] F.M. d'Heurle. Metallurgical topics in silicon device interconnections: Thin film stresses. *International Materials Reviews* vol. 34(2), pp. 53-68, 1989.

[76] D.A. Glocker and S. Ismat Shah (eds). *Handbook of Thin Film Process Technology*. IOP Pubishing, 1995.

[77] P. Singer. Copper Goes Mainstream: Low k to follow. *Semiconductor International* vol. 20(13), pp. 67-70, 1998.

[78] P. Singer. Tantalum, Copper and Damascene: The Future of Interconnects. *Semiconductor International* vol. 21(6), pp. 90-94, 1998.

[79] L. Peters. Low-k Dielectric. *Semiconductor International* vol. 21(10), pp. 64-74, 1998.

[80] N. Setter, L.E. Cross. An Optical Study of the Ferroelectric Relaxors $Pb(Mg_{1/3}Nb_{2/3})O_3$, $Pb(Sc_{1/2}Ta_{1/2})O_3$, and $Pb(Sc_{1/2}Nb_{1/2})O_3$, *Ferroelectrics* vol. 37, pp. 551-554, 1981.

[81] A.J. Bell, A.J. Moulson, L.E. Cross. The Effect of Grain Size on the Permittivity of $BaTiO_3$, *Ferroelectrics* vol. 54, pp. 147-150, 1984.

[82] N.M. Shorrocks, A. Patel, R.W.Whatmore. Pyroelectric Properties of Thin Film Lead Scandium Tantalate. *Ferroelectrics* vol. 133, pp. 35-40, 1992.

[83] A. Patel, N.M. Shorrocks, R.W.Whatmore. Physicochemical Properties of Sol-Gel Derived Lead Scandium Tantalate $Pb(Sc_{0.5}Ta_{0.5})O_3$ Thin Films. *Ferroelectrics* vol. 134, pp. 343-348, 1992.

[84] D. Liu, D.A. Payne. Lower Temperature Crystallisation and Ordering in Sol-Gel Derived $Pb(Sc_{0.5}Ta_{0.5})O_3$ Powders and Thin Layers. *J. Appl. Phys.* vol. 77(7), pp. 3361-3364, 1995.

[85] C. Bjormander, K. Sreenivas, A.M. Grishin, K.V. Rao. Pyroelectric $PbSc_{0.5}Ta_{0.5}O_3/Y_1Ba_2Cu_3O_{7-x}$ Thin-Film Heterostructures. *Appl. Phys. Lett.* vol. 67(1), pp. 58-60, 1995.

[86] M.A. Todd, P.P. Donohue, J.C. Jones, D.J. Wallis, M.J. Slater, M.A. Harper, R. Watton. Deposition and Annealing of Lead Scandium Tantalate Thin Films for High Performance Thermal Detector Arrays. *Integrated Ferroelectrics* vol. 25, pp. 113-123, 1999.

[87] S.B. Krupanidhi, N. Maffei, M. Sayer, K. El-Assal. RF Planar Magnetron Sputtering and Characterisation of Ferroelectric PZT Films. *J. Appl. Phys.* vol. 54(11), pp. 6601-6609, 1983.

[88] E.M. Griswold, L. Weaver, D.S. McIntyre, M. Sayer, I.D. Calder. Crystallisation of Rapid Thermal Processed PZT:Platinum and Ruthenium Oxide Electrodes. *Integrated Ferroelectrics* vol. 10, pp. 123-130, 1995.

[89] L.A. Bursill, K.G. Brooks. Crystallisation of Sol-Gel Derived Lead-Zirconate-Titanate Thin Films in Argon and Oxygen Atmospheres. *J. Appl. Phys.* vol. 75(9), pp. 4501-4509, 1994.

[90] J. Chen, K.R. Udayakumar, K.G. Brooks, L.E. Cross. Rapid Thermal Annealing of Sol-Gel Derived Lead Zirconate Titanate Thin Films. *J. Appl. Phys.* vol 71(9), pp. 4465-4469, 1992.

[91] C.V.R. Vasant Kumar, M. Sayer, R. Pascual, D.T. Amm, Z. Wu, D.M. Swanston. Lead Zirconate Titanate Films by Rapid Thermal Processing. *Appl. Phys. Lett.* vol. 58(11), pp. 1161-1163, 1991.

[92] E.M. Griswold, L. Weaver, I.D. Calder, M. Sayer. Rapid Thermal Processing and Crystallisation Kinetics in Lead Zirconate Titanate (PZT) Thin Films. *Mat. Res. Soc. Symp. Proc.* vol. 361, pp. 389-394, 1995.

[93] P.C. Joshi, S.B. Desu. Structural and Electrical Characteristics of Rapid Thermally Processed Ferroelectric $Bi_4Ti_3O_{12}$ Thin Films Prepared by Metalorganic Solution Deposition Technique. *J. Appl. Phys*. vol. 80(4), pp. 2349-2357, 1996.

[94] C.V.R. Vasant Kumar, M. Sayer, R. Pascual. Ferroelectric Lead Niobate Films by Pulsed Thermal Processing. *Appl. Phys. Lett.* vol. 60(18), pp. 2207-2209, 1992.

[95] J.A. Thornton. Influence of Apparatus Geometry and Deposition Conditions on the Structure and Topography of Thick Sputtered Coatings. *J. Vac. Sci. Technol.* vol. 11(4), pp. 666-670, 1974.

[96] R.W. Whatmore, Z. Huang, M. Todd. Sputtered Lead Scandium Tantalate Thin Films:Pb^{4+} in B-sites in the Perovskite Structure. *J. Appl. Phys.* vol. 82(11), pp. 5686-5694, 1997.

[97] W. Zhang, K. Sasaki, T. Hata. Analysis of Sputter Process on a New ZrTi+PbO Target System and its Application to Low-Temperature Deposition of Ferroelectric $Pb(Zr,Ti)O_3$. *Jpn. J. Appl. Phys.* vol. 35(3) Part 1, 1868-1872 (1996).

[98] C.D. Meekison, K.Z. Baba-Kishi, R. Watton, M.A. Todd. Epitaxy and Interfacial Phase in Thin Films of Lead Scandium Tantalate Deposited by Reactive Sputtering on a Platinum Interlayer. *Int. Ferroelectrics* vol. 8, pp. 283-291, 1995.

[99] T. Maeder, L. Sagalowicz, P. Muralt. Stabilised Platinum Electrodes for Ferroelectric Film Deposition using Ti, Ta and Zr Adhesion Layers. *Jpn. J. Appl. Phys.* vol 37(1/4A), pp. 2007-2012, 1998.

[100] Pt_xPb intermetallic XRD reference file. JCPDS file 6-574.

[101] Z. Huang, Q. Zhang, R.W. Whatmore. Structural Development in the Early Stages of Sol-Gel Prepared Lead Zirconate Titanate Thin Films. *J. Appl. Phys*. vol. 86(3), pp. 1662-1669, 1999.

[102] S. Chen, I. Chen. Temperature-Time Texture Transition of $Pb(Zr_{1-x}Ti_x)O_3$ Thin Films: I Role of Pb-rich Intermediate Phases *J. Am. Ceram. Soc.* vol 77, pp. 2332-2336, 1994.

[103] S. Aggarwal, S. Madhukar, N. Nagaraj, I.G. Jenkins, R. Ramesh, L. Boyer, J.T. Evans Jr. Can Non-Stoichiometry Influence Ferroelectric Properties of $Pb(Zr,Ti)O_3$ Thin Films. *Appl. Phys. Lett.* vol. 75(5), pp. 716-718, 1999.

[104] A. Seifert, P. Muralt, N. Setter. Electrical Properties and Microstructural Evolution of Porous $Pb_{1-x}Ca_xTiO_3$ Pyroelectric Thin Films. *Ferroelectrics* vol. 225, pp. 49-56, 1999.

[105] C.J. Brierley, N.I. Payne, N.M. Shorrocks, I.M. Watson, R.W. Whatmore. Ferroelectric Materials for Dielectric Bolometers. *Plessey Annual Research Report*, RP9-289, 1986.

[106] C.H. Lin, S.W. Lee, H. Chen, T.B. Wu. Dielectric Properties of Metal-Organic Chemical Vapour Deposited Highly Textured $Pb(ScTa)_{1-x}Ti_xO_3$ (x = 0-3) Relaxor Ferroelectric Thin Films on $LaNiO_3$ Electrode Buffered Si. *Appl. Phys. Lett*. vol. 65(16), pp. 2485-2487, 1999.

[107] Ferroelectric Materials, *Handbook of Thin Film Processing Technology,* IOP Publishing, 1995.

[108] H.D. Meierling. Charge Compensation by O^{2-} Vacancies in Cr^{3+} Doped $SrTiO_3$. *Phys. Stat. Sol*. (b) vol. 43, pp 191-197, 1971.

[109] N.M. Shorrocks, A. Patel, M.J. Walker and A.D. Parsons. Integrated Thin Film PZT Pyroelectric Detector Arrays. *Microelectronic Engineering* vol. 29, pp. 59-66, 1995.

[110] PbO, orthorhombic (Massicot), XRD reference file. JCPDS file 5-570.

[111] Y. Matsui, M. Okuyama, N. Fujita, Y. Hamakawa. Laser Annealing To Produce Ferroelectric-Phase $PbTiO_3$ Thin Films. *J. Appl. Phys*. vol. 52(8), pp. 5107-5111, 1981.

[112] C-T. Lin, J.D. McNeill, B.W. Scanlan, J.S. Webb, R.A. Lipeles, M.S. Leung. Localised Laser Annealing of PZT/Pt Films Based on Metallo-Organics in Aqueous Micellar Solutions. *Chemical Processing of Advanced Materials*, pp. 449-455, L.L. Hench and J.K. West (Eds), John Wiley & Sons, 1992.

[113] U. Varshney, B.D. Eischelberger, R.D. Churchill. Laser Crystallisation of Spin-on Ferroelectric Thin Films. Virtual Proceedings of 1996 NSF Design and Manufacturing Grantees Conference, Albuquerque, January 3-5, 2 pages, 1996.

[114] U. Varshney, A.I. Kingon. Method for Producing Low Thermal Budget Ferroelectric Thin Films for Integrated Device Structures using Laser-crystallisation of Spin-on Sol-Gel Films. United States Patent No. 5626670, May 1997.

[115] N. Kubo, N. Kusomoto, T. Inushima, S. Yamazaki. Characteristics of Polycrystalline-Si Thin Film Transistors Fabricated by Excimer Laser Annealing Method. *IEEE Trans. on Electron Devices* vol. 41(10), pp. 1876-1879, 1994.

[116] P. Boher, J.L. Stehle, M. Stehle, B. Godard. Single Shot Excimer Laser Annealing of Amorphous Silicon for AMLCD. *Applied Surface Science* 96-98, pp. 376-383, 1996.

[117] K. Sera, F. Okumura, H. Uchida, S. Itoh, S. Kaneko, K. Hotta. High-Performance TFT's Fabricated by XeCl Excimer Laser Annealing of Hydrogenated Amorphous-Silicon Film. *IEEE Transactions on Electron Devices* vol. 36(12), pp. 2868-2872, 1989.

[118] M.V. Efremov, V.V. Bolotov, V.A. Volodin, L.I. Fedina, E.A. Lipatnikov. Excimer Laser and Rapid Thermal Annealing Stimulation of Solid-Phase Nucleation and Crystallisation in Amorphous Silicon Films on Glass Substrates. *J. Phys.: Condens. Matter* vol**.** 8, pp. 273-286, 1996.

[119] H. Kuriyama, S. Kiyama, T. Kurahawa, S. Noguchi, S. Nakano. A New Method to Enhance Mobility of Poly-Si TFT Recrystallised by Excimer Laser Annealing. *IEEE Transactions on Electron Devices* vol. 38(12), pp. 2693, 1991.

[120] Y. Uchida, K. Shimizu, M. Matsumura. Effects of Excimer-Laser Annealing on Low-Temperature-Deposited Silicon-Nitride Film. *Applied Surface Science* vol. 79/80, pp. 350-355, 1994.

[121] V. Pfeufer, F. Voss, B. Becker-de Mos, U. Stamm, H. Endert, D. Basting. Optimisation of 200W excimer laser for TFT annealing. *SPIE* vol. 2992, pp. 35-44, 1997.

[122] T. Sameshima, S. Usui and M. Sekiya. XeCl Excimer Laser Annealing Used in the Fabrication of Poly-Si TFT's. *IEEE Electron Device Letters* vol EDL-7(5), pp. 276-278, 1986.

[123] P. Baeri, S.U. Campisano, G. Foti, E. Rimini. A Melting Model for Pulsed-Laser Annealing of Implanted Semiconductors. J. Appl. Phys. vol. 50(2), pp. 788-797, 1979.

[124] M.I. Kaganov, I.M. Lifshitz, L.V. Tanatarov. Relaxation between Electrons and the Crystalline Lattice. *Soviet Physics JETP* vol. 4(2), pp. 173-178, (1957).

[125] J.M. Poate and J.W. Mayer (eds). *Laser Annealing of Semiconductors.* Academic Press, 1982.

[126] H.S. Carslaw, J.C. Jaeger. *Conduction of Heat in Solids, 2nd Edition.* Clarendon Press, 1959.

[127] E. Abraham, J.M. Halley. Some Calculations of Temperature Profiles in Thin Films with Laser Heating. *Appl. Phys. A* vol 42, pp. 279-285, 1987.

[128] M. Lax. Temperature Rise Induced by a Laser Beam. *J. Appl. Phys.* vol. 48(9), pp. 3919-3924, 1977.

[129] M. Lax. Temperature Rise Induced by a Laser Beam II. The Nonlinear Case. *Appl. Phys. Lett.* vol. 33(8), pp. 786-788, 1978.

[130] I.D. Calder, R. Sue. Modeling of CW Laser Annealing of Multilayer Structures. *J. Appl. Phys* vol. 53(11), pp. 7545-7550, 1982.

[131] R.F. Wood, G.A. Geist. Modelling of Nonequilibrium Melting and Solidification in Laser-Irradiated Materials. *Phys. Rev. B* vol. 34(4), pp. 2606-2620, 1986.

[132] B.W. Arden and K.N. Astill. *Numerical Algorithms: Origins and Applications.* Addison-Wesley,

[133] C. Pickering. Nondestructive Characterisation of Semiconductor Multilayers. *JOM* vol. 46(9), pp. 60-64, 1994.

[134] E.D. Palik. *Handbook of Optical Constants of Solids II.* Academic Press, 1991.

[135] D.R. Lide. *CRC Handbook of Chemistry and Physics. 76th Ed.* CRC Press,

[136] N.M. Shorrocks. *RM200 PZT Thermal Diffusivity and Heat Capacity Data.* Private Communication.

[137] Z. Huang, M.A. Todd, R. Watton, R.W. Whatmore. Sputtered Lead Scandium Tantalate Thin Films: A Microstructural Study. *J. Mat. Sci.* vol. 33, pp. 363-370, 1998.

[138] R. Bruchhaus, D. Pitzer, R. Primig, W. Wersing, Y. Xu. Deposition of Self Polarised PZT Films by Planar Multi-Target Sputtering. Integrated *Ferroelectrics* vol. 14, pp. 141-149, 1997.

[139] P.P. Donohue, M.A. Todd. Laser Annealing of Ferroelectric Thin Films. International Patent Application No. PCT/GB00/00753.

[140] S.A. Impey, Z. Huang, A. Patel, R. Beanland, N.M. Shorrocks, R. Watton, R.W. Whatmore. Microstructural Characterisation of Sol-Gel Lead-Zirconate Titanate Thin Films. *J. Appl. Phys.* vol. 83(4), pp. 2202-2208, 1998.

[141] P.E. Dyer, R.J. Farley. Dynamics of Laser Induced Periodic Surface Structures in Excimer Laser Ablation of Polymers. *J. Appl. Phys.* vol. 74(2), pp. 1442-1444, 1993.

[142] PZT 52/58 perovskite XRD reference file. JCPDS file 33-784.

[143] PZT 50/50 perovskite XRD reference file. JCPDS file 14-31.

[144] S.L. Swartz, T.R. Shrout. Fabrication of Perovskite Lead Magnesium Niobate. *Mater. Res. Bull*. vol. 17, pp. 1245-1250, 1982.

[145] R. Beanland, A. Patel. Private communication. Unpublished.

[146] E. Hontzopoulos, E. Damigos. Excimer Laser Surface Treatment of Bulk Ceramics. *Appl. Phys. A* vol. 52, pp. 421-424, 1991.

[147] H. Baltes, O. Paul, O. Brand. Micromachined Thermally Based CMOS Microsensors. *Proc. IEEE* vol 86(8), pp. 1660-1678, 1998.

[148] O.M. Paul, J. Korvink, H. Baltes. Determination of the Thermal Conductivity of CMOS IC Polysilicon. *Sensors and Actuators A* (41-42), pp.161-164, 1994.

[149] J. Vancea, G. Reiss, H. Hoffmann. Comment on "Reinterpretation of the Thickness Dependent Conductivity of Thin Platinum B51". *J. Mat. Sci. Letters* vol. 6, pp. 985-986, 1987.

[150] R.W. Powell. Correlation of Metallic Thermal and Electrical Conductivities for both Solid and Liquid Phases. *Int. J. Heat Mass Transfer* vol. 8, pp. 1033-1045, 1965.

[151] M.B. Kleiner, S.A. Kuhn, W. Weber. Thermal Conductivity of Thin Silicon Dioxide Films in Integrated Circuits. *Proc. 25th Eur. Solid State Device Research Conf (ESSDERC)*, pp. 473-476, 1995.

[152] O. Paul, M. von Arx, H. Baltes. CMOS IC Layers: Complete Set of Thermal Parameters. *Semiconductor Characterisation: Present Status and Future Needs*, W.M. Bullis, D.G. Seiler, A.C. Diebold (eds), AIP Press, pp. 197-200, 1996.

[153] AMS. Austria Mikro Systeme International AG 1.2μm CMOS Process Parameters. Document number 9931004, Revision D.

[154] C. Kittel. *Introduction to Solid State Physics. 6th ed.* pp367-374, John Wiley & Sons, 1986.